VERLAG DER TECHNISCHEN UNIVERSITÄT GRAZ

Sebastian Strasser

Reprocessing Multiple GNSS Constellations and a Global Station Network from 1994 to 2020 with the Raw Observation Approach

GEOD 3

MONOGRAPHIC SERIES TU GRAZ
GEODESY

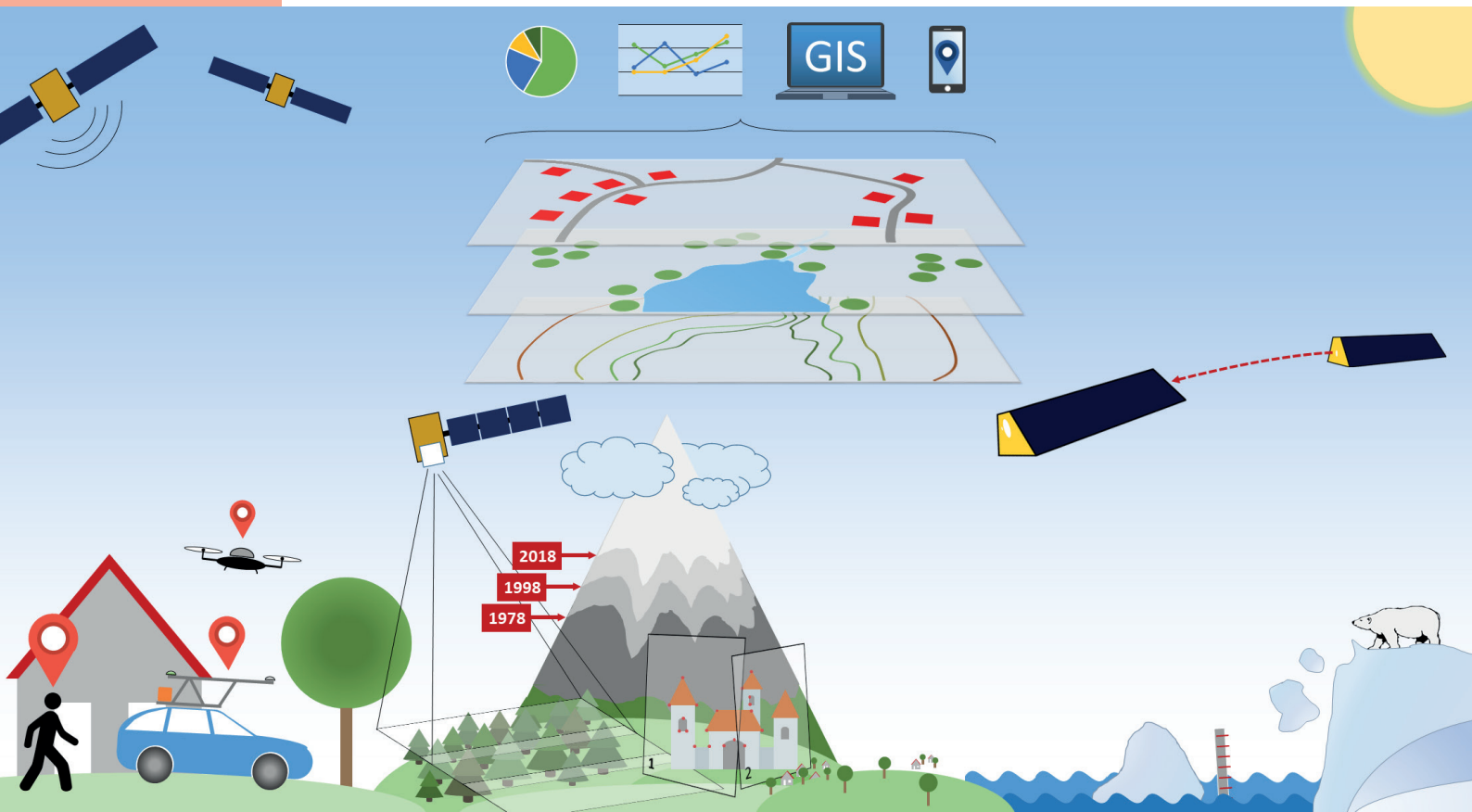

Sebastian Strasser

Reprocessing Multiple GNSS Constellations and a Global Station Network from 1994 to 2020 with the Raw Observation Approach

Monographic Series TU Graz

Geodesy

Monographic Series TU Graz

Geodesy Volume 3

Sebastian Strasser

Reprocessing Multiple GNSS Constellations and a Global Station Network from 1994 to 2020 with the Raw Observation Approach

---

This work is based on the dissertation *"Reprocessing Multiple GNSS Constellations and a Global Station Network from 1994 to 2020 with the Raw Observation Approach"*, presented at Graz University of Technology; submitted to the Faculty of Mathematics, Physics and Geodesy in 2022.

Supervision/Assessment:
Torsten Mayer-Gürr (Graz University of Technology)
Urs Hugentobler (Technical University of Munich)

Cover design Verlag der Technischen Universität Graz
Cover photo ifG, TU Graz

www.tugraz-verlag.at

E-Book
ISBN 978-3-85125-885-1
DOI 10.3217/978-3-85125-885-1

Abstract

An accurate and stable global geodetic reference frame, such as the International Terrestrial Reference Frame (ITRF), is fundamental for quantifying geophysical changes in the Earth system. Global navigation satellite systems (GNSS) are one of the four space-geodetic techniques contributing to the construction of the ITRF. In support of the upcoming ITRF2020 release, the International GNSS Service (IGS) conducted its third reprocessing campaign (repro3), covering the years 1994 to 2020. Graz University of Technology (TUG) participated for the first time as an analysis center in such a reprocessing.

This thesis thoroughly describes the methodologies behind TUG's repro3 contribution. The reprocessing included the three satellite constellations GPS, GLONASS, and Galileo as well as a total of 1182 ground stations. In the latter third of the time series, more than 800 stations were processed per day, resulting in equation systems with hundreds of millions of observations and millions of parameters. The thesis delineates how the raw observation approach was implemented to facilitate a GNSS processing of this scale. This includes methods and strategies developed to handle the extraordinary computational challenges of this reprocessing. All applied parametrizations, models, and corrections are elaborated in detail. For example, generalized methods for the parametrization of code and phase biases in a multi-signal environment are presented.

The evaluation of the resulting GNSS products showed that they are of very high quality. TUG's repro3 contribution gained the highest weight on average in the IGS reference frame combination. The consistency of the obtained satellite orbits is also very high, which was confirmed by preliminary orbit combination results. This means that the methods delineated in this thesis lead to GNSS products that are very competitive with those of other IGS analysis centers. Therefore, the targets of reaching this quality level and providing a valuable contribution to ITRF2020 were successfully achieved.

Acknowledgement

I would like to express my deep gratitude to my supervisor, Prof. Torsten Mayer-Gürr, for his incredible support and guidance throughout my doctoral studies. Our countless discussions were of great help and I appreciate the freedom I was given to work on what was most interesting to me. I am also very thankful to Prof. Urs Hugentobler for reviewing this thesis.

I gratefully acknowledge the Austrian Research Promotion Agency (FFG) for funding the projects that enabled me to work on this research topic. My appreciation also goes to the International GNSS Service (IGS) and the many people from that community who I cooperated with in the past few years.

In addition, I would like to thank my current and former colleagues at the Institute of Geodesy for the great work environment they helped to create. Special thanks go to Andreas Kvas for always being open to questions and discussions and for providing helpful suggestions and ideas whenever I felt stuck with an issue.

Finally, this journey would not have been possible without my family and friends and especially my partner, Victoria, who brings so much joy to my life. I would not have managed to write this doctoral thesis during a global pandemic without her support and love.

Contents

1 Introduction

The Earth is an incredibly complex geophysical system that constantly changes. For example, Earth's surface deforms due to plate tectonics, seismicity, the global water cycle, melting of the polar ice caps and glaciers, and other geophysical effects. An accurate, long-term stable global terrestrial reference frame is fundamental for quantifying these changes occurring in the Earth system (Altamimi et al., 2016). This was recognized by the United Nations General Assembly with the adoption of the first resolution on a global geodetic reference frame (United Nations General Assembly, 2015). The International Terrestrial Reference Frame (ITRF) fills this role since its first realization in 1992. This reference frame has been updated and improved over time. The latest realization (ITRF2014) has been in use for several years and a new version, called ITRF2020, is being prepared for release in 2022.

Four space-geodetic techniques contribute to the construction of the ITRF. These techniques comprise Doppler orbitography and radiopositioning integrated by satellite (DORIS), global navigation satellite systems (GNSS), satellite laser ranging (SLR), and very long baseline interferometry (VLBI). Each technique is represented by an International Association of Geodesy (IAG) service, which coordinates the respective ITRF contribution. The International GNSS Service (IGS; Johnston et al., 2017) conducted its third reprocessing campaign (repro3) in support of ITRF2020. The aim of this reprocessing was to generate a consistent time series of GNSS products ranging from 1994 to 2020. Eleven analysis centers contributed solutions to repro3, one of which was Graz University of Technology (TUG).

This thesis focuses on the methodologies behind the TUG repro3 contribution. They differ in several aspects from well-established methods used by other analysis centers. This is mainly because the raw observation approach (see Chapter 5) was used to process this contribution. The direct usage of uncombined and undifferenced observations offers several benefits but also poses additional challenges, specifically in the parametrization of the ionospheric influence and signal biases. In addition, this was the first time the raw observation approach was utilized in a processing of this scale, which meant special strategies had to be developed to overcome the extraordinary computational challenge. Ultimately, the aim of this thesis is to provide a thorough description of all methods and techniques applied in this reprocessing.

The motivation to participate in the IGS reprocessing campaign was to evaluate if these methods lead to competitive GNSS products. Therefore, the target was to reach the quality level of the other International GNSS Service (IGS) analysis centers. An additional objective was to generate a set of products that is as complete as possible. This means it should encompass as many of the proposed GNSS ground stations as feasible while covering multiple satellite constellations and a wide range of signal types. Achieving these targets and objectives ensures that the obtained solution provides a valuable contribution to the ITRF2020.

1.1 Outline

This thesis is structured as follows. After this brief introduction, Chapter 2 summarizes those aspects of GNSS that are most important for the understanding of subsequent chapters of this thesis. This includes an overview of the satellite constellations, signals and measurements, as well as the IGS. Chapter 3 presents the various reference frames utilized throughout the processing. They comprise global frames as well as reference frames local to a station, satellite, or antenna. The basic principles of parameter estimation are detailed in Chapter 4. This covers methods for the efficient setup and solution of the normal equation system, the application of constraints to resolve rank deficiencies, as well as variance component estimation to determine a proper relative weighting of the observations.

Chapter 5 then describes the raw observation approach in detail. Starting from the observation equations, a set of intermediate parameters are derived for each group of observations. This facilitates the preelimination of the ionospheric influence, which is delineated as well. Next, this chapter presents a way to structure the normal equation matrix that enables an efficient storage in memory. This is followed by a procedure to effectively obtain the residuals in order to determine new weights via variance component estimation. Finally, strategies for solving large systems including hundreds of millions of observations and millions of parameters are presented.

Chapter 6 provides insights into parametrizations, models, and corrections for the various components of the observation equations. It covers satellite attitude, satellite orbits, clock errors, ionosphere, troposphere, code and phase biases, phase ambiguities, Earth rotation, station positions, antennas, and other effects and corrections. Each section presents state-of-the-art models, if available, and/or ways to parameterize unknown effects. The raw observation approach leads to specific challenges in terms of handling

the unknown code and phase biases as well as ambiguities. Sections 6.5 and 6.6 detail approaches to obtain appropriate parametrizations that overcome these challenges.

Chapter 7 describes the methods applied during observation preprocessing. This step aims at detecting faulty or poor-quality observations that are subsequently removed or weighted down before the actual processing begins. Here, generalized methods for cycle slip and outlier detection in a multi-signal environment are presented.

Chapter 8 focuses on the reprocessing itself. The processing setup is delineated, including all the used models, settings, data, and metadata. This is followed by a description of the resulting GNSS products. The most important products are then evaluated internally and externally. This evaluation covers station positions, Earth rotation and reference frame parameters, satellite orbits, and signal biases. Finally, Chapter 9 concludes the thesis and provides an outlook on potential future research topics.

2 Global navigation satellite systems

This chapter briefly summarizes some aspects of GNSS that are important for subsequent chapters of this thesis. First, Section 2.1 gives an overview of the three satellite constellations considered in the analyses, mainly focusing on their different characteristics and satellite types. Furthermore, the notations for referencing specific satellites and signals (see Section 2.2) are presented. Finally, Section 2.3 briefly introduces the IGS and lists the analysis centers that contributed to the reprocessing campaign covered in this thesis.

2.1 Satellite constellations

There are four GNSS constellations and several regional systems providing positioning, navigation, and timing services. The four global satellite constellations are the US Global Positioning System (GPS), the Russian Globalnaya Navigatsionnaya Sputnikovaya Sistema (GLONASS), the European system Galileo, and the Chinese BeiDou Navigation Satellite System (BDS). GPS, GLONASS, and Galileo were part of the reprocessing campaign and thus are the main focus of this thesis. Their system characteristics are summarized in Table 2.1. While the methods detailed in later chapters generally also apply to BDS and regional systems, such as the Japanese Quasi-Zenith Satellite System (QZSS), those constellations are not discussed further here.

2.1.1 Satellite types

Each GNSS constellation consists of different satellite types. This is mostly due to technological advances and spacecraft manufacturer changes over time. Figure 2.1 provides an overview of the operational periods for the various satellite types. The main differentiating characteristics of these satellite types include spacecraft geometry, mass, surface material properties, antenna properties, attitude behavior, transmitted signals, and transmit power. Figure 2.2 displays different GPS and Galileo satellite types. It is

Table 2.1: System parameters for GPS, GLONASS, and Galileo (Hofmann-Wellenhof et al., 2008; Romero, 2020)

Characteristic	GPS	GLONASS	Galileo
Nominal satellites	24	24	27
Orbital planes	6	3	3
Orbit inclination	55°	64.8°	56°
Semimajor axis	26 560 km	25 508 km	29 601 km
Plane separation	60°	120°	120°
Revolution peroid	∼11 h 58 min	∼11 h 16 min	∼14 h 5 min
Ground track repeat	∼1 day	∼8 days	∼10 days
Signal separation	CDMA	FDMA	CDMA
Frequencies [MHz]	L1: 1575.420	G1: 1602.000	E1: 1575.420
	L2: 1227.600	G2: 1246.000	E5a: 1176.450
	L5: 1176.450	G3: 1202.025	E5b: 1207.140
			E6: 1278.750

clearly visible that their shapes vary significantly. This has implications for some of the models and parametrizations covered in Chapter 6. Illustrations of GLONASS satellites can be found, for example, in Revnivykh et al. (2017).

GPS satellite types, often also called blocks, include GPS-I, GPS-II, GPS-IIA, GPS-IIR-A, GPS-IIR-B, GPS-IIR-M, GPS-IIF, and GPS-IIIA. GPS-IIR-A and GPS-IIR-B satellites only differ in their antennas and are often referred to as just GPS-IIR if this differentiation is not relevant. More information about the GPS satellite types can be found, for example, in Hegarty (2017).

The GLONASS satellite types are called GLO, GLO-M, GLO-M+, GLO-K1A, and GLO-K1B. Here, GLO refers to the satellite type that formed the operational constellation from 1994 until the introduction of the later types. Before that, there were a few other satellite variations, which are not relevant for this thesis. Again, GLO-M and GLO-M+ as well as GLO-K1A and GLO-K1B are often just referred to as GLO-M and GLO-K, respectively. Revnivykh et al. (2017) provides further information on the GLONASS satellite types and their differences.

The Galileo constellation consists of two main satellite types. These are the four in-orbit validation (IOV) satellites, which are denoted as GAL-1 in this thesis, and the full operational capability (FOC) satellites, here called GAL-2. The two test satellites GAL-0A and GAL-0B have not been considered in the reprocessing contribution and are thus not discussed further. More details about the Galileo satellite types and their characteristics are given, for instance, in Falcone et al. (2017).

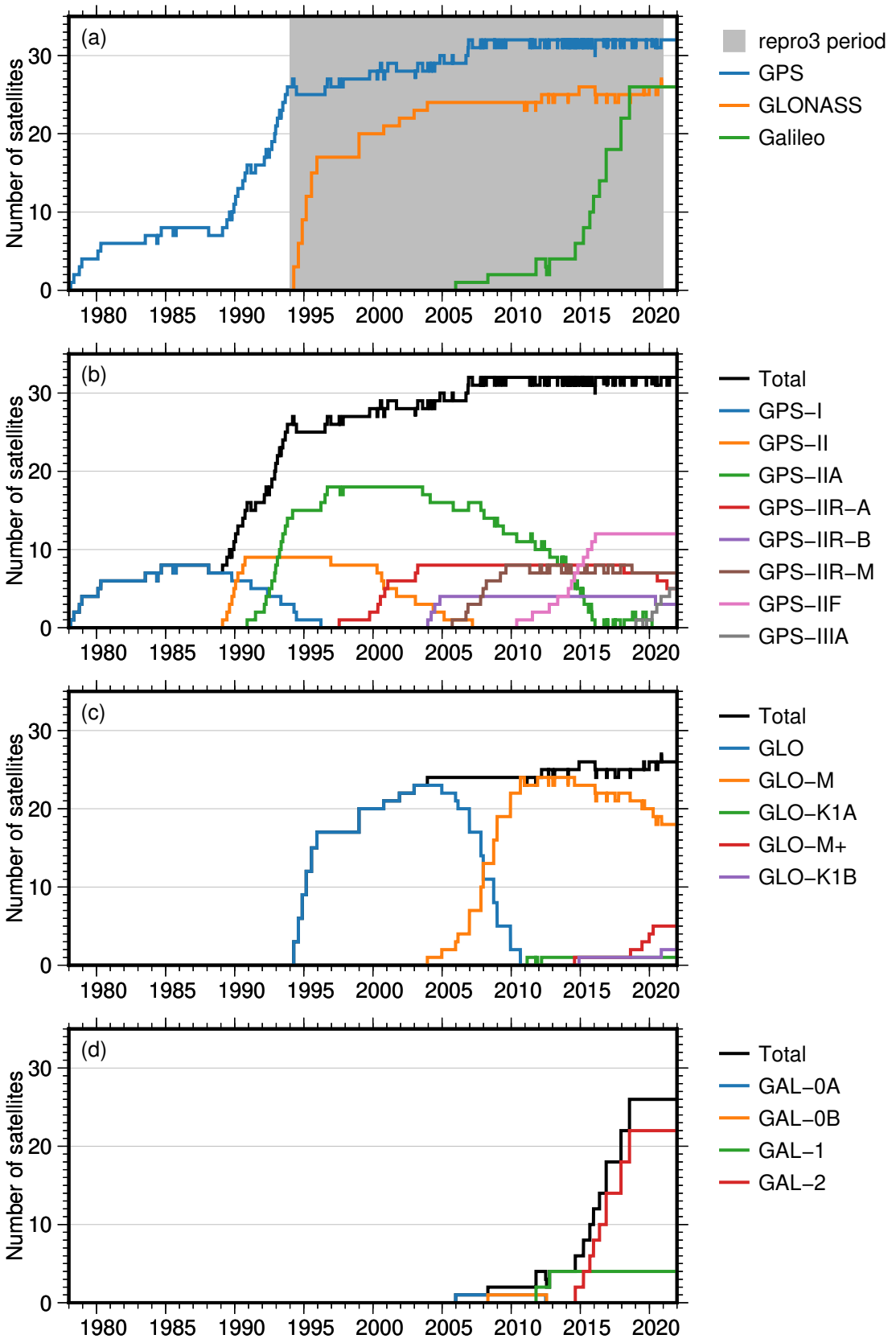

Figure 2.1: Number of operational GNSS satellites over time: **(a)** per constellation, **(b)** per type within GPS, **(c)** per type within GLONASS, **(d)** per type within Galileo

(a) GPS-II/GPS-IIA

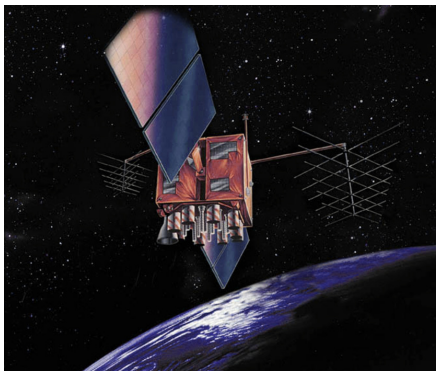

(b) GPS-IIR

(c) GPS-IIR-M

(d) GPS-IIF

(e) GPS-IIIA

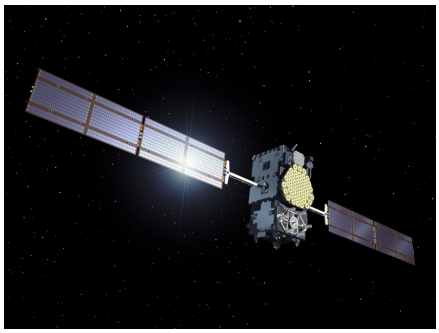

(f) GAL-1 (© ESA)

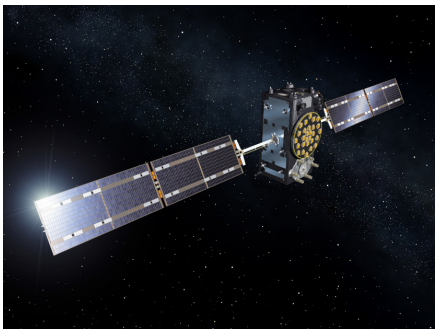

(g) GAL-2 (© ESA–Pierre Carril)

Figure 2.2: Artist's renditions of GPS and Galileo satellite types (courtesy of United States Government and ESA)

2.1.2 Satellite identifiers

Several identifiers can be used to refer to a specific satellite, two of which are primarily used within the IGS. The space vehicle number (SVN) is a unique identifier for a specific satellite that does not change over time. Within the IGS, SVNs are represented by a four-character code starting with a letter that represents the system (G for GPS, R for GLONASS, and E for Galileo) followed by a three-digit number. For example, G075 refers to the first GPS-IIIA satellite launched on 23 December 2018.

The satellite number, on the other hand, is a unique identifier within the active satellites of a constellation at a specific point in time. The Receiver Independent Exchange (RINEX) convention (Romero, 2020) defines this three-character code as a system identifier (same as for SVN) followed by a two-digit number that contains either the pseudorandom noise (PRN) code (GPS, Galileo) or the orbit slot number (GLONASS). For instance, the satellite G075 currently transmits the PRN code 18 and thus can be referred to as G18. In the past, G18 has referred to satellites G018 (1990–2000), G054 (2001–2018), and G034 (2018–2020). From a processing perspective, it is often easier to identify the observed satellites by satellite number (e.g., R01–R24 for the nominal 24 GLONASS satellites) instead of SVN. For this reason, the satellite number is primarily used to refer to satellites throughout this thesis.

2.2 Signals and measurements

GNSS processing in a modern multi-constellation environment involves a diverse set of signals and measurements. Meurer and Antreich (2017) describes the basic principles of signals and modulations used in satellite navigation. Won and Pany (2017) details how these signals are processed at the receiver side in order to obtain code and phase measurements. More information about the architecture of GNSS receivers and antennas can be found in Eissfeller and Won (2017) and Maqsood et al. (2017), respectively.

This thesis uses the signal type notation from the RINEX 3 convention (Romero, 2020). A signal type $[\tau\nu a]$ consists of the measurement type τ (C for code and L for phase), the frequency ν, and the signal attribute a. In case any part of this notation is omitted (e.g., $[\tau\nu]$) or replaced by a specific identifier (e.g., [L]), it implies that the omitted parts are not relevant.

Table 2.1 lists the frequencies on which satellites of the three constellations transmit their signals. Since RINEX only uses a single digit to encode the frequency, a direct mapping of the commonly used frequency band names to the RINEX notation is not

Table 2.2: Transmitted phase and code signals per satellite type in RINEX 3 notation, omitting military and other restricted signals (Falcone et al., 2017; Hegarty, 2017; Montenbruck et al., 2017; Revnivykh et al., 2017; Romero, 2020)

Satellite type	Phase signals	Code signals
GPS-I	L1, L2	C1C, C1W, C2W
GPS-II	L1, L2	C1C, C1W, C2W
GPS-IIA	L1, L2	C1C, C1W, C2W
GPS-IIR	L1, L2	C1C, C1W, C2W
GPS-IIR-M	L1, L2	C1C, C1W, C2W, C2S, C2L
GPS-IIF	L1, L2, L5	C1C, C1W, C2W, C2S, C2L, C5I, C5Q
GPS-IIIA	L1, L2, L5	C1C, C1W, C1S, C1L, C2W, C2S, C2L, C5I, C5Q
GLO	L1, L2	C1C, C1P, C2P
GLO-M	L1, L2	C1C, C1P, C2C, C2P
GLO-M+	L1, L2, L3	C1C, C1P, C2C, C2P, C3I, C3Q
GLO-K	L1, L2, L3	C1C, C1P, C2C, C2P, C3I, C3Q
GAL-1	L1, L5, L6, L7	C1B, C1C, C5I, C5Q, C6B, C6C, C7I, C7Q
GAL-2	L1, L5, L6, L7	C1B, C1C, C5I, C5Q, C6B, C6C, C7I, C7Q

always possible. For example, the Galileo bands are encoded as $\nu_{\mathrm{E1}} = 1$, $\nu_{\mathrm{E5a}} = 5$, $\nu_{\mathrm{E5b}} = 7$, and $\nu_{\mathrm{E6}} = 6$ in the RINEX notation. The adjoining bands E5a and E5b can also be measured as one wider band called E5 ($\nu_{\mathrm{E5}} = 8$ in RINEX).

GLONASS applies frequency division multiple access (FDMA) on its frequencies G1 and G2 (Revnivykh et al., 2017). This means that satellites transmit on slightly different frequencies, which can be utilized to uniquely identify them. The frequency offsets are $\Delta\nu_{\mathrm{G1}}(k) = \frac{9}{16}k\,\mathrm{MHz}$ and $\Delta\nu_{\mathrm{G2}}(k) = \frac{7}{16}k\,\mathrm{MHz}$, where k is a so-called frequency number. GLONASS originally utilized 25 frequency channels ($k \in [0, 24]$), one for each of the nominally 24 satellites and one for testing. This was later reduced to 14 channels ($k \in [-7, 6]$), one for each set of two antipodal satellites in the same orbital plane and two for testing purposes. Such a setup is sufficient because no receiver can observe two antipodal satellites at the same time. GLONASS plans to transition to code division multiple access (CDMA) using three frequencies that are going to be transmitted in addition to the two legacy FDMA frequencies (Romero, 2020). More recent GLONASS satellites already transmit signals on one of these new frequencies (see Table 2.2).

The signal attribute a differentiates between the various signals that are encoded onto the same frequency. Table 2.2 provides an overview of the signals transmitted by the different satellite types, excluding military and other restricted signals. In case of GPS, C1C is the so-called C/A code transmitted on frequency L1. C1W and C2W, on the other hand, are the encrypted P code signals on L1 and L2. The attribute W is used here instead of P since P refers to unencrypted P code measurements in the RINEX notation. In practice, commercial receivers measure the encrypted code (W) and not

Table 2.3: Analysis centers contributing to repro3

Abbrev.	Name	Main location
COD	Center for Orbit Determination in Europe	Bern, Switzerland
EMR	Natural Resources Canada	Ottawa, Canada
ESA	European Space Agency	Darmstadt, Germany
GFZ	GeoForschungsZentrum	Potsdam, Germany
GRG	Groupe de Recherche de Géodésie Spatiale	Toulouse, France
JPL	Jet Propulsion Laboratory	Pasadena, USA
MIT	Massachusetts Institute of Technology	Cambridge, USA
NGS	National Geodetic Survey	Silver Springs, USA
TUG	Graz University of Technology	Graz, Austria
ULR	Université de La Rochelle	La Rochelle, France
WHU	Wuhan University	Wuhan, China

the unencrypted code (P). Some receivers measure linear combinations of transmitted signals. A different attribute (e.g., X) is assigned to such measurements in the RINEX 3 convention (Romero, 2020).

2.3 International GNSS Service

Under the banner of the IGS, research institutions, universities, and agencies from around the world openly provide high-quality GNSS data and products to users (Johnston et al., 2017). GNSS observations are collected from a global network of ground stations, some of which have been continuously operating since the early 1990s. Products usually comprise satellite orbits and clocks, receiver positions and clocks, and Earth rotation parameters, but can also include troposphere parameters, ionosphere maps, signal biases, and satellite attitude. Analysis centers generate these products on an operational basis and in the form of occasional reprocessing campaigns. These usually cover the full time period since the launch of the IGS in 1994. The analysis centers contributing to the third reprocessing campaign (repro3) are listed in Table 2.3.

In addition, the IGS provides combinations of individual analysis center products (Weiss et al., 2017). Combined products include satellite orbits and clocks, receiver positions and clocks, Earth rotation parameters, and in the case of repro3 also signal biases. These combined products are generally more robust and often more precise than individual solutions. Furthermore, they are usually more complete since they join the different sets of satellites and stations processed by the individual analysis centers.

3 Reference frames

GNSS processing involves several different reference frames (e.g., Krakiwsky and Wells, 1971; Hofmann-Wellenhof et al., 2008; Misra and Enge, 2011; Jekeli and Montenbruck, 2017). Satellite orbits are commonly expressed in a celestial reference frame (CRF), while station positions are valid in a terrestrial reference frame (TRF). Antenna offsets are usually provided in a satellite body reference frame (SRF) at the satellite and a local topocentric reference frame (LRF) at the station. Offsets and variations within these antennas are then defined in an antenna reference frame (ARF). In addition, comparing station positions in a LRF and satellite orbits in a local orbit reference frame (ORF) often helps with the interpretation of results.

Sections 3.1 to 3.6 of this chapter detail how the above-mentioned reference frames are defined in this thesis. In addition, Figure 3.1 illustrates how these frames are connected to each other. Here, it separates between pure rotations ($\mathbf{R}$) and transformations ($\mathbf{T}$), which usually involve the flip of an axis direction. The latter is necessary when transitioning from a right-handed to a left-handed frame or vice versa.

Finally, Section 3.7 describes the 7-parameter Helmert transformation. It can be used to transform coordinates from one reference frame to another. In the context of this thesis, Helmert transformation parameters are estimated to align different realizations of the TRF. This is important when comparing different solutions and when a solution has to be aligned to a specific TRF realization.

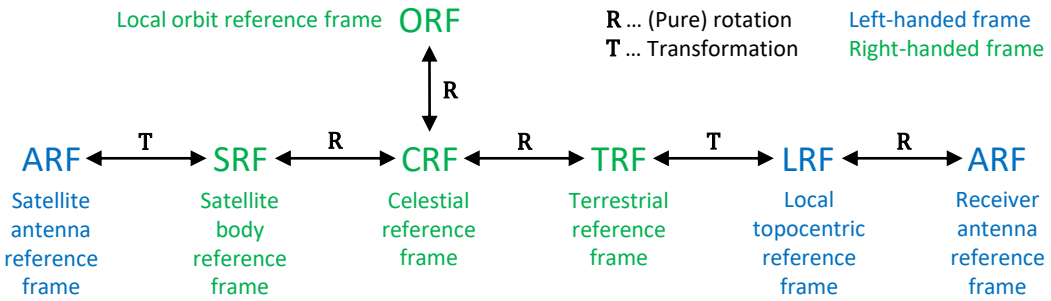

Figure 3.1: Overview of reference frames relevant for GNSS processing

3.1 Celestial reference frame

The celestial reference frame (CRF) refers to an Earth-centered quasi-inertial reference frame. It is defined as a right-handed frame with the following characteristics.

Origin Located in Earth's center of mass.

$\mathbf{e}_x$ **axis** Points towards the vernal equinox.

$\mathbf{e}_y$ **axis** Completes the right-handed frame ($\mathbf{e}_y = \mathbf{e}_z \times \mathbf{e}_x$).

$\mathbf{e}_z$ **axis** Points towards the celestial north pole.

The International Earth Rotation and Reference Systems Service (IERS) maintains the International Celestial Reference Frame (ICRF), which is the realization of the International Celestial Reference System (ICRS). More information about the ICRS and ICRF, such as the exact definition of the vernal equinox and celestial north pole, can be found in the IERS conventions (Petit and Luzum, 2010). The rotation between CRF and TRF is detailed in Section 6.8.

3.2 Terrestrial reference frame

The terrestrial reference frame (TRF) is both Earth-centered and Earth-fixed, meaning it rotates with Earth. This right-handed frame is defined as follows.

Origin Located in Earth's center of mass.

$\mathbf{e}_x$ **axis** Points towards the mean Greenwich meridian.

$\mathbf{e}_y$ **axis** Completes the right-handed frame ($\mathbf{e}_y = \mathbf{e}_z \times \mathbf{e}_x$).

$\mathbf{e}_z$ **axis** Points towards the terrestrial north pole.

The ITRF realizes the International Terrestrial Reference System (ITRS) and is maintained by the IERS. The IERS conventions (Petit and Luzum, 2010) provide a more detailed description of the ITRS and ITRF, including the definition of the mean Greenwich meridian and the terrestrial north pole. More information about the rotation between TRF and CRF can be found in Section 6.8.

3.3 Local topocentric reference frame

A local topocentric reference frame (LRF) is commonly used to describe coordinate differences relative to a point on Earth's surface. In this thesis, the LRF is defined as a left-handed frame with the following characteristics (e.g., Krakiwsky and Wells, 1971).

Origin Typically located at some point on Earth's surface (e.g., at a station).

$\mathbf{e}_n$ **axis** Points towards the local geographic north direction in the tangent plane.

$\mathbf{e}_e$ **axis** Points towards the local geographic east direction in the tangent plane.

$\mathbf{e}_u$ **axis** Points towards the local ellipsoidal zenith (i.e., up) direction.

This frame is helpful in interpreting station coordinate behavior. For example, certain geophysical models mainly affect the up component and seasonal signals are clearly visible in the corresponding time series. Station operators also provide receiver antenna eccentricities (see Section 6.10.1) in this frame. Another application of this frame is to describe the azimuth and elevation angle of incoming GNSS signals. Here, the azimuth angle is counted clockwise from $\mathbf{e}_n$ to $\mathbf{e}_e$. Azimuth and elevation angles are, for example, required to model tropospheric slant delays (see Section 6.7).

The LRF axes

$$\mathbf{e}_n = \mathbf{e}_u \times \mathbf{e}_e \tag{3.1}$$

$$\mathbf{e}_e = \begin{bmatrix} 0 \\ 0 \\ 1 \end{bmatrix} \times \mathbf{e}_u \tag{3.2}$$

$$\mathbf{e}_u = \begin{bmatrix} \cos\varphi \cos\lambda \\ \cos\varphi \sin\lambda \\ \sin\varphi \end{bmatrix} \tag{3.3}$$

can be determined based on the ellipsoidal latitude φ and longitude λ of a point $\mathbf{r}^{\text{TRF}}_{\text{Origin}}$ that describes the origin of the LRF in a global frame (i.e, the TRF), Consequently, the transformation matrix from the left-handed LRF to the right-handed TRF is

$$\mathbf{T}^{\text{TRF}}_{\text{LRF}} = \begin{bmatrix} \mathbf{e}_n & \mathbf{e}_e & \mathbf{e}_u \end{bmatrix} . \tag{3.4}$$

3.4 Satellite body reference frame

The satellite body reference frame (SRF) is fixed to the mechanical structure of a satellite. The origin and axis directions for the various GNSS satellite types depend on the satellite

manufacturer. Therefore, the IGS adopted a common SRF for all satellites (Montenbruck et al., 2015a). It is defined as follows.

Origin Located in the satellite's center of mass.

$\mathbf{e}_x$ **axis** Points towards the permanently sunlit panel of the satellite bus (i.e., roughly towards the Sun).

$\mathbf{e}_y$ **axis** Points along the solar panel rotation axis in the direction defined by $\mathbf{e}_y = \mathbf{e}_z \times \mathbf{e}_x$.

$\mathbf{e}_z$ **axis** Points along the antenna boresight direction (i.e., towards Earth).

The rotation matrix from this right-handed frame to the CRF is

$$\mathbf{R}_{\text{SRF}}^{\text{CRF}} = \begin{bmatrix} \mathbf{e}_x & \mathbf{e}_y & \mathbf{e}_z \end{bmatrix} . \tag{3.5}$$

It describes the satellite's attitude or orientation in space. Section 6.1 details the various attitude modes that are utilized by GNSS satellites. Most of them follow a nominal yaw-steering behavior outside of so-called eclipse seasons, which is when a satellite enters Earth's shadow once per revolution. In this nominal case, the axes from Equations (6.1) to (6.3) can be substituted into (3.5).

3.5 Antenna reference frame

The antenna reference frame (ARF) is fixed to the physical structure of a GNSS antenna. This frame is used to define the electronic center of the antenna as well as direction-dependent variations. For a receiver antenna, it has the following characteristics.

Origin Located at the antenna reference point (e.g., at the bottom of the antenna).

$\mathbf{e}_x$ **axis** Points towards a vendor-defined reference marker in the plane normal to the antenna boresight direction.

$\mathbf{e}_y$ **axis** Completes the left-handed frame ($\mathbf{e}_y = \mathbf{e}_x \times \mathbf{e}_z$).

$\mathbf{e}_z$ **axis** Points along the antenna boresight direction.

The azimuth angle is counted clockwise from the $\mathbf{e}_x$ to the $\mathbf{e}_y$ axis. Within this thesis, the same frame definition is also used for satellite antennas. The reason for this is that it allows for the generalization of all GNSS antennas.

Assuming that a receiver antenna is leveled horizontally, the rotation matrix from the left-handed LRF to the left-handed ARF is simply

$$\mathbf{R}_{\text{LRF}}^{\text{ARF}} = \mathbf{R}_z(\alpha) . \tag{3.6}$$

Here, the matrix $\mathbf{R}_z$ is the basic rotation around the z axis and α is the angle of misalignment from geographic north, counted clockwise from north to east. IGS stations are instructed to orient their antennas towards geographic north (IGS Infrastructure Committee, 2015). However, not all antennas of the more than 1200 stations considered in the reprocessing campaign have always been aligned in that way. A misalignment from geographic north is usually reported by station operators in the station log file. Section 6.10.3 provides more details on this topic.

For a satellite antenna, the transformation from the right-handed SRF to the left-handed ARF is

$$\mathbf{T}_{\text{SRF}}^{\text{ARF}} = \begin{bmatrix} 1 & 0 & 0 \\ 0 & -1 & 0 \\ 0 & 0 & 1 \end{bmatrix} \mathbf{R}_z(90°)\,. \tag{3.7}$$

This transformation aligns the satellite ARF in such a way that the azimuth angle matches the definition of the antenna center variation patterns provided by the IGS via the Antenna Exchange (ANTEX) file format (Rothacher and Schmid, 2010).

3.6 Local orbit reference frame

A local orbit reference frame (ORF) moves with the satellite and is used to describe effects related to the satellite orbit. This right-handed frame has the following definition (e.g., Krakiwsky and Wells, 1971).

Origin Usually located in the satellite's center of mass.

$\mathbf{e}_a$ **axis** Points in the along-track direction (i.e., close to the satellite's velocity vector).

$\mathbf{e}_c$ **axis** Points in the cross-track direction.

$\mathbf{e}_r$ **axis** Points in the radial direction (i.e., away from Earth).

This frame is particularly useful when comparing satellite orbits since several force models mainly affect the orbit's radial component. The rotation matrix from the ORF to the CRF is

$$\mathbf{R}_{\text{ORF}}^{\text{CRF}} = \begin{bmatrix} \mathbf{e}_a & \mathbf{e}_c & \mathbf{e}_r \end{bmatrix} \tag{3.8}$$

based on the unit vectors

$$\mathbf{e}_a = \mathbf{e}_c \times \mathbf{e}_r \tag{3.9}$$

$$\mathbf{e}_c = \frac{\mathbf{e}_r \times \dot{\mathbf{r}}^s_{\text{CRF}}}{\|\mathbf{e}_r \times \dot{\mathbf{r}}^s_{\text{CRF}}\|} \tag{3.10}$$

$$\mathbf{e}_r = \frac{\mathbf{r}^s_{\text{CRF}}}{\|\mathbf{r}^s_{\text{CRF}}\|} \tag{3.11}$$

with $\mathbf{r}^s_{\text{CRF}}$ and $\dot{\mathbf{r}}^s_{\text{CRF}}$ being the satellite's position and velocity in the CRF, respectively. Sometimes $\mathbf{e}_r$ is defined in the opposite (i.e., nadir) direction, resulting in $\mathbf{e}_c$ being flipped as well.

3.7 Helmert transformation

A 7-parameter Helmert transformation (e.g., Jekeli and Montenbruck, 2017)

$$\begin{bmatrix} x \\ y \\ z \end{bmatrix}_B = \begin{bmatrix} T_x \\ T_y \\ T_z \end{bmatrix} + (1+S) \begin{bmatrix} 0 & R_z & -R_y \\ -R_z & 0 & R_x \\ R_y & -R_x & 0 \end{bmatrix} \begin{bmatrix} x \\ y \\ z \end{bmatrix}_A \tag{3.12}$$

describes how coordinates can be transformed from reference frame A to B. The seven parameters comprise translation (T_x, T_y, T_z), rotation (R_x, R_y, R_z), and scale (S). Equation (3.12) assumes that the rotation angles are small and thus small-angle approximations can be applied. The functional relationship in (3.12) can be used to set up an equation system

$$\begin{bmatrix} \vdots \\ x_{B,i} - x_{A,i} \\ y_{B,i} - y_{A,i} \\ z_{B,i} - z_{A,i} \\ \vdots \end{bmatrix} = \begin{bmatrix} \vdots & \vdots & \vdots & \vdots & \vdots & \vdots & \vdots \\ 1 & 0 & 0 & 0 & z_{A,i} & -y_{A,i} & x_{A,i} \\ 0 & 1 & 0 & -z_{A,i} & 0 & x_{A,i} & y_{A,i} \\ 0 & 0 & 1 & y_{A,i} & -x_{A,i} & 0 & z_{A,i} \\ \vdots & \vdots & \vdots & \vdots & \vdots & \vdots & \vdots \end{bmatrix} \begin{bmatrix} T_x \\ T_y \\ T_z \\ R_x \\ R_y \\ R_z \\ S \end{bmatrix} . \tag{3.13}$$

Here, $x_{B,i}$, $y_{B,i}$, and $z_{B,i}$ are the coordinates for point i in frame B while $x_{A,i}$, $y_{A,i}$, and $z_{A,i}$ are those in frame A. Solving the equation system in (3.13) via least-squares adjustment results in estimates for the transformation parameters. At least three 3-dimensional coordinate sets are required to estimate all seven Helmert parameters.

There are two applications for a Helmert transformation within this thesis. Firstly, it forms the basis for no-net constraints on station coordinates (see Section 6.9.1). These are used to align the solution to a reference frame (e.g., the ITRF) and to resolve certain rank deficiencies in the normal equation system. Secondly, Helmert parameters are estimated in the comparison of coordinates that potentially realize different reference frames. Examples for this are when solutions from different analysis centers or time periods are compared.

4 Parameter estimation

Parameter estimation is the process of determining unknown parameters $\mathbf{x}$ from observations $\mathbf{l}$ based on a functional model, also called observation equations, of the form

$$\mathbf{l} = \boldsymbol{f}(\mathbf{x}) + \mathbf{e}\,. \tag{4.1}$$

The system of equations in (4.1) is usually overdetermined, which means there are more observations than parameters. Combined with inevitable measurement errors in $\mathbf{l}$ and incomplete models in $\boldsymbol{f}$, this leads to inconsistencies, which are represented by the observation residuals $\mathbf{e}$.

For the type of GNSS processing discussed in this thesis, the observation vector $\mathbf{l}$ generally contains code and phase measurements from a network of ground-based GNSS receivers to one or more satellite constellations. The function $\boldsymbol{f}$ then describes the relation between these measurements and a set of geometric and geophysical parameters, for example receiver positions or tropospheric delay parameters, based on a number of parametrizations, models, and corrections. A detailed description of the observation equations for code and phase measurements is given in Chapter 5, while the parametrizations, models, and corrections are the focus of Chapter 6.

Parameter estimation has been extensively described in the literature, for example in Koch (1999). Following Mayer-Gürr (2006), this chapter provides a summary of the main concepts of parameter estimation applied in this thesis. It starts with how to solve the system of equations in (4.1) based on a least-squares adjustment. This is followed by methods to improve the efficiency of setting up and solving the system of equations. These methods include the elimination of a part of the parameters in case they are not of interest, as well as how to avoid computationally expensive matrix inversions. Another topic is the addition of constraints in case the system of equations is not solvable due to a rank deficiency. Finally, it is shown how to determine individual weights for different observation groups using variance component estimation.

4.1 Nonlinear least-squares adjustment

In case of GNSS processing, the functional model in Equation (4.1) generally is nonlinear and has to be linearized by expanding it into a Taylor series

$$\mathbf{l} = \boldsymbol{f}(\mathbf{x}_0) + \left.\frac{\partial \boldsymbol{f}}{\partial \mathbf{x}}\right|_{\mathbf{x}_0} (\mathbf{x} - \mathbf{x}_0) + \cdots + \mathbf{e} \tag{4.2}$$

and truncating after the linear term. Moving the constant term to the left-hand side of the equation results in the linearized Gauss-Markov model

$$\mathbf{l} - \boldsymbol{f}(\mathbf{x}_0) = \mathbf{A}(\mathbf{x} - \mathbf{x}_0) + \mathbf{e}\,, \tag{4.3}$$

where the design matrix

$$\mathbf{A} = \left.\frac{\partial \boldsymbol{f}}{\partial \mathbf{x}}\right|_{\mathbf{x}_0} \tag{4.4}$$

is the Jacobian of $\boldsymbol{f}$ with respect to the parameters $\mathbf{x}$ at the initial values $\mathbf{x}_0$. Introducing the shorthands $\Delta\mathbf{l} = \mathbf{l} - \boldsymbol{f}(\mathbf{x}_0)$ for reduced observations and $\Delta\mathbf{x} = \mathbf{x} - \mathbf{x}_0$ for parameter corrections, (4.3) can also be written as

$$\Delta\mathbf{l} = \mathbf{A}\Delta\mathbf{x} + \mathbf{e}\,. \tag{4.5}$$

The observations in $\mathbf{l}$ can have different measurement accuracies and are possibly correlated. This information can be represented by the covariance matrix of observations $\boldsymbol{\Sigma}_\mathbf{l}$. Inverting this matrix results in the weight matrix

$$\mathbf{P} = s^2 {\boldsymbol{\Sigma}_\mathbf{l}}^{-1}\,, \tag{4.6}$$

where s^2 is an a priori unitless variance factor, for example $s^2 = 1$. Even though σ^2 is more commonly used to denote the variance factor in the literature, s^2 is used throughout this thesis to prevent confusion with the standard deviation σ of a measurement in later chapters. Minimizing the weighted sum of squared residuals

$$\|\mathbf{e}\|^2 = \mathbf{e}^T\mathbf{P}\mathbf{e} = (\Delta\mathbf{l} - \mathbf{A}\Delta\mathbf{x})^T\,\mathbf{P}\,(\Delta\mathbf{l} - \mathbf{A}\Delta\mathbf{x}) \rightarrow \min \tag{4.7}$$

leads to the so-called normal equations

$$\mathbf{A}^T\mathbf{P}\mathbf{A}\Delta\mathbf{x} = \mathbf{A}^T\mathbf{P}\Delta\mathbf{l}\,, \tag{4.8}$$

which can also be written as

$$\mathbf{N}\Delta\mathbf{x} = \mathbf{n}\,. \tag{4.9}$$

Here, $\mathbf{N} = \mathbf{A}^T\mathbf{P}\mathbf{A}$ is the normal equation matrix and $\mathbf{n} = \mathbf{A}^T\mathbf{P}\Delta\mathbf{l}$ is called right-hand side. Solving the system of equations results in the estimated parameter corrections

$$\Delta\hat{\mathbf{x}} = (\mathbf{A}^T\mathbf{P}\mathbf{A})^{-1}\mathbf{A}^T\mathbf{P}\Delta\mathbf{l} = \mathbf{N}^{-1}\mathbf{n} \tag{4.10}$$

and, in combination with the initial values $\mathbf{x}_0$, the estimated parameters

$$\hat{\mathbf{x}} = \mathbf{x}_0 + \Delta\hat{\mathbf{x}}\,. \tag{4.11}$$

In many cases, solving a nonlinear least-squares adjustment requires iteration, which means the estimated parameters $\hat{\mathbf{x}}$ are introduced back into (4.3) as initial values $\mathbf{x}_0$ and the system of equations is solved repeatedly until convergence is reached. The estimated variance factor

$$\hat{s}^2 = \frac{\hat{\mathbf{e}}^T\mathbf{P}\hat{\mathbf{e}}}{n-m} \tag{4.12}$$

can then be computed based on the estimated residuals

$$\hat{\mathbf{e}} = \Delta\mathbf{l} - \mathbf{A}\Delta\hat{\mathbf{x}} \tag{4.13}$$

and the number of observations n and parameters m. Finally, the covariance matrix of estimated parameters follows as

$$\mathbf{\Sigma}_{\hat{\mathbf{x}}} = \hat{s}^2(\mathbf{A}^T\mathbf{P}\mathbf{A})^{-1} = \hat{s}^2\mathbf{N}^{-1}\,. \tag{4.14}$$

4.2 Efficient setup and solution of the normal equations

Processing large systems with hundreds of GNSS receivers and multiple satellite constellations can lead to hundreds of millions of observations and millions of parameters for a single day. For example, the normal equation matrix $\mathbf{N}$ associated with a vector $\mathbf{x}$ containing 1 million parameters would require 8 terabytes of memory in case it were fully set up and populated. This becomes even more of a problem since $\mathbf{N}^{-1}$ appears in Equation (4.10) and matrix inversions are computationally expensive operations. Therefore, solving such a system directly as shown in (4.10) is unfeasible even for most

modern high-performance computing clusters, which means it is necessary to apply methods that reduce the problem to a more feasible size.

4.2.1 Homogenization

The first step is to homogenize the system of equations based on the weight matrix $\mathbf{P}$. As shown in Equation (4.6), $\mathbf{P}$ can be determined by inverting the covariance matrix of observations $\mathbf{\Sigma_l}$. Since this matrix has dimensions $n \times n$, with n being the number of observations, this can be a costly operation. In GNSS processing, the observations in $\mathbf{l}$ are generally assumed to be uncorrelated, which means $\mathbf{\Sigma_l}$ is a diagonal matrix. Several studies (e.g., El-Rabbany, 1994; Schön and Brunner, 2008; Amiri-Simkooei et al., 2016; Kermarrec, 2018) have shown that this assumption may be too simplistic, and a proper consideration of observation correlations can benefit the solution, making this one aspect of possible future improvements. Nevertheless, assuming $\mathbf{\Sigma_l}$ is a diagonal matrix, the diagonal elements of the weight matrix $\mathbf{P}$ are simply

$$p_{ii} = \frac{1}{\sigma_{l,ii}^2}\,, \tag{4.15}$$

with $\sigma_{l,ii}^2$ being the diagonal elements of $\mathbf{\Sigma_l}$ and $i := \{1, 2, \ldots, n\}$. The weights can then be directly applied to the design matrix elements

$$\tilde{a}_{ij} = \sqrt{p_{ii}} a_{ij} = \frac{a_{ij}}{\sigma_{l,ii}}\,, \tag{4.16}$$

where $j := \{1, 2, \ldots, m\}$ and m is the number of unknown parameters, and to the observations

$$\tilde{l}_i = \sqrt{p_{ii}} l_i = \frac{l_i}{\sigma_{l,ii}}\,. \tag{4.17}$$

The normal equations from (4.8) thus become

$$\tilde{\mathbf{A}}^T \tilde{\mathbf{A}} \Delta\mathbf{x} = \tilde{\mathbf{A}}^T \Delta\tilde{\mathbf{l}} \tag{4.18}$$

and the solution from (4.10) turns into

$$\Delta\hat{\mathbf{x}} = (\tilde{\mathbf{A}}^T \tilde{\mathbf{A}})^{-1} \tilde{\mathbf{A}}^T \Delta\tilde{\mathbf{l}} = (\mathbf{A}^T \mathbf{P} \mathbf{A})^{-1} \mathbf{A}^T \mathbf{P} \Delta\mathbf{l} = \mathbf{N}^{-1}\mathbf{n}\,. \tag{4.19}$$

As shown in (4.19), the homogenized solution is equivalent to the original one, except the need to explicitly set up $\mathbf{P}$. All subsequent sections of this thesis assume a homogenized system of equations, but omit the tilde notation for the sake of readability.

4.2.2 Parameter elimination

In some cases, not all parameters in $\mathbf{x}$ are of interest, but they have to be considered in the functional model to get a proper result. In the context of this thesis, an example are the millions of ionospheric slant total electron content (STEC) parameters that have to be set up per day, even though their values are not necessarily needed in further analyses. Since the computational effort of solving the system of equations scales cubically with the number of parameters, it is preferable to reduce this number by only keeping the parameters of interest while eliminating all others.

The linearized Gauss-Markov model in Equation (4.3) can be split into

$$\mathbf{l} - \boldsymbol{f}(\mathbf{x}_0, \mathbf{y}_0) = \mathbf{A}(\mathbf{x} - \mathbf{x}_0) + \mathbf{B}(\mathbf{y} - \mathbf{y}_0) + \mathbf{e} \tag{4.20}$$

or, introducing the shorthand $\Delta\mathbf{y} = \mathbf{y} - \mathbf{y}_0$,

$$\Delta\mathbf{l} = \mathbf{A}\Delta\mathbf{x} + \mathbf{B}\Delta\mathbf{y} + \mathbf{e} = \begin{bmatrix}\mathbf{A} & \mathbf{B}\end{bmatrix} \begin{bmatrix}\Delta\mathbf{x} \\ \Delta\mathbf{y}\end{bmatrix} + \mathbf{e}\,, \tag{4.21}$$

with $\mathbf{x}$ being the parameters of interest and $\mathbf{y}$ the ones to be eliminated. $\mathbf{x}_0$ and $\mathbf{y}_0$ are the respective initial values and $\mathbf{A}$ and $\mathbf{B}$ the respective design matrices.

Parameters can be eliminated either on the observation equation level or on the normal equation level. The former has the advantage of smaller dimensions in the resulting normal equations, thus requiring less mathematical operations and memory. This can become very important in case the number of parameters to be eliminated is large, possibly even preventing the setup of the full normal equations. The latter is useful if the number of parameters in $\mathbf{y}$ is small enough so that setting up the full normal equations is feasible. In this case, multiple normal equations can be accumulated (see Section 4.2.3) before eliminating the parameters only once, which reduces the computational effort. In the context of this thesis, both approaches are used to eliminate different sets of parameters, thus utilizing the advantages of both methods.

4.2.2.1 Parameter elimination on the observation equation level

The parameters $\Delta\mathbf{y}$ in (4.21) can be eliminated by projecting the equation to a space orthogonal to the column space of $\mathbf{B}$

$$\boldsymbol{\Pi}_B^{\perp}\Delta\mathbf{l} = \boldsymbol{\Pi}_B^{\perp}\mathbf{A}\Delta\mathbf{x} + \underbrace{\boldsymbol{\Pi}_B^{\perp}\mathbf{B}}_{\mathbf{0}}\Delta\mathbf{y} + \boldsymbol{\Pi}_B^{\perp}\mathbf{e} \tag{4.22}$$

using the orthogonal projector

$$\mathbf{\Pi}_B^{\perp} = \mathbf{I} - \mathbf{B}(\mathbf{B}^T\mathbf{B})^{-1}\mathbf{B}^T\,. \tag{4.23}$$

The normal equations of a homogenized system of equations (see Section 4.2.1) then become

$$\mathbf{A}^T\mathbf{\Pi}_B^{\perp T}\mathbf{\Pi}_B^{\perp}\mathbf{A}\Delta\mathbf{x} = \mathbf{A}^T\mathbf{\Pi}_B^{\perp T}\mathbf{\Pi}_B^{\perp}\Delta\mathbf{l}\,, \tag{4.24}$$

which, utilizing that orthogonal projectors are symmetric and idempotent (Koch, 1999), simplifies to

$$\mathbf{A}^T\mathbf{\Pi}_B^{\perp}\mathbf{A}\Delta\mathbf{x} = \mathbf{A}^T\mathbf{\Pi}_B^{\perp}\Delta\mathbf{l}\,. \tag{4.25}$$

Since (4.23) contains an inversion, a more efficient way to determine $\mathbf{\Pi}_B^{\perp}$ is by means of a QR decomposition (e.g., Golub and Van Loan, 2013)

$$\mathbf{B} = \mathbf{Q}\mathbf{R} = \begin{bmatrix}\mathbf{Q}_1 & \mathbf{Q}_2\end{bmatrix}\begin{bmatrix}\mathbf{R}_1 \\ \mathbf{0}\end{bmatrix}\,, \tag{4.26}$$

where $\mathbf{Q}$ is an orthogonal matrix and $\mathbf{R}$ is a regular upper triangular matrix. $\mathbf{Q}_1$ contains the base vectors of the column space of $\mathbf{B}$ and $\mathbf{Q}_2$ contains the base vectors of its orthogonal complement. By substituting (4.26) into (4.23), it can be shown that the orthogonal projector reduces to

$$\mathbf{\Pi}_B^{\perp} = \mathbf{Q}_2\mathbf{Q}_2^T\,. \tag{4.27}$$

Substituting (4.27) into (4.25) then leads to

$$\mathbf{A}^T\mathbf{Q}_2\mathbf{Q}_2^T\mathbf{A}\Delta\mathbf{x} = \mathbf{A}^T\mathbf{Q}_2\mathbf{Q}_2^T\Delta\mathbf{l} \tag{4.28}$$

and, introducing the transformations

$$\bar{\mathbf{A}} = \mathbf{Q}_2^T\mathbf{A} \quad \text{and} \quad \Delta\bar{\mathbf{l}} = \mathbf{Q}_2^T\Delta\mathbf{l}\,, \tag{4.29}$$

to normal equations in the same form as in (4.19)

$$\bar{\mathbf{A}}^T\bar{\mathbf{A}}\Delta\mathbf{x} = \bar{\mathbf{A}}^T\Delta\bar{\mathbf{l}}\,. \tag{4.30}$$

This means the parameters $\Delta\mathbf{y}$ can be efficiently eliminated from (4.21) on the level of observation equations by QR-decomposing $\mathbf{B}$ according to (4.26) and transforming the design matrix and observations using (4.29). After this step, the reduced system of

equations can then be solved in the same way as any linearized Gauss-Markov model via (4.19). Eliminating parameters on the observation equation level is a key factor in enabling the raw observation approach (see Chapter 5) to scale to large systems with millions of parameters.

4.2.2.2 Parameter elimination on the normal equation level

The normal equation system following from (4.21) is

$$\begin{bmatrix} \mathbf{A}^T\mathbf{A} & \mathbf{A}^T\mathbf{B} \\ \mathbf{B}^T\mathbf{A} & \mathbf{B}^T\mathbf{B} \end{bmatrix} \begin{bmatrix} \Delta\mathbf{x} \\ \Delta\mathbf{y} \end{bmatrix} = \begin{bmatrix} \mathbf{A}^T\Delta\mathbf{l} \\ \mathbf{B}^T\Delta\mathbf{l} \end{bmatrix} \tag{4.31}$$

or

$$\begin{bmatrix} \mathbf{N}_{\mathbf{xx}} & \mathbf{N}_{\mathbf{xy}} \\ \mathbf{N}_{\mathbf{xy}}^T & \mathbf{N}_{\mathbf{yy}} \end{bmatrix} \begin{bmatrix} \Delta\mathbf{x} \\ \Delta\mathbf{y} \end{bmatrix} = \begin{bmatrix} \mathbf{n}_{\mathbf{x}} \\ \mathbf{n}_{\mathbf{y}} \end{bmatrix} . \tag{4.32}$$

If $\mathbf{N}_{\mathbf{yy}}$ is invertible, the second equation in (4.32) can be solved for $\Delta\mathbf{y}$, resulting in

$$\Delta\mathbf{y} = \mathbf{N}_{\mathbf{yy}}^{-1}\left(\mathbf{n}_{\mathbf{y}} - \mathbf{N}_{\mathbf{xy}}^T\Delta\mathbf{x}\right) . \tag{4.33}$$

Substituting (4.33) into the first equation in (4.32) leads to

$$\begin{aligned} \mathbf{N}_{\mathbf{xx}}\Delta\mathbf{x} + \mathbf{N}_{\mathbf{xy}}\left[\mathbf{N}_{\mathbf{yy}}^{-1}\left(\mathbf{n}_{\mathbf{y}} - \mathbf{N}_{\mathbf{xy}}^T\Delta\mathbf{x}\right)\right] &= \mathbf{n}_{\mathbf{x}} \\ \mathbf{N}_{\mathbf{xx}}\Delta\mathbf{x} + \mathbf{N}_{\mathbf{xy}}\mathbf{N}_{\mathbf{yy}}^{-1}\mathbf{n}_{\mathbf{y}} - \mathbf{N}_{\mathbf{xy}}\mathbf{N}_{\mathbf{yy}}^{-1}\mathbf{N}_{\mathbf{xy}}^T\Delta\mathbf{x} &= \mathbf{n}_{\mathbf{x}} , \end{aligned} \tag{4.34}$$

which can be rearranged to

$$\left(\mathbf{N}_{\mathbf{xx}} - \mathbf{N}_{\mathbf{xy}}\mathbf{N}_{\mathbf{yy}}^{-1}\mathbf{N}_{\mathbf{xy}}^T\right)\Delta\mathbf{x} = \mathbf{n}_{\mathbf{x}} - \mathbf{N}_{\mathbf{xy}}\mathbf{N}_{\mathbf{yy}}^{-1}\mathbf{n}_{\mathbf{y}} . \tag{4.35}$$

By introducing the reduced normal equation matrix

$$\bar{\mathbf{N}} = \mathbf{N}_{\mathbf{xx}} - \mathbf{N}_{\mathbf{xy}}\mathbf{N}_{\mathbf{yy}}^{-1}\mathbf{N}_{\mathbf{xy}}^T \tag{4.36}$$

and the reduced right-hand side

$$\bar{\mathbf{n}} = \mathbf{n}_{\mathbf{x}} - \mathbf{N}_{\mathbf{xy}}\mathbf{N}_{\mathbf{yy}}^{-1}\mathbf{n}_{\mathbf{y}} , \tag{4.37}$$

the resulting normal equations $\bar{\mathbf{N}}\Delta\mathbf{x} = \bar{\mathbf{n}}$ are of the same form as (4.9) and can be solved accordingly. In case the eliminated parameters are of interest after solving the reduced normal equations, $\Delta\hat{\mathbf{y}}$ can be reconstructed based on $\Delta\hat{\mathbf{x}}$ using (4.33).

4.2.3 Accumulation of the normal equations

Due to the large number of observations involved in GNSS processing, it is usually not possible to set up the full design matrix $\mathbf{A}$. Fortunately, it is not necessary to do so, since $\mathbf{A}$ and the observation vector $\mathbf{l}$ can be split into multiple parts

$$\mathbf{A} = \begin{bmatrix} \mathbf{A}_1 \\ \mathbf{A}_2 \\ \vdots \\ \mathbf{A}_k \end{bmatrix} \quad \text{and} \quad \Delta\mathbf{l} = \begin{bmatrix} \Delta\mathbf{l}_1 \\ \Delta\mathbf{l}_2 \\ \vdots \\ \Delta\mathbf{l}_k \end{bmatrix} . \tag{4.38}$$

The full normal equations can then be set up by accumulating the individual normal equation matrices

$$\mathbf{N} = \sum_{i=1}^{k} \mathbf{N}_i = \sum_{i=1}^{k} \mathbf{A}_i^T \mathbf{A}_i \tag{4.39}$$

and right-hand sides

$$\mathbf{n} = \sum_{i=1}^{k} \mathbf{n}_i = \sum_{i=1}^{k} \mathbf{A}_i^T \Delta\mathbf{l}_i \, . \tag{4.40}$$

Accumulating the normal equations in this way has two major advantages. First, it can significantly reduce the required memory for setting up the normal equations, since each normal equation matrix $\mathbf{N}_i$ and its respective design matrix $\mathbf{A}_i$ can be freed from memory after the addition to $\mathbf{N}$ and $\mathbf{n}$. Second, the setup of the individual parts can be parallelized by distributing them among multiple processes, both within a multicore system and over several systems in a computer cluster. This parallelization can massively improve the performance of setting up the normal equations, as the only required communication between processes is the initial distribution of the parts and the final accumulation of all $\mathbf{N}_i$ and $\mathbf{n}_i$. Distributed setup and accumulation of normal equations is heavily utilized in the context of this thesis and is one of the key aspects that enable large-scale GNSS processing involving hundreds of millions of observations.

4.2.4 Solution of the normal equations

The solution of the normal equations

$$\Delta\hat{\mathbf{x}} = \mathbf{N}^{-1}\mathbf{n} \tag{4.41}$$

contains the inverse of the normal equation matrix, which is a costly operation, especially if the dimensions of $\mathbf{N}$ are large, as is often the case in GNSS processing. If $\mathbf{N}$ is positive definite, the inversion can be circumvented by using the Cholesky decomposition (e.g., Koch, 1999)

$$\mathbf{N} = \mathbf{W}^T\mathbf{W}\,, \tag{4.42}$$

where $\mathbf{W}$ is a regular upper triangular matrix called Cholesky factor. This decomposition can be done in-place to save memory. Substituting (4.42) into (4.41) yields

$$\Delta\hat{\mathbf{x}} = \left(\mathbf{W}^T\mathbf{W}\right)^{-1}\mathbf{n} = \mathbf{W}^{-1}\mathbf{W}^{-T}\mathbf{n} = \mathbf{W}^{-1}\left(\mathbf{W}^{-T}\mathbf{n}\right)\,, \tag{4.43}$$

which shows that the system of equations can be solved by two subsequent matrix-vector multiplications. This has the advantage that the inverse of $\mathbf{W}$ does not have to be computed explicitly, as the matrix-vector multiplications can be solved by forward and backward substitution (e.g., Golub and Van Loan, 2013). By introducing the intermediate vector $\mathbf{y} = \mathbf{W}^{-T}\mathbf{n}$, the equation system

$$\mathbf{W}^T\mathbf{y} = \mathbf{n} \tag{4.44}$$

can be solved directly for $\mathbf{y}$. Since $\mathbf{W}^T$ is a lower triangular matrix, the first row of this equation system is $W_{1,1}\,y_1 = n_1$, which directly gives y_1. Substituting y_1 into the second row solves that equation and the process can be continued until the last row is solved. The remaining equation $\Delta\hat{\mathbf{x}} = \mathbf{W}^{-1}\mathbf{y}$ can be solved in the same way by rearranging it to

$$\mathbf{W}\Delta\hat{\mathbf{x}} = \mathbf{y}\,. \tag{4.45}$$

With $\mathbf{W}$ being an upper triangular matrix, the equations are solved from bottom to top row in this case, which finally gives $\Delta\hat{\mathbf{x}}$.

4.3 Constraints

Constraints are a way to introduce additional information into a system of equations. The additional information can serve two different purposes. First, some parametrizations or combinations of certain parametrizations can result in there being more than one valid solution for the system of equations. This happens if the design matrix $\mathbf{A}_{n\times m}$ is rank-deficient with $\operatorname{rank}\mathbf{A} = r < m$, which means there is a linear dependency between some of its columns. In this case, $\dim C(\mathbf{A}) = r$ and $\dim N(\mathbf{A}) = m - r$, where $C(\mathbf{A})$

and $N(\mathbf{A})$ are the column space and nullspace of $\mathbf{A}$, respectively. The resulting normal equation matrix $\mathbf{N}$, also with $\dim C(\mathbf{N}) = r$ and $\dim N(\mathbf{N}) = m - r$, then becomes only positive semidefinite instead of positive definite and thus cannot be inverted (e.g., Koch, 1999). These rank deficiencies can be resolved by constraining the least-squares adjustment and thus removing the nullspace.

The nullspace $N(\mathbf{N})$ can be determined by means of an eigenvalue decomposition (e.g., Golub and Van Loan, 2013)

$$\mathbf{N} = \mathbf{Q}\mathbf{\Lambda}\mathbf{Q}^T\,, \tag{4.46}$$

where $\mathbf{Q}$ is the matrix of eigenvectors and $\mathbf{\Lambda}$ is a diagonal matrix containing the respective eigenvalues λ_i. The eigenvectors associated with the $m-r$ eigenvalues $\lambda_i = 0$ span the nullspace $N(\mathbf{N})$. Each eigenvector of a zero eigenvalue contains information about the linear combination of parameters that causes the respective rank deficiency.

Based on this information, appropriate pseudoobservation equations

$$\mathbf{b} = \mathbf{B}\Delta\mathbf{x} \tag{4.47}$$

can be designed to resolve the rank deficiencies. Here, $\mathbf{b}$ is a vector of pseudoobservations, also called bias vector, and $\mathbf{B}$ is the design matrix of constraints that relates the pseudoobservations to the parameter corrections $\Delta\mathbf{x}$. The constraint equations in (4.47) are assumed to be linear in the context of this thesis. The covariance matrix of pseudoobservations $\mathbf{\Sigma_b}$ contains information about the strength or strictness of the applied constraints. $\mathbf{\Sigma_b}$ usually is a diagonal matrix, which means the constraint equations can be homogenized following the procedure shown in Section 4.2.1 to achieve a proper weighting. The normal equation matrix of constraints $\mathbf{M} = \mathbf{B}^T\mathbf{B}$ and its respective right-hand side $\mathbf{m} = \mathbf{B}^T\mathbf{b}$ can then be added to the full normal equation system

$$(\mathbf{N} + \mathbf{M})\Delta\mathbf{x} = \mathbf{n} + \mathbf{m}\,. \tag{4.48}$$

$\mathbf{M}$ and $\mathbf{m}$ can also be accumulated from multiple parts as shown in Section 4.2.3. If the constraints were designed appropriately, the constrained normal equation matrix $\tilde{\mathbf{N}} = \mathbf{N} + \mathbf{M}$ has full rank, meaning its nullspace vanishes and it becomes invertible. The constrained normal equation system in (4.48) can then be solved following Section 4.2.4.

One example for the usage of constraints to resolve a rank deficiency is the combined estimation of transmitter and receiver clock errors. The rank deficiency is caused by the observations between transmitters and receivers being only relative and not absolute.

Therefore, all clocks could be shifted by the same arbitrary value without influencing the relative observations. This can be solved by applying a constraint equation over multiple clock parameters, for example stating that their mean value must be zero. Another option would be to constrain a single clock to its a priori value, or to remove the related parameter altogether, thus introducing that clock as an absolute reference.

The second purpose of constraints is to limit the estimable range of values for certain parameters. For instance, so-called pseudostochastic pulse parameters are often used in satellite orbit determination to cope with force model insufficiencies (see Section 6.2). These parameters, which represent instantaneous velocity changes, are constrained towards zero in order to prevent them from becoming too large and possibly absorbing unrelated effects. Constraints of this kind can be applied in the same way as the first kind by setting up pseudoobservation equations and adding the resulting normal equations to the full system.

The strength or strictness of a constraint depends on its objective. An example for the application of loose constraints are certain tropospheric correction parameters (see Section 6.7) that can be set up as time-variable functions over a day, for instance as splines. The knots of these splines are evenly distributed over the day, and their values can be loosely constrained towards zero, meaning the standard deviation σ_i of its associated pseudoobservation b_i is much larger than the expected parameter value. If there are no observations at a station for the first hours of the day, the constraint resolves the rank deficiency caused by the spline knots located within that time period. This makes the system solvable even in the absence of observations for these parameters, although their estimated values might not be meaningful. If there are observations, however, the large standard deviation and thus small weight of the constraint hardly influences the estimated values of the parameters.

Tight constraints, on the other hand, force the affected parameters to a specified value. For instance, the absolute value of the Universal Time 1 (UT1), which is one of the Earth orientation parameters, cannot be estimated by GNSS directly. Nevertheless, it can be added to the normal equations in preparation for their combination with those of other space-geodetic techniques that can estimate UT1, for example VLBI. Therefore, UT1 is usually tightly constrained to its a priori value and hence does not affect other parameters.

4.4 Variance component estimation

Proper weighting of the different observation types involved in GNSS processing is important to obtain the best estimate of the unknown parameters. The measurement accuracy of the various code and phase observations is influenced by many factors, for example the antenna and receiver model or the observation incident angle. For this reason, measurement accuracies are only known approximately, making the a priori observation weighting suboptimal. Variance component estimation (VCE), as described in Koch and Kusche (2002), is a data-driven approach to determine proper weights of different observation groups during processing.

Section 4.2.3 outlines how the normal equation matrix $\mathbf{N}$ and its right-hand side $\mathbf{n}$ can be accumulated from multiple parts. These parts can be weighted relatively to each other by introducing a corresponding variance factor $\hat{s}_i^2$, which gives

$$\mathbf{N} = \sum_{i=1}^{k} \frac{1}{\hat{s}_i^2} \mathbf{N}_i \tag{4.49}$$

and

$$\mathbf{n} = \sum_{i=1}^{k} \frac{1}{\hat{s}_i^2} \mathbf{n}_i \,. \tag{4.50}$$

The variance factors

$$\hat{s}_i^2 = \frac{\hat{\mathbf{e}}_i^T \hat{\mathbf{e}}_i}{r_i} \tag{4.51}$$

are based on the squared sum of estimated residuals $\hat{\mathbf{e}}_i$ associated with their respective observation group and its partial redundancy

$$r_i = n_i - \frac{1}{s_i^2} \operatorname{trace}\left(\mathbf{N}_i \mathbf{N}^{-1}\right) , \tag{4.52}$$

where n_i is the number of observations in the group. Equation (4.51) assumes a homogenized system of equations as detailed in Section 4.2.1.

VCE is an iterative process. This becomes clear from (4.51), where determining the variance factors requires estimated residuals $\hat{\mathbf{e}}_i$ and the partial redundancy r_i, which requires the variance factor itself. Starting from some initial variance factors, for example $s_i^2 = 1$, the normal equations are accumulated according to (4.49) and (4.50). Then the normal equation system is solved, which allows the computation of the residuals $\hat{\mathbf{e}}_i$ and, consequently, the determination of the newly-estimated variance factors $\hat{s}_i^2$. In the next

iteration, these are then introduced into the accumulation of the normal equations and the process is repeated until convergence is reached.

The direct computation of the trace in Equation (4.52) should be avoided, as it is a very costly operation. It involves the inverse of the full normal equation matrix, which is never explicitly determined when solving the system of equations (see Section 4.2.4). As an alternative, the trace can be determined using a stochastic trace estimator (Koch and Kusche, 2002). If $\mathbf{Q}$ is a symmetric $m \times m$ matrix and $\mathbf{z}$ is a $m \times 1$ vector containing m realizations of a discrete random variable Z, for which $\mathbb{E}(Z) = 0$ and $\mathbb{D}(Z) = 1$ and which takes with 50% probability each the values 1 and -1, then

$$\operatorname{trace} \mathbf{Q} = \mathbb{E}\left(\mathbf{z}^T \mathbf{Q} \mathbf{z}\right) . \tag{4.53}$$

The trace in (4.52) can be rearranged to

$$\operatorname{trace}\left(\mathbf{N}_i \mathbf{N}^{-1}\right) = \operatorname{trace}\left(\mathbf{A}_i^T \mathbf{A}_i \mathbf{W}^{-1} \mathbf{W}^{-T}\right) = \operatorname{trace}\left(\mathbf{W}^{-T} \mathbf{A}_i^T \mathbf{A}_i \mathbf{W}^{-1}\right) \tag{4.54}$$

utilizing the Cholesky decomposition from (4.42) and the cyclic property of the trace operator. Based on (4.53), the trace can then be expressed as

$$\begin{aligned} \operatorname{trace}\left(\mathbf{W}^{-T} \mathbf{A}_i^T \mathbf{A}_i \mathbf{W}^{-1}\right) &= \mathbb{E}\left(\mathbf{z}^T \mathbf{W}^{-T} \mathbf{A}_i^T \mathbf{A}_i \mathbf{W}^{-1} \mathbf{z}\right) \\ &= \mathbb{E}\left[\left(\mathbf{A}_i \mathbf{W}^{-1} \mathbf{z}\right)^T \left(\mathbf{A}_i \mathbf{W}^{-1} \mathbf{z}\right)\right] \\ &= \mathbb{E}\left(\mathbf{u}_i^T \mathbf{u}_i\right) \end{aligned} \tag{4.55}$$

with $\mathbf{u}_i = \mathbf{A}_i \mathbf{W}^{-1} \mathbf{z}$. Finally, substituting (4.55) into (4.52) leads to

$$r_i = n_i - \frac{\mathbb{E}\left(\mathbf{u}_i^T \mathbf{u}_i\right)}{s_i^2} . \tag{4.56}$$

Multiple independent realizations of the vector $\mathbf{z}$ can lead to different trace estimates. Therefore, it might be necessary to compute the mean over multiple trace estimates to get a more stable result.

5 GNSS processing with the raw observation approach

Attribution The concepts and algorithms presented in this chapter were largely developed and implemented by the author's supervisor, Torsten Mayer-Gürr. The author of this thesis was involved in discussions on these concepts and in testing their implementation at several stages. While some aspects of this chapter have been published in a very general sense, for example in Strasser et al. (2019), Strasser and Mayer-Gürr (2020), and Mayer-Gürr et al. (2021), the mathematical and computational details have not been fully published so far. Therefore, this chapter is intended to provide these details to give a complete description of the processing approach used in the context of this thesis.

The raw observation approach naturally relates measurements from a GNSS receiver to space-geodetic parameters based on functional models. These functional models are the basic observation equations for code and phase measurements, which are described in any GNSS textbook (e.g., Hofmann-Wellenhof et al., 2008; Misra and Enge, 2011; Hauschild, 2017a). The observation equations have to include all effects that influence the measurements, either in the form of corrections based on a priori models or as unknown parameters. Since many effects cannot be modeled adequately, the large number of parameters that have to be set up in GNSS processing can hinder the ability to solve the system of equations efficiently.

This is one of the reasons why, historically, other approaches have been developed and are still most prevalent in GNSS processing today, for example among the IGS analysis centers (Weiss et al., 2017). These approaches aim at combining observations in ways that remove certain parameters from the observation equations, thus enabling the system of equations to be solved more efficiently. The most widely used linear combination is the ionosphere-free combination (e.g., Hauschild, 2017b), which removes the first-order ionospheric influence and, therefore, allows the omission of a large number of parameters related to this effect. Another common approach is to utilize double differences (e.g., Hauschild, 2017b), which are a combination of observations from two receivers to the same two satellites, because they remove clock and signal bias parameters from the observation equations. Clock parameters usually constitute the

largest number of parameters next to the ionospheric influence, so their removal further reduces the computational effort of solving the system of equations.

Nevertheless, the raw observation approach has become more and more popular in recent years. One reason is that the vast computational resources available today make its application more feasible than in the past. Another reason is the increased number of available signals transmitted by modern GNSS satellite constellations. The nature of this approach suits the inclusion of various different signals on multiple frequencies, as each observation has its own observation equation and is not obfuscated by linear combinations. The raw observation approach was first demonstrated in Schönemann et al. (2011) in the context of single-station precise point positioning (PPP) and later detailed in Schönemann (2014) for standalone and network applications. Zehentner and Mayer-Gürr (2014, 2016) and Zehentner (2016) applied the approach to kinematic orbit determination of low Earth orbit (LEO) satellites. Strasser et al. (2019) showed that processing GNSS constellations and ground station networks with the raw observation approach produces results of at least equivalent quality to well-established approaches used by IGS analysis centers for this purpose. Many more studies have utilized this approach for different applications in recent years, for example P. Li et al. (2018), Cao et al. (2019), Reckeweg (2020), and Zeng et al. (2021).

This chapter details the raw observation approach as applied by TUG. The following sections describe how observation equations are defined and set up, how weights are applied to them, and how the ionospheric influence can be effectively preeliminated. Furthermore, a normal equation matrix structure aiming at high sparsity, which is a prerequisite for processing large equation systems, is introduced and visualized. Additional sections focus on the reconstruction of the ionospheric parameters and the computation of residuals and redundancies, which are utilized to determine new weights for the observations. Finally, strategies that enable an efficient solution of large systems with hundreds of stations are presented, followed by a brief introduction of the processing software used in the context of this thesis.

5.1 Observation equations

The code and phase observation equations can be found in various forms in the literature. Depending on the focus of the publication, different attributions and dependencies of the involved components are either included or omitted. Components in this context refer to effects or values that have to be modeled, corrected, or estimated, for instance the tropospheric influence or signal biases. The approach taken in this thesis is to highlight

the components involved in the observation equations by representing them as general functions that are specified further in Chapter 6. The notation $\square[\tau\nu a]_r^s(\ldots)$ used in Equation (5.1) describes the attribution of a scalar value or function $\square$ to a signal type τ (i.e., C or L), frequency ν, signal attribute a (e.g., C, W, Q, X), observed satellite s, and observing receiver r. More information on the RINEX 3 signal notation $[\tau\nu a]$ is given in Section 2.2. All of these attributions are optional, meaning $\square$ may, for example, be attributed only to a satellite ($\square^s$) or receiver ($\square_r$), but it may also be attributed to the combination of both ($\square_r^s$). Dependencies of the various components, for example on the epoch t or signal path $\boldsymbol{p}_r^s$, are listed in parentheses.

The observation equation for code or phase measurements is thus defined as

$$\begin{aligned}\mathrm{obs}[\tau\nu a]_r^s(t) = {} & \mathrm{range}(\mathbf{r}^s, \mathbf{r}_r) + \mathrm{clock}^s(t) + \mathrm{clock}_r(t) + \mathrm{tropo}(t, \boldsymbol{p}_r^s) \\ & + \mathrm{iono}([\tau\nu], t, \boldsymbol{p}_r^s) + \mathrm{bias}[\tau\nu a]^s + \mathrm{bias}[\tau\nu a]_r + \lambda[\mathrm{L}\nu]\, N[\mathrm{L}\nu]_r^s \\ & + \mathrm{ant}[\tau\nu a]^s(\boldsymbol{p}_r^s) + \mathrm{ant}[\tau\nu a]_r(\boldsymbol{p}_r^s) + \mathrm{other}(\ldots) + \epsilon[\tau\nu a]_r^s(t)\,,\end{aligned} \tag{5.1}$$

where

$\mathrm{obs}[\tau\nu a]_r^s(t)$	is a measurement of signal $[\tau\nu a]$ from receiver r to satellite s at epoch t,
$\mathrm{range}(\mathbf{r}^s, \mathbf{r}_r)$	is a function representing the geometric range between satellite position $\mathbf{r}^s$ at transmission time and receiver position $\mathbf{r}_r$ at reception time,
$\mathrm{clock}^s(t)$	is a function for the satellite clock error at epoch t,
$\mathrm{clock}_r(t)$	is a function describing the receiver clock error at epoch t,
$\mathrm{tropo}(t, \boldsymbol{p}_r^s)$	is a function for the tropospheric influence at epoch t along the path $\boldsymbol{p}_r^s$,
$\mathrm{iono}([\tau\nu], t, \boldsymbol{p}_r^s)$	is a function representing the ionospheric influence at epoch t based on the signal $[\tau\nu]$ and its path $\boldsymbol{p}_r^s$,
$\mathrm{bias}[\tau\nu a]^s$	is the satellite signal bias for signal $[\tau\nu a]$,
$\mathrm{bias}[\tau\nu a]_r$	is the receiver signal bias for signal $[\tau\nu a]$,
$\lambda[\mathrm{L}\nu]$	is the wavelength of signal $[\mathrm{L}\nu]$,
$N[\mathrm{L}\nu]_r^s$	is the phase ambiguity of signal $[\mathrm{L}\nu]$ between receiver r and satellite s,
$\mathrm{ant}[\tau\nu a]^s(\boldsymbol{p}_r^s)$	is a function describing the satellite antenna correction for signal $[\tau\nu a]$ in the direction of its exiting path $\boldsymbol{p}_r^s$,
$\mathrm{ant}[\tau\nu a]_r(\boldsymbol{p}_r^s)$	is a function for the receiver antenna correction for signal $[\tau\nu a]$ in the direction of its incoming path $\boldsymbol{p}_r^s$,
$\mathrm{other}(\ldots)$	is a function representing other corrections (see Section 6.11), and
$\epsilon[\tau\nu a]_r^s(t)$	are measurement errors of signal $[\tau\nu a]$ between receiver r and satellite s at epoch t.

All components in (5.1) are in units of length (i.e., meters) except for the phase ambiguity $N[\mathrm{L}\nu]_r^s$, which is in cycles. $N[\mathrm{L}\nu]_r^s$ is only defined for phase observations, thus $N[\mathrm{L}\nu]_r^s = 0$ if $\tau = \mathrm{C}$. The continuous function $\boldsymbol{p}_r^s$ describes the curved path in $\mathbb{R}^3$ along which the signal travels from the satellite antenna at transmission time to the receiver antenna at reception time. Consequently, the positions $\mathbf{r}^s$ and $\mathbf{r}_r$ refer to the antenna reference points of the respective antennas. The relationship between $\mathbf{r}^s$ and the satellite's center of mass and between $\mathbf{r}_r$ and the station marker point is detailed in Section 6.10.

Equation (5.1) relies on some assumptions. First, it assumes that the clock errors, troposphere, and ionosphere do not change significantly within a small margin (e.g., 0.1 s) around an epoch. For example, this allows the setup of a single clock parameter per satellite at each epoch, which is the same for all receivers observing that satellite at the respective epoch, even though the individual observations refer to slightly different points in time. Second, it assumes that signal biases are constant over the processing period, for instance one day, which is generally the case (Håkansson et al., 2017). In special cases, such as the L5 phase bias of GPS IIF satellites (Montenbruck et al., 2012), biases can also be time-variable and have to be treated accordingly (see Section 6.6.1.4). Another assumption is that the phase ambiguity $N[\mathrm{L}\nu]_r^s$ is constant as long as a track is observed continuously and no cycle slip (see Section 7.1) occurs.

The function for the geometric range in (5.1) is

$$\mathrm{range}(\mathbf{r}^s, \mathbf{r}_r) = \rho_r^s = \|\mathbf{r}^s(t^s) - \mathbf{r}_r(t_r)\| \ , \tag{5.2}$$

where $t_r(t) = t - \frac{\mathrm{clock}_r(t)}{c}$ is the reception time (i.e., the receiver clock reading corrected for the clock error) and $t^s(t, \boldsymbol{p}_r^s) = t_r(t) - \Delta t_{\text{transit}}(\boldsymbol{p}_r^s)$ is the transmission time, which accounts for the transit time $\Delta t_{\text{transit}}$ along the signal path $\boldsymbol{p}_r^s$. Equation (5.2) requires that $\mathbf{r}^s$ and $\mathbf{r}_r$ are in the same reference frame. Since satellite positions usually refer to the CRF and station positions refer to the TRF, this implies a frame transition for either $\mathbf{r}^s$ or $\mathbf{r}_r$. This transition between CRF and TRF is described by the Earth orientation, which is detailed in Section 6.8.

5.2 Ionospheric influence

Section 4.2.3 shows how the full normal equation system can be accumulated from multiple parts. This means that the observation equations and design matrix can be set up in parts using small sets of observations, which has several benefits. For instance, it can significantly reduce the amount of required memory and it enables parallelization. The biggest benefit, however, is that it enables an efficient preelimination of the ionospheric

influence, which massively reduces the number of parameters in the system of equations. The prerequisite for this preelimination of the ionospheric influence is to set up the observation equations

$$\Delta \mathbf{l}_r^s(t) = \mathbf{A}_r^s(t)\Delta\mathbf{x} + \mathbf{B}_r^s(t)\mathbf{y}_r^s(t) + \mathbf{e}_r^s(t) \tag{5.3}$$

for a group of observations between one receiver r and one satellite s at one epoch t. In the following equations, the subscript notation $\square_g = \square_r^s(t)$ is introduced to represent such a group of observations g in order to increase readability. Equation (5.3) thus becomes

$$\Delta \mathbf{l}_g = \mathbf{A}_g\Delta\mathbf{x} + \mathbf{B}_g\mathbf{y}_g + \mathbf{e}_g\,. \tag{5.4}$$

As detailed in Chapter 4, $\Delta\mathbf{l}_g$ is the vector of reduced observations in the group. For example, $\Delta\mathbf{l}_g$ might contain three code (C1C, C1W, C2W) and two phase (L1W, L2W) observations from a receiver to a GPS satellite or four code and phase observations each (τ1C, τ5Q, τ7Q, τ8Q) from a receiver to a Galileo satellite. $\mathbf{y}_g$ is the vector of parameters representing the ionospheric influence on the observations in the group and $\Delta\mathbf{x}$ is the vector of corrections for all other parameters. The design matrices $\mathbf{A}_g$ and $\mathbf{B}_g$ relate the few observations in $\Delta\mathbf{l}_g$ to $\Delta\mathbf{x}$, which can comprise millions of parameters, and $\mathbf{y}_g$, respectively. Finally, $\mathbf{e}_g$ are the observation residuals.

For each observation group the ionospheric influence represented by $\mathbf{y}_g$ can be parameterized as a single STEC parameter. This is valid since all signals in the group travel along the same path through the ionosphere (Fritsche et al., 2005), except for some minor frequency-dependent deviations that can be corrected (see Section 6.4 for more details). The design matrix

$$\mathbf{B}_g = \left.\frac{\partial \boldsymbol{f}_g}{\partial \mathrm{STEC}}\right|_{\mathbf{y}_{g,0}} \tag{5.5}$$

has dimensions $n_g \times 1$, with n_g being the number of observations in the group. The partial derivatives depend on the signal type and frequency of the observation and include first, second, and third order ionospheric corrections as well as a bending effect for phase observations (Hoque and Jakowski, 2008). These corrections and their partial derivatives with respect to the STEC parameter are detailed in Section 6.4.

The ionospheric influence could now be eliminated on the observation equation level as described in Section 4.2.2. However, this would involve a transformation of the design matrix $\mathbf{A}_g$ as stated in Equation (4.29). Since $\mathbf{A}_g$ can potentially contain millions of columns, such a transformation would be a costly operation. In order to avoid

this, a set of intermediate parameters are introduced and the preelimination of the ionospheric influence is instead applied to the observation equations with respect to these parameters.

5.3 Intermediate parameters

Splitting the design matrix $\mathbf{A}_g$ into two parts by introducing intermediate parameters $\mathbf{z}_g$ and applying the chain rule gives

$$\mathbf{A}_g = \frac{\partial \boldsymbol{f}_g}{\partial \mathbf{x}}\bigg|_{\mathbf{x}_0} = \frac{\partial \boldsymbol{f}_g}{\partial \mathbf{z}_g}\bigg|_{\mathbf{z}_{g,0}} \frac{\partial \mathbf{z}_g}{\partial \mathbf{x}}\bigg|_{\mathbf{x}_0} = \mathbf{C}_g \mathbf{D}_g \,. \tag{5.6}$$

The intermediate parameters $\mathbf{z}_g$ comprise the position and clock error for the satellite and receiver ($\mathbf{r}^s$, $\mathbf{r}_r$, δ^s, δ_r), a slant delay parameter s_g covering effects that are the same for all signals in the group (e.g., the tropospheric influence), as well as satellite and receiver signal biases ($\mathbf{b}^s$, $\mathbf{b}_r$). The associated design matrix

$$\mathbf{C}_g = \left[\underbrace{\frac{\partial \boldsymbol{f}_g}{\partial \mathbf{r}^s}}_{n_g \times 3} \;\middle|\; \underbrace{\frac{\partial \boldsymbol{f}_g}{\partial \delta^s}}_{n_g \times 1} \;\middle|\; \underbrace{\frac{\partial \boldsymbol{f}_g}{\partial \mathbf{r}_r}}_{n_g \times 3} \;\middle|\; \underbrace{\frac{\partial \boldsymbol{f}_g}{\partial \delta_r}}_{n_g \times 1} \;\middle|\; \underbrace{\frac{\partial \boldsymbol{f}_g}{\partial s_g}}_{n_g \times 1} \;\middle|\; \underbrace{\frac{\partial \boldsymbol{f}_g}{\partial \mathbf{b}^s}}_{n_g \times b^s} \;\middle|\; \underbrace{\frac{\partial \boldsymbol{f}_g}{\partial \mathbf{b}_r}}_{n_g \times b_r} \right]\Bigg|_{\mathbf{z}_{g,0}} \tag{5.7}$$

contains the partial derivatives of the observation equations with respect to these intermediate parameters. Here, n_g is the number of observations in the group and b^s and b_r are the number of involved satellite and receiver signal bias parameters, respectively. The dimensions of $\mathbf{A}_g$ are $n_g \times m$, those of $\mathbf{C}_g$ are $n_g \times m_g$, and $\mathbf{D}_g$ has dimensions $m_g \times m$, with m being the number of overall parameters and m_g the number of intermediate parameters for the group.

5.3.1 Partial derivatives with respect to intermediate positions and clocks

The partial derivatives of the observation equations with respect to $\mathbf{r}^s$, $\mathbf{r}_r$, δ^s, and δ_r can be determined by rephrasing (5.2). This section assumes that all of these parameters are to be estimated in meters. Since δ_r and $\Delta t_{\text{transit}}$ are generally small (i.e., below 0.1 s) and both satellites and ground-based stations move smoothly through space, the satellite position can be expressed as

$$\mathbf{r}^s(t^s) = \mathbf{r}^s(t) - \frac{\delta_r(t)}{c}\dot{\mathbf{r}}^{\mathbf{s}}(t) - \Delta t_{\text{transit}}\dot{\mathbf{r}}^s(t) \tag{5.8}$$

and the receiver position as

$$\mathbf{r}_r(t_r) = \mathbf{r}_r(t) - \frac{\delta_r(t)}{c}\dot{\mathbf{r}}_\mathbf{r}(t)\,, \tag{5.9}$$

where $\dot{\mathbf{r}}^\mathbf{s}$ and $\dot{\mathbf{r}}_\mathbf{r}$ are the satellite and receiver velocity in the chosen reference frame, respectively, and c is the speed of light. Substituting (5.8) and (5.9) into (5.2) gives

$$\text{range}(\mathbf{r}^s, \mathbf{r}_r) = \rho_g = \left\| \mathbf{r}^s(t) - \frac{\delta_r(t)}{c}\dot{\mathbf{r}}^\mathbf{s}(t) - \Delta t_{\text{transit}}\dot{\mathbf{r}}^s(t) - \mathbf{r}_r(t) - \frac{\delta_r(t)}{c}\dot{\mathbf{r}}_r(t) \right\| \tag{5.10}$$

or, with $\Delta t_{\text{transit}} \approx \frac{\rho_g}{c}$ as well as omitting the time dependency to improve readability,

$$\rho_g = \left\| \mathbf{r}^s - \frac{\delta_r}{c}\dot{\mathbf{r}}^\mathbf{s} - \frac{\rho_g}{c}\dot{\mathbf{r}}^s - \mathbf{r}_r + \frac{\delta_r}{c}\dot{\mathbf{r}}_r \right\| . \tag{5.11}$$

Equation (5.11) shows that the range depends not only on the satellite and receiver position but also on the receiver clock error and, by proxy of the transit time, on itself. Therefore, the transmission time t^s and the corresponding satellite position $\mathbf{r}^s(t^s)$ can be determined iteratively based on the reception time t_r and the receiver position $\mathbf{r}_r(t_r)$. Applying the chain rule with $\rho_g = \|\mathbf{h}\|$ and $\mathbf{h} = \mathbf{r}^s - \frac{\delta_r}{c}\dot{\mathbf{r}}^\mathbf{s} - \frac{\rho_g}{c}\dot{\mathbf{r}}^s - \mathbf{r}_r + \frac{\delta_r}{c}\dot{\mathbf{r}}_r$ gives

$$\frac{\partial f_g}{\partial \mathbf{z}} = \frac{\partial f_g}{\partial \mathbf{h}}\frac{\partial \mathbf{h}}{\partial \mathbf{z}}\,. \tag{5.12}$$

Utilizing that the partial derivative of the Euclidean norm of a vector in $\mathbb{R}^n$ with respect to its components is the same as the normalized vector leads to

$$\frac{\partial f_g}{\partial \mathbf{h}} = \frac{\mathbf{h}}{\|\mathbf{h}\|} = \frac{\mathbf{r}^s - \frac{\delta_r}{c}\dot{\mathbf{r}}^\mathbf{s} - \frac{\rho_g}{c}\dot{\mathbf{r}}^s - \mathbf{r}_r + \frac{\delta_r}{c}\dot{\mathbf{r}}_r}{\rho_g} = -\mathbf{k}_g\,, \tag{5.13}$$

where $\mathbf{k}_g$ is the normalized line-of-sight vector from the satellite to the receiver.

The partial derivative of the observation equations with respect to one of the receiver coordinates, for example r_{r_x}, then is

$$\begin{aligned}
\frac{\partial f_g}{\partial r_{r_x}} = \frac{\partial \rho_g}{\partial \mathbf{h}}\frac{\partial \mathbf{h}}{r_{r_x}} &= -\mathbf{k}_g \cdot \left(-\frac{1}{c}\dot{\mathbf{r}}^\mathbf{s}\frac{\partial \rho_g}{\partial r_{r_x}} - \begin{bmatrix}1\\0\\0\end{bmatrix} \right) \\
&= -\mathbf{k}_g \cdot \left\{ -\frac{1}{c}\dot{\mathbf{r}}^\mathbf{s}\left[-\mathbf{k}_g \cdot \left(-\frac{1}{c}\dot{\mathbf{r}}^\mathbf{s}\frac{\partial \rho_g}{\partial r_{r_x}} - \begin{bmatrix}1\\0\\0\end{bmatrix} \right) \right] - \begin{bmatrix}1\\0\\0\end{bmatrix} \right\} \\
&= -\mathbf{k}_g \cdot \left[\underbrace{-\frac{1}{c^2}\left|\dot{\mathbf{r}}^\mathbf{s}\right|^2 \mathbf{k}_g \frac{\partial \rho_g}{\partial r_{r_x}}}_{\approx \mathbf{0}} - \frac{1}{c}\dot{\mathbf{r}}^\mathbf{s}\left(\mathbf{k}_g \cdot \begin{bmatrix}1\\0\\0\end{bmatrix} \right) - \begin{bmatrix}1\\0\\0\end{bmatrix} \right] \\
&= k_{g_x}\left(1 + \frac{1}{c}\dot{\mathbf{r}}^\mathbf{s} \cdot \mathbf{k}_g \right) ,
\end{aligned} \tag{5.14}$$

where $\square \cdot \square$ is the dot product of two vectors and the subscript $\square_x$ refers to the first component of a vector in 3D space (i.e., $\mathbf{k}_g = [\ k_{g_x}\ k_{g_y}\ k_{g_z}\ ]^T$). Therefore, the partial derivative with respect to the intermediate receiver position vector is

$$\frac{\partial f_g}{\partial \mathbf{r}_r} = \mathbf{k}_g^T \left(1 + \frac{1}{c}\dot{\mathbf{r}}^{\mathbf{s}} \cdot \mathbf{k}_g\right) . \tag{5.15}$$

For one of the satellite coordinates, for instance r_x^s, the partial derivative is

$$\begin{aligned}
\frac{\partial f_g}{\partial r_x^s} = \frac{\partial \rho_g}{\partial \mathbf{h}} \frac{\partial \mathbf{h}}{r_x^s} &= -\mathbf{k}_g \cdot \left(\begin{bmatrix}1\\0\\0\end{bmatrix} - \frac{1}{c}\dot{\mathbf{r}}^{\mathbf{s}} \frac{\partial \rho_g}{\partial r_x^s}\right) \\
&= -\mathbf{k}_g \cdot \left\{\begin{bmatrix}1\\0\\0\end{bmatrix} - \frac{1}{c}\dot{\mathbf{r}}^{\mathbf{s}} \left[-\mathbf{k}_g \cdot \left(\begin{bmatrix}1\\0\\0\end{bmatrix} - \frac{1}{c}\dot{\mathbf{r}}^{\mathbf{s}} \frac{\partial \rho_g}{\partial r_x^s}\right)\right]\right\} \\
&= -\mathbf{k}_g \cdot \left[\begin{bmatrix}1\\0\\0\end{bmatrix} + \frac{1}{c}\dot{\mathbf{r}}^{\mathbf{s}} \left(\mathbf{k}_g \cdot \begin{bmatrix}1\\0\\0\end{bmatrix}\right) - \underbrace{\frac{1}{c^2} |\dot{\mathbf{r}}^{\mathbf{s}}|^2 \mathbf{k}_g \frac{\partial \rho_g}{\partial r_x^s}}_{\approx \mathbf{0}}\right] \\
&= -k_{g_x} \left(1 + \frac{1}{c}\dot{\mathbf{r}}^{\mathbf{s}} \cdot \mathbf{k}_g\right) .
\end{aligned} \tag{5.16}$$

In this case, the partial derivative with respect to the intermediate satellite position vector is

$$\frac{\partial f_g}{\partial \mathbf{r}^s} = -\mathbf{k}_g^T \left(1 + \frac{1}{c}\dot{\mathbf{r}}^{\mathbf{s}} \cdot \mathbf{k}_g\right) . \tag{5.17}$$

Equations (5.15) and (5.17) show that the intermediate receiver and satellite coordinates are influenced by the projection of the satellite velocity into the line of sight between receiver and satellite. The same approach can also be used for the partial derivative with respect to the receiver clock error δ_r, resulting in

$$\begin{aligned}
\frac{\partial f_g}{\partial \delta_r} = \frac{\partial \,\mathrm{clock}_r}{\partial \delta_r} + \frac{\partial \rho_g}{\partial \mathbf{h}} \frac{\partial \mathbf{h}}{\delta_r} &= 1 + (-\mathbf{k}_g) \cdot \left(-\frac{1}{c}\dot{\mathbf{r}}^{\mathbf{s}} - \underbrace{\frac{1}{c}\dot{\mathbf{r}}^{\mathbf{s}} \frac{\partial \rho_g}{\partial \delta_r}}_{\approx \mathbf{0}} + \frac{1}{c}\dot{\mathbf{r}}_{\mathbf{r}}\right) \\
&= 1 + \frac{1}{c}\mathbf{k}_g \cdot (\dot{\mathbf{r}}^{\mathbf{s}} - \dot{\mathbf{r}}_{\mathbf{r}}) ,
\end{aligned} \tag{5.18}$$

which reveals that the receiver clock error is affected by the relative velocity between satellite and receiver projected into their line of sight. Finally, the partial derivative with respect to the satellite clock error δ^s is simply

$$\frac{\partial f_g}{\partial \delta^s} = \frac{\partial \,\mathrm{clock}_r}{\partial \delta^s} = -1 . \tag{5.19}$$

5.3.2 Partial derivatives with respect to other intermediate parameters

The partial derivative with respect to the slant delay parameter s_g is

$$\frac{\partial f_g}{\partial s_g} = 1 \tag{5.20}$$

for all signals, as it covers the effect that is the same for each observation, for instance the tropospheric delay.

At the receiver, an intermediate bias parameter is set up for each observed code and phase signal. The reason for this is that usually these signals are processed largely independently within receivers and thus each signal presumably has an individual bias. The partial derivatives with respect to the signal biases for the observation group thus follow as

$$\frac{\partial \boldsymbol{f}_g}{\partial \mathbf{b}_r} = \mathbf{I}\,. \tag{5.21}$$

The situation is slightly different for the signal biases at the satellite. GNSS satellites transmit a clearly defined set of signals, for instance the code signals C1C, C1W, and C2W in case of older GPS satellites. Some receivers, however, do not measure each of these signals directly, rather they sometimes measure a linear combination of multiple transmitted signals (Won and Pany, 2017). For example, many early GPS receivers measured the linear combination C2D $=$ C1C $+$ (C1W $-$ C2W) (Woo, 2000). It is also assumed that while the different codes that are modulated onto the carrier phases might lead to individual code biases at the satellite, the phase biases are identical for all signals transmitted on the same frequency. All of this means that the observed signal types need to be mapped to the original signal types transmitted by the satellite in order to factor in the correct signal bias parameters. An example for one of the aforementioned legacy GPS receivers are the partial derivatives

$$\frac{\partial \boldsymbol{f}_g}{\partial \mathbf{b}^s} = \begin{array}{c} \\ \text{C1C} \\ \text{C2D} \\ \text{L1C} \\ \text{L2D} \end{array} \begin{array}{c} \begin{array}{ccccc} \text{C1C} & \text{C1W} & \text{C2W} & \text{L1} & \text{L2} \end{array} \\ \begin{bmatrix} 1 & & & & \\ 1 & -1 & 1 & & \\ & & & 1 & \\ & & & & 1 \end{bmatrix} \end{array}, \tag{5.22}$$

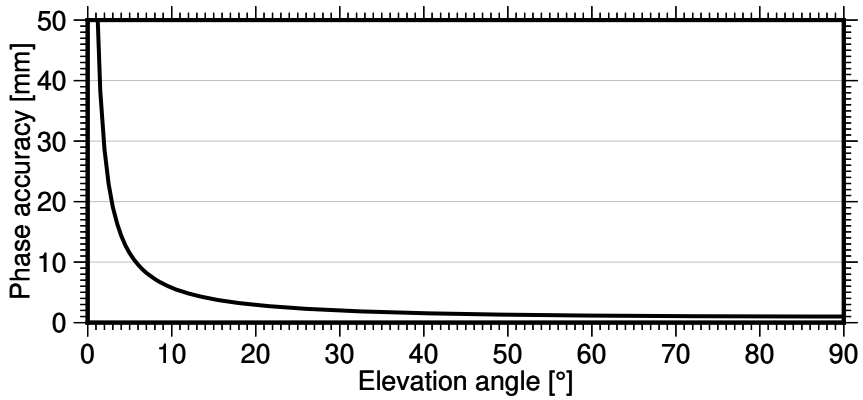

Figure 5.1: A priori phase accuracy over elevation angle used for initial observation weighting

which map the four observed signal types C1C, C2D, L1C, and L2D to the five bias parameters covering the signals transmitted by the satellite. More information about the mapping of signal types can be found in Sections 6.5 and 6.6.

5.4 Observation weighting

Observation weighting is directly applied to the observation equations in (5.4) by homogenizing them as shown in Section 4.2.1. Each reduced observation in $\Delta\mathbf{l}_g$ and its corresponding rows in the design matrices $\mathbf{C}_g$ and $\mathbf{B}_g$ covering the intermediate parameters and the STEC parameter are divided by the standard deviation (i.e., measurement accuracy) of the respective observation.

Initially, observations are weighted based on their elevation angle (e.g., Vermeer, 1997; Rothacher et al., 1998). The a priori standard deviation of a signal of type τ depending on the elevation angle e can be expressed as

$$\sigma[\tau](e) = \frac{\sigma_z[\tau]}{\sin e}\,. \tag{5.23}$$

Equation (5.23) maps the measurement accuracy at zenith $\sigma_z[\tau]$ (e.g., $\sigma_z[\mathrm{L}] = 1\,\mathrm{mm}$ and $\sigma_z[\mathrm{C}] = 20\,\mathrm{cm}$) to the elevation angle of an observation. Figure 5.1 visualizes the phase accuracy from horizon to zenith and clearly shows that the accuracy quickly deteriorates close to the horizon and thus these observations get a much lower weight. The main reason for the lower measurement accuracy close to the horizon is the antenna gain (Maqsood et al., 2017). Other reasons include the longer signal path through the atmosphere, multipath effects, and orbit errors (Kermarrec, 2018).

Section 5.7 details how new observation weights can be determined by analyzing the residuals after solving the least-squares adjustment and applying variance component estimation. The determined weights comprise individual weights for each code observation and a combined weight for all phase observations in an observation group. They are applied by adjusting the standard deviations of the observations, which then takes effect in the homogenization step of a subsequent iteration in the least-squares adjustment.

5.5 Preelimination of the ionospheric influence

In the next step, the STEC parameter contained in $\mathbf{y}_g$ is eliminated from the observation equations

$$\Delta\mathbf{l}_g = \mathbf{C}_g\mathbf{D}_g\Delta\mathbf{x} + \mathbf{B}_g\mathbf{y}_g + \mathbf{e}_g\,. \tag{5.24}$$

Splitting the design matrix as $\mathbf{A}_g = \mathbf{C}_g\mathbf{D}_g$ has the benefit that the transformation described in Section 4.2.2 can be applied to $\mathbf{C}_g$ instead of $\mathbf{A}_g$. Therefore, only a small number of parameters are involved in the parameter elimination process and relatively few mathematical operations are required. Combining this with the possibility to process observation groups in parallel enables high computational efficiency.

Note that the following equations represent the general form valid for eliminating one or more parameters from an observation group. The equations can be simplified significantly in case only a single STEC parameter is eliminated. However, this simplification is not shown here.

Based on the QR decomposition (e.g., Golub and Van Loan, 2013)

$$\mathbf{B} = \mathbf{Q}\mathbf{R} = \begin{bmatrix}\mathbf{Q}_1 & \mathbf{Q}_2\end{bmatrix}\begin{bmatrix}\mathbf{R}_1\\ \mathbf{0}\end{bmatrix}\,, \tag{5.25}$$

where $\mathbf{B}$ has dimensions $n_g \times 1$, $\mathbf{Q}_2$ is an $n_g \times (n_g - 1)$ matrix, and n_g is the number of observations in the group, the transformations

$$\bar{\mathbf{C}}_g = \mathbf{Q}_2^T\mathbf{C}_g \quad \text{and} \quad \Delta\bar{\mathbf{l}}_g = \mathbf{Q}_2^T\Delta\mathbf{l}_g \tag{5.26}$$

lead to reduced observation equations

$$\Delta\bar{\mathbf{l}}_g = \bar{\mathbf{C}}_g\mathbf{D}_g\Delta\mathbf{x} + \bar{\mathbf{e}}_g\,. \tag{5.27}$$

Due to the elimination of the STEC parameter, the observation vector $\Delta\bar{\mathbf{l}}_g$, the design matrix $\bar{\mathbf{C}}_g$, and the residual vector $\bar{\mathbf{e}}_g$ have one fewer row than $\Delta\mathbf{l}_g$, $\mathbf{C}_g$, and $\mathbf{e}_g$, respectively. All STEC parameters are later reconstructed during residual analysis (see Section 5.7). The full design matrix with respect to all parameters in $\Delta\mathbf{x}$ is

$$\bar{\mathbf{A}}_g = \bar{\mathbf{C}}_g \mathbf{D}_g = \bar{\mathbf{C}}_g \frac{\partial \mathbf{z}_g}{\partial \mathbf{x}}\bigg|_{\mathbf{x}_0} . \tag{5.28}$$

The composition of $\mathbf{D}_g$ depends on the parametrization of the different components involved in the full observation equations. These parametrizations and their corresponding design matrix entries are discussed in detail in Chapter 6. The subsequent sections assume that STEC parameters have been eliminated from the observation equations and the bar notation is omitted for the sake of readability.

5.6 Normal equation structure

The type of GNSS processing described in this thesis usually results in a highly sparse normal equation matrix. Since the normal equations are solved via Cholesky decomposition (see Section 4.2.4), it is important that the upper triangular Cholesky factor $\mathbf{W}$ involved in this step remains sparse. This can be achieved by ordering the parameters in $\Delta\mathbf{x}$ in a specific way. The sparsity of both matrices can then be utilized by splitting them into smaller subblocks. As many of these subblocks will only contain zeros, they do not have to be kept in memory and their matrix operations may be skipped. This is an important aspect with respect to computational efficiency, specifically memory usage in case of a large number of parameters.

Figure 5.2 schematically visualizes the structure of the design matrix $\mathbf{A}_g$ for one observation group. For an easier interpretation of the connection between observations and design matrix columns, this visualization assumes that the STEC parameter has not been eliminated as described in Section 5.5. Therefore, the original observations are listed on the left and no row has been eliminated from the design matrix. The structure comprises blocks for all epochs and one block each for receiver, satellite, and global parameters as well as ambiguities. Global parameters refer to those parameters that cannot be attributed to a specific receiver or satellite, for example Earth orientation parameters or ionosphere maps. An observation group is only related to one receiver and satellite at a single epoch and thus only concerns a small number of the overall parameters covered by the design matrix $\mathbf{A}_g$. Therefore, only a few columns in the design matrix of a specific observation group are filled.

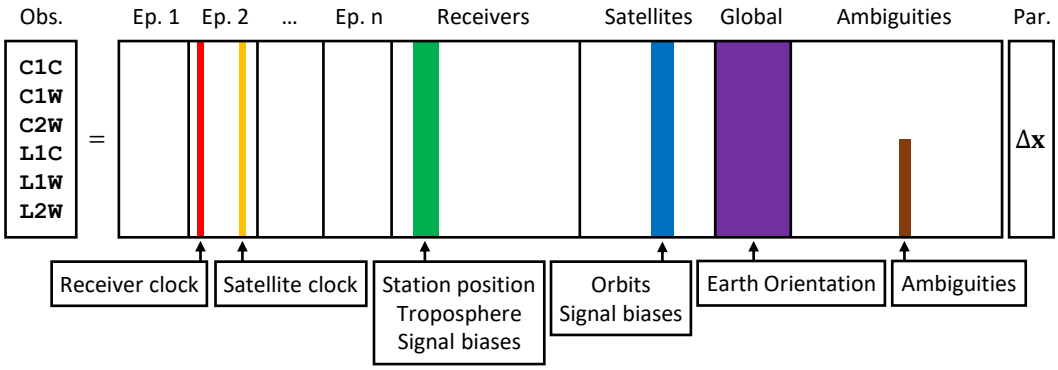

Figure 5.2: Schematic view of design matrix structure for one observation group (not to scale)

The full normal equations are set up by accumulating individual normal equation matrices and right-hand sides of each observation group according to Section 4.2.3. This means the design matrices for all observation groups can be set up consecutively, which massively reduces the memory requirements compared to setting up the design matrix for all observations at once. As the individual observation groups are independent of each other, their design matrices can also be setup up in parallel, further improving computational performance in distributed computing environments.

5.6.1 Schematic structure of the normal equation matrix

Whenever multiple parameters occur in the same observation equation, the resulting normal equation matrix contains off-diagonal elements. For example, the observation equations displayed in Figure 5.2 lead to populated off-diagonal elements between all highlighted parameters. Figure 5.3 schematically visualizes the structure of the final accumulated normal equation matrix. This visualization contains the same blocks and colors as the design matrix in Figure 5.2. Ordering parameters in the described way yields a so-called kite structure (Tewarson and Cheng, 1973; Boxhammer and Schuh, 2006), which is largely retained during Cholesky decomposition. The structure features individual blocks for each epoch followed by the blocks for receiver, satellite, and global parameters as well as the ambiguity block on its diagonal.

The epoch parameter section of the normal equation matrix has a block-diagonal structure. This is the case because observation equations only ever contain clock parameters from a single epoch and thus no off-diagonal elements between epochs are populated. In principal, this structure also facilitates the introduction of off-diagonal blocks between epoch blocks. An example for this would be the stochastic modeling of clock parameters, which connects subsequent epochs and would result in a block-banded structure. Epoch

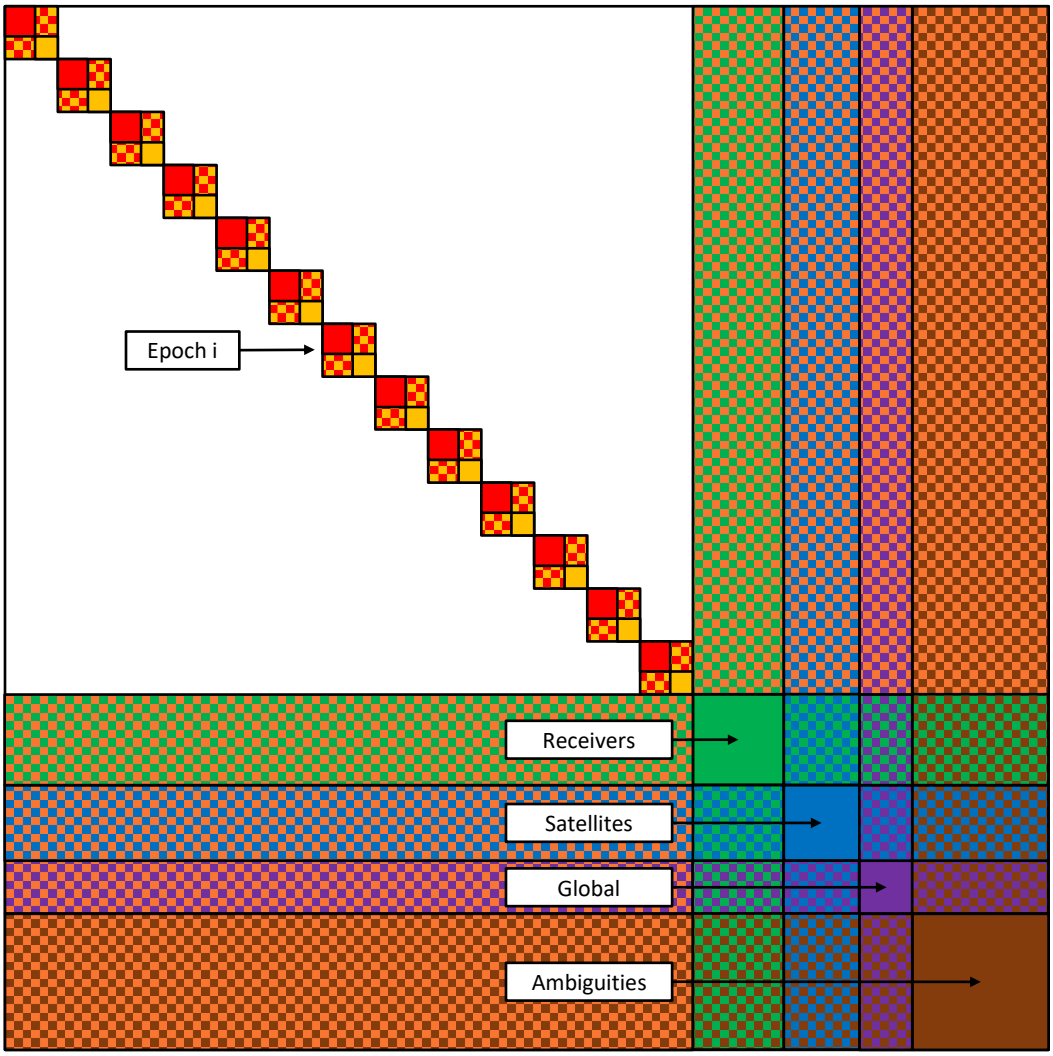

Figure 5.3: Schematic view of normal equation matrix structure (not to scale)

blocks usually contain receiver (red) and satellite (yellow) clock parameters. The populated off-diagonal elements between receiver and satellite clocks within one epoch block are represented by the checkered pattern of the respective colors.

The off-diagonal blocks between epoch and nonepoch parameters are largely populated, which is again visualized by the checkerboard pattern in Figure 5.3. These elements are populated because the same nonepoch parameters can appear in the observation equations of multiple epoch. For example, station positions are usually estimated as constant values over one day and thus the same three parameters appear in all observation equations of a receiver. These observation equations also contain the clock parameter of that receiver and those of the observed satellites at the respective epoch, resulting in the off-diagonal elements. The off-diagonal blocks between epoch and nonepoch blocks make up the majority of the required memory for the normal equation matrix. Hence, it is important that they are as dense as possible. Since the matrix is symmetric, only its upper or lower triangle has to be kept in memory, almost halving its overall memory demands.

5.6.2 Example of actual normal equation matrix structure

The schematic view in Figure 5.3 is not to scale and, therefore, somewhat misleading with respect to how the normal equation matrix looks like in practice. Figure 5.4 shows the actual (to-scale) structure based on an example. This example involves a small network of 56 stations and the GPS constellation and uses a 5-minute sampling period. For this visualization, the matrix is divided into subblocks covering around 90 parameters each. Black and white pixels represent nonzero and zero subblocks, respectively. The global block is not clearly discernible as it only contains six Earth orientation parameters in this example and is thus represented by a single pixel.

Figure 5.4 reveals several characteristics of the normal equation matrix. First of all, the receiver, satellite, and ambiguity blocks are block-diagonal in the unconstrained normal equations. For the receiver and satellite blocks, this is the case because observation equations only concern one receiver and one transmitter at a time. The structure slightly changes once constraints are added to the normal equation matrix in order to resolve the rank deficiencies. An example for this are no-net rotation constraints on the station positions (see Section 6.9.1), which result in populated off-diagonal elements between the position parameters of all involved receivers. While the addition of these constraints results in fully populated receiver and satellite blocks, the overall structure of the normal equation matrix stays largely the same. Ambiguity parameters for different tracks never

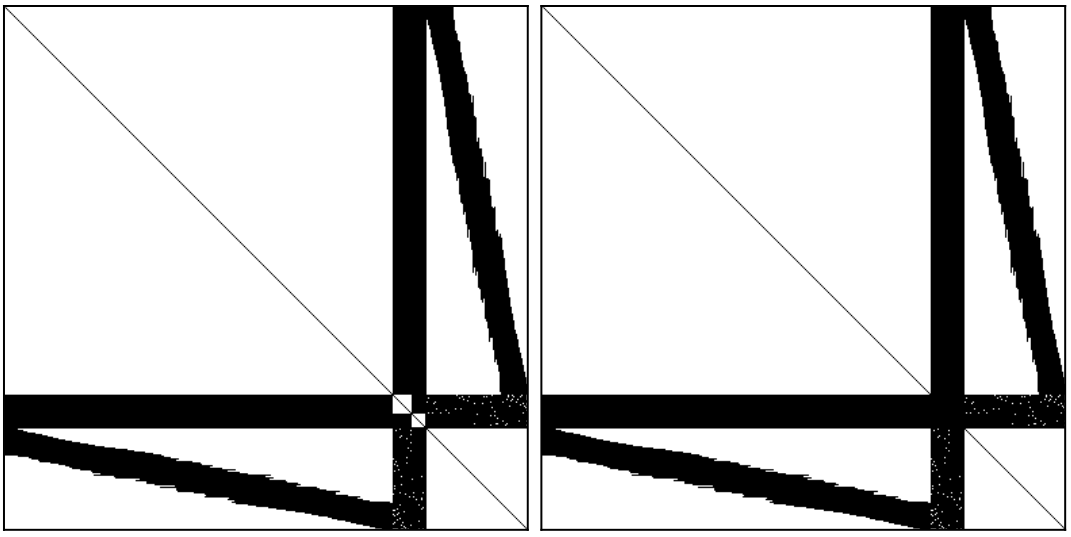

(a) Unconstrained **(b)** Constrained

Figure 5.4: Actual (to-scale) structure of the example normal equation matrix. Each black pixel represents a nonzero subblock of ≈90 parameters

appear in the same observation equations, which is why only the subblocks on the main diagonal of that section are populated.

Second, the off-diagonal block between the epoch and ambiguity blocks has a roughly block-banded structure. This is the result of ordering the ambiguity parameters by the mean time of their associated tracks. The benefit of this ordering is that the band is densely populated, while around 75% of the overall block is unpopulated. Splitting this off-diagonal block into subblocks and only keeping the dense nonzero blocks in memory thus results in high memory efficiency.

Finally, the off-diagonal blocks between the ambiguity block and the other nonepoch blocks are not fully populated and contain some zero subblocks. The ratio of zero to nonzero subblocks depends on the chosen subblock size. Smaller subblocks result in more zero blocks and, therefore, lower memory demand. On the other hand, the efficiency of matrix-matrix operations decreases with smaller matrix dimensions (e.g., Goto and Van De Geijn, 2008). Therefore, choosing the size of the subblocks is a trade-off between memory usage and computational performance.

Zooming into a single epoch block reveals its composition, which is shown in Figure 5.5. Here, each pixel represents a single matrix element, with white being zero. In the unconstrained case, the receiver and satellite parts are diagonal matrices, as observation equations only contain clock parameters for a single receiver and satellite. The off-diagonal elements between receiver and satellite clock parameters are partly populated and depend on which satellites each receiver is observing at that epoch. In this example,

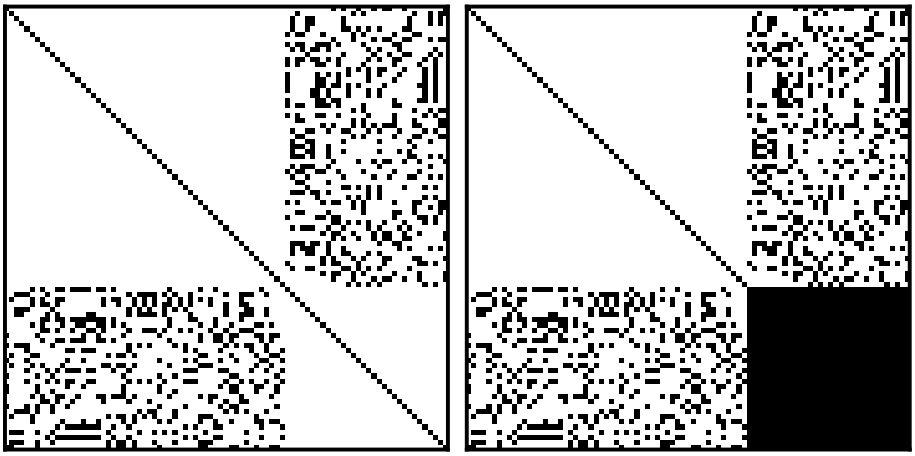

(a) Unconstrained **(b)** Constrained

Figure 5.5: Structure of a single epoch block in the example normal equation matrix. Receiver clock parameters on the top left and satellite clock parameters on the bottom right

the rank deficiency of the clock parameters is resolved by a zero-mean constraint over all satellite clocks at each epoch (see Section 6.3.2). This is clearly visible as the satellite part becomes fully populated once the constraints are added.

As mentioned at the beginning of this section, it is important that the Cholesky decomposition of the normal equation matrix keeps a sparse structure. Figure 5.6 visualizes the upper triangular Cholesky factor $\mathbf{W}$ from the Cholesky decomposition $\mathbf{N} = \mathbf{W}^T\mathbf{W}$ next to the example normal equation matrix $\mathbf{N}$. It is clearly visible that the structure is largely retained and only the triangle covering the receiver, satellite, and ambiguity parameters becomes fully populated. As the Cholesky decomposition can be performed in place, another benefit of the similar structure is that no major reallocation of subblocks outside of the mentioned triangle is required.

The sparsity of the normal equation matrix is highly influenced by the size of the problem to be solved. The example described in this section, which is rather small with its 56 stations, 32 GPS satellites, and 5-minute sampling period, produces a normal equation matrix with 388×388 subblocks of around 90 parameters each. Out of the 75 466 subblocks in one triangle of the symmetric matrix, only 15 771 or 21% are populated, resulting in a sparsity of 79%. Storing this matrix in memory takes up $15\,771 \cdot 90^2 \cdot 8$ bytes or approximately 1 GB. In the last years of the contribution to the IGS reprocessing campaign, more than 800 stations and up to 80 satellites were processed at a 30-second sampling period. With optimized subblock sizes, the full normal equation matrix for a problem of such a large size would have a sparsity of 99%. Even with such an extreme sparsity, storing the populated subblocks would require several hundred gigabytes of memory. Therefore, it is necessary to adapt the processing

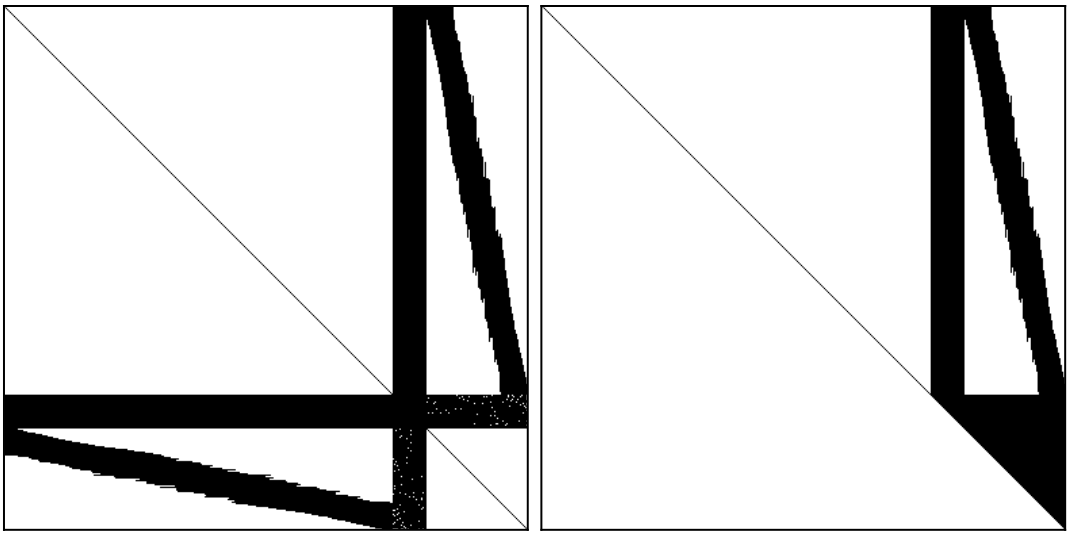

(a) Normal equation matrix $\mathbf{N}$ **(b)** Cholesky factor $\mathbf{W}$

Figure 5.6: Actual (to-scale) structure of the Cholesky decomposition of the example normal equation matrix. Each black pixel represents a nonzero subblock of ≈90 parameters

strategy in order to reduce the problem to a more manageable size. More details on this topic are provided in Section 5.9.

5.7 Residual computation and reconstruction of ionospheric influence

Once the normal equation system has been solved, the residuals can be computed in order to determine new weights via VCE. This step can again be performed on the basis of the observation groups as introduced in Section 5.3. Since the components of the observation equations are discarded after a group's normal equations are added to the full normal equations, they have to be set up again in this step. However, this time the STEC parameter is not immediately preeliminated from the observation equations. Instead, the full observation equations

$$\Delta\mathbf{l}_g = \mathbf{A}_g\Delta\mathbf{x} + \mathbf{B}_g\mathbf{y}_g + \mathbf{e}_g\,. \tag{5.29}$$

are set up, containing the full number of rows for all observation in $\Delta\mathbf{l}_g$. Note that these observation equations are again homogenized and weighted according to Section 5.4.

Based on the estimated parameter corrections $\Delta\hat{\mathbf{x}}$, biased residuals $\tilde{\mathbf{e}}_g$ can then be computed via

$$\tilde{\mathbf{e}}_g = \mathbf{e}_g + \mathbf{B}_g\mathbf{y}_g = \Delta\mathbf{l}_g - \mathbf{A}_g\Delta\hat{\mathbf{x}}\,. \tag{5.30}$$

These residuals are biased because the ionospheric influence was not preeliminated from the observation equations as was the case when the parameter corrections $\Delta\hat{\mathbf{x}}$ were estimated. This can be utilized to reconstruct the eliminated STEC parameters by estimating them from the biased residuals $\tilde{\mathbf{e}}_g$. Note that the following equations represent the general form valid for reconstructing one or more eliminated parameters within an observation group. In the case of a single STEC parameter, the equations can be simplified significantly. However, this is not shown here. Introducing the biased residuals as pseudoobservations into a small equation system

$$\tilde{\mathbf{e}}_g = \mathbf{B}_g\mathbf{y}_g + \mathbf{e}_g \tag{5.31}$$

allows the estimation of $\mathbf{y}_g$ containing the STEC parameter for the observation group and the subsequent computation of the unbiased estimated residuals $\hat{\mathbf{e}}_g$. The equation system in (5.31) can be solved efficiently based on the QR decomposition

$$\mathbf{B}_g = \mathbf{Q}\mathbf{R} = \begin{bmatrix}\mathbf{Q}_1 & \mathbf{Q}_2\end{bmatrix}\begin{bmatrix}\mathbf{R}_1 \\ \mathbf{0}\end{bmatrix}\,. \tag{5.32}$$

Since $\mathbf{R}_1$ is an upper triangular matrix and $\mathbf{Q}^{-1} = \mathbf{Q}^T$ due to the orthogonality of $\mathbf{Q}$, the equation system

$$\mathbf{Q}_1^T\tilde{\mathbf{e}}_g = \mathbf{R}_1\mathbf{y}_g \tag{5.33}$$

can be solved directly for $\mathbf{y}_g$ via backward substitution and without having to compute the inverse matrices $\mathbf{Q}^{-1}$ and $\mathbf{R}_1^{-1}$ (e.g., Golub and Van Loan, 2013). The STEC parameter contained in $\mathbf{y}_g$ has thus been reconstructed. It can be introduced as an initial value for the computation of higher-order ionospheric corrections and their partial derivatives in a subsequent iteration of the full equation system.

The unbiased estimated residuals can be obtained as

$$\bar{\mathbf{e}}_g = \begin{bmatrix}\mathbf{Q}_1 & \mathbf{Q}_2\end{bmatrix}\begin{bmatrix}\mathbf{0} & \mathbf{0} \\ \mathbf{0} & \mathbf{I}\end{bmatrix}\begin{bmatrix}\mathbf{Q}_1^T \\ \mathbf{Q}_2^T\end{bmatrix}\tilde{\mathbf{e}}_g = \mathbf{Q}_2\mathbf{Q}_2^T\tilde{\mathbf{e}}_g\,. \tag{5.34}$$

Here, the biased residuals $\tilde{\mathbf{e}}_g$ are first transformed into the space of the ionospheric parameters via multiplication with $\mathbf{Q}^T$. In this space, the first p rows or transformed pseudoobservations are solely used to determine the p ionospheric parameters and

do not contribute to the residuals. Therefore, setting these rows to zero removes the influence of these parameters from the residuals. Transforming the modified vector back to the original space via multiplication with $\mathbf{Q}$ results in the unbiased estimated residuals $\bar{\mathbf{e}}_g$. As (5.34) shows, this is the same as projecting the biased residuals into the space orthogonal to the column space of $\mathbf{B}$ using the orthogonal projector $\mathbf{\Pi}_B^{\perp} = \mathbf{Q}_2\mathbf{Q}_2^T$.

The residuals contained in $\bar{\mathbf{e}}_g$ are homogenized. This is the case because the observation equations have been homogenized as described in Section 5.4. The actual residuals can be obtained as $\hat{e}_i = \sigma_i \bar{e}_i$, where σ_i is the standard deviation of the corresponding observation.

5.8 Redundancy computation and weight determination

The determination of new weights based on VCE requires the computation of the redundancies, as described in Section 4.4. Equation (4.56) shows that the redundancies can be computed based on a stochastic trace estimator (Koch and Kusche, 2002) using the vector

$$\mathbf{u}_g = \mathbf{A}_g\mathbf{W}^{-1}\mathbf{z}\,, \tag{5.35}$$

where $\mathbf{A}_g$ is the design matrix for an observation group g, $\mathbf{W}$ is the Cholesky factor of the full normal equation matrix, and $\mathbf{z}$ contains m discrete realizations of a random variable. Here, m is the number of parameters in the full normal equation system. The design matrix $\mathbf{A}_g$ is the same one as used for residual computation in the previous section, meaning ionospheric parameters have not been preeliminated. The inversion of $\mathbf{W}$ in (5.35) can again be avoided by setting up the equation system

$$\mathbf{W}\mathbf{v} = \mathbf{z} \tag{5.36}$$

and solving it directly for $\mathbf{v}$ via backward substitution. Equation (5.35) then becomes

$$\mathbf{u}_g = \mathbf{A}_g\mathbf{v}\,. \tag{5.37}$$

Section 4.4 also mentions that multiple independent realizations of $\mathbf{z}$ can lead to different trace estimates and, therefore, a mean over multiple realizations gives a more stable estimate. By defining a matrix

$$\mathbf{V} = \begin{bmatrix}\mathbf{v}_1 & \mathbf{v}_2 & \cdots & \mathbf{v}_z\end{bmatrix} \tag{5.38}$$

containing z columns $\mathbf{v}_i = \mathbf{W}^{-1}\mathbf{z}_i$ based on z independent realizations of $\mathbf{z}$, the trace computation can be performed for all realizations at once. In practice, $z = 100$ realizations have been determined to be sufficient for getting a stable trace estimate in the context of GNSS processing. The vector $\mathbf{u}_g = \mathbf{A}_g\mathbf{v}$ then becomes a matrix $\mathbf{U}_g = \mathbf{A}_g\mathbf{V}$ with z columns. Since $\mathbf{V}$ is independent of the observation group, it only has to be set up once and can be used for all groups.

The influence of the ionospheric parameters on the redundancy computation can be removed via

$$\bar{\mathbf{U}}_g = \begin{bmatrix}\mathbf{Q}_1 & \mathbf{Q}_2\end{bmatrix}\left(\begin{bmatrix}\mathbf{0} & \mathbf{0}\\ \mathbf{0} & \mathbf{I}\end{bmatrix}\begin{bmatrix}\mathbf{Q}_1^T\\ \mathbf{Q}_2^T\end{bmatrix}\mathbf{U}_g + \begin{bmatrix}\mathbf{I}\\ \mathbf{0}\end{bmatrix}\right) = \mathbf{Q}\begin{bmatrix}\mathbf{I}_{p\times z}\\ \mathbf{Q}_2^T\mathbf{U}_g\end{bmatrix}. \tag{5.39}$$

Similar to the computation of unbiased residuals in (5.34), the matrix $\mathbf{U}_g$ is first transformed to the space of the ionospheric parameters via multiplication with $\mathbf{Q}^T$. This time, however, the first p rows of the transformed matrix are replaced by an $p \times z$ unit matrix instead of setting them to zero. Imagining $\mathbf{Q}^T\mathbf{U}_g$ as a transformed design matrix, this has the effect that the first p rows of the associated observation vector are solely used to determine the ionospheric parameters. Hence, these rows do not contribute to the redundancies in the same way that the corresponding rows in the biased residual vector transformed to this space do not contribute to the unbiased residuals. The modified matrix is then transformed back to the original space via multiplication with $\mathbf{Q}$.

Another way to show this is by transforming the design matrix $\mathbf{A}$ to the space of the ionosphere parameters and adding $\mathbf{R}$ as additional columns for the ionospheric parameters. In case of representing the ionospheric influence by the STEC parameter, this is a single additional column. Note that the subscript g is omitted in the following equations to increase readability. The extended design matrix

$$\tilde{\mathbf{A}} = \begin{bmatrix}\mathbf{R}_1 & \tilde{\mathbf{A}}_1\\ \mathbf{0} & \tilde{\mathbf{A}}_2\end{bmatrix} = \begin{bmatrix}\mathbf{R}_1 & \mathbf{Q}_1^T\mathbf{A}\\ \mathbf{0} & \mathbf{Q}_2^T\mathbf{A}\end{bmatrix} \tag{5.40}$$

can then be used to form the normal equation matrix

$$\tilde{\mathbf{N}} = \tilde{\mathbf{A}}^T\tilde{\mathbf{A}} = \begin{bmatrix}\mathbf{R}_1^T\mathbf{R}_1 & \mathbf{R}_1^T\tilde{\mathbf{A}}_1\\ \tilde{\mathbf{A}}_1\mathbf{R}_1 & \tilde{\mathbf{A}}_1^T\tilde{\mathbf{A}}_1 + \tilde{\mathbf{A}}_2^T\tilde{\mathbf{A}}_2\end{bmatrix}. \tag{5.41}$$

Since $\tilde{\mathbf{A}}_2 = \mathbf{Q}_2^T\mathbf{A}$ is the same matrix as if the ionospheric parameters had been preeliminated from the observation equations (see Section 5.5), it can be shown that

$\tilde{\mathbf{A}}_2^T \tilde{\mathbf{A}}_2 = \mathbf{W}^T\mathbf{W} = \mathbf{N}$. Here, $\mathbf{W}$ is the Cholesky factor of the normal equation matrix $\mathbf{N}$ obtained by these reduced observation equations. The Cholesky factor

$$\tilde{\mathbf{W}} = \begin{bmatrix} \mathbf{R}_1 & \tilde{\mathbf{A}}_1 \\ \mathbf{0} & \mathbf{W} \end{bmatrix} \tag{5.42}$$

of $\tilde{\mathbf{N}}$ can thus be expressed as an extension of the Cholesky factor $\mathbf{W}$. Substituting (5.40) and (5.42) into $\tilde{\mathbf{U}} = \mathbf{Q}\tilde{\mathbf{A}}\tilde{\mathbf{W}}^{-1}\tilde{\mathbf{Z}}$ along with an extended matrix $\tilde{\mathbf{Z}} = \begin{bmatrix} \mathbf{I} & \mathbf{Z} \end{bmatrix}^T$ leads to

$$\begin{aligned}
\tilde{\mathbf{U}} &= \mathbf{Q}\tilde{\mathbf{A}}\tilde{\mathbf{W}}^{-1}\tilde{\mathbf{Z}} \\
&= \mathbf{Q} \begin{bmatrix} \mathbf{R}_1 & \tilde{\mathbf{A}}_1 \\ \mathbf{0} & \tilde{\mathbf{A}}_2 \end{bmatrix} \begin{bmatrix} \mathbf{R}_1 & \tilde{\mathbf{A}}_1 \\ \mathbf{0} & \mathbf{W} \end{bmatrix}^{-1} \begin{bmatrix} \mathbf{I} \\ \mathbf{Z} \end{bmatrix} \\
&= \mathbf{Q} \begin{bmatrix} \mathbf{R}_1 & \tilde{\mathbf{A}}_1 \\ \mathbf{0} & \tilde{\mathbf{A}}_2 \end{bmatrix} \begin{bmatrix} \mathbf{R}_1^{-1}\left(\mathbf{I} - \tilde{\mathbf{A}}_1\mathbf{W}^{-1}\mathbf{Z}\right) \\ \mathbf{W}^{-1}\mathbf{Z} \end{bmatrix} \\
&= \mathbf{Q} \begin{bmatrix} \mathbf{I} - \tilde{\mathbf{A}}_1\mathbf{W}^{-1}\mathbf{Z} + \tilde{\mathbf{A}}_1\mathbf{W}^{-1}\mathbf{Z} \\ \tilde{\mathbf{A}}_2\mathbf{W}^{-1}\mathbf{Z} \end{bmatrix} \\
&= \mathbf{Q} \begin{bmatrix} \mathbf{I} \\ \tilde{\mathbf{A}}_2\mathbf{W}^{-1}\mathbf{Z} \end{bmatrix} \\
&= \mathbf{Q} \begin{bmatrix} \mathbf{I} \\ \mathbf{Q}_2^T\mathbf{U} \end{bmatrix},
\end{aligned} \tag{5.43}$$

which is the same as $\bar{\mathbf{U}}_g$ obtained from (5.39). The redundancy for the ith observation in the group can then be computed from $\bar{\mathbf{u}}_i^T := \mathrm{row}_i\, \bar{\mathbf{U}}_g$ as

$$r_i = 1 - \frac{\bar{\mathbf{u}}_i^T \bar{\mathbf{u}}_i}{z}, \tag{5.44}$$

where z is the number of independent realizations of the random vector $\mathbf{z}$ used in the stochastic trace estimation. As (5.44) gives the redundancy for a single observation, the variance factor appearing in Equation (4.56) has already been applied implicitly by homogenizing the observation equations.

5.8.1 Determination of new weights

Once residuals and redundancies have been computed for all observations in all groups, new weights can be determined for the observations. This is done by adjusting the standard deviation of an observation by two factors such that

$$\hat{\sigma}_i = \hat{s}_0[\tau\nu a]_r \, w(\hat{s}_i) \, \sigma_i \, . \tag{5.45}$$

Here, $\hat{\sigma}_i$ is the adjusted standard deviation and σ_i is the standard deviation of the measurement from the a priori elevation-dependent weighting or from the previous iteration in the VCE process. The first factor in (5.45) is the variance factor $\hat{s}_0[\tau\nu a]_r$, which is determined separately for each receiver and signal based on all epochs and observed satellites. τ, ν, and a refer to the signal type, frequency, and attribute, respectively, and r denotes the receiver. Code observations are treated as individual signals per frequency, attribute, and satellite constellation, while all phase observations per constellation are treated as one group. For example, if a receiver measures the GPS signals C1C, C2W, L1C, L2W and the Galileo signals C1C, C5Q, C7Q, L1C, L5Q, L7Q, variance factors are determined for GPS C1C, C2W, L and Galileo C1C, C5Q, C7Q, L. The reason for grouping the phase observation is their low redundancy, which hinders the determination of robust variance factors for individual signals. The signal-specific estimated variance factor is

$$\hat{s}_0[\tau\nu a]_r^2 = \alpha \, \frac{\sum\limits_{i=1}^{k} \frac{\hat{e}_i^2}{\sigma_i^2}}{\sum\limits_{i=1}^{k} r_i} \, , \tag{5.46}$$

where the sum over k includes all measurements of that signal over all epochs and observed satellites at the respective receiver. σ_i is the current standard deviation of a measurement, $\hat{e}_i$ is its actual residual and not the homogenized one, and r_i is its redundancy. Equation (5.46) contains a normalization factor

$$\alpha = \frac{\int_{-\infty}^{\infty} x^2 f(x) \, dx}{\int_{-\infty}^{\infty} \left(\frac{x}{w(x)} \right)^2 f(x) \, dx} \qquad X \sim N(0,1) \, . \tag{5.47}$$

It corrects for the deviation from a normal distribution due to the fact that observations with a standard deviation above a certain threshold are weighted down by the factor

$$w(x) = \begin{cases} \left(\frac{x}{T_\sigma} \right)^p & \text{if } x > T_\sigma \\ 1 & \text{otherwise} \end{cases} \, . \tag{5.48}$$

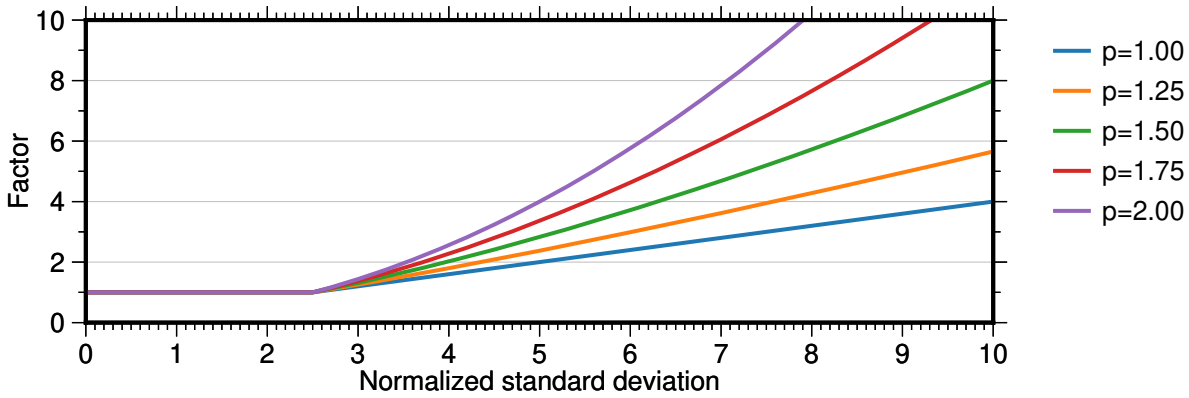

Figure 5.7: Weighting factor for $T_\sigma = 2.5$ and various powers p

Here, T_σ represents the normalized threshold over which observations start to get weighted down and the power p controls how strongly the observations are weighted down above that threshold (Huber, 1981). In practice, $T_\sigma = 2.5$ and $p = 1.5$ have proven to be effective values. Figure 5.7 shows the weighting factors for various powers p for a threshold of $T_\sigma = 2.5$. The integrals in (5.47) can be solved by numerical approximation.

The second factor $w(\hat{s}_i)$ in (5.45) is obtained by providing the square root of the observation-specific variance factor

$$\hat{s}_i^2 = \frac{e_i^2}{\hat{s}_0 [\tau\nu a]_r^2 \, \sigma_i^2 \, r_i} \,. \tag{5.49}$$

to the function in (5.48). Here, the current standard deviation σ_i is already scaled by the signal-specific estimated variance factor. This has the effect that only observations that are significantly less accurate than other measurements of the same signal at a receiver, for example outliers, are weighted down further. In addition, single observations are only weighted down if their redundancy is not too low (i.e. $r_i > 0.1$).

Once the new weights are applied to all observations by adjusting their standard deviations, the VCE process is finished for the current iteration. The adjusted standard deviations take effect in the observation weighting step (see Section 5.4) of the next iteration in the iterative least-squares adjustment. With each iteration, the relative weights between receivers and signals are adjusted automatically and outliers are weighted down until the process converges and a robust solution is obtained.

5.9 Strategies for solving large systems

The computational complexity of GNSS processing depends on many factors. Some of these factors are the selection of stations, satellites, and signals to be processed as well as the chosen sampling period. For example, the complexity of processing observations from hundreds of stations to multiple satellite constellations at three or more frequencies together at a 30-second sampling period is orders of magnitude higher than that of a dual-frequency, GPS-only processing using 100 stations and a 5-minute sampling period. While the latter scenario can be processed on a standard desktop computer, the former may not even be computationally feasible on high-performance computer clusters. Therefore, special strategies can be applied to facilitate the solution of large-scale systems with the approach described in this chapter.

5.9.1 Elimination and reconstruction of epoch parameters

The structure of the normal equation matrix described in Section 5.6 is clearly dominated by the number of epoch parameters (i.e., clock errors). In large-scale processing involving several hundred stations and multiple satellite constellations, setting up the full normal equation matrix would require hundreds of gigabytes of memory even with optimized subblock management. In order to circumvent this problem, it is possible to eliminate the epoch parameters before solving the normal equation system and to reconstruct them afterwards. This eliminates the need to keep all off-diagonal blocks between epoch and nonepoch parameters, which account for the majority of required memory, in memory at the same time and thus massively reduces the overall memory usage.

The prerequisite for the elimination of epoch parameters is that the normal equations are set up epoch by epoch. After setting up the normal equations for an epoch, they are added to the full normal equations as described in Section 4.2.3. In case constraints have to be applied to the parameters of the epoch, for example to resolve the rank deficiency in the clock errors (see Section 6.3.2), they are added to the normal equations as well. Figure 5.8 schematically visualizes the structure of the normal equation matrix from a single epoch. As can be seen, large parts of the overall normal equation matrix are unpopulated and the respective subblocks do not have to be kept in memory.

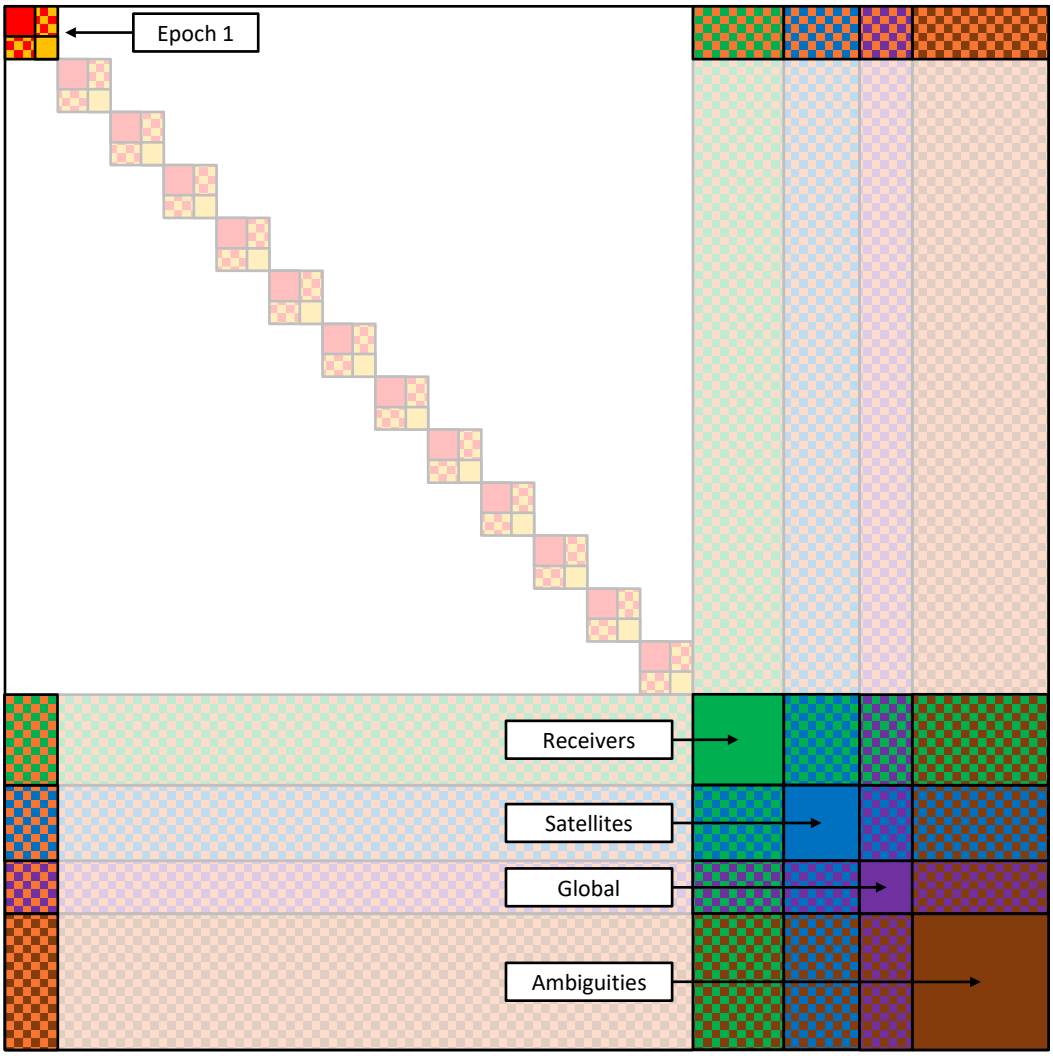

Figure 5.8: Schematic view of normal equation matrix structure from a single epoch (not to scale, full structure in the background)

Epoch parameters are then eliminated on the normal equation level as detailed in Section 4.2.2. In this case, however, the epoch parameters contained in $\Delta\mathbf{x}$ are to be eliminated from the normal equations

$$\begin{bmatrix} \mathbf{N_{xx}} & \mathbf{N_{xy}} \\ \mathbf{N_{xy}}^T & \mathbf{N_{yy}} \end{bmatrix} \begin{bmatrix} \Delta\mathbf{x} \\ \Delta\mathbf{y} \end{bmatrix} = \begin{bmatrix} \mathbf{n_x} \\ \mathbf{n_y} \end{bmatrix} \tag{5.50}$$

instead of $\Delta\mathbf{y}$, which contain all nonepoch parameters. Therefore, the reduced normal equation matrix follows as

$$\bar{\mathbf{N}} = \mathbf{N_{yy}} - \mathbf{N_{xy}}^T \mathbf{N_{xx}}^{-1} \mathbf{N_{xy}} \tag{5.51}$$

and the reduced right-hand side is

$$\bar{\mathbf{n}} = \mathbf{n_y} - \mathbf{N_{xy}}^T \mathbf{N_{xx}}^{-1} \mathbf{n_x} \,. \tag{5.52}$$

Based on the blocked Cholesky decomposition

$$\begin{bmatrix} \mathbf{N_{xx}} & \mathbf{N_{xy}} \\ \mathbf{N_{xy}}^T & \mathbf{N_{yy}} \end{bmatrix} = \begin{bmatrix} \mathbf{W_{xx}}^T & \\ \mathbf{W_{xy}}^T & \mathbf{W_{yy}^T} \end{bmatrix} \begin{bmatrix} \mathbf{W_{xx}} & \mathbf{W_{xy}} \\ & \mathbf{W_{yy}} \end{bmatrix} , \tag{5.53}$$

where $\mathbf{W_{xx}}$ and $\mathbf{W_{yy}}$ are upper triangular matrices and $\mathbf{W_{xy}}$ is a fully populated rectangular matrix, it follows that

$$\mathbf{N_{xx}} = \mathbf{W_{xx}}^T \mathbf{W_{xx}} \tag{5.54}$$

and

$$\mathbf{N_{xy}} = \mathbf{W_{xx}}^T \mathbf{W_{xy}} \,. \tag{5.55}$$

Substituting (5.54) and (5.55) into (5.51) leads to a reduced normal equation matrix

$$\begin{aligned} \bar{\mathbf{N}} &= \mathbf{N_{yy}} - \mathbf{W_{xy}}^T \mathbf{W_{xx}} \mathbf{W_{xx}}^{-1} \mathbf{W_{xx}}^{-T} \mathbf{W_{xx}}^T \mathbf{W_{xy}} \\ &= \mathbf{N_{yy}} - \mathbf{W_{xy}}^T \mathbf{W_{xy}} \end{aligned} \tag{5.56}$$

with eliminated epoch parameters $\Delta\mathbf{x}$. This is exactly what happens during an in-place Cholesky decomposition, which operates row by row, or in case of a blocked matrix block row by block row, from top to bottom (e.g., Golub and Van Loan, 2013). Therefore, applying a partial, blocked, in-place Cholesky decomposition over an epoch block row efficiently eliminates these epoch parameters from the normal equation matrix. The

reduced right-hand side can be obtained by substituting (5.54) and (5.55) into (5.52) such that

$$\begin{aligned}\bar{\mathbf{n}} &= \mathbf{n_y} - \mathbf{W_{xy}}^T \mathbf{W_{xx}} \mathbf{W_{xx}}^{-1} \mathbf{W_{xx}}^{-T} \mathbf{n_x} \\ &= \mathbf{n_y} - \mathbf{W_{xy}}^T \mathbf{W_{xx}}^{-T} \mathbf{n_x} \\ &= \mathbf{n_y} - \mathbf{W_{xy}}^T \mathbf{z}\end{aligned} \quad , \tag{5.57}$$

where $\mathbf{z}$ is determined by solving the equation system $\mathbf{W_{xx}}^T \mathbf{z} = \mathbf{n_x}$ via forward substitution. After the parameters are eliminated, the $\mathbf{N_{yy}}$ block, which now actually contains $\mathbf{W_{xy}}$ due to the in-place Cholesky decomposition, can be freed from memory. The matrix $\mathbf{W_{xx}}$ now contained in the $\mathbf{N_{xx}}$ block is kept in memory as it does not require much space and is needed later to reconstruct the epoch parameters.

This process can be repeated after each epoch's normal equations are set up and added to the full normal equations. Once all epoch parameters have been eliminated, the reduced normal equations can be solved as described in Section 4.2.4. The resulting parameter correction vector $\Delta\hat{\mathbf{y}}$ contains estimates for all nonepoch parameters, which are the same as if they had been estimated together with all epoch parameters.

In the next step, the eliminated epoch parameters are reconstructed one epoch block at a time. The first row of the equation system in (5.50) can be rewritten as

$$\Delta\mathbf{x} = \mathbf{N_{xx}}^{-1} \left(\mathbf{n_x} - \mathbf{N_{xy}} \Delta\mathbf{y} \right) \tag{5.58}$$

Since the epoch's off-diagonal block $\mathbf{N_{xy}}$ has been freed to reduce memory usage during the previous step, it would have to be reconstructed to solve (5.58) directly. However, the epoch parameters can be reconstructed more efficiently by setting up the equation system

$$\mathbf{N_{xx}} \Delta\mathbf{x} = \tilde{\mathbf{n}}_\mathbf{x} \tag{5.59}$$

using the right-hand side

$$\tilde{\mathbf{n}}_\mathbf{x} = \tilde{\mathbf{A}}^T \Delta\tilde{\mathbf{l}} = \tilde{\mathbf{A}}^T \left(\Delta\mathbf{l} - \tilde{\mathbf{A}} \Delta\hat{\mathbf{y}} \right) . \tag{5.60}$$

This involves setting up the design matrix $\mathbf{A}$ for the epoch again as described in Sections 5.2 to 5.5. The matrix $\tilde{\mathbf{A}}$ is the slice (i.e., the columns) of $\mathbf{A}$ that covers only the nonepoch parameters. The right-hand side vector $\tilde{\mathbf{n}}_\mathbf{x}$ can then be computed based on the reduced observations $\Delta\tilde{\mathbf{l}}$, which are obtained by correcting the original observations $\Delta\mathbf{l}$ for the influence of the estimated nonepoch parameters in $\Delta\hat{\mathbf{y}}$. This means that the information related to the epoch parameters stays contained in $\Delta\tilde{\mathbf{l}}$. The equation system

in (5.59) is then solved for $\Delta\mathbf{x}$ via forward and backward substitution based on the Cholesky decomposition $\mathbf{N_{xx}} = \mathbf{W_{xx}}^T\mathbf{W_{xx}}$. As $\mathbf{W_{xx}}$ has been kept in memory from the preceding elimination step, the decomposition does not actually have to be performed again. After this process has been repeated for all epochs, estimates for all epoch and nonepoch parameters have been determined.

Eliminating and reconstructing the epoch parameters is one of the strategies that enabled the large scale of the processing described in Chapter 8. It can reduce the memory requirements for solving large systems from several hundred gigabytes to a more feasible size. From this perspective, it is usually well worth the drawback of a slightly increased computational effort and processing time compared to directly solving all parameters.

5.9.2 Core network, PPP, and full network processing scheme

Another key strategy to solve large systems efficiently is to circumvent having to deal with the phase ambiguities of the full network all at once. As can be seen in Figures 5.3 and 5.4, the off-diagonal block between epoch parameters and ambiguities accounts for a major part of the overall memory usage. Therefore, removing ambiguity parameters from the equation system greatly reduces the memory requirements and computational cost of solving the normal equations. Section 6.6.2 details how ambiguities, which are initially estimated as float values together with all other parameters, can be resolved to their integer values. Once fixed, they can be introduced as known corrections into the observation equations and do not have to be estimated as unknown parameters in further iterations of the least-squares adjustment.

Unfortunately, the integer nature of ambiguities is obfuscated by unknown satellite and receiver phase biases (see Section 6.6). This prevents simply resolving them station by station. The correlation between phase biases and ambiguities necessitates a network solution involving the combined processing of multiple stations and satellites. This can become an issue as the complexity of integer ambiguity resolution scales exponentially with the number of ambiguities (Verhagen et al., 2012). Using sophisticated ambiguity resolution techniques is already a challenge in small station networks, but for large networks with hundreds of stations it can become an insurmountable computational bottleneck (Jazaeri et al., 2012). For example, a large network of 800 stations combined with 80 satellites can lead to approximately 155 000 ambiguity parameters. Therefore, network-based ambiguity resolution is more manageable with smaller networks.

The processing scheme described in Strasser et al. (2019) and visualized in Figure 5.9 is a solution to both problems mentioned above. It separates the processing into three

major parts. Initially, the processing is limited to a small subset of stations from the full network. This core network has to be well-distributed around the globe to ensure full coverage and stable estimation of all relevant parameters. Too few stations might lead to a weak and inaccurate solution, while too many stations might prevent resolving the ambiguities efficiently. In practice, a network of 50–60 stations has proven to be sufficient for a stable solution while still keeping the ambiguity resolution complexity on a feasible level.

The initial iterative least-squares adjustment using the core network stops once a convergence threshold or a maximum number of iterations has been reached. New observation weights are determined at the end of each iteration and outliers are automatically weighted down, leading to a robust float solution. At this point, all parameters have usually been determined sufficiently precise to enable ambiguity resolution. Fixing the ambiguities to integer values can lead to significant changes in other parameter estimates. Therefore, some additional iterations of the least-squares adjustment may be necessary after this step to reach convergence again. At this point, the satellite parameters related to their orbits, clocks, and signal biases have been determined precisely enough to enable the next part of the processing.

In the second part, all satellite and global parameters are held fixed and are introduced as known into the observation equations. This enables the individual processing of all stations that are not part of the core network. Blewitt (2008) presented a similar concept to enable the processing of massive networks. By introducing the satellite parameters as known, this step is equivalent to PPP (Zumberge et al., 1997). The processing scheme for a single station follows that of the core network, meaning several iterations of a least-squares adjustment are followed by ambiguity resolution and possibly more iterations afterwards. PPP with ambiguity resolution (e.g., Ge et al., 2008; Laurichesse et al., 2009; Collins et al., 2010; Geng et al., 2010; Shi and Gao, 2014; Glaner and Weber, 2021) is possible at this point because the satellite phase biases have been determined using the core network. The stations can be processed in parallel as the involved steps can all be performed independently. Once all stations have been processed, all ambiguity parameters in the equation system have been resolved and can be introduced as known into the final part.

At the end, all stations in the full network are processed together in order to get the best estimates for all parameters. In this part, all parameters, including the satellite and global parameters, are estimated again. The only exception are the ambiguity parameters, which do not have to be set up again since they have already been fixed. Therefore, the issue of an exceedingly large normal equation matrix described at the beginning of this section is much reduced. Multiple iterations of the full network adjustment

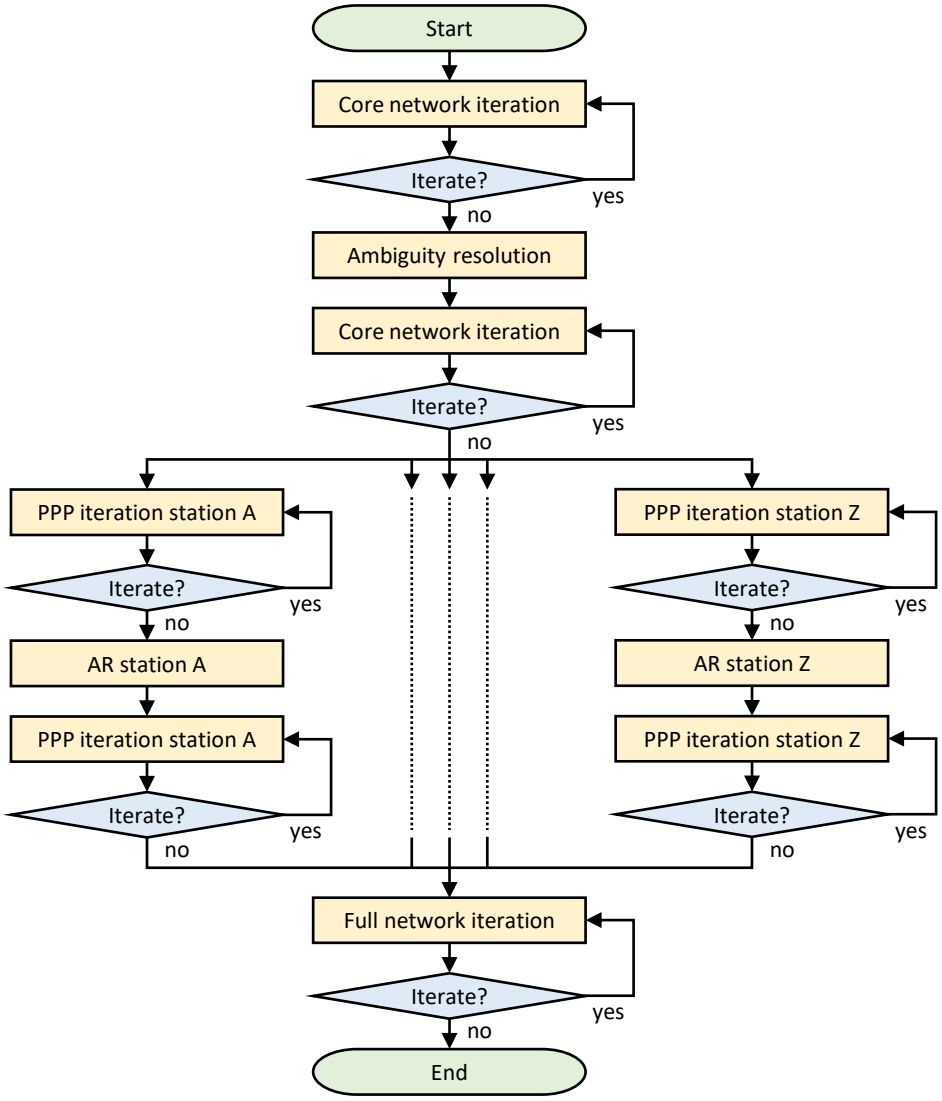

Figure 5.9: Flowchart of processing scheme starting with processing only the core network, followed by individual processing of all noncore stations, and finally processing the full network together

usually improve the solution, because adding observations from potentially hundreds of additional stations to the system can have a significant impact on the parameters. Here, new observation weights are again determined at the end of each iteration, and the end result is a robust solution based on a large station network.

5.9.3 Separation of ionosphere and signal biases in an intermediate step

Section 5.2 describes how an ionospheric STEC parameter is set up for each observation group. These parameters cannot be fully separated from signal bias parameters without introducing additional information about the ionosphere (Schaer, 1999). This means the resulting signal biases are biased by the ionosphere. Other parameters, such as satellite orbits or station positions, are unaffected by this bias. Therefore, this issue only has to be resolved in case signal biases are a product of interest.

Section 6.4 details how the ionospheric influence can be modeled and parameterized. This includes possible ways to introduce the additional information that is required to separate it from the signal biases. The approach used for the reprocessing conducted within the context of this thesis was to introduce an ionospheric mapping function that maps the STEC from a specific signal path to the zenith direction at each station (see Section 6.4.2). However, this approach potentially leads to millions of additional epoch parameters in the main equation system when large networks with hundreds of stations are processed. Even when applying the strategies described in the previous sections, this can significantly increase the required computational effort of a large-scale GNSS processing.

One way to circumvent this issue is to determine the part of the signal biases that is affected by the ionosphere in a separate step (Strasser et al., 2019). This step features a separate equation system using the full observation equations described in Section 5.1. However, only specific signal bias and ionosphere parameters are set up and all other parameters are introduced as known. Therefore, this intermediate step is only possible after the main equation system has been solved at least once. Section 6.5.3.3 describes how the set of parameters for this separate equation system is determined. Once it has been solved, the obtained signal bias corrections can be introduced as known in subsequent iterations of the main least-squares adjustment in order to obtain signal bias estimates that are not biased by the ionosphere anymore. Further information about the estimation of signal biases is provided in Sections 6.5 and 6.6.

5.10 GROOPS

All algorithms described in this chapter are implemented into the software Gravity Recovery Object Oriented Programming System (GROOPS). GROOPS is an open-source software toolkit for core geodetic tasks. Mayer-Gürr et al. (2021) gives an overview of the software and its features, which include gravity recovery, GNSS-based orbit determination for LEO satellites, and the processing of GNSS constellations and ground station networks as described in this thesis. The source code of GROOPS is available on GitHub (`https://github.com/groops-devs/groops`) together with documentation and guided examples.

The software is written in C++ and supports both desktop computers and large computer clusters through its implementation of the Message Passing Interface (MPI) standard. This is especially important for the type of large-scale processing conducted within the context of this thesis. Mayer-Gürr et al. (2021) provides more details on how large distributed least-squares problems are solved within GROOPS. This includes the handling of highly-sparse blocked matrices such as the normal equation matrix described in Section 5.6. For example, it provides more information on the block-cyclic distribution (e.g., Blackford et al., 1997) of matrix blocks among parallel processes. Mayer-Gürr et al. (2021) further notes that the operations for solving the normal equations via in-place Cholesky decomposition and forward and backward substitution are implemented as parallel block algorithms following Choi et al. (1996).

The author of this thesis has contributed to the software in numerous ways, for example in the form of source code, testing, user interface design, and documentation. Most of these contributions concern the parametrizations, models, and corrections involved in GNSS processing (see Chapter 6) as well as the handling of the associated large amounts of data and metadata. Much of this work directly benefited the reprocessing campaign conducted in the context of this thesis, which is further described in Chapter 8.

6 Parametrizations, models, and corrections

The GNSS observation equations described in Section 5.1 contain various parametrizations and corrections based on a number of physical models. The choice of representing a certain component by unknown parameters, relying on an a priori model, or not considering it at all can depend on the application and its accuracy requirements (Kouba et al., 2017). The type of GNSS processing conducted in the context of this thesis aims for the highest possible accuracy and precision and thus often applies a combination of parametrizations and a priori corrections for the different components. For this reason, each section in this chapter covers a component of the observation equations and details the various relevant parametrizations, corrections, and models. Some sections also present analyses and comparisons of different models and parametrizations and their effect on GNSS products.

6.1 Satellite attitude

The knowledge of a GNSS satellite's attitude or orientation in space is vital for high-precision applications (Kouba and Héroux, 2001). Montenbruck et al. (2015a) lists three areas that require accurate satellite attitude modeling. First, it is necessary to correctly account for horizontal (i.e., in the plane normal to the antenna boresight) satellite antenna offsets with respect to the center of mass (Schmid et al., 2016) and potential direction-dependent variations (see Section 6.10). Second, the circularly-polarized nature of GNSS signals leads to variations of the phase measurement depending on the relative orientation between the transmitting and receiving antennas (J. T. Wu et al., 1993). The correction for this so-called phase wind-up, which is detailed in Section 6.11.2, is essential in the determination of high-quality satellite products. Finally, knowing the orientation of a satellite's body and solar panels is important for modeling accelerations induced by solar and Earth radiation pressure during orbit integration (Rodriguez-Solano, 2014). Section 6.2 provides more information on satellite orbit modeling and the effects of these forces.

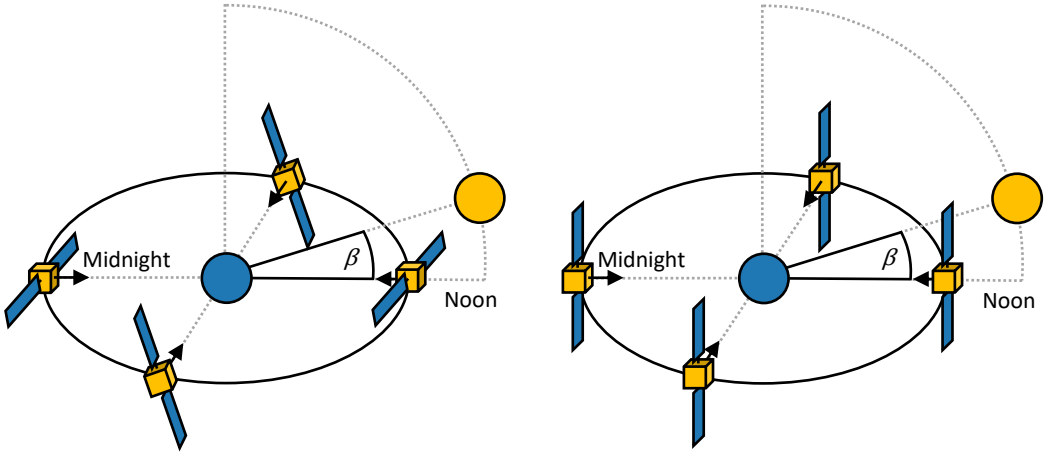

(a) Yaw-steering mode **(b)** Orbit normal mode

Figure 6.1: Default attitude modes applied by GNSS satellites and their satellite orientation at specific points along the orbit (adapted from Montenbruck et al., 2015a)

GNSS satellites usually apply either a yaw-steering or an orbit normal mode for their default attitude (Montenbruck et al., 2015a). Figure 6.1 visualizes a satellite's orientation in space at different points in an orbit for each mode. Both modes have in common that the satellite's main transmission antenna always points towards the center of Earth. In yaw-steering mode, which is predominantly used by GNSS satellites in medium Earth orbit (MEO), the satellite actively rotates (i.e., yaws) around the Earth-pointing axis in order to keep its solar panels aligned towards the Sun (Bar-Sever, 1996). A satellite in orbit normal mode, on the other hand, does not yaw around the Earth-pointing axis and instead keeps a constant alignment in the local orbit frame (see Section 3.6). Orbit normal mode is usually applied by GNSS satellites in geostationary or geosynchronous orbits, which occur in the BDS and QZSS constellations (e.g., Hauschild et al., 2012; Lou et al., 2014).

6.1.1 Principal axes and angles

The three unit vectors

$$\mathbf{e}_x^{\mathrm{YS}} = \mathbf{e}_y^{\mathrm{YS}} \times \mathbf{e}_z^{\mathrm{YS}} \tag{6.1}$$

$$\mathbf{e}_y^{\mathrm{YS}} = \frac{\mathbf{e}_\odot \times \mathbf{e}_r}{\|\mathbf{e}_\odot \times \mathbf{e}_r\|} \tag{6.2}$$

$$\mathbf{e}_z^{\mathrm{YS}} = -\mathbf{e}_r \tag{6.3}$$

define the axes of a yaw-steering frame. Here, $\mathbf{e}_r = \frac{\mathbf{r}}{\|\mathbf{r}\|}$ is the normalized satellite position vector, or radial vector, and $\mathbf{e}_\odot = \frac{\mathbf{r}_{\mathrm{Sun}} - \mathbf{r}}{\|\mathbf{r}_{\mathrm{Sun}} - \mathbf{r}\|}$ is the unit vector pointing from the

satellite towards the Sun. $\mathbf{r}_{\text{Sun}}$ and $\mathbf{r}$ are the position vectors of the Sun and satellite, respectively. This section assumes that all vectors are given in the CRF unless otherwise noted. If a satellite is in yaw-steering mode and the definition of its body axes follows the IGS conventions (Montenbruck et al., 2015a), its body frame is nominally aligned to this frame. The same axes can be obtained by rotating the orbit normal frame, which is defined by the three unit vectors

$$\mathbf{e}_x^{\text{ON}} = \mathbf{e}_a \tag{6.4}$$
$$\mathbf{e}_y^{\text{ON}} = -\mathbf{e}_c \tag{6.5}$$
$$\mathbf{e}_z^{\text{ON}} = -\mathbf{e}_r\,, \tag{6.6}$$

around the $\mathbf{e}_z$ axis by the nominal yaw angle (Bar-Sever, 1996)

$$\psi_{\text{nom}} = \operatorname{atan2}\left(-\tan\beta,\, \sin\mu\right)\,. \tag{6.7}$$

The unit vectors $\mathbf{e}_a$, $\mathbf{e}_c$, and $\mathbf{e}_r$ represent the along, cross, and radial axes of a local orbit frame. Their definition can be found in Section 3.6. The orbit angle

$$\mu = u(\mathbf{r}) - u(\mathbf{r}_{\text{Sun}}) + \pi \tag{6.8}$$

describes the position of the satellite along the orbit counting from orbit midnight, which is the point farthest from the Sun (Beutler et al., 1994). Since the orbit midnight point moves with the Sun, the orbit angle is computed based on the argument of latitude of the satellite and Sun. The argument of latitude of an object projected into the satellite's orbital plane is

$$u(\mathbf{r}) = \operatorname{atan2}\left(\mathbf{r}\cdot\left(\mathbf{e}_c\times\mathbf{e}_h\right),\, \mathbf{r}\cdot\mathbf{e}_h\right)\,, \tag{6.9}$$

where $\mathbf{r}$ is the position vector of the object and $\mathbf{e}_h = \frac{[\,0\;0\;1\,]^T\times\mathbf{e}_c}{\|[\,0\;0\;1\,]^T\times\mathbf{e}_c\|}$. The angle between the Earth-Sun vector $\mathbf{r}_{\text{Sun}}$ and the satellite's orbital plane is (Kouba, 2009b)

$$\beta = \operatorname{acos}\left(-\mathbf{e}_c\cdot\frac{\mathbf{r}_{\text{Sun}}}{\|\mathbf{r}_{\text{Sun}}\|}\right) - \frac{\pi}{2}\,. \tag{6.10}$$

Figure 6.2 visualizes the three principal angles from (6.7), (6.8), and (6.10).

6.1.2 Special attitude behavior around orbit noon and midnight

A major problem of the yaw-steering attitude mode is that a satellite would have to yaw at a very high rate around the orbit noon and midnight points when the Sun is

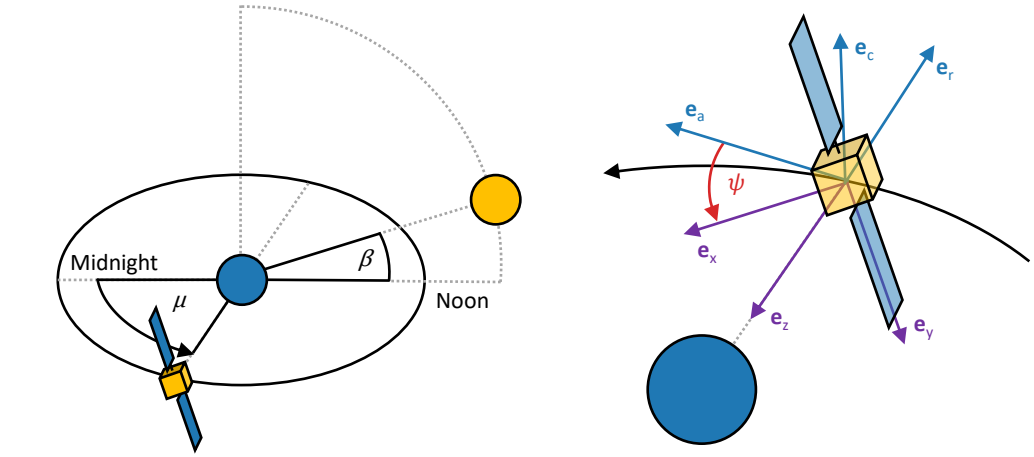

(a) Orbit angle μ and angle β between Earth-Sun vector and satellite orbital plane

(b) Yaw angle ψ

Figure 6.2: Principal angles for attitude modeling (adapted from Montenbruck et al., 2015a)

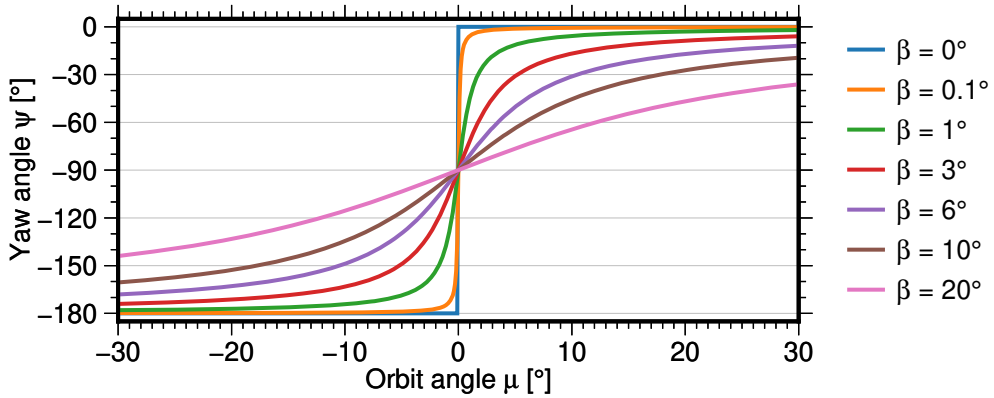

Figure 6.3: Nominal yaw angle around orbit midnight for various angles β

close to the orbital plane (Bar-Sever, 1996). Figure 6.3 shows the yaw angle close to orbit midnight for various angles β. It is clearly visible that the satellite would have to yaw instantly by 180° at $\beta = 0°$, which is impossible. At very low angles, for example $|\beta| = 1°$, the yaw rate required to maintain the nominal attitude usually exceeds the maximum yaw rate a satellite can physically achieve. Another problem is that when a satellite crosses Earth's shadow, which happen once per revolution at orbit midnight when β is below a certain threshold (e.g., $|\beta| \approx 14°$ for GPS), solar sensors mounted on the satellite cannot provide information to the attitude control system (Bar-Sever, 1996).

For these reasons, satellite manufacturers developed special attitude behavior around orbit noon and midnight. This behavior can differ between manufacturers, but also between different satellite types from the same manufacturer (Kouba, 2009b). For example,

GPS-IIR satellites were manufactured by Lockheed Martin and behave differently during shadow crossings than GPS-IIA and GPS-IIF satellites, which were both manufactured by Rockwell International/Boeing. GPS-IIA and GPS-IIF satellites also do not share the same behavior. In addition, satellites might not necessarily behave the same way around orbit noon and midnight (e.g., Bar-Sever, 1996; Dilssner, 2010; Dilssner et al., 2011b).

Figure 6.4 visualizes all known attitude modes for GPS, GLONASS, and Galileo satellites. The attitude models for Galileo satellites have been officially published by the European GNSS Service Centre (2017). In the absence of official models for GPS and GLONASS satellites, researchers have developed attitude models based on confidential information or empirical observations. For example, Dilssner et al. (2011b) applied reverse kinematic PPP to determine the attitude behavior of GLO-M satellites and subsequently developed an analytical model that describes this behavior. An attitude model for GPS-II and GPS-IIA satellites is described in Bar-Sever (1996) and simplified in Kouba (2009b), which also provides a model for GPS-IIR and GPS-IIR-M satellites. When one of these satellite types is mentioned subsequently, it is implied that the same is valid for the other type sharing the same model. Finally, Kuang et al. (2017) presents an attitude model for GPS-IIF satellites. As of yet, no attitude models have been published for the new GPS-IIIA and GLO-K satellites as well as for the original GPS-I and GLO satellites. An overview and comparison of all known attitude models including BDS and QZSS, which are not covered in this thesis, can be found in Strasser et al. (2021).

6.1.3 Generalization of attitude models

Satellite attitude models can be quite complex and often contain many special cases. Therefore, correctly implementing them into GNSS software packages is not always an easy task. Loyer et al. (2021) compares attitude data from several IGS analysis centers, which presumably have implemented the same attitude models into their software packages. While the differences for Galileo satellites are minimal, GPS and GLONASS attitude often deviates significantly between analysis centers. The analyses and comparisons conducted in preparation of this study also revealed some issues in the implementation of attitude models in the software GROOPS used at Graz University of Technology. This prompted a complete reimplementation of all models in a generalized way, the result of which was presented in Strasser et al. (2021). This section provides more details on the generalized models, focusing on GPS, GLONASS, and Galileo.

Table 6.1 provides an overview of the implemented attitude modes used by GNSS satellites around orbit noon and midnight. It includes BDS and QZSS to better highlight that several attitude modes can be reused across satellite types. The generalization is

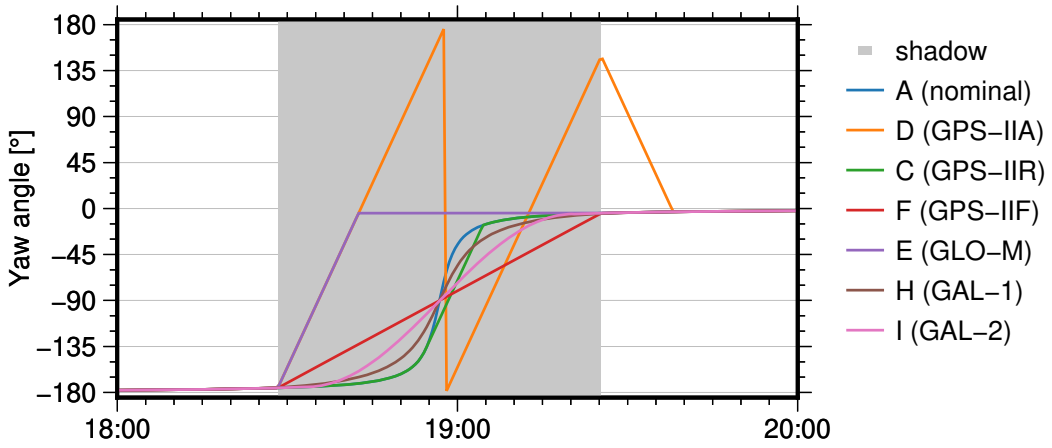

(a) Attitude behavior around orbit midnight

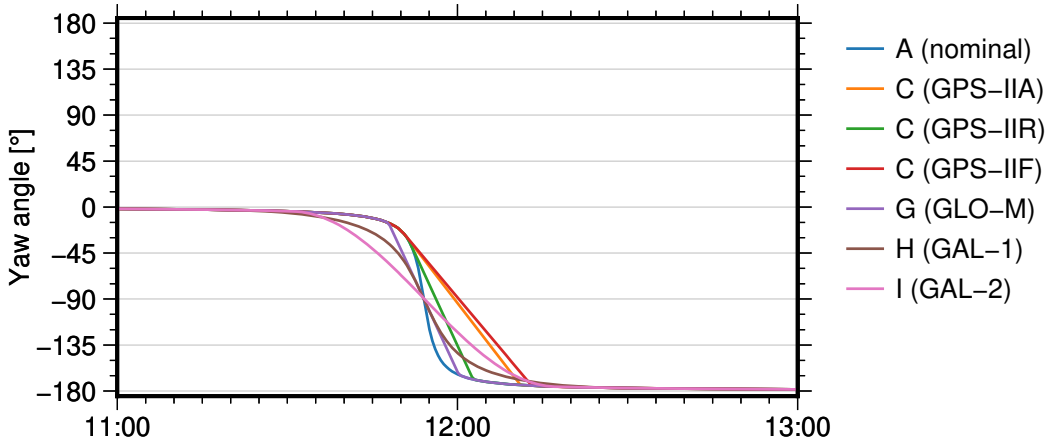

(b) Attitude behavior around orbit noon

Figure 6.4: Examples of known attitude behavior for GPS, GLONASS, and Galileo satellites

Table 6.1: Overview of satellite attitude modes (Strasser et al., 2021)

Satellite type	Default	Midnight	Noon	Reference
GPS-II/IIA	A	C	D	Bar-Sever (1996), Kouba (2009b)
GPS-IIR/IIR-M	A	C	C	Kouba (2009b)
GPS-IIF	A	C	F	Kuang et al. (2017)
GLO-M	A	E	G	Dilssner et al. (2011b)
GAL-1	A	H	H	European GNSS Service Centre (2017)
GAL-2	A	I	I	European GNSS Service Centre (2017)
BDS-2G/3G	B	B	B	C. Wang et al. (2018), P. Li et al. (2018)
BDS-2I/2M*	A	J	J	C. Wang et al. (2018)
BDS-3I/3M	A	I	I	P. Li et al. (2018)
QZS-1	A	J	J	Cabinet Office, Gov. of Japan (2021)
QZS-2G	B	B	B	Cabinet Office, Gov. of Japan (2021)
QZS-2I	A	G	G	Cabinet Office, Gov. of Japan (2021)

*Most BDS-2I/2M satellites have transitioned to BDS-3I/3M modes

based on three attitude modes: midnight and noon modes used around those points in the orbit, and a default mode that is used when neither of these two modes is active or relevant. The default mode for all GPS, GLONASS, and Galileo satellites is the nominal yaw-steering mode (A). The orbit normal mode (B) is only applied by geostationary satellites and as part of a mode that switches between yaw-steering and orbit normal attitude under certain conditions (J). These two modes are not discussed further here. The two "smoothed" (Montenbruck et al., 2015a) yaw-steering modes (H and I) applied by Galileo satellites do not offer much room for simplification. However, P. Li et al. (2018) showed that one of them (I) can be reused to describe the behavior of certain BDS satellites by replacing some of the variables used in the mode.

6.1.3.1 Example implementations of modes with constant yaw rate

Figure 6.4 reveals that GPS and GLONASS satellites only feature yaw maneuvers with constant yaw rate. In reality, the maneuvers must contain some yaw acceleration and deceleration phases, as described in Bar-Sever (1996), but they are usually disregarded because their impact is small and the information required to model these phases is often not available (Kouba, 2009b). Several satellites show the same yaw behavior, for example GPS-IIA (orange), GPS-IIR (green), and GPS-IIF (red) around orbit noon. They only differ in their maximum yaw rates, which are approximately 0.12°/s, 0.20°/s, and 0.11°/s for GPS-IIA, GPS-IIR, and GPS-IIF, respectively (Kouba, 2009b; Dilssner, 2010).

Most of the simplifications and generalizations thus concern these modes applying linear yaw changes (C, D, E, F, and G). All modes only require an approximate orbit and some

satellite- or type-specific metadata, for example the maximum yaw rate, as input. In a first step, the principal angles μ and β, the nominal yaw angle ψ_{nom}, and the nominal yaw rate (Bar-Sever, 1996)

$$\dot{\psi}_{\text{nom}} = \frac{\dot{\mu} \tan\beta \cos\mu}{\sin^2\mu + \tan^2\beta} \tag{6.11}$$

are computed at each epoch. The orbit angle rate $\dot{\mu} = \frac{\|\dot{\mathbf{r}}\|}{\|\mathbf{r}\|}$ in (6.11) depends on the position and velocity vector of the satellite at that epoch. In order to ensure proper and precise modeling even for very short maneuvers, these steps should be performed at a high sampling rate, for example every second.

The type-specific attitude modes with linear yaw changes can then all be implemented based on a single common function. This function yaws at a constant rate $\dot{\psi}$ forward or backward in time starting from a reference epoch t_0 with yaw angle ψ_0 and stops once the computed yaw angle

$$\psi(t, \dot{\psi}) = \psi_0 + (t - t_0) \cdot \dot{\psi} \tag{6.12}$$

catches up with the nominal yaw angle ψ_{nom} at some epoch. The sign of $\dot{\psi}$ (i.e., the yaw direction) is set to that of the nominal yaw rate $\dot{\psi}_{\text{nom}}$ at the reference epoch. The described function is called *catchUpYawAngle* in Listings 6.1 to 6.6, which show example implementations for the modes C, D, E, F, and G in the form of simplified pseudocode. Actual C++ implementations of these modes can be found in the source code of GROOPS, which is openly available on GitHub (see Section 5.10).

Listing 6.1 reveals that mode C can be implemented simply using the aforementioned function and only requires the maximum yaw rate $\dot{\psi}_{\text{max}}$ of the satellite and the starting epoch at which $\dot{\psi}_{\text{nom}} > \dot{\psi}_{\text{max}}$, which can be easily determined. Dilssner et al. (2011a), Kouba (2013), and Kuang et al. (2017) note that GPS-IIA and GPS-IIF satellites yaw into the wrong direction around orbit noon if $0° < \beta < 0.5°$ and $-0.7° < \beta < 0°$, respectively. This anomalous behavior is caused by a yaw bias introduced into the attitude control system of these satellites and must be considered in the function described above.

```
1 catchUpYawAngle(epochWhereYawRateIsExceeded, maxYawRate, forward)
```

Listing 6.1: Simplified pseudocode for mode C (Strasser et al., 2021)

Satellites applying mode D (see Listing 6.2) start yawing at maximum yaw rate once they enter Earth's shadow and continue to do so until shadow exit, at which point they try to align themselves back to nominal attitude. This can be achieved by either continuing to yaw in the same direction or by reversing the yaw direction. The decision usually

depends on the yaw angle at shadow exit and which direction requires less yawing to achieve nominal attitude. For GPS-IIA satellites, which apply this mode around orbit midnight, the yaw direction becomes ambiguous if the difference between actual and nominal yaw angle at shadow exit is close to 180°. This is the reason why observations during this post-shadow recovery period are often discarded in GNSS processing (Bar-Sever, 1996). The yaw direction of GPS-IIA satellites within Earth's shadow can also be ambiguous due to solar sensor noise being misinterpreted as signals when the Sun is not visible. For this reason, the satellite operator introduced the aforementioned yaw bias into their attitude control system, which results in predictable yaw directions (Bar-Sever, 1996). To consider this, the constant yaw rate inside Earth's shadow is set to $\dot{\psi}_{\text{max}}$ with the same sign as the yaw bias. If there is no yaw bias, $\dot{\psi}_{\text{max}}$ with the same sign as $\dot{\psi}_{\text{nom}}$ at shadow entry is used instead.

```
for each epoch between shadowEntry and shadowExit:
    epoch.yawAngle = shadowEntry.yawAngle +
                     (epoch.time - shadowEntry.time) * shadowYawRate
catchUpYawAngle(shadowExit, maxYawRate, forward)
```

Listing 6.2: Simplified pseudocode for mode D (Strasser et al., 2021)

In mode E, which is applied by GLO-M satellites during shadow crossings, satellites start yawing at maximum rate once they enter Earth's shadow and stop once they arrive at the nominal yaw angle ψ_{nom} at shadow exit. They then keep this angle until they exit the shadow. As Listing 6.3 shows, this behavior can be easily modeled by setting the yaw angle of all epochs inside Earth's shadow (except for the shadow entry epoch) to the nominal yaw angle ψ_{nom} at shadow exit. Starting from the shadow entry epoch, the yaw angle then simply has to catch up with the modified nominal yaw angle, resulting in the behavior displayed in Figure 6.4.

```
for each epoch between shadowEntry+1 and shadowExit:
    epoch.yawAngle = shadowExit.yawAngle
catchUpYawAngle(shadowEntry, maxYawRate, forward)
```

Listing 6.3: Simplified pseudocode for mode E (Strasser et al., 2021)

Mode F describes a behavior where satellites start yawing at a constant yaw rate $\dot{\psi}$ once they enter Earth's shadow such that they exit the shadow at the nominal yaw angle ψ_{nom}. This mode is applied by GPS-IIF satellites around orbit midnight. Listings 6.4 and 6.5 show two ways to implement this behavior. In both cases, the yaw rate $\dot{\psi}$ is computed based on the yaw angle and time at shadow entry and exit. Listing 6.4 simply computes the yaw angle at each shadow epoch based on Equation (6.12), while Listing 6.5 starts at

orbit midnight and catches up to the nominal yaw angle ψ_{nom} forwards and backwards in time.

```
yawRate = (shadowExit.yawAngle - shadowEntry.yawAngle) /
          (shadowExit.time - shadowEntry.time)
for each epoch between shadowEntry and shadowExit:
    epoch.yawAngle = shadowEntry.yawAngle +
                     (epoch.time - shadowEntry.time) * yawRate
```

Listing 6.4: Simplified pseudocode for mode F (Strasser et al., 2021)

```
yawRate = (shadowExit.yawAngle - shadowEntry.yawAngle) /
          (shadowExit.time - shadowEntry.time)
catchUpYawAngle(orbitMidnight, yawRate, backward)
catchUpYawAngle(orbitMidnight, yawRate, forward)
```

Listing 6.5: Simplified alternative pseudocode for mode F (Strasser et al., 2021)

Finally, satellites applying mode G (see Listing 6.6) yaw at their maximum yaw rate around orbit noon or midnight, ensuring that their yaw angle ψ matches the nominal yaw angle ψ_{nom} at the respective reference point. For instance, GLO-M satellites use this mode around orbit noon. This mode is similar to the alternative implementation of mode F shown in Listing 6.5, except that the satellite yaws at its maximum yaw rate.

```
catchUpYawAngle(orbitMidnightOrNoon, maxYawRate, backward)
catchUpYawAngle(orbitMidnightOrNoon, maxYawRate, forward)
```

Listing 6.6: Simplified pseudocode for mode G (Strasser et al., 2021)

6.1.3.2 Reusing models and handling special cases

The attitude behavior is not necessarily identical for all GNSS satellites of the same type and may also change over time. For example, Kouba (2009a) lists estimated yaw rates that slightly vary per GPS-IIA satellite and also notes that the yaw biases of those satellites were routinely changed in the early 1990s. This can be considered by storing time-variable attitude metadata in a database or, in the case of GROOPS, in type- or satellite-specific files. The metadata should include the applied modes as well as any mode-specific values that might vary over time or between satellites, such as the maximum yaw rate, yaw bias, or certain activation thresholds.

Tables 6.2 to 6.7 list example metadata for several GNSS satellites. Comparing Table 6.2 and Table 6.3 reveals the varying maximum yaw rates $\dot{\psi}_{\text{max}}$ for different GPS-IIA satellites

as well as the changes to their yaw biases ψ_{bias} over time. Special cases, such as GLO-M satellite R713 behaving similar to GPS-IIR satellites due to malfunctioning solar sensors (Dilssner et al., 2011b), can be accommodated by changing the mode for this specific satellite (see Table 6.4). All other GLO-M satellites keep their default metadata (e.g., mode G only activates if $|\beta| \leq \beta^{\text{Noon}}_{\text{threshold}}$), as shown for R714 in Table 6.5. Another special case occurs for some BDS-2M satellites, which have switched from their original attitude behavior to one very similar to that of GAL-2 satellites (Dilssner et al., 2018; C. Wang et al., 2018). Table 6.7 shows this mode switch, which happened sometime in mid-2017 for satellite C015, as well as the constants $\beta_{\text{threshold}}$, $\epsilon_{\text{threshold}}$, and T_{max} required for mode I (cf. European GNSS Service Centre, 2017). These values are different than those for GAL-2 satellites, which are exemplified in Table 6.6.

6.2 Satellite orbits

Satellite orbits are usually determined in a kinematic or dynamic way. In kinematic orbit determination, satellite positions are estimated at each epoch purely from the observational geometry. The main advantage of this approach is that the physical forces acting on a satellite do not have to be known. This is why it is often applied to determine orbits of LEO satellites in the context of gravity field recovery (e.g., Švehla and Rothacher, 2005; Zehentner, 2016). However, kinematic orbit determination also has several disadvantages. The determined satellite positions are affected by noise, might contain gaps and outliers, and are sensitive to measurement errors and poor observational geometry. The latter is especially relevant in case of ground station-based GNSS satellite orbit determination due to the acute angles of intersection between satellite-station vectors at the satellites. Therefore, the kinematic approach is not commonly used for this task. Still, Koch et al. (2017) shows that it can be used to validate GNSS satellite orbits when combined with clock modeling.

In contrast, dynamic orbit determination is based on force models that describe the motion of a satellite in space (Ashkenazi et al., 1990). This results in a smooth orbit containing positions at an arbitrary sampling rate that is independent of the observation sampling rate. Dynamic orbits are free of gaps and outliers and are less affected by measurement errors at specific epochs. For these reasons, GNSS satellite orbits are usually determined dynamically. The quality of dynamic orbits is mainly limited by that of the applied force models. While gravitational or conservative forces, such as Earth's gravity field or tidal forces, can be modeled with sufficient accuracy, the same is not the case for some of the nongravitational or nonconservative forces, particularly solar radiation pressure. Therefore, empirical model parameters are often estimated during

Table 6.2: Attitude metadata for GPS-IIA satellite G023

Start time	Default	Midnight	Noon	$\dot{\psi}_{\text{max}}$ [°/s]	ψ_{bias} [°]
1990-11-26 21:39	A	D	C	0.1152	0
1992-12-31 23:59	A	D	C	0.1152	0.5
1995-02-08 05:59	A	D	C	0.1152	-0.5
1995-02-08 17:59	A	D	C	0.1152	0.5
1995-08-03 23:59	A	D	C	0.1152	-0.5
1995-08-06 10:04	A	D	C	0.1152	0.5
2002-01-20 23:59	A	D	C	0.1152	-3.5
2006-12-31 23:59	A	D	C	0.1152	0.5

Table 6.3: Attitude metadata for GPS-IIA satellite G024

Start time	Default	Midnight	Noon	$\dot{\psi}_{\text{max}}$ [°/s]	ψ_{bias} [°]
1991-07-04 02:32	A	D	C	0.1089	0
1992-12-31 23:59	A	D	C	0.1089	0.5
1995-06-11 23:59	A	D	C	0.1089	-0.5
1995-06-13 04:58	A	D	C	0.1089	0.5

Table 6.4: Attitude metadata for GLO-M satellite R713

Start time	Default	Midnight	Noon	$\dot{\psi}_{\text{max}}$ [°/s]	$\beta^{\text{Noon}}_{\text{threshold}}$ [°]
2005-12-25 05:07	A	C	C	0.25	–

Table 6.5: Attitude metadata for GLO-M satellite R714

Start time	Default	Midnight	Noon	$\dot{\psi}_{\text{max}}$ [°/s]	$\beta^{\text{Noon}}_{\text{threshold}}$ [°]
2005-12-25 05:07	A	E	G	0.25	2

Table 6.6: Attitude metadata for GAL-2 satellite E201

Start time	Default	Midnight	Noon	$\beta_{\text{threshold}}$ [°]	$\epsilon_{\text{threshold}}$ [°]	T_{max} [s]
2014-08-22 12:27	A	I	I	4.1	10	5656

Table 6.7: Attitude metadata for BDS-2M satellite C015

Start time	Default	Midnight	Noon	$\beta_{\text{threshold}}$ [°]	$\epsilon_{\text{threshold}}$ [°]	T_{max} [s]
2012-09-18 19:10	A	J	J	4	5	–
2017-07-01 00:00	A	I	I	3	6	3090

dynamic orbit determination to overcome these modeling deficiencies (e.g., Beutler et al., 1994; Montenbruck et al., 2005; Jäggi et al., 2006). If this is the case, the approach is generally called reduced-dynamic orbit determination (S. C. Wu et al., 1991).

This section is structured as follows. The basic principle of orbit modeling is discussed in Section 6.2.1. This is followed by a summary of all relevant force models in Section 6.2.2. Section 6.2.3 describes how unknown orbit parameters can be linked to the GNSS observation equations. Finally, Section 6.2.4 presents some analyses regarding the sensitivity of satellite orbits with respect to certain force models.

6.2.1 Orbit modeling

Orbit modeling is part of dynamic orbit determination and describes the process of integrating force models to obtain a satellite orbit. Newton's second law of motion

$$\mathbf{F} = m\ddot{\mathbf{r}} \tag{6.13}$$

states that a force $\mathbf{F}$ acting on a satellite with mass m results in an acceleration

$$\ddot{\mathbf{r}} = \frac{\mathbf{F}}{m} = \boldsymbol{a}(t, \mathbf{r}, \dot{\mathbf{r}}, \mathbf{p})\,. \tag{6.14}$$

Equation (6.14) is called equation of motion (e.g., Hugentobler and Montenbruck, 2017). In this case, it describes the motion of a satellite around a central body (i.e., Earth). The function $\boldsymbol{a}$ represents the sum of all accelerations acting on the satellite and depends on the time t, the satellite's position $\mathbf{r}$ and velocity $\dot{\mathbf{r}}$, and a number of additional force model parameters $\mathbf{p} = [\, p_1 \;\; \ldots \;\; p_n \,]^T$. These parameters are required to model the accelerations due to gravitational and nongravitational forces acting on the satellite. They are either known or unknown, in which case they have to be estimated during orbit determination. Integrating (6.14) twice leads to the velocity

$$\dot{\mathbf{r}}(t) = \dot{\mathbf{r}}_0 + \int_{t_0}^{t} \boldsymbol{a}(t', \ldots)\, dt' \tag{6.15}$$

and center-of-mass position

$$\mathbf{r}(t) = \mathbf{r}_0 + (t - t_0)\, \dot{\mathbf{r}}_0 + \int_{t_0}^{t} \int_{t_0}^{t'} \boldsymbol{a}(t'', \ldots)\, dt''\, dt'\,, \tag{6.16}$$

which together form a system of second-order differential equations. The satellite state vector $\mathbf{y}(t) = [\, \mathbf{r}(t) \;\; \dot{\mathbf{r}}(t) \,]^T$ at each epoch depends on the unknown initial state vector $\mathbf{y}_0 = [\, \mathbf{r}_0 \;\; \dot{\mathbf{r}}_0 \,]^T$ and the vector of force model parameters $\mathbf{p}$.

6.2.2 Force models

The IERS conventions (Petit and Luzum, 2010) provide in-depth descriptions of gravitational forces and how to apply the respective models. The following brief summary aims to give an overview of the gravitational forces that have to be considered for orbit modeling.

Earth's gravity field The gravitational attraction acting on a satellite orbiting Earth varies depending on its location due to the inhomogeneous distribution of mass inside the planet. This effect is usually separated into a static and time-variable part. The former describes the mean gravity field over the period it was observed by space-geodetic techniques. Temporal variations of this mass distribution commonly include a trend and annual component derived from monthly snapshots of satellite gravimetry missions.

Astronomical tides Other bodies in the solar system also cause gravitational attraction, which can be modeled in the form of a tidal potential. The two main sources are the Sun due to its large mass and the Moon due to its close proximity. The effect of other planets is much smaller but can still be significant. Third-body attractions vary over time because of the changing relative geometry.

Solid Earth tides Earth's body deforms due to the gravitational attraction of other bodies, primarily the Sun and Moon. The resulting redistribution of mass can be modeled in terms of a tidal potential.

Ocean tides External gravitational forces also affect the oceans. Ocean tide models describe the mass redistribution in the oceans in the form of a tidal potential at several tidal frequencies. Continents and large land masses inhibit the free flow of water, resulting in complex geographical patterns, especially close to coastal regions.

Atmospheric tides The atmosphere is affected by external gravitational forces in the same way as the oceans. This effect describes the redistribution of atmospheric masses in terms of a tidal potential.

Pole tides Earth's rotational axis varies over time relative to its solid body. This polar motion results in a centrifugal effect that deforms Earth's body and causes mass redistribution. The pole tides describe this effect in terms of a perturbation in the gravitational potential.

Ocean pole tides Similar to the gravitational pull of external bodies, the centrifugal effect of polar motion not only affects the solid Earth but the oceans as well. The resulting redistribution of ocean masses can again be described as gravitational potential perturbations.

Nontidal mass variations As the name suggests, this effect describes mass variations on Earth's surface that cannot be expressed in the form of a tidal potential. The main sources for these are variations in atmospheric pressure, wind-induced ocean currents, and changes in terrestrial water storage.

Nongravitational or nonconservative forces acting on GNSS satellites include solar radiation pressure, Earth radiation pressure, and antenna thrust. These forces can often not be modeled with sufficient accuracy. The main issue is that modeling them correctly requires accurate knowledge of a satellite's physical properties, such as its shape and the materials used for its body and solar panels. In most cases, this information has not been officially disclosed by satellite operators. Therefore, nonconservative force models are often based on approximate satellite properties, which severely limits their accuracy.

Figure 6.5 compares the magnitude of the forces acting on GNSS satellites in terms of the resulting acceleration on the various satellite types. Orbit altitude and inclination as well as satellite mass, size, shape, and transmit power are the main sources for the differences between satellite types. After Earth's gravity field and astronomical tides, nonconservative forces are among the most significant forces affecting GNSS satellites. Therefore, improvements in the accuracy of nonconservative force models directly benefit the quality of the modeled orbits. One of the most direct ways to achieve this would be if satellite operators were publishing more accurate satellite metadata.

6.2.2.1 Solar radiation pressure

Solar radiation induces an acceleration on satellites that are exposed to it. The total acceleration depends on the satellite's mass as well as the area, material properties, and orientation of all exposed surfaces. Photons emitted by the Sun are either reflected or absorbed by a surface depending on its material properties.

Following Milani et al. (1987), Fliegel et al. (1992), Rodriguez-Solano et al. (2012a), and Rodriguez-Solano (2014), the acceleration acting on a surface is

$$\mathbf{a}_{\mathrm{SRP}}^{\mathrm{surface}} = \left(\frac{1\,\mathrm{AU}}{d}\right)^2 \frac{S_0}{c}\frac{A}{m}\cos\theta\left[(\alpha+\delta)\,\mathbf{e}_D - (C_1\delta + C_2\,\rho\cos\theta)\,\mathbf{e}_N\right]. \tag{6.17}$$

Here, d is the distance between satellite and Sun, $S_0 \approx 1367\,\mathrm{W/m^2}$ is the solar irradiance at a distance of one astronomical unit (AU) from the Sun, A is the surface area, m is the satellite's mass, and α, δ, and ρ are the absorption, diffuse reflection, and specular reflection coefficients of the surface, respectively. $\mathbf{e}_D$ is the unit vector from Sun to satellite (i.e., the direction of radiation), $\mathbf{e}_N$ is the unit normal vector of the surface, and $\cos\theta = -\mathbf{e}_D \cdot \mathbf{e}_N$. The coefficients C_1 and C_2 depend on the shape of the surface, with

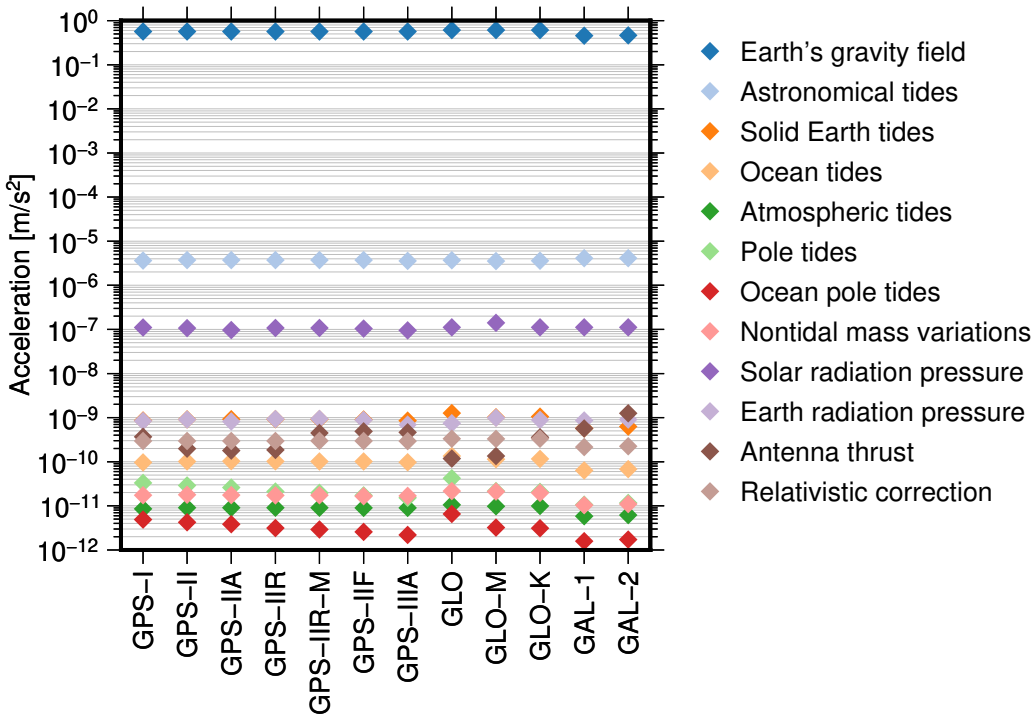

Figure 6.5: Mean force model accelerations per satellite type

$C_1 = \frac{2}{3}$ and $C_2 = 2$ in case of a flat surface or $C_1 = \frac{\pi}{6}$ and $C_2 = \frac{4}{3}$ in case of a cylindrical surface.

According to Fliegel et al. (1992), most materials used to cover the satellite bus instantly reradiate the absorbed energy in the form of heat. This thermal reradiation (TRR) can be modeled as

$$\mathbf{a}_{\text{TRR}}^{\text{surface}} = -\left(\frac{1\,\text{AU}}{d}\right)^2 \frac{S_0}{c}\frac{A}{m}\cos\theta\, C_1 \alpha\, \mathbf{e}_N\,. \tag{6.18}$$

The total acceleration induced by solar radiation can then be obtained as the sum of the accelerations from all surfaces

$$\mathbf{a}_{\text{SRP}} = \nu \sum_{i}^{\text{surfaces}} \left(\mathbf{a}_{\text{SRP},i}^{\text{surface}} + \mathbf{a}_{\text{TRR},i}^{\text{surface}}\right)\,. \tag{6.19}$$

The factor $0 \leq \nu \leq 1$ scales the acceleration based on a conical shadow model, for example as described in Montenbruck and Gill (2000). It represents the percentage of the Sun that is visible from the satellite's point of view. Thus, $\nu = 0$ means the satellite is fully inside the occulting body's shadow (umbra) and $0 < \nu < 1$ means it is in partial shadow (penumbra). Figure 6.6 visualizes the conical shadow model and the partial occultation occuring when a satellite is inside penumbra.

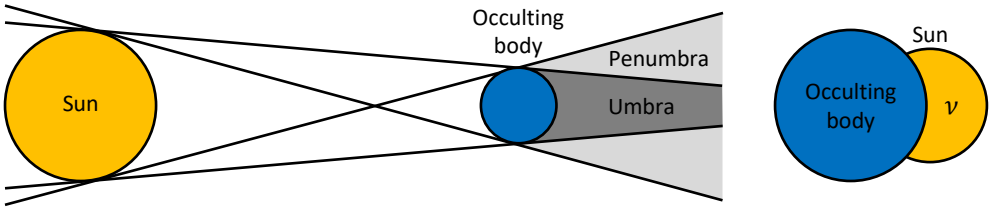

(a) Conical shadow model **(b)** Partial occultation

Figure 6.6: Schematic visualization of conical shadow model and partial occultation (adapted from Montenbruck and Gill, 2000)

In case of GNSS satellites, the main occulting body is Earth. The relative geometry between Earth, Sun, and a satellite's orbital plane leads to GPS, GLONASS, and Galileo satellites entering a so-called eclipse season approximately twice per year. An eclipse season usually lasts for around one month, during which a satellite crosses Earth's shadow once per revolution. Contrary to how it might appear in Figure 6.6, GNSS satellites usually cross Earth's penumbra in a few minutes, while the period in full shadow can last up to an hour at the center of an eclipse season. Moon shadow crossings, which can be modeled in the same way as for Earth, occur less frequently but should be taken into account as well.

As mentioned at the beginning of this section, modeling solar radiation pressure analytically based on Equations (6.17) to (6.19) requires detailed information about all satellite surfaces. In most cases, this information is only available in simplified form, for example as a so-called box-wing model. Such a model represents the satellite bus as a cuboid shape with six surfaces and two additional flat surfaces for the solar panels, hence the name. Since most GNSS satellites have cuboid buses, this is a good approximation, although it is missing many detailed structures on the surfaces, such as antennas, radiators, and thrusters. Therefore, even if the areas and material properties of a box-wing model were known perfectly, which is often not the case, the accuracy of such an analytical model is limited.

Another limiting factor is that box-wing models do not account for self-shadowing (e.g., antennas or solar panels casting shadows on the bus) as they consider a satellite as a set of independent surfaces and not as a whole. One reason for this is that in many cases only values for the surface areas and not the full dimensions of the satellite are publicly available. If detailed 3D models of the satellites were available publicly, solar radiation pressure could ideally be modeled analytically based on ray tracing, as demonstrated, for example, in Ziebart and Dare (2001), Z. Li et al. (2018), and Bhattarai et al. (2019). Nevertheless, box-wing models allow for a physics-based approximate a priori modeling of solar radiation pressure.

In absence of sufficiently accurate analytical solar radiation pressure models, empirical models are commonly applied in GNSS satellite orbit determination. These models aim to describe the effect of solar radiation pressure on satellite orbits by means of a set of empirical coefficients, which can be set up as parameters in the orbit determination process. While empirical models usually improve the fit of orbits to observation data, it is often difficult to derive physical meaning from their coefficients.

The most widely used empirical models are the Empirical CODE Orbit Model (ECOM) presented in Beutler et al. (1994) and its extension ECOM2 (Arnold et al., 2015). They represent the acceleration caused by solar radiation pressure (SRP) as

$$\mathbf{a}_{\text{SRP}} = \mathbf{a}_{0,\text{SRP}} + \nu \left[D(\Delta u)\, \mathbf{e}_D + Y(\Delta u)\, \mathbf{e}_Y + B(\Delta u)\, \mathbf{e}_B \right] , \tag{6.20}$$

where $\mathbf{a}_{0,\text{SRP}}$ is the acceleration from an optional a priori model, ν is the scale factor from a conical shadow model, and

$$D(\Delta u) = D_0 + D_{C1} \cos \Delta u + D_{S1} \sin \Delta u \tag{6.21}$$
$$Y(\Delta u) = Y_0 \ + Y_{C1} \cos \Delta u \ + Y_{S1} \ \sin \Delta u \tag{6.22}$$
$$B(\Delta u) = B_0 + B_{C1} \cos \Delta u + B_{S1} \sin \Delta u \tag{6.23}$$

in case of ECOM or

$$D(\Delta u) = D_0 + D_{C2} \cos 2\Delta u + D_{S2} \sin 2\Delta u + D_{C4} \cos 4\Delta u + D_{S4} \sin 4\Delta u \tag{6.24}$$
$$Y(\Delta u) = Y_0 \tag{6.25}$$
$$B(\Delta u) = B_0 + B_{C1} \cos \Delta u + B_{S1} \sin \Delta u \tag{6.26}$$

in case of ECOM2. These functions describe the accelerations along three axes of a satellite-Sun reference frame, where $\mathbf{e}_D$ points from the satellite to the Sun, $\mathbf{e}_Y$ points along the satellite's solar panel axis, and $\mathbf{e}_B$ completes the right-handed frame. The acceleration along each axis consists of constant ($\square_0$) and x-per-revolution sine and cosine ($\square_{Sx}$, $\square_{Cx}$) terms. The angular argument for ECOM was originally the argument of latitude of the satellite u_{Sat}, but was changed to the difference between the argument of latitude of the satellite and Sun $\Delta u = u_{\text{Sat}} - u_{\text{Sun}}$ with the introduction of ECOM2. According to Arnold et al. (2015), this better suits the interpretation of the estimated model parameters.

Not all of the terms in Equations (6.21) to (6.26) have to be used. Arnold et al. (2015) compares several variations with different terms used in the parametrization of solar radiation pressure during orbit determination. Within the analysis centers of the IGS, the two most common parametrizations comprise D_0, Y_0, B_0, B_{C1}, B_{S1} (subsequently

dubbed ECOM-5), as proposed in Springer et al. (1999b), and D_0, D_{C2}, D_{S2}, Y_0, B_0, B_{C1}, B_{S1} (subsequently dubbed ECOM2-7). They only differ by the addition of the twice-per-revolution terms along the satellite-Sun axis, which improves the ability of the model to catch systematic effects caused by the elongated shape of GLONASS and Galileo satellite buses (Arnold et al., 2015; Prange et al., 2017). In the reprocessing campaign conducted within the context of this thesis, a combination of a priori box-wing model and ECOM2-7 was used for all satellites.

It is also possible to use an empirical instead of an analytical model to determine a priori solar radiation pressure. These models usually represent the acceleration due to solar radiation pressure as a Fourier series with predetermined coefficients. Examples are the ROCK-T models (Fliegel et al., 1992; Fliegel and Gallini, 1996), the model presented in Springer et al. (1999a), and the GPS Solar Pressure Model (GSPM; Bar-Sever and Kuang, 2004). The latter two models have been derived from multiple years of in-orbit GPS data. While they can be more accurate than box-wing models, the limited availability of such models for newer satellite types and constellations means they are not widely used for multi-GNSS orbit determination.

Rodriguez-Solano et al. (2012a) proposed an adjustable box-wing model as an intermediate approach between analytical and empirical model. In this model the optical properties of the satellite surfaces are estimated together with parameters for an acceleration bias along the solar panel axis and a solar panel rotation lag. Rodriguez-Solano et al. (2012a) showed that the model performs comparable to the ECOM in terms of orbit overlaps, though there were systematic differences in the obtained orbits due to the different nature of the two models. Duan et al. (2019, 2020) and Duan and Hugentobler (2021) applied a similar approach to determine adjusted optical properties for several satellite types that can be used in an a priori box-wing model. While these adjusted optical properties do not strictly fulfill the constraint $\alpha + \delta + \rho = 1$, they have been found to improve orbit discontinuities, ECOM parameter estimates, and SLR residuals. Unfortunately, extended tests with these adjusted optical properties could not be made in time for them to be considered in the reprocessing campaign presented in this thesis.

6.2.2.2 Earth radiation pressure

Earth reflects some of the incoming solar radiation back to space, thus inducing indirect radiation pressure on orbiting satellites (Ziebart et al., 2004). This effect, called Earth albedo, is limited to the illuminated part of Earth that is visible from a satellite's point of view. In addition, part of the incoming radiation is absorbed by Earth's surface and reemitted as thermal radiation. The absorbed heat is usually released slowly over time,

which is the reason why thermal radiation can also originate from the dark side of Earth.

Rodriguez-Solano (2009) and Rodriguez-Solano et al. (2012b) developed an Earth radiation pressure model that is now widely used in GNSS satellite orbit determination. It is based on a box-wing representation of the satellite and reflectivity and emissivity maps of Earth's surface. These maps were derived as monthly means over ten years (2000-2009) of data from the Clouds and the Earth's Radiant Energy System (CERES) mission (Wielicki et al., 1996).

Following Knocke et al. (1988), the acceleration due to Earth radiation pressure (ERP) can be computed by dividing Earth's surface into small segments. On the satellite side, the radiation from one segment of Earth's surface induces an acceleration on all illuminated surfaces of the box-wing model. Equations (6.17) and (6.18) can be reused for this purpose. As the unit vector $\mathbf{e}_D$ represents the direction of radiation in these equations, here $\mathbf{e}_D$ is the unit vector from the segment's center (instead of the Sun) to the satellite. The acceleration caused by one segment of Earth's surface then is

$$\mathbf{a}_{\text{ERP}}^{\text{segment}} = \frac{A}{\pi s^2} \cos\phi \sum_{i}^{\text{surfaces}} \Big[\tau R \cos\gamma \left(\mathbf{a}_{\text{SRP},i}^{\text{surface}}(\alpha_O, \delta_O, \rho_O) + \mathbf{a}_{\text{TRR},i}^{\text{surface}}(\alpha_O) \right) + \frac{E}{4} \left(\mathbf{a}_{\text{SRP},i}^{\text{surface}}(\alpha_I, \delta_I, \rho_I) + \mathbf{a}_{\text{TRR},i}^{\text{surface}}(\alpha_I) \right) \Big] . \tag{6.27}$$

Here, $\cos\phi = \mathbf{e}_D \cdot \mathbf{n}$ represents the angle of reflected radiation, with $\mathbf{n}$ being the unit normal vector of the segment. A is the surface area of the segment and s is the distance between the satellite and the segment's center. $\cos\gamma = \mathbf{e}_{\text{Sun}} \cdot \mathbf{n}$ is the cosine of the angle of incident radiation, based on the unit vector $\mathbf{e}_{\text{Sun}}$ from the segment's center to the Sun. The factor τ is 1 if the segment is illuminated by the Sun (i.e., $\cos\gamma > 0$) or 0 otherwise. Therefore, only illuminated segments produce an albedo effect based on the reflectivity R of the segment. Since albedo concerns the visible spectrum of light, the respective optical properties α_O, δ_O, and ρ_O of a satellite surface are used. The effect caused by thermal radiation, on the other hand, depends on the emissivity E of a segment and the infrared properties α_I, δ_I, and ρ_I of the satellite's surface materials.

The total acceleration acting on the satellite can thus be obtained by accumulating the accelerations caused by the individual visible segments

$$\mathbf{a}_{\text{ERP}} = \sum_{j}^{\substack{\text{visible} \\ \text{segments}}} \mathbf{a}_{\text{ERP,j}}^{\text{segment}} . \tag{6.28}$$

A segment is only visible from the satellite's point of view if $\cos\phi > 0$.

Modeling Earth radiation pressure reduces several systematic effects in GNSS products (Rodriguez-Solano et al., 2012c). It mainly affects the radial component of the satellite orbits in the order of 1–2 cm. While the effect in the along and cross track components is much smaller, it leads to systematic north-south biases in the station coordinates. Therefore, it is important to consider this effect in GNSS processing.

6.2.2.3 Antenna thrust

GNSS satellites continuously transmit their navigation signals towards Earth. This radiation results in a small, constant acceleration along the direction opposite to the antenna boresight (i.e., away from Earth). Following Milani et al. (1987), this acceleration can be modeled as

$$\mathbf{a}_{\text{AT}} = -\frac{P}{c\,m}\mathbf{e}_z\,, \tag{6.29}$$

where P is the transmit power of the satellite, c is the speed of light, m is the satellite's mass, and $\mathbf{e}_z$ is the antenna boresight direction. Steigenberger et al. (2018) provides transmit power values, which were measured with a large dish antenna, for several types of GNSS satellites. Transmit power largely depends on the satellite type, with most types only showing small variations between their satellites. In general, modern satellites transmit at higher power levels than older ones due to more signals being transmitted on more frequencies.

6.2.2.4 Relativistic correction of the equations of motion

It is important to consider relativistic effects in the equations of motion during orbit modeling of near-Earth satellites. According to Petit and Luzum (2010), this relativistic correction can be expressed in the form of an acceleration

$$\begin{aligned}\mathbf{a}_{\text{rel}} = \frac{GM_{\text{Earth}}}{c^2 r^3}\left\{\left[2\left(\beta+\gamma\right)\frac{GM_{\text{Earth}}}{r} - \gamma\,\dot{\mathbf{r}}\cdot\dot{\mathbf{r}}\right]\mathbf{r} + 2\left(1+\gamma\right)\left(\mathbf{r}\cdot\dot{\mathbf{r}}\right)\dot{\mathbf{r}}\right\} \\ + \left(1+\gamma\right)\frac{GM_{\text{Earth}}}{c^2 r^3}\left[\frac{3}{r^2}\left(\mathbf{r}\times\dot{\mathbf{r}}\right)\left(\mathbf{r}\cdot\mathbf{J}\right) + \left(\dot{\mathbf{r}}\times\mathbf{J}\right)\right] \\ + \left(1+2\gamma\right)\frac{GM_{\text{Sun}}}{c^2 r_{\text{Sun}}^3}\left[\left(\mathbf{r}_{\text{Sun}}\times\dot{\mathbf{r}}_{\text{Sun}}\right)\times\dot{\mathbf{r}}\right]\,.\end{aligned} \tag{6.30}$$

Here, GM_{Earth} and GM_{Sun} are the gravitational coefficients of Earth and the Sun, c is the speed of light, β and γ are post-Newtonian parameters ($\beta = 1$ and $\gamma = 1$ in general relativity), and $\mathbf{J}$ is the vector of Earth's angular momentum per unit mass

($\|\mathbf{J}\| \cong 9.8 \cdot 10^8\,\mathrm{m}^2/\mathrm{s}$). The vectors $\mathbf{r}$, $\dot{\mathbf{r}}$, $\mathbf{r}_{\mathrm{Sun}}$, and $\dot{\mathbf{r}}_{\mathrm{Sun}}$ are the geocentric positions and velocities of the satellite and Sun, while r and r_{Sun} are their respective norms.

The relativistic correction in (6.30) comprises different effects. The first line describes the main relativistic effect, which is induced by Earth's Schwarzschild field and results in a shift of the argument of perigee (Ashby and Bertotti, 1986). The terms in the second and third line represent the Lense-Thirring and de Sitter precession, respectively. As their names suggest, these effects cause a small precession of the orbital plane.

6.2.3 Variational equations and orbit parametrization

Variational equations (e.g., Montenbruck and Gill, 2000; Beutler, 2005) are one approach to solve the system of equations in (6.15) and (6.16). Ellmer (2018) details how variational equations are used to determine orbits of the Gravity Recovery And Climate Experiment (GRACE) mission at Graz University of Technology. The same concept and implementation is also used for GNSS orbit determination. The following brief summary of variational equations is based on the above-mentioned references.

The equations of motion can be expressed as a first-order differential equation system

$$\dot{\mathbf{y}}(t) = \boldsymbol{f}(t, \mathbf{y}, \mathbf{p}, \ldots) \tag{6.31}$$

based on the satellite state vector

$$\mathbf{y}(t) = \begin{bmatrix} \mathbf{r}(t) \\ \dot{\mathbf{r}}(t) \end{bmatrix}, \tag{6.32}$$

its time derivative

$$\dot{\mathbf{y}}(t) = \begin{bmatrix} \dot{\mathbf{r}}(t) \\ \mathbf{a}(t, \mathbf{r}, \mathbf{p}, \ldots) \end{bmatrix}, \tag{6.33}$$

and the vector of force model parameters $\mathbf{p} = \begin{bmatrix} p_1 & \ldots & p_n \end{bmatrix}^T$. Derivating Equation (6.31) with respect to the initial state vector $\mathbf{y}_0 = \begin{bmatrix} \mathbf{r}_0 & \dot{\mathbf{r}}_0 \end{bmatrix}^T$ leads to

$$\frac{\partial \dot{\mathbf{y}}(t)}{\partial \mathbf{y}_0} = \underbrace{\frac{\partial \boldsymbol{f}(t, \mathbf{y}, \mathbf{p}, \ldots)}{\partial \mathbf{y}_0}}_{=\mathbf{0}} + \frac{\partial \boldsymbol{f}(t, \mathbf{y}, \mathbf{p}, \ldots)}{\partial \mathbf{y}} \frac{\partial \mathbf{y}(t)}{\partial \mathbf{y}_0}. \tag{6.34}$$

By introducing the state transition matrix

$$\boldsymbol{\Phi}(t) = \frac{\partial \mathbf{y}(t)}{\partial \mathbf{y}_0} = \begin{bmatrix} \dfrac{\partial \mathbf{r}(t)}{\partial \mathbf{r}_0} & \dfrac{\partial \mathbf{r}(t)}{\partial \dot{\mathbf{r}}_0} \\ \dfrac{\partial \dot{\mathbf{r}}(t)}{\partial \mathbf{r}_0} & \dfrac{\partial \dot{\mathbf{r}}(t)}{\partial \dot{\mathbf{r}}_0} \end{bmatrix}, \tag{6.35}$$

which contains the partial derivatives of the satellite position and velocity with respect to the initial position and velocity, (6.34) can be written as

$$\dot{\boldsymbol{\Phi}}(t) = \frac{\partial \boldsymbol{f}(t, \mathbf{y}, \mathbf{p}, \ldots)}{\partial \mathbf{y}} \boldsymbol{\Phi}(t) = \begin{bmatrix} \mathbf{0}_{3\times3} & \mathbf{I}_{3\times3} \\ \dfrac{\partial \mathbf{a}(t, \mathbf{r}, \mathbf{p}, \ldots)}{\partial \mathbf{r}(t)} & \mathbf{0}_{3\times3} \end{bmatrix} \boldsymbol{\Phi}(t)\,. \tag{6.36}$$

Starting from the initial value $\boldsymbol{\Phi}_0 = \mathbf{I}$, the state transition matrix for each epoch t can be determined by numerical integration using (6.36). Derivating Equation (6.31) with respect to the unknown force model parameters $\mathbf{p}$ gives

$$\frac{\partial \dot{\mathbf{y}}(t)}{\partial \mathbf{p}} = \frac{\partial \boldsymbol{f}(t, \mathbf{y}, \mathbf{p}, \ldots)}{\partial \mathbf{p}} + \frac{\partial \boldsymbol{f}(t, \mathbf{y}, \mathbf{p}, \ldots)}{\partial \mathbf{y}} \frac{\partial \mathbf{y}(t)}{\partial \mathbf{p}}\,. \tag{6.37}$$

The parameter sensitivity matrix

$$\mathbf{S}(t) = \frac{\partial \mathbf{y}(t)}{\partial \mathbf{p}} = \begin{bmatrix} \dfrac{\partial \mathbf{r}(t)}{\partial \mathbf{p}} \\ \dfrac{\partial \dot{\mathbf{r}}(t)}{\partial \mathbf{p}} \end{bmatrix} \tag{6.38}$$

contains the partial derivatives of the satellite state with respect to the n unknown force model parameters $\mathbf{p}$ and can also be computed via numerical integration (e.g., see Ellmer, 2018). Alternatively, it can be determined directly at each epoch t from the state transition matrix via

$$\mathbf{S}(t) = -\boldsymbol{\Phi}(t) \int_{t_0}^{t} \boldsymbol{\Phi}^{-1}(t') \begin{bmatrix} \mathbf{0}_{3\times n} \\ \dfrac{\partial \mathbf{a}(t', \mathbf{r}, \mathbf{p}, \ldots)}{\partial \mathbf{p}} \end{bmatrix} dt'\,. \tag{6.39}$$

The state transition and parameter sensitivity matrices are then used to connect the GNSS observation equations to the orbit parameters ($\mathbf{y}_0$, $\mathbf{p}$). The intermediate parameters $\mathbf{z}_g$ of an observation group (see Section 5.3) already contain the satellite position $\mathbf{r}^s$ at the respective epoch. Therefore, only the partial derivatives of $\mathbf{r}^s(t)$ with respect to the

satellite's orbit parameters are missing to complete the link. The respective entries in the design matrix $\mathbf{D}_g$ are

$$\frac{\partial \mathbf{r}^s(t)}{\partial \mathbf{y}_0} = \mathbf{\Phi}_\mathbf{r}(t) \tag{6.40}$$

and

$$\frac{\partial \mathbf{r}^s(t)}{\partial \mathbf{p}} = \mathbf{S}_\mathbf{r}(t)\,. \tag{6.41}$$

Here, $\mathbf{\Phi}_\mathbf{r}$ and $\mathbf{S}_\mathbf{r}$ refer to the position-related parts (i.e., the top half) of the respective matrices. The partial derivatives of the velocity with respect to the orbit parameters are not needed for the design matrix $\mathbf{D}_g$ as the intermediate parameters do not contain satellite velocities.

The most common force model parameters in GNSS orbit determination are those of the ECOM model. In this case, the partial derivatives in (6.38) are determined by derivating (6.20) with respect to the ECOM parameters, for example

$$\frac{\partial \mathbf{a}_\text{SRP}(t)}{\partial D_{C2}} = \nu \cos 2\Delta u\, \mathbf{e}_D\,. \tag{6.42}$$

Additional empirical parameters are often set up to further improve the fit of an orbit to observations. This is done to mitigate imperfections in the applied force models. Various parametrizations are possible (see Jäggi, 2007, for examples) and in use among the IGS analysis centers. One parametrization, which was used for the reprocessing campaign presented in this thesis, are so-called pseudostochastic pulses (Beutler et al., 1994). These are small, instantaneous velocity changes at specific epochs, for example at the center of a 24-hour orbit arc. Such empirical parameters are usually constrained in order to limit their impact. The main reason is that they usually do not have a physical interpretation and the dynamic nature of an orbit should be maintained as much as possible. Ideally, future improvements in force modeling would render this type of parameter unnecessary.

6.2.4 Sensitivity analysis

This section presents analyses of how sensitive GNSS satellite orbits are to certain forces being disregarded or modeled in different ways. The motivation for these analyses was threefold: Firstly, to assess the impact of certain forces that are not commonly modeled by IGS analysis centers but were included in the reprocessing conducted at

TUG. Secondly, to see how some model changes introduced for repro3 affect the modeled orbits. Lastly, to get an overview of how the various satellite types in use over the years and constellations are affected by certain models.

The analyses were conducted by integrating daily orbits based on various force model configurations. These orbits were then fitted to the orbits determined in the reprocessing campaign by estimating the initial state vector and a set of solar radiation pressure parameters. The reference solution followed the configuration of the reprocessing campaign (see Section 8.1.1). For each solution, only the targeted force model was disabled or replaced by another model, while all other force models remained identical to the reference solution. The analyses covered all GPS, GLONASS, and Galileo satellites over the period 1994–2020. The impact of the respective model was then assessed in terms of 1D root mean square (RMS) of the orbit differences between that solution and the reference solution. The RMS values were computed per day and satellite type since this is the main differentiating factor for certain forces.

The results of these analyses are briefly summarized in the following list.

Satellite attitude Satellite attitude not only affects the GNSS phase observations, but also directly influences the effects of nonconservative forces, mainly solar radiation pressure. Figure 6.7 shows the impact of using the attitude models described in Section 6.1 versus using nominal yaw-steering attitude. The values are limited to those satellites that are in eclipse season at the respective days. The largest differences can be seen for GPS-II and GPS-IIA mainly due to their post-shadow recovery maneuvers, where the yaw angle can deviate significantly from its nominal value while the satellite is exposed to solar radiation pressure. Other satellite types show RMS values up to a few millimeters, which can largely be attributed to their attitude behavior around orbit noon. Overall, the results show that attitude modeling definitely should be applied during orbit integration.

A priori box-wing solar radiation pressure The impact of using an a priori box-wing model in addition to estimating the ECOM2-7 parameters can be seen in Figure 6.8. An RMS of around 3 mm for most satellite types shows that empirical parameters alone cannot fully replace a physics-based model. This is even more obvious for Galileo satellites, where even the additional D_{C2} and D_{S2} ECOM parameters do not appear to be able to fully account for their elongated bus shape. The large differences for GPS-I satellites, on the other hand, can more likely be attributed to an inadequate box-wing model.

Empirical solar radiation pressure Figure 6.9 showcases the very significant impact of the additional D_{C2} and D_{S2} parameters of ECOM2-7 compared to ECOM-5. An a priori box-wing model was used in both cases. Galileo satellites being among

the smallest differences indicates that their box-wing model already accounts for a good part of these twice-per-revolution effects.

Antenna thrust Figure 6.10 makes it clear why modeling antenna thrust is important. This is especially true for newer satellites that usually transmit at a higher power level, and even more so for the comparatively lightweight Galileo satellites.

Ocean tides The choice of ocean tide model (FES2004, EOT11a, FES2014b) does not have a significant impact on orbit modeling. Differences are below 1 mm, which accords with the findings of Dach et al. (2021).

Atmospheric tides The impact of atmospheric tides on modeled orbits is below 1 mm.

Nontidal mass variations Variations in atmospheric pressure, wind-induced ocean currents, and changes in terrestrial water storage affect GNSS satellite orbits at a level below 1 mm.

C_{20} gravity field coefficient In the 1990s and early 2000s, the trend component of the C_{20} gravity field coefficient diverges between recent gravity field models (e.g., GOCO06s) and what is observed by SLR (e.g., Meyer et al., 2019). However, the impact of using the SLR-based trend on GNSS satellite orbits is well below 1 mm.

Secular pole The adoption of the secular pole (Ries, 2017) instead of the mean pole originally stated in the IERS conventions (Petit and Luzum, 2010) does not meaningfully affect orbit modeling.

These analyses confirm that some of the investigated models, such as atmospheric tides and nontidal mass variations, can be safely disregarded during orbit modeling at the current level of GNSS orbit accuracy. However, they may become significant once higher orbit accuracies can be achieved in the future.

6.3 Clock errors

The fundamental principle of GNSS is a one-way runtime measurement using two clocks, one at the transmitter and one at the receiver (e.g., Beard and Senior, 2017). Since these clocks are usually not synchronized, their clock readings refer to different time scales. In high-precision GNSS processing, it is essential that all measurements are processed in a common reference time scale. Therefore, the offset or error between the individual time scales and the reference time scale has to be accounted for.

In undifferenced processing approaches, such as the raw observation approach described in this thesis, clock errors have to be estimated as unknown parameters. Since clocks are affected by noise and other short-term variability, clock errors are commonly set up

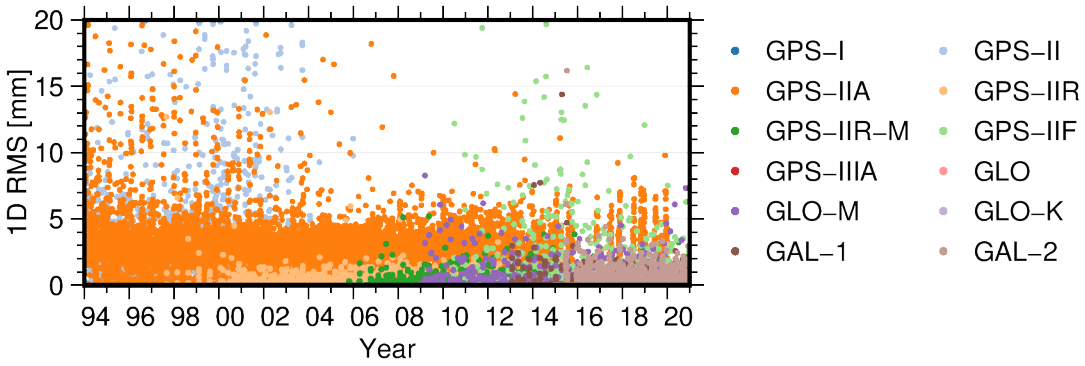

Figure 6.7: Impact of attitude modeling on orbits

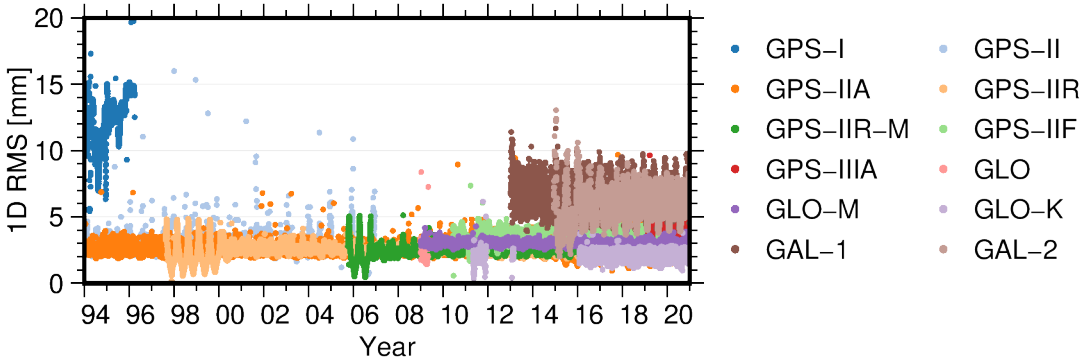

Figure 6.8: Impact of a priori solar radiation pressure box-wing model on orbits

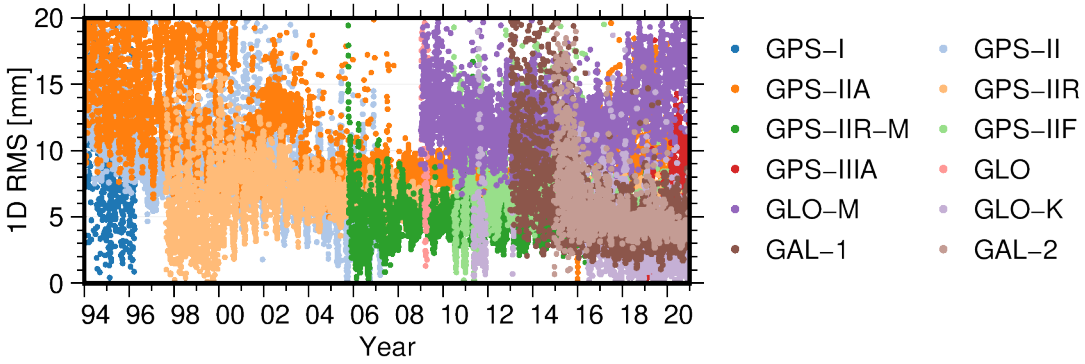

Figure 6.9: Impact of empirical solar radiation pressure model (ECOM-5 vs. ECOM2-7) on orbits

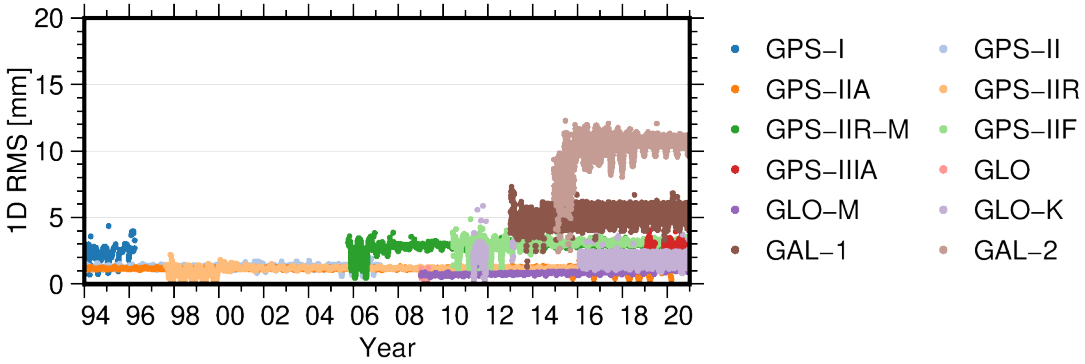

Figure 6.10: Impact of antenna thrust on orbits

as independent epoch-wise parameters per transmitter and receiver (e.g., Weiss et al., 2017). Several studies (e.g., Weinbach and Schön, 2011; Orliac et al., 2012; Hackel et al., 2015; Koch et al., 2017; Qing et al., 2017) have investigated clock modeling techniques that introduce stochastic and/or deterministic connections between epochs. They found that this benefits the resulting GNSS solutions in various ways, for example by reducing orbit midnight discontinuities and SLR residuals. Nonetheless, clock modeling is not yet commonly applied by IGS analysis centers and was also not used during the reprocessing presented in this thesis. Therefore, it is not discussed further here, even though research in this direction is currently ongoing at Graz University of Technology.

6.3.1 Clock parametrization

As described in Section 5.3, the intermediate parameters for an observation group contain clock errors at the transmitter and receiver. The partial derivatives of the observation equations with respect to these parameters are already addressed in the design matrix $\mathbf{C}_g$. Therefore, the elements of the design matrix $\mathbf{D}_g$ that connect the intermediate clock parameters to the final clock parameters of the respective receiver and transmitter at that epoch are simply 1.

6.3.2 Rank deficiencies and time scale alignment

Estimating clock errors for all transmitters and receivers at the same time leads to a rank deficiency in the normal equation matrix (e.g., Weiss et al., 2017). The reason for this is that there are only relative observations between the satellites and receivers while there is no absolute alignment of the clocks. A common way to resolve this rank deficiency is to introduce one highly stable clock as a known absolute reference. For example, this could be a GNSS receiver that is connected to a hydrogen maser operated at a timing laboratory. This implies that the time scale of that clock is used as the reference time scale in the processing.

Alternatively, it is also possible to use the mean over a set of clocks as an absolute alignment. This could comprise several highly stable ground-based clocks or, for example, all satellite clocks of one or more GNSS constellations. Since these satellites also have highly stable on-board atomic clocks, in case of Galileo even hydrogen masers, they are well suited for such a zero-mean constraint. In principle, a combination of receivers and satellites is possible as well.

In case of epoch-wise clock estimation, a zero-mean constraint has to be added at each epoch. It can be introduced in the form of an additional observation equation

$$0 = \overset{\text{zero-mean satellites}}{\sum_i} \delta^{s_i}(t) + \overset{\text{zero-mean receivers}}{\sum_j} \delta_{r_j}(t)\,. \tag{6.43}$$

The resulting row in the design matrix $\mathbf{A}(t)$ then contains ones at the parameter indices of the receiver and/or satellite clocks used for the zero-mean constraint. The strength of the constraint can be controlled via the standard deviation associated to the pseudoobservation.

As mentioned above, a zero-mean constraint can be used to absolutely align the reference time scale. In the reprocessing conducted in the context of this thesis, a zero-mean constraint over all GPS satellites was applied to resolve the rank deficiency and to align the reference time scale to GPS time. Since the clock errors at the receivers are the same for all GNSS constellations, this means that any offsets in system-wide time scales with respect to GPS time are shifted to the satellite clocks of the other systems (i.e., GLONASS and Galileo). Therefore, no additional parameters have to be set up to account for such inter-system time offsets.

Clock errors at the satellites and receivers are also fully correlated with their respective code biases. Thus, additional rank deficiencies occur when clock errors and code biases are estimated together. Section 6.5 addresses this issue and how it can be solved.

6.4 Ionosphere

The ionosphere is the part of Earth's atmosphere that contains a high density of ionized molecules and free electrons (e.g., Hofmann-Wellenhof et al., 2008; Hernández-Pajares et al., 2011; Hobiger and Jakowski, 2017). It typically ranges from 50 km to 1000 km altitude. Radio waves traveling through the ionosphere are refracted. The refractive index mainly depends on the electron density n_e. The STEC describes the integral

$$\mathrm{STEC} = \int n_e \, ds \tag{6.44}$$

of this density along the signal path $\boldsymbol{p}_r^s$. The vertical total electron content (VTEC), on the other hand, is the integral

$$\mathrm{VTEC} = \int n_e \, dh \tag{6.45}$$

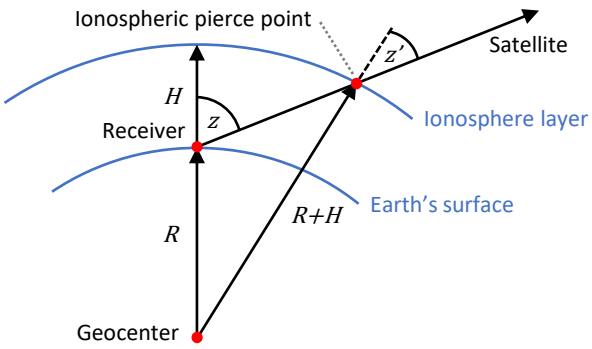

Figure 6.11: Single-layer ionosphere model (adapted from Schaer, 1999)

along the zenith direction starting from a point usually located on Earth's surface. Both are commonly expressed in TEC units (TECU), with $1\,\mathrm{TECU} = 10^{16}\,\mathrm{electrons/m^2}$.

The ionosphere is a dispersive medium with respect to the frequency bands used in GNSS (Hofmann-Wellenhof et al., 2008). Therefore, the ionospheric refraction depends on the signal frequency. In addition, the ionosphere increases the phase velocity of waves traveling through it while decreasing the velocity of the signal group envelope (i.e., codes modulated onto the carrier wave). For GNSS signals, this means that phase observations are measured too short and code observations too long.

The ionosphere can be modeled using so-called Chapman layers (Chapman, 1931). These layers describe the electron density at a certain altitude. The most important layers are called D, E, F_1, and F_2 (e.g., Budden, 1985). They describe regions of special interest in terms of ionospheric characteristics. A detailed description of these layers and their vertical distribution can be found, for example, in Hobiger and Jakowski (2017). In practice, the ionosphere is often approximated by a single thin layer at a certain altitude (Hoque and Jakowski, 2008). Such a single-layer model is visualized in Figure 6.11.

6.4.1 Ionospheric correction

The ionospheric correction becomes a nonlinear function of the STEC when higher-order ionospheric effects are taken into account. Higher-order ionospheric corrections were first considered by Brunner and Gu (1991) and Bassiri and Hajj (1993) and can amount to several centimeters under severe ionospheric conditions, especially at low elevation angles. Following Fritsche et al. (2005) and Hoque and Jakowski (2008), the ionospheric correction for code and phase measurements (in meters) on frequency ν are

$$\mathrm{iono}([\mathrm{C}\nu], t, \boldsymbol{p}_r^s) = \frac{q}{\nu^2}\mathrm{STEC} + \frac{s}{\nu^3}\mathrm{STEC} + \frac{r}{\nu^4}\mathrm{STEC}^2 \tag{6.46}$$

and

$$\begin{aligned}\mathrm{iono}([\mathrm{L}\nu], t, \boldsymbol{p}_r^s) = &- \frac{q}{\nu^2}\mathrm{STEC} - \frac{s}{2\nu^3}\mathrm{STEC} - \frac{r}{3\nu^4}\mathrm{STEC}^2 \\ &+ \frac{b_{\text{geometric}} - b_{\text{dTEC}}}{\nu^4}\mathrm{STEC}^2\,,\end{aligned} \tag{6.47}$$

respectively. Here, ν is in Hz and STEC is in electrons/m^2.

The first three terms in both equations are the first-, second-, and third-order corrections. The first-order term uses the constant factor

$$q = \frac{e^2}{8\pi^2\epsilon_0 m_e} \approx 40.309\,\mathrm{m}^3/\mathrm{s}^2\,, \tag{6.48}$$

where e is the elementary charge (i.e., the electric charge of a proton), ϵ_0 is the vacuum permittivity, and m_e is the electron rest mass (Hobiger and Jakowski, 2017).

The second-order term contains

$$s = 7527\,c\,\mathbf{b}\cdot\mathbf{k}\,, \tag{6.49}$$

where c is the speed of light, $\mathbf{b}$ is the magnetic field vector at the point where the signal path pierces the single ionosphere layer (see Figure 6.11), and $\mathbf{k}$ is the line-of-sight unit vector from the satellite to the receiver as defined in Equation (5.13). Both vectors must be expressed in the same reference frame (e.g., the CRF). The magnetic field vector $\mathbf{b}$ can be determined from a magnetosphere model, for example the International Geomagnetic Reference Field (IGRF; Alken et al., 2021). The choice of altitude for the single ionosphere layer usually varies between 350 km and 450 km depending on the study (e.g., Schaer, 1999; Fritsche et al., 2005; Hernández-Pajares et al., 2007). In this thesis, the layer is set at an altitude of $H = 450\,\mathrm{km}$.

The third-order term uses the coefficient

$$r = 2437\,\eta\,N_{\text{max}} \tag{6.50}$$

with the peak electron density $N_{\text{max}} = \frac{(20-6)\,10^{12}}{(4.55-1.38)\,10^{18}}$ and a shape parameter $\eta = 0.66$ (Fritsche et al., 2005).

The fourth term in (6.47) is a combined correction for what Hoque and Jakowski (2008) calls excess path length and range error due to TEC difference at different frequencies. They are also commonly referred to as geometric bending and dTEC bending. The former describes the difference in length between the geometrical range and the curved path for a signal on frequency ν, while the latter corrects for the slightly different STEC that

signals experience on their curved paths compared to the STEC along the line-of-sight path. The geometric bending factor is

$$b_{\text{geometric}} = \frac{7.5\, e^{-2.13\, E}}{10^9\, H_{F_2}\, h_{m,F_2}^{0.25}} \tag{6.51}$$

and the dTEC bending factor is

$$b_{\text{dTEC}} = q\, \frac{0.1108\, e^{-2.1844\, E}}{H_{F_2}\, h_{m,F_2}^{0.3}}\,. \tag{6.52}$$

Here, q is the constant factor from (6.48), E is the elevation angle of the incoming signal at the receiver, $H_{F_2} = 70\,\mathrm{km}$ is the F_2 layer scale height in kilometers, and $h_{m,F_2} = 350\,\mathrm{km}$ is the F_2 peak ionization height, also in kilometers. Equations (6.51) and (6.52) have been slightly reformulated compared to Hoque and Jakowski (2008) such that all terms in (6.47) result in units of length (i.e. meters) given that ν is in Hz and STEC is in electrons/m^2. In this thesis, the two bending corrections are only applied to phase observations, as they are insignificant with respect to the relatively low precision of code observations.

Hobiger and Jakowski (2017) provides approximate values for the magnitude of the different corrections. The following ranges are representative for phase observations on the typical GNSS frequency bands, with GPS L1 on the low end and L5 on the high end of the spectrum. The corrections for code observations are larger by factors 2 and 3 for the second- and third-order effects, see (6.46) and (6.47). The first-order correction can amount up to 100–150 m. Under high solar activity and at low elevations, the second-order correction can reach 12–29 cm. The third-order correction should not exceed 6–19 mm even under extreme conditions. The geometric bending errors are usually only significant at elevations below 30°, where they can exceed 1 cm. Under severe solar activity, they can, however, reach up to 5–17 cm. No values are given for dTEC bending, but since it has opposite sign, it at least partially cancels the geometric bending (Petrie et al., 2010).

6.4.2 Parametrization of the ionosphere

Section 5.2 describes how the ionospheric influence can be considered by preeliminating an STEC parameter from the observation equations of an observation group. The design matrix $\mathbf{B}_g$ from Equation (5.5) contains the partial derivatives of the observation

equations with respect to the STEC parameter. Based on (6.46) and (6.47), these partial derivatives are

$$\frac{\partial \operatorname{iono}([\mathrm{C}\nu], t, \boldsymbol{p}_r^s)}{\partial \mathrm{STEC}} = \frac{q}{\nu^2} + \frac{s}{\nu^3} + \frac{2r}{\nu^4}\mathrm{STEC} \tag{6.53}$$

and

$$\frac{\partial \operatorname{iono}([\mathrm{L}\nu], t, \boldsymbol{p}_r^s)}{\partial \mathrm{STEC}} = -\frac{q}{\nu^2} - \frac{s}{2\nu^3} - \frac{2r}{3\nu^4}\mathrm{STEC} + 2\frac{b_{\text{geometric}} - b_{\text{dTEC}}}{\nu^4}\mathrm{STEC} \tag{6.54}$$

for code and phase observations, respectively. The third-order and bending terms in (6.53) and (6.54) already depend on the STEC. Section 5.7 describes how the preeliminated STEC parameters can be reconstructed after the normal equation system is solved. Thus, the estimated STEC values can be stored and used as a priori values in (6.53) and (6.54) for subsequent iterations of the least-squares adjustment. For the first iteration, when no STEC values have been determined yet, setting $\mathrm{STEC} = 0$ is sufficient, as the third-order and bending terms only have a small effect on the solution. They are then considered starting from the second iteration. Alternatively, an a priori ionosphere model could be used to determine STEC values for the first iteration, if available.

One issue of estimating ionospheric STEC parameters is that they cannot be separated from clock and code bias parameters (Schaer, 1999). This results in biased estimates for these parameters. A proper separation is only possible if additional information is introduced into the equation system. This can be done in several ways. One option is to apply an ionospheric mapping function. Such a function maps the STEC values from the different observation groups at one point in time to a common VTEC value for each receiver.

Schaer (1999) proposed a mapping function m_I based on a modified single-layer model in the form of

$$\mathrm{STEC}(z) = m_I(z)\,\mathrm{VTEC} = \frac{1}{\cos z'}\mathrm{VTEC} \tag{6.55}$$

with

$$\sin z' = \frac{R}{R+H}\sin(\alpha z)\,. \tag{6.56}$$

Here, z is the zenith angle of the incoming signals at the receiver, $R = 6371\,\mathrm{km}$ is the radius of Earth, $H = 506.7\,\mathrm{km}$ is the altitude of the single ionosphere layer (see Figure 6.11), and $\alpha = 0.9782$ is a correction factor (Feltens et al., 2018).

VTEC parameters are usually set up for each station and each epoch. The corresponding entry for a VTEC parameter in the design matrix $\mathbf{D}_g$ is

$$\frac{\partial \boldsymbol{f}_g}{\partial \mathrm{VTEC}} = m_I(z)\,\frac{\partial \boldsymbol{f}_g}{\partial \mathrm{STEC}} = m_I(z)\,\mathbf{B}_g\,. \tag{6.57}$$

As described above, m_I is the mapping function from (6.55). The design matrix $\mathbf{B}_g$ contains the partial derivatives with respect to the STEC parameter as defined in (6.53) and (6.54) . Note that in this case $\mathbf{B}_g$ refers to the respective design matrix before the homogenization step described in Section 5.4.

Ionospheric mapping functions cannot fully describe the ionosphere. Therefore, if they are used to set up VTEC parameters, it is still necessary to parameterize ionospheric scintillations in the form of residual STEC parameters $\Delta\mathrm{STEC}$, resulting in

$$\mathrm{STEC} = m_I(z)\,\mathrm{VTEC} + \Delta\mathrm{STEC}\,. \tag{6.58}$$

These parameters should be loosely constrained (e.g., with $\sigma_{\Delta\mathrm{STEC}} = 40\,\mathrm{TECU}$) so that they only capture residual scintillations while the VTEC parameters represent the main part of the ionospheric delay. Such a constraint can be applied by adding an additional observation equation

$$0 = \Delta\mathrm{STEC} \tag{6.59}$$

to each observation group. The standard deviation assigned to this pseudoobservation defines the strength of the constraint.

Setting up epoch-wise VTEC parameters for each station results in a large number of parameters. This can become an issue when processing large networks with hundreds of stations at a high sampling period. In such a case, the equation system can contain millions of VTEC parameters. Additionally, the ionospheric parameters themselves are not of primary interest in the analyses described in this thesis. The main goal of introducing additional information about the ionosphere is to obtain unbiased signal bias estimates.

These considerations lead to another possible approach (see Section 5.9.3). Instead of introducing potentially millions of VTEC parameters into the main equation system, the additional ionospheric information is introduced in a separate step. Section 6.5.3 describes how code biases are parameterized in the form of linear combinations. Some of these bias linear combinations are not estimable due to the influence of the ionosphere. However, they can be estimated in a separate equation system that only contains VTEC

parameters and the inestimable bias linear combinations while all other parameters are introduced as known. This procedure is described further in Section 6.5.3.3.

An alternative to estimating VTEC parameters at each receiver is to estimate global ionosphere maps. They usually represent the ionosphere in the form of spherical harmonics. However, they were not used for the reprocessing conducted in the context of this thesis and are thus not discussed further here. For more information on global ionosphere maps, see, for example, Schaer (1999), Hernández-Pajares et al. (2009), and Wielgosz et al. (2021)

6.5 Code biases

Signal biases are hardware delays that occur during the transmission and reception of GNSS signals (Håkansson et al., 2017). On the satellite side, there is a delay between the generation of a signal and its transmission at the antenna. The same is the case on the receiver side, where a delay occurs between signal reception at the antenna and the actual measurement of a specific signal in the receiver. As the name suggests, code biases refer to the delays affecting code observations. Similarly, phase observations are affected by phase biases, which are discussed in Section 6.6. In general, signal biases differ per constellation, satellite, frequency, signal attribute (e.g., C, W, I, Q), as well as receiver hardware and settings (Hauschild and Montenbruck, 2016; Sleewaegen and Clemente, 2018; N. Wang et al., 2020). This section assumes that code biases are constant over the processing period (e.g., one day), which is usually valid according to Håkansson et al. (2017).

The main issue with signal biases is that they are usually not known. Therefore, they have to be estimated during GNSS processing. However, the relative nature of GNSS observations prevents the estimation of absolute signal biases (Villiger et al., 2019). Furthermore, code biases are highly correlated with clock errors (see Section 6.3) and the ionospheric STEC described in Section 6.4 (e.g., Schaer, 1999; N. Wang et al., 2020). This results in several rank deficiencies in the normal equation system, which have to be resolved in some way. One possible solution to resolve these rank deficiencies is presented in Section 6.5.3.

6.5.1 Composite signals

Another issue is that some receivers track linear combinations of the signals transmitted by the satellites (e.g., Won and Pany, 2017). For instance, some legacy GPS receivers

track the linear combination C2D = C1C + (C1W − C2W) of the basic signals C1C, C1W, and C2W (Woo, 2000). Another common technique is to track a combination of data and pilot signal (e.g., Borio and Lo Presti, 2008). One example for this are the Galileo X signals (e.g., C1X, C5X), which are linear combinations of the respective data (C1B, C5I) and pilot (C1C, C5Q) signals (Romero, 2020). However, in an exemplary linear combination C5X = α C5I + β C5Q, it is not always clear what the factors α and β are (Sleewaegen and Clemente, 2018). They might be split evenly (i.e., $\alpha = \beta = 0.5$), but some receivers might also employ more sophisticated techniques, such as adjusting the factors depending on the elevation angle. Since receiver manufacturers often implement proprietary tracking techniques, information on this is usually not publicly available. In absence of this information, an even split is assumed for all composite signals in this thesis (except for GPS C2D, see above).

In terms of parametrization, composite signals are handled differently at the receiver and satellite. At the receiver side, each observed code signal has its own bias parameter, regardless of whether it is one of the basic signals transmitted by a satellite or a composite signal. The reason for this is that biases for the composite signals generally cannot be separated at the receiver level. Even if a receiver would additionally track the basic signals that form the composite signals, they would likely be processed in separate channels within the receiver, which could result in differing biases.

In contrast, code biases are only set up for the basic signals that are actually transmitted at the satellite side. For instance, at one of the older GPS satellites, only code biases for C1C, C1W, and C2W are set up. This implies the need for a transformation matrix that maps observed signal types to transmitted signal types. An example of such a transformation matrix for legacy GPS signals is given in Equation (5.22). For a receiver tracking Galileo X signals, this transformation matrix (limited to code signals) could be

$$\frac{\partial \boldsymbol{f}[\mathrm{C}]_g}{\partial \mathbf{b}[\mathrm{C}]^s} = \begin{array}{c} \\ \mathrm{C1X} \\ \mathrm{C5X} \\ \mathrm{C7X} \\ \mathrm{C8X} \end{array} \begin{array}{c} \begin{array}{cccccccc} \mathrm{C1B} & \mathrm{C1C} & \mathrm{C5I} & \mathrm{C5Q} & \mathrm{C7I} & \mathrm{C7Q} & \mathrm{C8I} & \mathrm{C8Q} \end{array} \\ \begin{bmatrix} 0.5 & 0.5 & & & & & & \\ & & 0.5 & 0.5 & & & & \\ & & & & 0.5 & 0.5 & & \\ & & & & & & 0.5 & 0.5 \end{bmatrix} \end{array}. \tag{6.60}$$

This transformation already gets taken into account when setting up the intermediate parameters (see Section 5.3). As stated in (6.60), the transformation matrix represents the partial derivatives of the code observation equations $\boldsymbol{f}[\mathrm{C}]_g$ with respect to the intermediate satellite code biases $\mathbf{b}[\mathrm{C}]^s$.

6.5.2 GLONASS

In contrast to other GNSS, GLONASS employs FDMA to distinguish between satellites (e.g., Revnivykh et al., 2017). This means that their satellites transmit at slightly different frequencies, denoted by a frequency number (see Section 2.2). As a result, the receiver code bias for a specific code observation type (e.g., C1P) can differ per frequency number (N. Wang et al., 2020). Therefore, it is necessary to set up an individual code bias parameter for each combination of code observation type and frequency number that is observed at the receiver. This significantly increases the number of signal bias parameters that have to be set up per receiver, resulting in longer processing times and increased memory demand. In addition, it further increases the complexity of resolving the rank deficiencies in the normal equation system, as the GLONASS constellation practically splits up into a number of subconstellations. Each of these subconstellations consists of one or two satellites that transmit on the same frequencies and thus share the same receiver code biases.

6.5.3 Parametrization and resolution of rank deficiencies

Code biases are most commonly considered in the form of differential code biases (e.g., Montenbruck et al., 2014; N. Wang et al., 2016; Xue et al., 2016; Sanz et al., 2017). However, with an increasing number of different signals transmitted by the GNSS constellations, it becomes more and more complex to analytically define differential parametrizations for code biases. Another approach is to estimate observable-specific, pseudo-absolute code biases (Villiger et al., 2019). In this case, each observable has its own code bias. This simplifies the formulation of the bias parameters, but additional conditions have to be introduced in order to deal with the rank deficiencies arising from the increase in parameters. Both parametrizations are compatible, meaning code biases can be transformed from observable-specific to differential and vice versa (e.g., Håkansson et al., 2017; Villiger et al., 2019; Banville et al., 2020).

As mentioned above, estimating code biases for each signal together with ionospheric parameters and clock errors leads to rank deficiencies in the normal equation system. The approach taken in this thesis is to utilize linear combinations of code biases. The basic idea is to not estimate the individual code biases directly, but to instead determine estimable linear combinations of biases. These estimable linear combinations are, however, not defined analytically. The reason for this is that it is exceptionally complex to define which linear combinations of biases are estimable in a particular multi-GNSS environment. Some of the main challenges (i.e., composite signals, GLONASS using FDMA, network splits) have been mentioned in the previous sections. Instead, the linear

combinations of code biases that are estimable are determined numerically. This process can be separated into a local and a global component. The former is local to one receiver or satellite, while the latter concerns the collective of all receivers and satellites in the system.

6.5.3.1 Local satellite and receiver rank deficiencies

A simplified normal equation system is set up independently for each satellite and each receiver. In case of a satellite, each receiver tracking that satellite contributes a single time-independent group of pseudoobservations. The respective observation equations are of the simplified form

$$f[\mathrm{C}\nu a]_r^s = -\delta^s + \mathbf{t}[\mathrm{C}\nu a]_r \cdot \mathbf{b}[\mathrm{C}]^s + \frac{q}{\nu^2}\mathrm{STEC}_r^s\,, \tag{6.61}$$

where δ^s is the (mean) satellite clock error and $\mathbf{t}[\mathrm{C}\nu a]_r$ is a vector containing the mapping from the observed code type to the signal biases of the transmitted code types in $\mathbf{b}[\mathrm{C}]^s$. For instance, this mapping could be $\mathbf{t}[\mathrm{C}\nu a]_r = [1 \quad 1 \quad -1]^T$ in case of a legacy C2D observation to an older GPS satellite that only transmits C1C, C1W, and C2W. More generally, it follows from

$$\frac{\partial \boldsymbol{f}[\mathrm{C}]_g}{\partial \mathbf{b}[\mathrm{C}]^s} = \mathbf{T}_r = \begin{bmatrix} \mathbf{t}[\mathrm{C}\nu a]_{r,1}^T \\ \vdots \\ \mathbf{t}[\mathrm{C}\nu a]_{r,n}^T \end{bmatrix}\,, \tag{6.62}$$

for which an example was given in (6.60). The last term in (6.61) represents the (mean) ionospheric influence in these simplified observation equations. Here, it is sufficient to only consider the first-order correction based on q from Equation (6.48) and the signal frequency ν. If additional information about the ionosphere is introduced into the overall normal equation system, for instance in the form of VTEC mapping functions (see Section 6.4.2), this last term is discarded and no STEC parameter is set up in the simplified normal equation system. Otherwise, the STEC parameter is eliminated from each group on the observation equation level following the procedure described in Section 4.2.2.1 and using the design matrices

$$\mathbf{A} = \begin{bmatrix} \frac{\partial \boldsymbol{f}[\mathrm{C}]_r^s}{\partial \delta^s} & \frac{\partial \boldsymbol{f}[\mathrm{C}]_r^s}{\partial \mathbf{b}[\mathrm{C}]^s} \end{bmatrix} = \begin{bmatrix} -1 & \mathbf{t}[\mathrm{C}\nu a]_{r,1}^T \\ \vdots & \vdots \\ -1 & \mathbf{t}[\mathrm{C}\nu a]_{r,n}^T \end{bmatrix} \quad \text{and} \quad \mathbf{B} = \frac{\partial \boldsymbol{f}[\mathrm{C}]_r^s}{\partial \mathrm{STEC}_r^s} = \begin{bmatrix} \frac{q}{\nu^2}1 \\ \vdots \\ \frac{q}{\nu^2}n \end{bmatrix}\,. \tag{6.63}$$

If one wants to follow the IGS convention of defining the clock datum based on the GPS C1W and C2W signals (e.g., Kouba, 2009a; Villiger et al., 2019), the respective two columns in $\mathbf{A}$ have to be set to zero (or removed) for GPS satellites. The code biases for the two types are then implicitly set to zero at the satellites.

In the next step, the individual normal equation matrices $\mathbf{N}_i = \mathbf{A}_i^T \mathbf{A}_i$ for each receiver are accumulated following Section 4.2.3. The satellite clock parameter can then be eliminated from this accumulated normal equation matrix (see Section 4.2.2.2), leaving only the bias parameters. The eigenvalue decomposition (e.g., Golub and Van Loan, 2013)

$$\mathbf{N} = \mathbf{Q}\mathbf{\Lambda}\mathbf{Q}^T \tag{6.64}$$

of this matrix reveals its nullspace. The eigenvectors linked to zero eigenvalues contain the linear combinations of the code bias parameters that are not estimable, while those linked to nonzero eigenvalues are. The dimension of the nullspace changes depending on whether additional ionospheric information has been introduced or not. It is smaller when, for example, additional VTEC parameters are set up based on mapping functions and residual STEC parameters are loosely constrained to zero (see Section 6.4.2). If no additional information about the ionosphere is introduced and all STEC parameters are estimated freely, the resulting nullspace is larger and fewer linear combinations are estimable.

Figure 6.12 shows some examples of the eigenvector matrices for this case. Each column represents a linear combination and each cell in a column corresponds to the factor of the respective observable. For instance, the nullspace at satellite G01 is fully defined by applying the above-mentioned IGS convention (i.e., setting C1W and C2W to zero). Another interpretation of this nullspace is that one linear combination represents a clock bias and the other a common TEC bias to all GPS receivers. This TEC bias cannot be determined without additional information about the ionosphere. The nullspace for Galileo satellite E01 contains three linear combinations because the receiver network splits into one set of receivers tracking the pilot (C, Q) signals and another tracking a combination of data and pilot (X) signals. Therefore, the nullspace comprises a clock bias and two TEC biases, one for each subnetwork.

The rank deficiencies local to the satellite can be resolved by removing the local nullspace. This can be achieved with the parameter transformation

$$\mathbf{b}[\mathrm{C}]^s = \bar{\mathbf{Q}}^s \mathbf{x}_{\bar{\mathbf{b}}[\mathrm{C}]^s}\,, \tag{6.65}$$

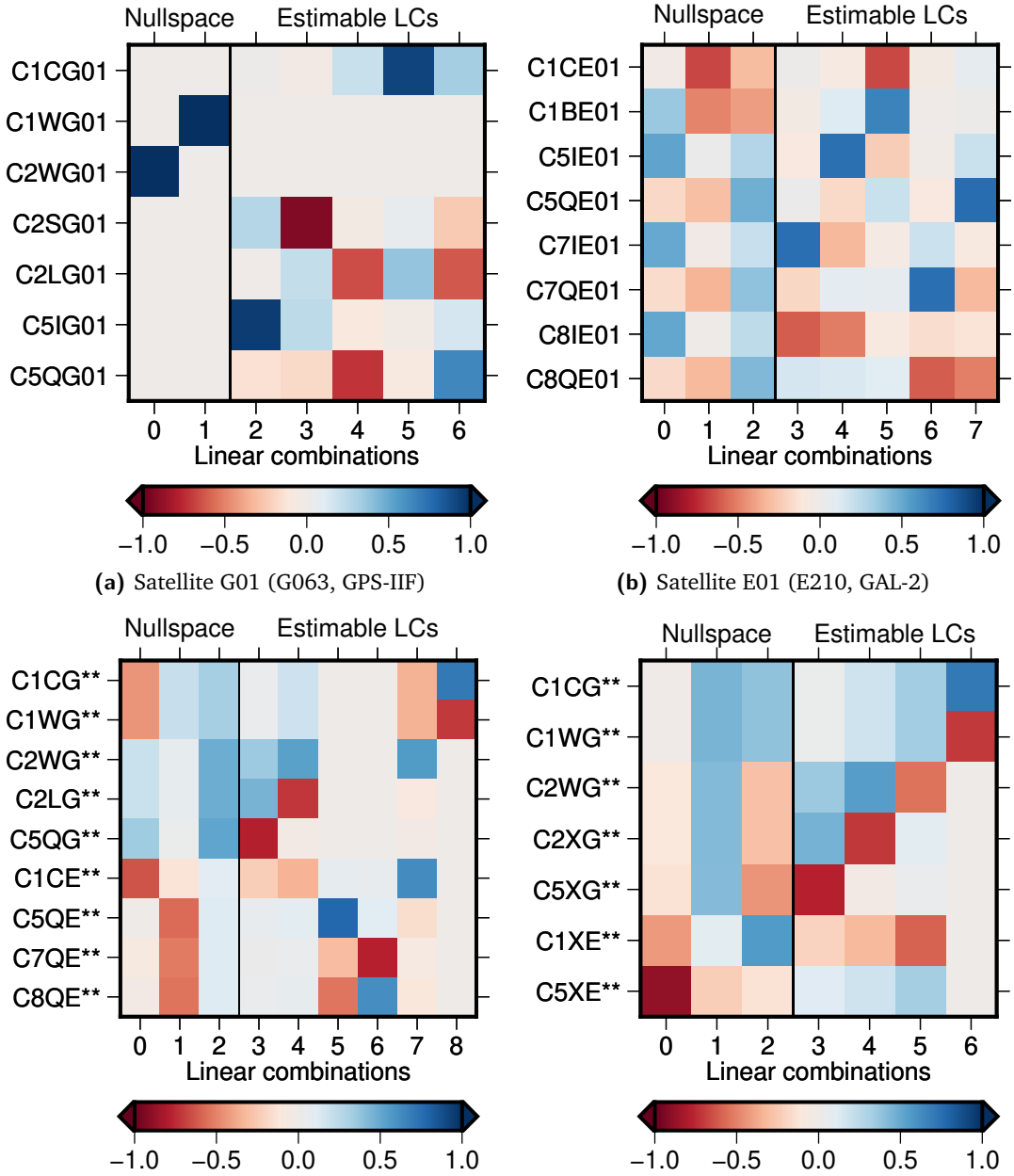

(a) Satellite G01 (G063, GPS-IIF)

(b) Satellite E01 (E210, GAL-2)

(c) Station DRAO (Penticton, Canada) with receiver SEPT POLARX5

(d) Station WTZ3 (Wettzell, Germany) with receiver JAVAD TRE_G3TH DELTA

Figure 6.12: Examples for eigenvector matrices ($\mathbf{Q}^s$, $\mathbf{Q}_r$) used to determine nullspace and estimable code bias linear combinations at each satellite and receiver in case of GPS and Galileo processing and no additional ionospheric information

where $\mathbf{b}[\mathrm{C}]^s$ are the observable-specific satellite code bias parameters, $\mathbf{x}_{\bar{\mathbf{b}}[\mathrm{C}]^s}$ are the parameters for the estimable satellite code bias linear combinations, and $\bar{\mathbf{Q}}^s$ is the slice of the eigenvector matrix $\mathbf{Q}$ that only contains the eigenvectors linked to nonzero eigenvalues in its columns. This implies that no parameters are set up for the linear combinations that cannot be estimated. The slice of the design matrix $\mathbf{D}_g$ containing the partial derivatives of the intermediate satellite code bias parameters $\mathbf{b}[\mathrm{C}]^s$ of an observation group g (see Section 5.3) with respect to the estimable satellite code bias linear combinations then follows as

$$\frac{\partial \mathbf{b}[\mathrm{C}]^s}{\partial \mathbf{x}_{\bar{\mathbf{b}}[\mathrm{C}]^s}} = \bar{\mathbf{Q}}^s \,. \tag{6.66}$$

The procedure is almost identical for the code biases local to a receiver. In this case, each satellite tracked by the receiver contributes a single time-independent group of pseudoobservations. The simplified observation equations

$$f[\mathrm{C}\nu a]_r^s = \delta_r + b[\mathrm{C}\nu a]_r + \frac{q}{\nu^2}\mathrm{STEC}_r^s \tag{6.67}$$

contain the receiver clock error δ_r and the observable-specific receiver code bias $b[\mathrm{C}\nu a]_r$. No bias type mapping is necessary here since each code observable has its own code bias at the receiver. Again, the STEC parameter is only set up in case no additional information about the ionosphere has been introduced. The STEC (if set up) and clock parameters are eliminated in the same way as detailed above and the normal equations are accumulated over all satellites. The accumulated normal equation matrix is eigenvalue decomposed and the columns of the eigenvector matrix linked to nonzero eigenvalues form a parameter transformation matrix $\bar{\mathbf{Q}}_r$ for the receiver. Two examples of eigenvector matrices for receivers observing GPS and Galileo are shown in Figure 6.12. The three linear combinations in the nullspace at each receiver can again be interpreted as a clock bias and two TEC biases, one for the GPS and one for Galileo constellation. The entries in the design matrix $\mathbf{D}_g$ that contain the partial derivatives of the intermediate receiver code bias parameters $\mathbf{b}[\mathrm{C}]_r$ with respect to the estimable receiver code bias linear combinations $\mathbf{x}_{\bar{\mathbf{b}}[\mathrm{C}]_r}$ are

$$\frac{\partial \mathbf{b}[\mathrm{C}]_r}{\partial \mathbf{x}_{\bar{\mathbf{b}}[\mathrm{C}]_r}} = \bar{\mathbf{Q}}_r \,. \tag{6.68}$$

The parameter transformation matrices $\bar{\mathbf{Q}}^s$ and $\bar{\mathbf{Q}}_r$ can be stored and used later to transform the estimated code bias linear combinations back to observable-specific code biases. With the local rank deficiencies resolved, there still remain global rank deficiencies, which are discussed in the next section.

6.5.3.2 Global rank deficiencies

Global rank deficiencies occur when both satellite and receiver code biases are estimated together. This issue is comparable to the combined estimation of satellite and receiver clock errors (see Section 6.3.2). However, in the case of code biases the situation is much more complex. Firstly, the signals transmitted by the satellites differ per constellation and sometimes within a constellation. Secondly, some receivers measure linear combinations of the transmitted signals. Lastly, the network of receivers might split into subnetworks that do not share any observation types to a specific constellation. For example, most Galileo-capable receivers observe either the pilot signals (e.g., C1C, C5Q, C7Q, C8Q) or a combination of data and pilot (e.g., C1X, C5X, C7X, C8X), but usually none of the receivers in the network observe both at the same time. All of this makes it exceptionally hard to define an analytical resolution to these rank deficiencies that is valid under all circumstances.

An alternative approach is to dynamically determine the linear combinations of code biases that are not estimable globally. Similar to the local case, a small, time-independent normal equation system that only contains the relevant parameters is set up. In this case, the pseudoobservation equations between a receiver and a satellite have the form

$$f[\mathrm{C}\nu a]_r^s = \delta_r - \delta^s + \bar{\mathbf{q}}[\mathrm{C}\nu a]_r \cdot \mathbf{x}_{\bar{\mathbf{b}}[\mathrm{C}]_r} + \mathbf{t}[\mathrm{C}\nu a]_r \cdot \left(\bar{\mathbf{Q}}^s \mathbf{x}_{\bar{\mathbf{b}}[\mathrm{C}]^s}\right) + \frac{q}{\nu^2}\mathrm{STEC}_r^s\,. \tag{6.69}$$

They contain the receiver and satellite clock errors (δ_r, δ^s), the estimable linear combinations of receiver and transmitter code biases ($\mathbf{x}_{\bar{\mathbf{b}}[\mathrm{C}]_r}$, $\mathbf{x}_{\bar{\mathbf{b}}[\mathrm{C}]^s}$), and the ionospheric STEC. Identical to the local case, the STEC term is discarded if additional information about the ionosphere has been introduced (see Section 6.4.2). The vector $\bar{\mathbf{q}}[\mathrm{C}\nu a]_r$ contains the transformation from the observable-specific receiver code bias to the estimable bias linear combinations and can be obtained from

$$\bar{\mathbf{Q}}_r = \begin{bmatrix} \bar{\mathbf{q}}[\mathrm{C}\nu a]_{r,1}^T \\ \vdots \\ \bar{\mathbf{q}}[\mathrm{C}\nu a]_{r,n}^T \end{bmatrix}\,. \tag{6.70}$$

The matrix $\bar{\mathbf{Q}}_r$ has been determined during the resolution of the local rank deficiencies at each receiver. Similarly, $\bar{\mathbf{Q}}^s$ comes from resolving the local rank deficiencies at each satellite. The transformation $\mathbf{t}[\mathrm{C}\nu a]_r$ from observed signal type to transmitted signal types is defined in (6.62).

The design matrices for one group of pseudoobservations between a receiver and transmitter are

$$\mathbf{A} = \begin{bmatrix} \frac{\partial \boldsymbol{f}[\mathrm{C}]_r^s}{\partial \delta_r} & \frac{\partial \boldsymbol{f}[\mathrm{C}]_r^s}{\partial \delta^s} & \frac{\partial \boldsymbol{f}[\mathrm{C}]_r^s}{\partial \mathbf{x}_{\bar{\mathbf{b}}[\mathrm{C}]_r}} & \frac{\partial \boldsymbol{f}[\mathrm{C}]_r^s}{\partial \mathbf{x}_{\bar{\mathbf{b}}[\mathrm{C}]^s}} \end{bmatrix} = \begin{bmatrix} \mathbf{1} & -\mathbf{1} & \bar{\mathbf{Q}}_r & \mathbf{T}_r \bar{\mathbf{Q}}^s \end{bmatrix} \tag{6.71}$$

and $\mathbf{B}$ as defined in (6.63) in case the STEC parameter has been set up. In (6.71), $\mathbf{1}$ is a vector populated by ones and $\mathbf{T}_r$ follows from (6.62). Equivalently to the local case, the ionospheric STEC parameter is eliminated on the observation equation level (see Section 4.2.2.1) if it has been set up (i.e., no additional information about the ionosphere has been introduced). Then, the normal equation matrices $\mathbf{N}_i = \mathbf{A}_i^T \mathbf{A}_i$ are formed for each observation group (i.e., receiver-satellite pair). All individual normal equation matrices are then accumulated. The accumulated normal equation matrix contains clock error and code bias parameters for each receiver and satellite.

In the next step, all clock error parameters are eliminated on the normal equation level (see Section 4.2.2.2). However, in the global case, a rank deficiency occurs when receiver and transmitter clock errors are set up together. It can be resolved by adding a zero-mean constraint over all receiver and satellite clock parameters to the normal equations in the form of an additional pseudoobservation equation (see Section 6.3.2). After the constraint has been added and all clock errors have been eliminated, only the code bias parameters remain in the normal equation matrix.

Finally, the eigenvalue decomposition $\mathbf{N} = \mathbf{Q}\boldsymbol{\Lambda}\mathbf{Q}^T$ of this normal equation matrix reveals its nullspace. In contrast to the local case, the inestimable parameters are not removed globally. Instead, the matrix $\tilde{\mathbf{Q}}$, which contains the eigenvectors from $\mathbf{Q}$ that are linked to zero eigenvalues in its columns, is used to define constraint equations

$$\mathbf{0} = \tilde{\mathbf{Q}} \mathbf{x}_{\bar{\mathbf{b}}[\mathrm{C}]} \,. \tag{6.72}$$

Here, $\mathbf{x}_{\bar{\mathbf{b}}[\mathrm{C}]}$ contains all estimable receiver and satellite code bias linear combinations as determined in Section 6.5.3.1. These constraint equations can be introduced into the full normal equation system, where they resolve the remaining global rank deficiencies of the code bias parameters.

As mentioned further above, after the code bias linear combinations have been estimated, they can be transformed back to observable-specific code biases via $\mathbf{b}[\mathrm{C}]^s = \bar{\mathbf{Q}}^s \mathbf{x}_{\bar{\mathbf{b}}[\mathrm{C}]^s}$ and $\mathbf{b}[\mathrm{C}]_r = \bar{\mathbf{Q}}_r \mathbf{x}_{\bar{\mathbf{b}}[\mathrm{C}]_r}$. At the receiver end, they include all observed code types (including composite signals). The satellite code biases, on the other hand, comprise the code types that are actually transmitted.

6.5.3.3 Determination of inestimable linear combinations in a separate step

Some of the bias linear combinations mentioned in Section 6.5.3.1 cannot be estimated without introducing additional information about the ionosphere. Section 6.4.2 describes several ways in which such information can be introduced. The approach of adding VTEC parameters directly to the main equation system has already been covered in the previous two sections. Another way is to estimate these bias linear combinations together with VTEC parameters in a separate least-squares adjustment while introducing all other parameters as known. This section briefly describes the process for this estimation.

The first step is to determine which bias linear combinations are inestimable without additional ionospheric information. This procedure is almost identical to the one described in Section 6.5.3.1, as the inestimable linear combinations are part of the local rank deficiencies at the receivers and satellites. However, the clock parameters in Equations (6.61) and (6.67) are not set up because the clock errors are introduced as known. Thus, there is no rank deficiency due to the estimation of the clock parameters and only the rank deficiencies due to the ionospheric influence remain. As described in Section 6.5.3.1, the STEC parameter is eliminated on the observation equation level before the normal equation matrix is accumulated and then eigenvalue decomposed.

In this case, however, the nullspaces of the eigenvector matrices are of interest. The matrices $\tilde{\mathbf{Q}}_s$ and $\tilde{\mathbf{Q}}_r$ contain the respective columns of $\mathbf{Q}_s$ and $\mathbf{Q}_r$ that are linked to zero eigenvalues. $\tilde{\mathbf{Q}}_s$ and $\tilde{\mathbf{Q}}_r$ can then be used to transform the signal-specific code bias parameters ($\mathbf{b}[\mathrm{C}]^s$, $\mathbf{b}[\mathrm{C}]_r$) to the linear combination parameters ($\mathbf{x}_{\tilde{\mathbf{b}}[\mathrm{C}]^s}$, $\mathbf{x}_{\tilde{\mathbf{b}}[\mathrm{C}]_r}$) as stated in (6.65). These parameters are then set up together with the VTEC parameters in the separate equation system. This equation system uses the full observation equations as described in Section 5.1. They also include all models and parametrizations described in Chapter 6, with all parameters except those mentioned above introduced as known. This implies that these parameters have already been estimated in a preceding iteration of the main least-squares adjustment.

The separate equation system suffers from global rank deficiencies since the bias linear combinations are estimated at receivers and satellites at the same time. These rank deficiencies can be resolved in a similar way as described in Section 6.5.3.2. In this case, the pseudoobservation equations from (6.69) do not contain the clock parameters and the STEC parameter. The former are omitted since the clock errors are introduced as known and the latter is not required because the separate equation system includes

additional ionospheric information in the form of TEC mapping functions. Therefore, Equation (6.69) becomes

$$f[\mathrm{C}\nu a]_r^s = \tilde{\mathbf{q}}[\mathrm{C}\nu a]_r \cdot \mathbf{x}_{\tilde{\mathbf{b}}[\mathrm{C}]_r} + \mathbf{t}[\mathrm{C}\nu a]_r \cdot \left(\tilde{\mathbf{Q}}^s \mathbf{x}_{\tilde{\mathbf{b}}[\mathrm{C}]^s}\right) , \tag{6.73}$$

where $\tilde{\mathbf{q}}[\mathrm{C}\nu a]_r$ is a part of $\tilde{\mathbf{Q}}_r$ as defined in (6.70). Following the procedure described in Section 6.5.3.2, the accumulated normal equation matrix from this system of equations is eigenvalue decomposed into $\mathbf{N} = \mathbf{Q}\mathbf{\Lambda}\mathbf{Q}^T$. The matrix $\tilde{\mathbf{Q}}$ containing the eigenvectors from $\mathbf{Q}$ that are linked to zero eigenvalues is then used to define constraint equations

$$\mathbf{0} = \tilde{\mathbf{Q}}\mathbf{x}_{\tilde{\mathbf{b}}[\mathrm{C}]} . \tag{6.74}$$

These are introduced into the separate equation system to resolve the global rank deficiencies.

The separate equation system can now be solved via least-squares adjustment. The estimates for the bias linear combinations ($\mathbf{x}_{\tilde{\mathbf{b}}[\mathrm{C}]^s}$, $\mathbf{x}_{\tilde{\mathbf{b}}[\mathrm{C}]_r}$) can be transformed back to (partial) observable-specific code biases ($\tilde{\mathbf{b}}[\mathrm{C}]^s$, $\tilde{\mathbf{b}}[\mathrm{C}]_r$) using $\tilde{\mathbf{Q}}_s$ and $\tilde{\mathbf{Q}}_r$. They are subsequently introduced as known corrections into the main equation system, where the set of bias linear combinations that does not require additional ionospheric information is estimated. As a result, the full code biases $\mathbf{b}[\mathrm{C}]^s = \tilde{\mathbf{b}}[\mathrm{C}]^s + \bar{\mathbf{b}}[\mathrm{C}]^s$ and $\mathbf{b}[\mathrm{C}]_r = \tilde{\mathbf{b}}[\mathrm{C}]_r + \bar{\mathbf{b}}[\mathrm{C}]_r$ are not biased by the ionosphere anymore.

6.6 Ambiguities and phase biases

The introduction of Section 6.5 briefly describes the concept of signal biases and code biases in particular. Phase biases are the unknown hardware delays that affect phase measurements (Håkansson et al., 2017). These measurements also contain an unknown phase ambiguity, which is an integer number of full phase cycles (e.g., Hauschild, 2017a). The presence of phase biases, specifically their fractional cycle part, prohibits direct access to these ambiguities. Several methods have been developed to handle phase biases in undifferenced GNSS processing in order to facilitate integer ambiguity resolution (e.g., Ge et al., 2008; Laurichesse et al., 2009; Collins et al., 2010; Geng et al., 2010; Loyer et al., 2012; Shi and Gao, 2014).

The connection between phase biases and ambiguities can be described using a simple ambiguity observation equation

$$n[\mathrm{L}\nu a]_{r,i}^s = b[\mathrm{L}\nu a]_r + b[\mathrm{L}\nu]^s + N[\mathrm{L}\nu a]_{r,i}^s , \tag{6.75}$$

where $n[\mathrm{L}\nu a]^s_{r,i}$ is the biased ambiguity for a phase observation with frequency ν and signal attribute a between receiver r and satellite s. It consists of a signal-specific receiver phase bias $b[\mathrm{L}\nu a]_r$ and a frequency-specific satellite phase bias $b[\mathrm{L}\nu]^s$ as well as the actual ambiguity $N[\mathrm{L}\nu a]^s_{r,i}$. The relation between the phase biases in Equation (6.75) and the intermediate signal bias parameters described in Section 5.3 is discussed in Section 6.6.1.3. In contrast to the GNSS observation equation (5.1), where the signal biases are expressed in meters, all components in (6.75) are expressed in cycles.

The index i in (6.75) represents a track or arc. This is the time period where a receiver continuously tracks a passing satellite and keeps track of the changing phase cycles. As a result, the unknown phase ambiguity is constant over a track and can thus be parameterized as a constant value (e.g., Hofmann-Wellenhof et al., 2008). The track identifier i distinguishes between multiple tracks involving the same receiver and satellite within the processing period. For example, GPS satellites usually pass over the same location on Earth twice per day.

Section 6.6.1 details how phase biases and ambiguities can be separated by an appropriate parametrization. It also discusses how to handle issues such as time-variable phase biases and GLONASS using FDMA instead of CDMA. Finally, Section 6.6.2 describes how the ambiguity parameters, which are estimated as float values in the least-squares adjustment, can be resolved to actual integer values.

6.6.1 Parametrization

The classic approach to separate ambiguities and phase biases is to form double differences of the observations (e.g., Hofmann-Wellenhof et al., 2008; Hauschild, 2017b). This eliminates the phase biases from the observation equations and parameters can be directly set up for the double-differenced ambiguities. However, when processing raw observations, for example with the approach described in this thesis, forming observation differences is not an option.

Another approach operates in the parameter space instead of the observation space (Reckeweg, 2020). Here, parameters are set up directly for all biased ambiguities. These parameters are then constrained by applying constraint equations based on double differences of the parameters. Such a constraint equation states that the double difference of four specific biased ambiguity parameters must result in an integer value. One drawback of this approach is that the ambiguity parameters remain in the equation system, which can become problematic in terms of computational performance when processing large systems.

The approach chosen in this thesis is to find a parametrization that directly separates phase biases and ambiguities. The idea is that once the ambiguities have been resolved to integer values, they become known corrections and their corresponding parameters do not have to be set up anymore. Thus, only phase bias parameters and possibly a few unresolved ambiguity parameters remain in the normal equation system. In combination with the processing scheme described in Section 5.9.2, this approach keeps the computational requirements on a manageable level even for very large networks such as the one used for the reprocessing campaign conducted within the context of this thesis.

6.6.1.1 Algorithm for phase bias and ambiguity parametrization

The algorithm to find an appropriate parametrization for phase biases and ambiguities relies on the following assumptions.

1. Receiver and satellite phase biases are constant over the processing period (e.g., one day). The only exception to this are the L5 phase biases of GPS-IIF satellites, which show an additional temporal variation (see Section 6.6.1.4).
2. Based on assumption 1, ambiguities of multiple tracks between the same receiver and satellite must only differ by an integer number of cycles. For example, ground-based receivers typically observe GPS satellites twice per day. Tracks might also be split during observation preprocessing in case of cycle slips (see Section 7).
3. There is only one carrier phase per frequency at a satellite. Thus, all signals transmitted on this frequency (e.g., L1C, L1W, L1S, and L1L in case of a GPS-IIIA satellite) share a common phase bias.
4. Different phase signals are processed independently at the receiver, for example in separate hardware or software channels. In addition, it is uncertain if a phase alignment, such as required by the RINEX format (Romero, 2020), has been performed (correctly) within the receiver or conversion software. Therefore, each phase observation type has an independent receiver phase bias.

Algorithm 6.1 describes how the phase bias and ambiguity parameters are defined. This algorithm is performed independently for each frequency ν and satellite constellation. The input is a sequence of biased ambiguities A containing one or more (if the receiver tracks multiple phase attributes a on the same frequency) biased ambiguities $n[\mathrm{L}\nu a]^s_{r,i}$ for each track i between one receiver r and one satellite s. The algorithm sets up a type-specific receiver phase bias parameter $b[\mathrm{L}\nu a]_r$ or frequency-specific satellite phase bias parameter $b[\mathrm{L}\nu]^s$ the first time it encounters a biased ambiguity involving that receiver or satellite. Only for the very first biased ambiguity both are set up, but this reference

satellite phase bias parameter is removed at the end of the algorithm. At this point, no ambiguity parameter $N[\mathrm{L}\nu a]^s_{r,i}$ is set up for the biased ambiguity, as it is required purely for the definition of the phase bias. An ambiguity parameter $N[\mathrm{L}\nu a]^s_{r,i}$ is only assigned to a biased ambiguity once the phase biases at both the receiver and satellite corresponding to this ambiguity have been defined. Finally, the first satellite phase bias parameter that was set up is removed (i.e., implicitly set to zero) to solve the rank deficiency that occurs when receiver and satellite phase biases are estimated together. This means the satellite s_0 acts as a reference for the satellite phase biases of frequency ν and all other phase biases are defined relative to the reference bias. An alternative to removing the phase bias parameter would be to add a zero-mean constraint over all satellite phase biases of this frequency.

Data: Sequence of biased ambiguities (A) for one frequency ν
Result: Sets of phase biases (B_r, B^s) and ambiguities (N) for this frequency

```
1  s_0 ← null                                              /* reference satellite */
2  while A ≠ 0 do
3      restart ← false
4      foreach n[Lνa]^s_{r,i} ∈ A do
5          if b[Lνa]_r ∉ B_r and b[Lν]^s ∉ B^s then
6              if s_0 is null then
7                  s_0 ← s                                 /* set reference satellite */
8              else
9                  continue      /* skip n[Lνa]^s_{r,i} for now and try again later */
10         if b[Lνa]_r ∈ B_r and b[Lν]^s ∈ B^s then
11             add N[Lνa]^s_{r,i} to N                     /* set up ambiguity */
12         if b[Lνa]_r ∉ B_r then
13             add b[Lνa]_r to B_r                 /* set up receiver phase bias */
14             restart ← true
15         if b[Lν]^s ∉ B^s then
16             add b[Lν]^s to B^s                 /* set up satellite phase bias */
17             restart ← true
18         remove n[Lνa]^s_{r,i} from A
19         if restart = true then
20             break           /* new phase bias defined → restart search */
21 remove b[Lν]^{s_0} from B^s   /* do not set up bias for reference satellite */
```

Algorithm 6.1: Definition of phase biases and ambiguities for one frequency

The workings of the algorithm are best shown based on a simple example. It involves three satellites (G01, G02, G03) and three receivers (A, B, C). All ambiguities have the same signal type (e.g., L1C), which is omitted for the sake of readability. The sequence

Table 6.8: Ambiguity observation equations for example 1 using the sequence of biased ambiguities $A = \{n_{\mathrm{A}}^{\mathrm{G01}}, n_{\mathrm{A}}^{\mathrm{G02}}, n_{\mathrm{A}}^{\mathrm{G03}}, n_{\mathrm{B}}^{\mathrm{G01}}, n_{\mathrm{B}}^{\mathrm{G02}}, n_{\mathrm{B}}^{\mathrm{G03}}, n_{\mathrm{C}}^{\mathrm{G01}}, n_{\mathrm{C}}^{\mathrm{G02}}, n_{\mathrm{C}}^{\mathrm{G03}}\}$

	Receiver A	Receiver B	Receiver C
G01	$n_{\mathrm{A}}^{\mathrm{G01}} = b_{\mathrm{A}} + \cancel{b^{\mathrm{G01}}}$	$n_{\mathrm{B}}^{\mathrm{G01}} = b_{\mathrm{B}} + \cancel{b^{\mathrm{G01}}}$	$n_{\mathrm{C}}^{\mathrm{G01}} = b_{\mathrm{C}} + \cancel{b^{\mathrm{G01}}}$
G02	$n_{\mathrm{A}}^{\mathrm{G02}} = b_{\mathrm{A}} + b^{\mathrm{G02}}$	$n_{\mathrm{B}}^{\mathrm{G02}} = b_{\mathrm{B}} + b^{\mathrm{G02}} + N_{\mathrm{B}}^{\mathrm{G02}}$	$n_{\mathrm{C}}^{\mathrm{G02}} = b_{\mathrm{C}} + b^{\mathrm{G02}} + N_{\mathrm{C}}^{\mathrm{G02}}$
G03	$n_{\mathrm{A}}^{\mathrm{G03}} = b_{\mathrm{A}} + b^{\mathrm{G03}}$	$n_{\mathrm{B}}^{\mathrm{G03}} = b_{\mathrm{B}} + b^{\mathrm{G03}} + N_{\mathrm{B}}^{\mathrm{G03}}$	$n_{\mathrm{C}}^{\mathrm{G03}} = b_{\mathrm{C}} + b^{\mathrm{G03}} + N_{\mathrm{C}}^{\mathrm{G03}}$

Table 6.9: Ambiguity observation equations for example 2 using the sequence of biased ambiguities $A = \{n_{\mathrm{B}}^{\mathrm{G03}}, n_{\mathrm{A}}^{\mathrm{G02}}, n_{\mathrm{A}}^{\mathrm{G01}}, n_{\mathrm{C}}^{\mathrm{G01}}, n_{\mathrm{B}}^{\mathrm{G02}}, n_{\mathrm{A}}^{\mathrm{G03}}, n_{\mathrm{C}}^{\mathrm{G03}}, n_{\mathrm{C}}^{\mathrm{G02}}, n_{\mathrm{B}}^{\mathrm{G01}}\}$

	Receiver A	Receiver B	Receiver C
G01	$n_{\mathrm{A}}^{\mathrm{G01}} = b_{\mathrm{A}} + b^{\mathrm{G01}}$	$n_{\mathrm{B}}^{\mathrm{G01}} = b_{\mathrm{B}} + b^{\mathrm{G01}} + N_{\mathrm{B}}^{\mathrm{G01}}$	$n_{\mathrm{C}}^{\mathrm{G01}} = b_{\mathrm{C}} + b^{\mathrm{G01}}$
G02	$n_{\mathrm{A}}^{\mathrm{G02}} = b_{\mathrm{A}} + b^{\mathrm{G02}}$	$n_{\mathrm{B}}^{\mathrm{G02}} = b_{\mathrm{B}} + b^{\mathrm{G02}}$	$n_{\mathrm{C}}^{\mathrm{G02}} = b_{\mathrm{C}} + b^{\mathrm{G02}} + N_{\mathrm{C}}^{\mathrm{G02}}$
G03	$n_{\mathrm{A}}^{\mathrm{G03}} = b_{\mathrm{A}} + \cancel{b^{\mathrm{G03}}} + N_{\mathrm{A}}^{\mathrm{G03}}$	$n_{\mathrm{B}}^{\mathrm{G03}} = b_{\mathrm{B}} + \cancel{b^{\mathrm{G03}}}$	$n_{\mathrm{C}}^{\mathrm{G03}} = b_{\mathrm{C}} + \cancel{b^{\mathrm{G03}}} + N_{\mathrm{C}}^{\mathrm{G03}}$

of biased ambiguities $A = \left\{n_{\mathrm{A}}^{\mathrm{G01}}, n_{\mathrm{A}}^{\mathrm{G02}}, n_{\mathrm{A}}^{\mathrm{G03}}, n_{\mathrm{B}}^{\mathrm{G01}}, n_{\mathrm{B}}^{\mathrm{G02}}, n_{\mathrm{B}}^{\mathrm{G03}}, n_{\mathrm{C}}^{\mathrm{G01}}, n_{\mathrm{C}}^{\mathrm{G02}}, n_{\mathrm{C}}^{\mathrm{G03}}\right\}$ serves as input to the algorithm. Table 6.8 shows the ambiguity observation equations that the algorithm sets up for each of these biased ambiguities. The first four biased ambiguities ($n_{\mathrm{A}}^{\mathrm{G01}}, n_{\mathrm{A}}^{\mathrm{G02}}, n_{\mathrm{A}}^{\mathrm{G03}}, n_{\mathrm{B}}^{\mathrm{G01}}$) are used purely to define the receiver phase biases b_{A} and b_{B} and the satellite phase biases b^{G01}, b^{G02}, and b^{G03}. Then, $n_{\mathrm{B}}^{\mathrm{G02}}$ and $n_{\mathrm{B}}^{\mathrm{G03}}$ are assigned ambiguities ($N_{\mathrm{B}}^{\mathrm{G02}}, N_{\mathrm{B}}^{\mathrm{G03}}$) since the phase biases for the involved receiver and satellites have already been defined. Next, $n_{\mathrm{C}}^{\mathrm{G01}}$ defines the receiver phase bias b_{C}. Finally, ambiguities are again assigned to $n_{\mathrm{C}}^{\mathrm{G02}}$ and $n_{\mathrm{C}}^{\mathrm{G03}}$. The first biased ambiguity in the sequence involves satellite G01, which becomes the reference satellite and thus the phase bias b^{G01} is removed at the end of the algorithm.

In practice, the estimation becomes more robust when the phase biases are defined by the most precise biased ambiguities. Assuming that longer tracks can be determined more precisely, one option is to sort the biased ambiguities in A by descending track length. For instance, the sequence of biased ambiguities from the first example sorted by track length could be $A = \left\{n_{\mathrm{B}}^{\mathrm{G03}}, n_{\mathrm{A}}^{\mathrm{G02}}, n_{\mathrm{A}}^{\mathrm{G01}}, n_{\mathrm{C}}^{\mathrm{G01}}, n_{\mathrm{B}}^{\mathrm{G02}}, n_{\mathrm{A}}^{\mathrm{G03}}, n_{\mathrm{C}}^{\mathrm{G03}}, n_{\mathrm{C}}^{\mathrm{G02}}, n_{\mathrm{B}}^{\mathrm{G01}}\right\}$. The resulting ambiguity observation equations are shown in Table 6.9. Since the first biased ambiguity now involves satellite G03, the satellite phase bias parameter b^{G03} is removed at the end. The set of ambiguities N also differs compared to the first example because different biased ambiguities have been used to define the receiver and satellite phase biases.

6.6.1.2 Reduction of ambiguity parameters

Once the algorithm has finished, the number of ambiguity parameters in N can usually be reduced. Assumptions 1, 3, and 4 listed above imply that two or more ambiguities

on the same track and frequency that only differ in their attribute (e.g., $N[\mathrm{L1C}]^{\mathrm{G01}}_{\mathrm{A},1}$ and $N[\mathrm{L1W}]^{\mathrm{G01}}_{\mathrm{A},1}$) must differ by an integer number of cycles. This integer difference can be determined in advance by forming observation differences

$$\begin{aligned}\Delta n(t) &= \frac{\nu}{c}\Big(\operatorname{obs}[\mathrm{L}\nu a_2]^s_r(t) - \operatorname{obs}[\mathrm{L}\nu a_1]^s_r(t)\Big) \\ &= b[\mathrm{L}\nu a_2]_r - b[\mathrm{L}\nu a_1]_r + N[\mathrm{L}\nu a_2]^s_{r,i} - N[\mathrm{L}\nu a_1]^s_{r,i} + \epsilon(t)\end{aligned} \tag{6.76}$$

for all epochs of all tracks i involving the receiver r, satellites of one constellation, and two signal types $[\mathrm{L}\nu a_1]$ and $[\mathrm{L}\nu a_2]$ on the same frequency ν. Only the difference between the receiver biases and ambiguities as well as the combined observation noise ϵ remain since all other components cancel. The receiver bias difference $\Delta b = b[\mathrm{L}\nu a_2]_r - b[\mathrm{L}\nu a_1]_r$ can be approximated as the median of all float components

$$\Delta\bar{n}(t) = \Delta n(t) - \operatorname{round}(\Delta n(t)) \tag{6.77}$$

of these differential ambiguity values. Finally, the observations of type $[\mathrm{L}\nu a_2]$ can be corrected by the difference in ambiguities to those of the reference type $[\mathrm{L}\nu a_1]$ via

$$\operatorname{obs}[\mathrm{L}\nu a_2]^s_r(t) := \operatorname{obs}[\mathrm{L}\nu a_2]^s_r(t) - \frac{c}{\nu}\operatorname{round}(\Delta n(t) - \Delta b)\,. \tag{6.78}$$

This process is performed independently for each receiver, where it involves different combinations of two signals of the same frequency and constellation. Thus, it is possible to set up a single ambiguity parameter $N[\mathrm{L}\nu]^s_{r,i}$ per frequency and track that is independent of the signal attribute. This can significantly reduce the number of ambiguities in the system, especially in modern multi-GNSS environments, where multiple signals per frequency become more and more common.

6.6.1.3 Design matrix entries

The design matrix $\mathbf{D}_g$ contains the partial derivatives of the intermediate parameters of an observation group g (see Section 5.3) with respect to the final parameters. Once the algorithm described in Section 6.6.1.1 has determined which phase bias and ambiguity parameters have to be set up, the composition of this matrix is straightforward. The intermediate parameters include a receiver phase bias for each observed phase type $[\mathrm{L}\nu a]$ and a satellite phase bias per transmitted frequency $[\mathrm{L}\nu]$. Therefore, the partial derivatives of the intermediate phase bias parameters with respect to the final phase bias parameters are either 1 if they are to be estimated in meters or $\lambda[\mathrm{L}\nu] = \frac{c}{\nu}$ in case of cycles. As mentioned in Section 6.6.1.1, for each frequency one satellite acts as a reference and no final parameter is set up for the respective satellite phase bias.

The intermediate satellite phase bias parameter represents the component of the observation equations that is the same for each phase observation on one frequency. Following the reduction described in Section 6.6.1.2, only a single ambiguity parameter has to be set up per frequency and track. As both definitions match, the ambiguity parameters can be determined from the intermediate satellite phase bias parameters. The partial derivative of the intermediate satellite phase bias parameter with respect to the ambiguity parameter is $\lambda[\mathrm{L}\nu] = \frac{c}{\nu}$ since ambiguities are set up in cycles.

The order of the ambiguity parameters in the normal equation matrix is important for the computational performance. Section 5.6.2 mentions that ordering these parameters by the mean time of the corresponding track leads to a roughly block-banded structure in the off-diagonal block between epoch and ambiguity parameters. Splitting the off-diagonal block into subblocks and only storing the densely populated subblocks of the band significantly reduces the memory requirements of this part of the normal equation matrix.

6.6.1.4 Time-variable phase biases

Montenbruck et al. (2012) found that GPS-IIF satellites are affected by time-variable phase biases on the L5 frequency. This variation seems to originate from thermal effects within the satellite. Its amplitude mainly depends on the angle of the Sun with respect to the orbital plane and can reach up to approximately 20 cm. The total satellite L5 phase bias

$$\bar{b}[\mathrm{L5}]^s(t) = b[\mathrm{L5}]^s + \Delta b[\mathrm{L5}]^s(t) \tag{6.79}$$

can be split into the constant part $b[\mathrm{L5}]^s$, which is parameterized as described in Sections 6.6.1.1 to 6.6.1.3, and the time-variable part $\Delta b[\mathrm{L5}]^s(t)$. This latter part can be represented by a linear combination

$$\Delta b[\mathrm{L5}]^s(t) = \sum_i x_{b[\mathrm{L5}]^s,i}\, \psi_i(t)\,, \tag{6.80}$$

where $\psi_i(t)$ are basis functions in time and $x_{b[\mathrm{L5}]^s,i}$ are the corresponding coefficients that can be estimated. For example, the time-variable behavior of the L5 phase bias can be parameterized as a cubic spline with hourly knots. Figure 6.13 displays estimated time-variable L5 phase biases for GPS-IIF and GPS-IIIA satellites. While the former show large variations in agreement with Montenbruck et al. (2012), the latter do not seem to be affected by these variations. This indicates that the thermal issue does not occur in

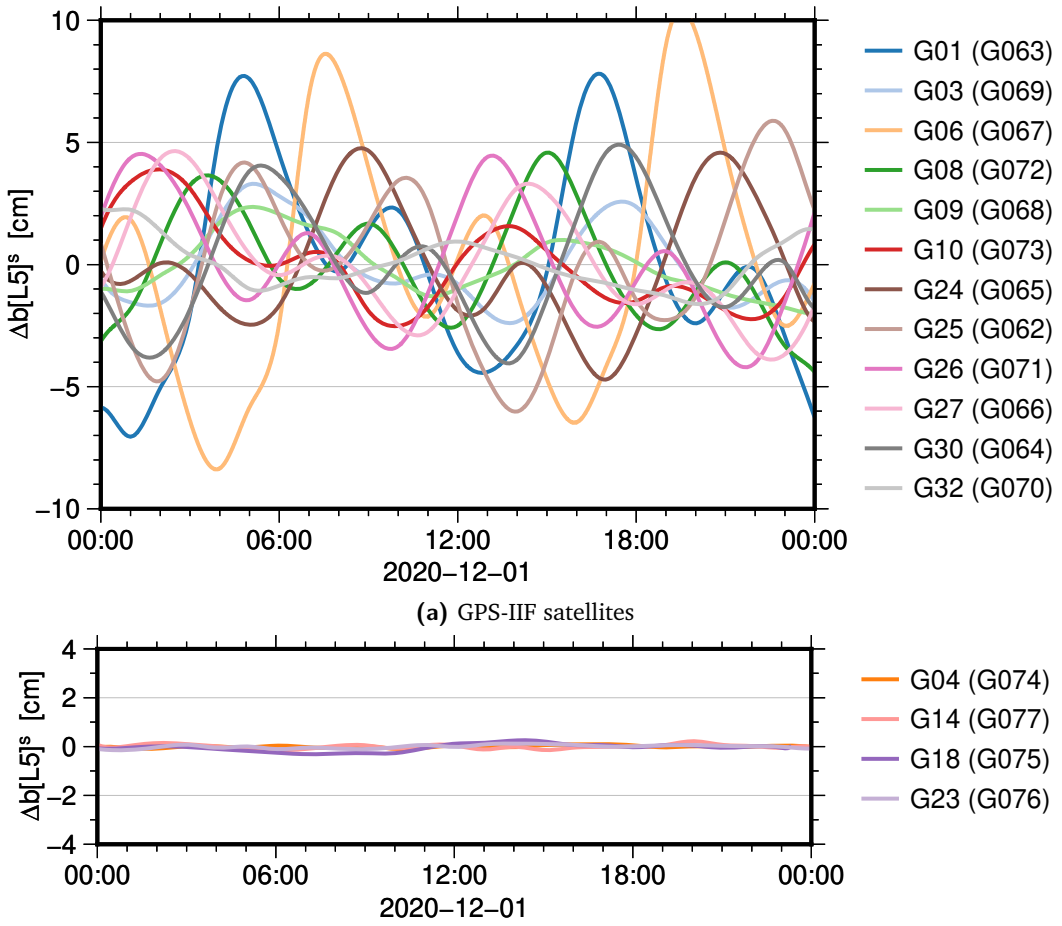

(a) GPS-IIF satellites

(b) GPS-IIIA satellites

Figure 6.13: Example of L5 phase biases for GPS-IIF and GPS-IIIA satellites parameterized as cubic splines with hourly knots. Y-axis limits differ, but scale is identical

the GPS-IIIA satellites, which are newer and built by a different manufacturer than the GPS-IIF satellites.

6.6.1.5 GLONASS

As mentioned in Sections 2.2 and 6.5.2, GLONASS applies FDMA to distinguish between satellites (e.g., Revnivykh et al., 2017). Therefore, the receiver phase biases can differ depending on the frequency number (i.e., per two satellites transmitting on the same frequency). This means that the algorithm described in Section 6.6.1.1 has to be performed separately for each frequency number. Another interpretation of this is that the GLONASS satellite constellation splits into subconstellations with one or two satellites each and the algorithm is performed independently per subconstellation. As one satellite phase bias parameter is removed per frequency and subconstellation, the

number of estimated GLONASS satellite phase bias parameters is much lower than that of other constellations. On the other hand, the number of receiver phase bias parameters is much higher because one phase bias parameter per frequency number and subconstellation has to be set up at each receiver. This also implies that fewer ambiguity parameters can be set up for GLONASS compared to other GNSS constellations.

Some studies (e.g., Sleewaegen et al., 2012; Wanninger, 2012; Al-Shaery et al., 2013; Banville et al., 2013; Banville, 2016) suggest a linear relationship between the receiver phase biases on different frequency numbers. This would reduce the number of GLONASS receiver phase bias parameters significantly from one per frequency number to two (i.e., constant and trend components). However, such a parametrization was not used in the reprocessing conducted within the context of this thesis and thus is not discussed further here.

6.6.2 Ambiguity resolution

Teunissen (2017) provides a comprehensive overview of the concept of integer ambiguity resolution. The process used in this thesis was first described in Strasser et al. (2019). It is based on the least-squares ambiguity decorrelation adjustment (LAMBDA) method (Teunissen, 1995) and includes modifications of the MLAMBDA algorithm presented in Chang et al. (2005) and Al Borno et al. (2014), which increase the computational efficiency. While these methods perform well for small problems with a few hundred ambiguities (Li and Teunissen, 2011), a GNSS processing involving hundreds of stations and multiple satellite constellations leads to tens of thousands of ambiguities. Unfortunately, the complexity of the ambiguity search process and, consequently, the required computational effort scale exponentially with the dimension of the ambiguity vector (Verhagen et al., 2012). As outlined in Strasser et al. (2019), this issue is circumvented by splitting the search process into smaller problems that can be solved more efficiently. This approach can be broadly assigned to what Teunissen et al. (2021) defines as vectorial integer bootstrapping methods. Massarweh et al. (2021) compares the approach used in this thesis to a simple vectorial integer bootstrapping implementation and a classic (scalar) integer bootstrapping algorithm in terms of methodology and resulting orbit quality from a small GNSS processing.

6.6.2.1 Preparation for the search process

Several steps are performed in preparation of integer ambiguity resolution. First, the full normal equation system is set up. All parameters except for the ambiguity parameters are

then eliminated on the normal equation level (see Section 4.2.2.2). Next, the resulting normal equation matrix is Cholesky decomposed (e.g., Koch, 1999) into

$$\mathbf{N} = \mathbf{W}^T\mathbf{W}\,, \tag{6.81}$$

where $\mathbf{W}$ is a regular upper triangular matrix. During this decomposition, a pivoting as described in the MLAMBDA method (Chang et al., 2005) is performed to order the ambiguity parameters by their formal accuracy. This pivoting increases the performance of subsequent steps in the ambiguity resolution process. By inverting the Cholesky factor $\mathbf{W}$, the covariance matrix

$$\mathbf{\Sigma} = \mathbf{W}^{-1}\mathbf{W}^{-T} = \mathbf{L}^T\mathbf{D}\mathbf{L} \tag{6.82}$$

can be obtained. As Equation (6.82) shows, it is possible to transform this decomposition of the covariance matrix into a $\mathbf{L}^T\mathbf{D}\mathbf{L}$ decomposition (e.g. Golub and Van Loan, 2013). Here, $\mathbf{L}$ is a lower triangular matrix and $\mathbf{D}$ is a diagonal matrix. In the next step, these matrices are used to decorrelate the ambiguities as described in Al Borno et al. (2014), where this process is called reduction. The purpose of this reduction is to increase the efficiency of the subsequent integer least-squares (ILS) search process by transforming the original search problem to a new one with more favorable conditions (Chang et al., 2005). This is achieved by so-called Z-transformations, which maintain the integer nature of the ambiguities.

6.6.2.2 Blocked search algorithm

After these preparatory steps, the actual search process begins. The blocked search algorithm applied in this thesis has been broadly described in Strasser et al. (2019) and Massarweh et al. (2021). For the purpose of completeness, this section includes a more in-depth description of the algorithm including some additional aspects not discussed in the listed references. Algorithm 6.2 describes the logic behind the process and Figure 6.14 shows a schematic visualization based on an example.

The basic idea of the algorithm is to move a search window over the full ambiguity vector and resolve it block by block. The reason for this is that performing an ILS search over the full vector is computationally infeasible in case of a large number of ambiguities. It starts with the most accurate ambiguities, which have the highest fixing probability and are located at the end of the vector. A block size of 200 has proven to be a good trade-off between performance and robustness of the overall solution. Once an ILS search has been completed for a block, the remaining unresolved ambiguities in the vector are conditioned based on the ILS solution of this block. Then, the window moves

Data: Vector of float ambiguities $\mathbf{x}_{\text{float}}$ (sorted from least to most accurate), matrices $\mathbf{L}^T$ and $\mathbf{D}$, $\sigma_{\text{threshold}}$, *searchBlockSize*, *maxSearchSteps*, and *incompleteAction*
Result: Vector of integer ambiguities $\mathbf{x}_{\text{int}}$ resolved up to *indexResolved*

$\mathbf{d} \leftarrow \operatorname{diag} \mathbf{D}$
dimension $\leftarrow \dim \mathbf{x}_{\text{Float}}$
$\mathbf{x}_{\text{int}} \leftarrow \mathbf{0}$ of *dimension*
minIndex $\leftarrow$ index of first ambiguity in $\mathbf{x}_{\text{float}}$ with $\sigma < \sigma_{\text{threshold}}$
defaultBlockSize $\leftarrow \min($*dimension* $-$ *minIndex*, *searchBlockSize*$)$
blockSize $\leftarrow$ *defaultBlockSize*
blockStart $\leftarrow$ *dimension* $-$ *blockSize*
prevBlockStart $\leftarrow$ *dimension*
indexResolved $\leftarrow$ *dimension*
while *true* **do**
    $\bar{\mathbf{x}} \leftarrow \mathbf{x}_{\text{float}} - \mathbf{x}_{\text{int}}$
    blockEnd $\leftarrow$ *blockStart* $+$ *blockSize*
    for $i \leftarrow$ *dimension* $- 1$ **to** *blockEnd* **by** -1 **do**
        $\bar{\mathbf{x}}[0:i] \leftarrow \bar{\mathbf{x}}[0:i] - \bar{x}_i \, \mathbf{L}^T[0:i, i]$ `/* conditioning */`
    completed, $\Delta\mathbf{x}_{\text{int}} \leftarrow$ ILS(*maxSearchSteps*, $\bar{\mathbf{x}}$[*blockStart* : *blockEnd*], $\mathbf{L}^T$[*blockStart* : *blockEnd*, *blockStart* : *blockEnd*], $\mathbf{d}$[*blockStart* : *blockEnd*])
    $\mathbf{x}_{\text{int}}$[*blockStart* : *blockEnd*] $\leftarrow \mathbf{x}_{\text{int}}$[*blockStart* : *blockEnd*] $+ \Delta\mathbf{x}_{\text{int}}$
    indexResolved $\leftarrow$ *blockStart*
    if *completed* $=$ *false* **then**
        switch *incompleteAction* **do**
            case *STOP* **do**
                indexResolved $\leftarrow$ *blockEnd*
                break
            case *SHRINK_BLOCK_SIZE* **do**
                defaultBlockSize $\leftarrow$ (*defaultBlockSize* $+ 1) \mathbin{/\!/} 2$
                blockStart $\leftarrow \min($*prevBlockStart*, *blockStart* $+$ (*blockSize* $+ 1) \mathbin{/\!/} 2)$
                blockSize $\leftarrow$ *blockSize* $-$ (*blockSize* $+ 1) \mathbin{/\!/} 2$
                continue `/* try again with half block size */`
            `/* default: use best solution found after maxSearchSteps */`
    if $\|\Delta\mathbf{x}_{int}$[*prevBlockStart* $-$ *blockStart* $:]\| > 0$ **then** `/* if overlap differs */`
        prevBlockStart $\leftarrow$ *blockStart* $+$ *blockSize*
        blockSize $\leftarrow$ *blockSize* $+ \min($*defaultBlockSize* $\mathbin{/\!/} 2$, *dimension* $-$ *prevBlockStart*$)$
        continue `/* try again with joint block */`
    if *blockStart* $=$ *minIndex* **then** `/* if accuracy threshold is reached */`
        break
    prevBlockStart $\leftarrow$ *blockStart*
    blockSize $\leftarrow$ *defaultBlockSize*
    blockStart $\leftarrow$ $\max($*blockStart*, *minIndex* $+$ *defaultBlockSize* $\mathbin{/\!/} 2) -$ *defaultBlockSize* $\mathbin{/\!/} 2$

Algorithm 6.2: Blocked search algorithm. Notation definition: x_i is the ith element of vector $\mathbf{x}$, $\mathbf{x}[i:j]$ is the slice of vector $\mathbf{x}$ from index i to j (exclusive), $\mathbf{A}[i:j, k:l]$ is the slice of matrix $\mathbf{A}$ from row index i to j and column index k to l (exclusive in both cases), omitted slice indices (e.g., $[:]$) imply from start and/or until end, and $\mathbin{/\!/}$ is an integer division

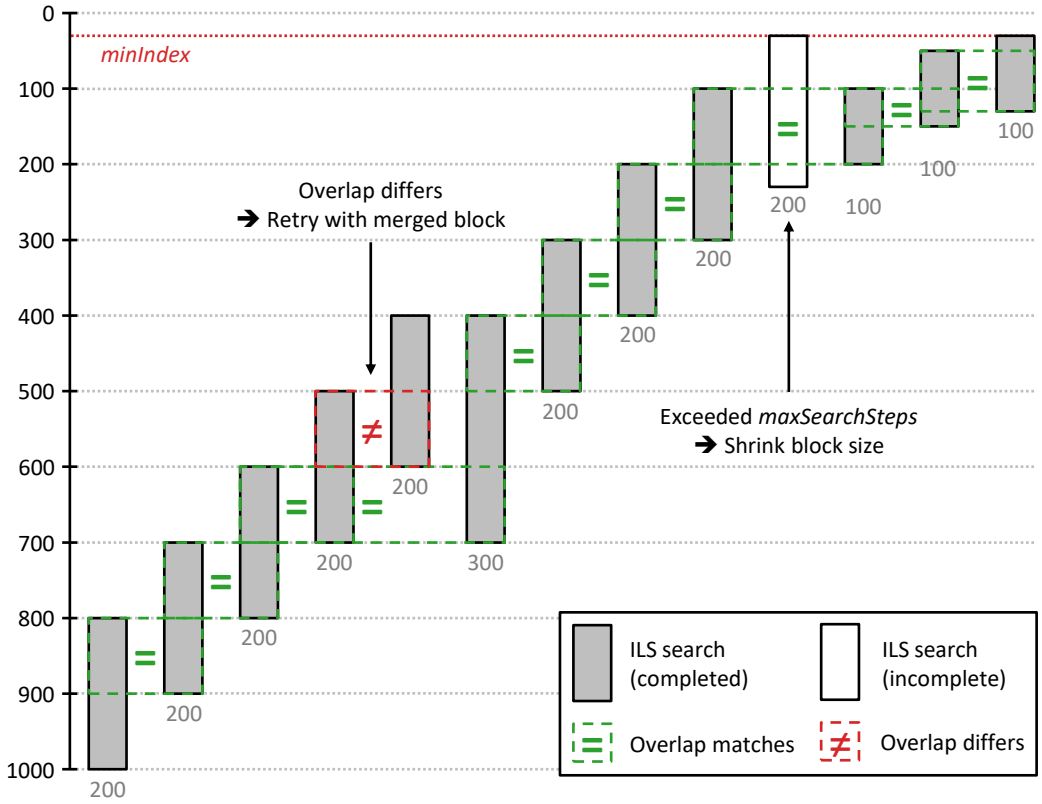

Figure 6.14: Schematic visualization of blocked search algorithm for an example with 1000 ambiguities and a search block size of 200. The algorithm operates from bottom (most accurate) to top (least accurate)

by half the block size and the next ILS search is performed. The ILS solutions of two subsequent blocks should match within the overlapping part. If this is the case, the algorithm continues by moving the block further and comparing the solution of the next two subsequent blocks.

Two issues can arise during the processing. First, the overlapping part of two subsequent solutions does not match. In this case, the two blocks are merged into one block and the ILS search is performed over the joint block. A larger block size increases the robustness and likeliness to obtain a solution closer to the global optimum. If the overlap between this joint block and the block preceding those merged together matches, the search window reverts back to the original size and moves on to the next block. Otherwise, both blocks are merged again, resulting in an even larger joint block.

The second issue arises when the ILS search within one block does not complete after some maximum number of steps. This can happen when the block size increases too much because the overlaps keep differing, which often points to bad observation data hampering the resolution of certain ambiguities. Another point where the ILS iteration

threshold might be reached is towards the end of the process, when a block mainly contains ambiguities with lower accuracy, making it more difficult to find the optimal solution. In both cases, the threshold serves to limit the overall processing time, which might otherwise increase to infeasible levels.

There are a few options to deal with this second issue. Firstly, the algorithm can just stop and all remaining ambiguities are left as float values. Secondly, the best ILS solution found before the iteration threshold was reached can be used and the process continues with the next block. In this case, however, it is likely that the overlap will not match, leading to a joint block that is even more unlikely to be completed within the iteration threshold. The third option is to shrink the block size (e.g., by halving it) and to try solving a smaller block. This can lead to more of the remaining ambiguities being resolved to integer values. However, the chance of wrong fixes increases for smaller block sizes. Practical experience has shown that this option often leads to better results than leaving the remaining ambiguities as float values. Nevertheless, this should not be taken as a general recommendation as it might differ from case to case.

In case the algorithm has not been stopped prematurely, it continues until all ambiguities have been resolved or an accuracy threshold $\sigma_{\text{threshold}}$ has been reached. Ambiguities with a lower accuracy than this threshold are not resolved in any case because the chance of wrong fixes is too high.

6.7 Troposphere

Earth's troposphere contains dry gases and water particles that delay GNSS signals traveling through it. The troposphere is a nondispersive medium with respect to GNSS signals, which means this delay does not depend on the frequency of the signal. The effect is commonly split into a hydrostatic part and a wet part. The hydrostatic part describes the delay due to dry gases and accounts for roughly 90% of the total delay (Petit and Luzum, 2010). This component can be modeled accurately, as it mainly depends on the surface pressure, which is well observed globally. The wet part, on the other hand, can change rapidly in space and time due to the fluctuating nature of water vapor and water particles in the troposphere. Therefore, this part can usually not be modeled with sufficient accuracy, which is why it is essential to estimate a residual wet delay in high-precision GNSS processing. More detailed background information on tropospheric signal propagation can be found, for example, in Hobiger and Jakowski (2017).

Tropospheric delays can also be systematically biased with respect to a horizontal direction. This can be interpreted as a tilting of the zenith direction at a specific location (i.e., a station) towards some azimuth angle. Bar-Sever et al. (1998), Rothacher et al. (1998), and Meindl et al. (2004) show that taking this bias into account by additionally estimating horizontal north-south and east-west gradient delays improves station coordinate repeatability.

The tropospheric slant delay is thus usually considered in the form

$$\begin{aligned} D(A,e) = {} & m_{\mathrm{H}}(e)\, D_{\mathrm{ZH}} + m_{\mathrm{W}}(e)\, (D_{\mathrm{ZW}} + \Delta D_{\mathrm{ZW}}) \\ & + m_{\mathrm{G}}(e)\, (D_{\mathrm{GN}} \cos A + D_{\mathrm{GE}} \sin A)\ . \end{aligned} \tag{6.83}$$

Here, D_{ZH} and D_{ZW} are the a priori hydrostatic and wet delays in zenith direction, respectively. The residual zenith wet delay ΔD_{ZW} is specifically listed to highlight the fact that this part has to be estimated. Similarly, D_{GN} and D_{GE} are the north-south and east-west gradient delays that have to be estimated. They depend on the azimuth angle A of the observation at the station. The mapping functions m_{H}, m_{W}, and m_{G} map these components from zenith direction to the elevation angle e of an observation. Herring (1992) proposed the form

$$m_{\mathrm{H,W}}(e) = \cfrac{1 + \cfrac{a}{1 + \cfrac{b}{1+c}}}{\sin e + \cfrac{a}{\sin e + \cfrac{b}{\sin e + c}}} \tag{6.84}$$

for the hydrostatic and wet mapping functions. The coefficients a, b, and c are nowadays usually determined based on numerical weather models, which offer a global representation of the atmospheric state and its changes over time (Niell, 2001). Chen and Herring (1997) introduced the commonly used gradient mapping function

$$m_{\mathrm{G}}(e) = \frac{1}{\sin e \tan e + C} \tag{6.85}$$

and suggested values of $C_{\mathrm{H}} = 0.0031$ and $C_{\mathrm{W}} = 0.0007$ for the hydrostatic and wet component, respectively, or $C = 0.0032$ in case both components are estimated together.

6.7.1 Troposphere models

Several models have been developed over time to determine the coefficients for the mapping function in (6.84). Examples are the Niell Mapping Function (NMF; Niell,

1996), the Isobaric Mapping Function (IMF; Niell, 2000), and the Vienna Mapping Functions 1 (VMF1; Böhm et al., 2006). The most sophisticated representation of the troposphere based on mapping functions that is currently available is Vienna Mapping Functions 3 (VMF3; Landskron and Böhm, 2018).

6.7.1.1 Vienna Mapping Functions 3 (VMF3)

An in-depth description of the development and evaluation of VMF3 can be found in Landskron (2017). The coefficients of VMF1 and VMF3 are determined via ray tracing using the numerical weather model of the European Centre for Medium-Range Weather Forecasts (ECMWF). VMF3 is an an evolution of VMF1 that better approximates the underlying ray-traced delays, particularly at low elevations (Landskron and Böhm, 2018).

VMF3 includes an empirical spatio-temporal representation of the mapping function coefficients b_{H}, b_{W}, c_{H}, and c_{W}. Landskron and Böhm (2018) states that these coefficients were determined by first computing monthly means of ray tracing delays on a global $1\times1^\circ$ grid for the years 2001–2010. Mean, annual, and semiannual components were then fitted to the time series of each grid point to represent its temporal variations. Finally, these grid-based parameters were converted to spherical harmonic coefficients (e.g., Borden and Luscombe, 2017) up to degree and order 12. Users of the model can then evaluate this spatio-temporal representation at any point on Earth's surface and in time to get the respective mapping function coefficients. Figure 6.15 shows an example of the spatial variations of these coefficients at the beginning of 2020.

Discrete mapping function coefficients a_{H} and a_{W} are then estimated at a 6-hour sampling period. This is done by substituting the empirical coefficients b_{H}, b_{W}, c_{H}, and c_{W} into (6.84) and then fitting the mapping functions to ray tracing delays over several elevations in a least-squares adjustment. The VMF3 data service (re3data.org, 2016) provides the coefficients a_{H} and a_{W} together with zenith hydrostatic and wet delays (D_{ZH}, D_{ZW}) either on a global grid or directly at specific GNSS station locations. The grid version is provided at a maximum resolution of $1\times1^\circ$ and is valid at the mean height of the topography in each grid cell. Each variant optionally includes horizontal hydrostatic and wet gradient delays (D_{GNH}, D_{GEH}, D_{GNW}, D_{GEW}) at the same sampling rate. These gradient delays are intended to be used with Equation (6.85) and the respective hydrostatic or wet value for C. Landskron (2017) provides a detailed description of how the VMF3 gradient delays are determined.

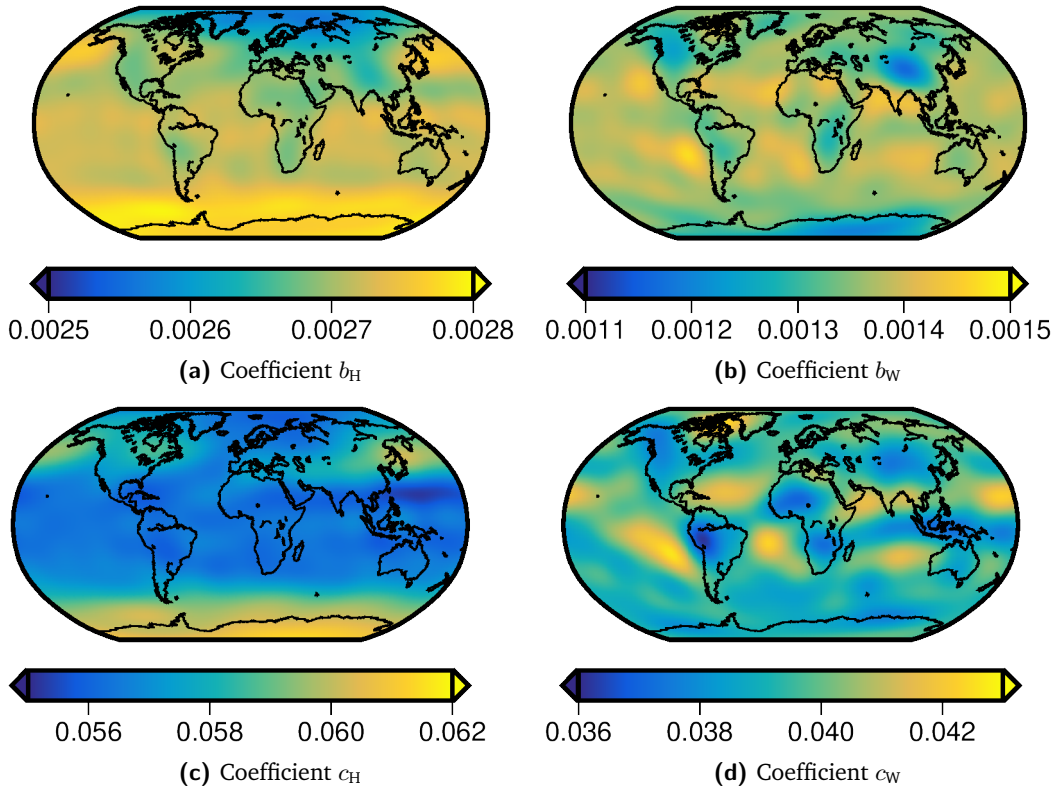

(a) Coefficient b_{H} **(b)** Coefficient b_{W}

(c) Coefficient c_{H} **(d)** Coefficient c_{W}

Figure 6.15: Empirical VMF3 coefficients evaluated on 2020-01-01

6.7.1.2 Global Pressure and Temperature 3 (GPT3)

Landskron and Böhm (2018) also presents the purely empirical model Global Pressure and Temperature 3 (GPT3), which is fully consistent with VMF3. This model has been determined by fitting mean, annual, and semiannual components to the a_{H} and a_{W} coefficients of the $1\times1°$ grid version of VMF3. GPT3 also contains an empirical representation of horizontal hydrostatic and wet gradient delays with mean, annual, and semiannual components on the same grid. The model further includes a spatio-temporal representation of several meteorological parameters that are needed to empirically determine the zenith delays. Examples are the pressure p_0 (in Pa) and temperature T_0 (in K) at grid height, the specific humidity Q (in kg/kg), the water vapor decrease factor λ, and the mean temperature of water vapor T_m (in K).

These parameters can be bilinearly interpolated from the grid points to a specific longitude and latitude, after which the interpolated mean, annual, and semiannual temporal components can be evaluated at any point in time. For a station at latitude φ

and ellipsoidal height h_{ell}, the zenith hydrostatic delay (ZHD) can then be computed as (Saastamoinen, 1972)

$$D_{\text{ZH}} = \frac{0.0022768\,p}{1 - 0.00266\cos(2\varphi) - 0.00000028\,h_{\text{ell}}} \tag{6.86}$$

and the zenith wet delay (ZWD) as (Askne and Nordius, 1987)

$$D_{\text{ZW}} = 10^{-6}\left(k_2' + \frac{k_3}{T_m}\right)\frac{p\,R_g\,Q}{g\,M_d\,(0.622 + 0.378\,Q)(1+\lambda)} \tag{6.87}$$

using the universal gas constant $R_g = 8.3143\,\text{J/K/mol}$, the molar mass of dry air $M_d = 0.028\,965\,\text{kg/mol}$, the mean gravity $g = 9.806\,65\,\text{m/s}^2$, as well as the refractivity constants $k_1 = 77.604\,\text{K/hPa}$, $k_2 = 64.79\,\text{K/hPa}$, $k_2' = k2 - \frac{18.0152}{28.9644}\,k1 = 16.522\,\text{K/hPa}$, and $k_3 = 377\,600\,\text{K}^2\text{/hPa}$. Further, $\Delta h = h_{\text{ell}} - h_{\text{grid}}$ is the reduced height in meters, $T_v = T_0\,(1 + 0.6077\,Q)$ is the virtual temperature in Kelvin, and

$$p = p_0\,e^{-\frac{g\,M_d\,\Delta h}{R_g\,T_v}} \tag{6.88}$$

is the pressure at height h_{ell} based on the pressure p_0 at grid height. Equations (6.86) and (6.87) expect p in hPa.

6.7.1.3 Height correction

One important aspect to consider is that gridded VMF3 and GPT3 data is valid at the mean height of each grid cell. This value can deviate significantly from the actual station height. An extreme example is the station MKEA on Mauna Kea, Hawaii, USA, which is located at a height of 3754 m. Figure 6.16 shows that three of the four surrounding grid points have a mean height close to 0 m because their grid cells mostly cover the ocean. Only one cell covers most of the island and thus has a mean height of 589 m. A difference of more than 3000 m between the bilinearly interpolated grid height and the actual station height has a large impact on the tropospheric parameters, for example pressure. Therefore, applying a height correction to some of the data and coefficients is important in order to model the tropospheric delay at such stations properly.

Kouba (2008) recommends to apply a height correction to ZHDs, ZWDs, and the mapping function coefficients a_{H}. Equation (6.86) already considers the station height h_{ell}, thus GPT3 ZHDs determined with this equation do not have to be corrected further. Gridded VMF3 ZHDs, on the other hand, have to be brought to station height via

$$D_{\text{ZH}}(h_{\text{station}}) = D_{\text{ZH}}(h_{\text{grid}})\,e^{-\frac{g\,M_d\,\Delta h}{R_g\,T_v}}\,, \tag{6.89}$$

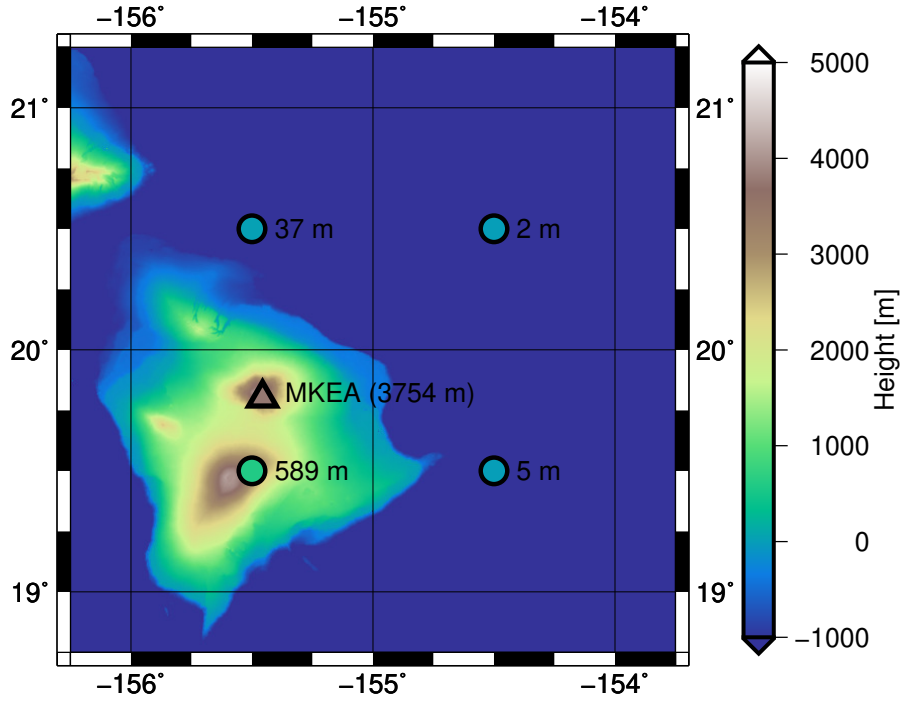

Figure 6.16: Height of station MKEA (Mauna Kea, Hawaii) and surrounding VMF3 grid points

which has the same form as the pressure correction in (6.88). For ZWD height correction, Kouba (2008) provides the equation

$$D_{\mathrm{ZW}}(h_{\mathrm{station}}) = D_{\mathrm{ZW}}(h_{\mathrm{grid}})\; e^{-\frac{\Delta h}{2000}}\,. \tag{6.90}$$

For the hydrostatic mapping function, Landskron and Böhm (2018) suggests using the height correction formula from Niell (1996), which is

$$m_{\mathrm{H}}(h_{\mathrm{station}}) = m_{\mathrm{H}}(h_{\mathrm{grid}}) + \frac{h_{\mathrm{station}}}{1000} \cdot \left(\frac{1}{\sin e} - \frac{1 + \dfrac{a_{\mathrm{height}}}{1 + \dfrac{b_{\mathrm{height}}}{1 + c_{\mathrm{height}}}}}{\sin e + \dfrac{a_{\mathrm{height}}}{\sin e + \dfrac{b_{\mathrm{height}}}{\sin e + c_{\mathrm{height}}}}} \right), \tag{6.91}$$

with the constants $a_{\mathrm{height}} = 2.53 \cdot 10^{-5}$, $b_{\mathrm{height}} = 5.49 \cdot 10^{-3}$, and $c_{\mathrm{height}} = 1.14 \cdot 10^{-3}$. No general correction formula is provided for the wet mapping function as there the height difference is usually not significant (Kouba, 2008).

6.7.2 Slant delay correction and parametrization

With the inclusion of a priori horizontal gradient delays in VMF3 and GPT3, the tropospheric slant delay correction in the observation equations (5.1) becomes

$$\begin{aligned}\mathrm{tropo}(t, \boldsymbol{p}_r^s) = {} & m_{\mathrm{H}}(e)\, D_{\mathrm{ZH}} + m_{\mathrm{W}}(e)\, (D_{\mathrm{ZW}} + \Delta D_{\mathrm{ZW}}) \\ & + m_{\mathrm{GH}}(e)\, (D_{\mathrm{GNH}} \cos A + D_{\mathrm{GEH}} \sin A) \\ & + m_{\mathrm{GW}}(e)\, (D_{\mathrm{GNW}} \cos A + D_{\mathrm{GEW}} \sin A) \\ & + m_{\mathrm{G}}(e)\, (\Delta D_{\mathrm{GN}} \cos A + \Delta D_{\mathrm{GE}} \sin A)\ .\end{aligned} \tag{6.92}$$

Here, m_{GH}, m_{GW}, and m_{G} come from (6.85) with coefficients $C_{\mathrm{H}} = 0.0031$, $C_{\mathrm{W}} = 0.0007$, and $C = 0.0032$, respectively. D_{GNH} and D_{GEH} are the a priori north-south and east-west hydrostatic gradient delays, while D_{GNW} and D_{GEW} are those for wet gradient delays. Finally, ΔD_{GN} and ΔD_{GE} are the residual gradient delays that are estimated in addition to the a priori model values. While the separation of the zenith wet delay into an a priori (D_{ZW}) and residual (ΔD_{ZW}) part in (6.92) is not technically necessary, the residual gradient delays are based on a different mapping function than the a priori gradient delays and, therefore, cannot be lumped together. Furthermore, (6.92) implies that all a priori delays and mapping functions are valid at epoch t and the location of the station. In time domain, they have to be interpolated from a discrete time series or evaluated from empirical functions. In space domain, bilinear interpolation combined with height correction can be used in case no station-specific values are available.

ΔD_{ZW}, ΔD_{GN}, and ΔD_{GE} are usually estimated as station-wise time-variable parameters over the processing period. This means they are represented by a linear combination

$$x(t) = \sum_i x_i\, \psi_i(t)\,, \tag{6.93}$$

where $\psi_i(t)$ are basis functions in time and x_i are the coefficients of these functions that are estimated as parameters. For example, gradient delays are estimated as linear functions per day in the form

$$x(t) = x_{\mathrm{const}} + (t - t_0)\, x_{\mathrm{trend}}\,, \tag{6.94}$$

with x_{const} and x_{trend} being the two parameters to be estimated and 1 and $(t - t_0)$ being their respective basis functions. Zenith wet delays are usually parameterized as splines of degree 1 with two-hourly knots. In this case, $\psi_i(t)$ are the basis splines and x_i the delay values at each knot. Both parametrizations are visualized in Figure 6.17.

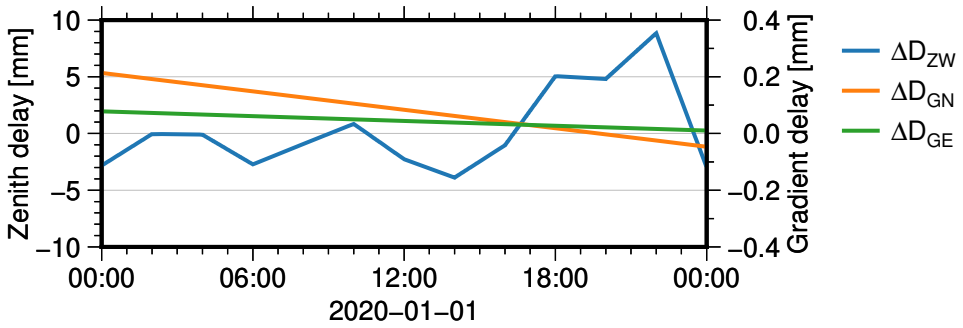

Figure 6.17: Temporal representation of residual zenith wet and gradient delays

The partial derivatives of the intermediate slant delay parameter s_g (see Section 5.3) with respect to the tropospheric parameters can thus be determined using the chain rule. First, Equation (6.92) is partially derived for ΔD_{ZW}, ΔD_{GN}, and ΔD_{GE}. These derivatives are then multiplied by the partial derivatives of the tropospheric parameters with respect to the coefficients of their temporal representations. Taking the north gradient delay as an example, the slice of the design matrix $\mathbf{D}_g$ that connects the intermediate parameter s_g with the constant and trend parameters of the station's north gradient delay has dimensions 1×2 and is

$$\frac{\partial s_g}{\partial \mathbf{x}_{\Delta D_{\text{GN},r}}} = \frac{\partial s_g}{\partial \Delta D_{\text{GN},r}} \frac{\partial \Delta D_{\text{GN},r}}{\partial \mathbf{x}_{\Delta D_{\text{GN},r}}} = m_{\text{G}}(e) \cos A \begin{bmatrix} 1 & (t - t_0) \end{bmatrix} . \tag{6.95}$$

For the east gradient delay, (6.95) contains $\sin A$ instead of $\cos A$, while the partial derivatives for the residual zenith wet delay are $m_{\text{W}}(e)$ multiplied with a 1×13 matrix containing the factors for the two-hourly spline knots over a 24-hour day.

6.7.3 Model selection

The availability of two VMF3 variants (station-specific and gridded) as well as GPT3 raises the question of which one is best suited for GNSS processing. In theory, the station-specific VMF3 model should be preferable. This is because it is based on ray tracing computations at the actual station locations, presumably making it the most accurate variant. However, its main drawback is that model data is only provided for a predefined set of 546 (as of 2020-11-25) GNSS stations, which covers only 523 (or 44%) of the 1182 stations processed by TUG for the reprocessing campaign. This leaves the choice between gridded VMF3 data and GPT3, which can both be evaluated anywhere on Earth.

Both models can be analyzed with respect to how well they can recreate the station-specific VMF3 data, which is chosen as a reference due to its presumably higher accuracy.

Table 6.10: Means and standard deviations (in mm) of zenith delay differences when comparing GPT3 and gridded VMF3 data to station-wise VMF3 data (with/without height correction)

	Without height correction		With height correction	
	GRAZ	MKEA	GRAZ	MKEA
GPT3 D_{ZH}	-5.1 ± 17.6	15.6 ± 4.0	-5.1 ± 17.6	15.6 ± 4.0
GPT3 D_{ZW}	-5.4 ± 29.3	84.8 ± 16.5	-0.2 ± 29.1	-0.2 ± 14.4
GPT3 $\hat{D}_{\mathrm{ZW}}$	5.7 ± 16.8	-9.2 ± 4.9	5.7 ± 16.7	-9.3 ± 3.9
GPT3 $D_{\mathrm{ZH}} + \hat{D}_{\mathrm{ZW}}$	0.5 ± 2.7	6.4 ± 3.0	0.6 ± 2.5	6.4 ± 0.8
VMF3 D_{ZH}	-27.9 ± 0.9	727.0 ± 3.9	-0.2 ± 0.5	16.3 ± 2.2
VMF3 D_{ZW}	-4.8 ± 5.0	140.7 ± 24.8	0.5 ± 3.9	10.3 ± 9.7
VMF3 $\hat{D}_{\mathrm{ZW}}$	28.0 ± 2.1	-699.0 ± 25.7	1.5 ± 0.7	-9.6 ± 2.4
VMF3 $D_{\mathrm{ZH}} + \hat{D}_{\mathrm{ZW}}$	0.1 ± 1.9	28.0 ± 25.5	1.3 ± 0.4	6.7 ± 1.0

This analysis was not only conducted to decide which model to choose for the reprocessing, but also to confirm that the findings about height correction presented in Kouba (2008) with respect to VMF1 are still valid for VMF3. Table 6.10 summarizes the results in terms of zenith delays for two select stations, GRAZ in Graz, Austria, and MKEA on Mauna Kea, Hawaii, USA. Station GRAZ is located on the southeastern end of the Alps and its height of 538 m does not differ from its surrounding grid points by more than a few hundred meters. As mentioned further above, the height difference for station MKEA is more than 3000 m. The analysis was conducted over the period of one year (2020) with daily processing intervals.

Table 6.10 shows that height correction significantly improves the a priori zenith delays. The height-corrected a priori zenith delay differences for both stations are also visualized in Figures 6.18 and 6.19. VMF3 ZHDs (D_{ZH}) show the largest impact, with a mean difference to the station-specific delays of 727 mm for the extreme example of MKEA. This bias decreases to only 16.3 mm when height correction is applied and is then similar to the bias of 15.6 mm from GPT3, which does not have to be corrected since the station height is already considered in Equation (6.86). For station GRAZ, the mean ZHD difference is significantly smaller for both models, and the height-corrected VMF3 delays show no significant remaining bias. Interestingly, the GPT3 ZHD differences for GRAZ only have a small bias of -5.1 mm, but a large standard deviation of 17.6 mm. This can also be seen in Figure 6.18 and indicates that the empirical mean, annual, and semiannual components of GPT3 cannot adequately represent short-term ZHD variations.

In addition, the height correction leads to a significant improvement in a priori ZWDs (D_{ZW}). The bias of around -5 mm at GRAZ vanishes for both models, although the standard deviation again remains very high in case of GPT3. For station MKEA, the biases

Table 6.11: Means and standard deviations (in mm) of gradient delay differences when comparing GPT3 and gridded VMF3 data to station-wise VMF3 data

	GPT3 data		Gridded VMF3 data	
	GRAZ	MKEA	GRAZ	MKEA
D_{GNH}	-16.3 ± 1.8	-2.9 ± 3.0	0.0 ± 0.0	0.0 ± 0.0
D_{GEH}	-5.6 ± 2.4	-6.7 ± 0.7	0.0 ± 0.0	0.0 ± 0.0
D_{GNW}	-3.0 ± 1.1	-4.8 ± 2.3	0.0 ± 0.0	-0.1 ± 0.2
D_{GEW}	-5.0 ± 4.2	-1.5 ± 3.5	0.0 ± 0.1	-0.1 ± 0.3
$\Delta\hat{D}_{\mathrm{GN}}$	19.5 ± 2.5	8.0 ± 3.2	0.0 ± 0.0	-0.1 ± 0.1
$\Delta\hat{D}_{\mathrm{GE}}$	11.1 ± 3.6	8.4 ± 3.2	0.0 ± 0.1	0.2 ± 0.4

decrease from 84.8 mm to -0.2 mm for GPT3 and from 140.7 mm to 10.3 mm for VMF3. While it can be useful to have good a priori wet delays, for example during observation preprocessing, the fact that residual ZWDs are estimated makes it more interesting to look at the sum of modeled and estimated wet delays ($\hat{D}_{\mathrm{ZW}}$). Here, Table 6.10 and Figures 6.20 and 6.21 reveal that this parameter not only compensates for any modeling issues with a priori ZWDs, but also largely absorbs mismodeled ZHDs. Both models show small biases at both stations when compared to station-specific VMF3 data and temporal variations that largely mirror those of the ZHDs. Finally, the zenith total delay (ZTD; $D_{\mathrm{ZH}} + \hat{D}_{\mathrm{ZW}}$) is almost unbiased for station GRAZ, although GPT3 has larger temporal variations with a standard deviation of 2.5 mm compared to 0.4 mm for VMF3. The biases and standard deviations at MKEA are almost identical for both models.

The analysis results for gradient delays are summarized in Table 6.11. It is clearly visible that the gridded VMF3 gradient delays are almost identical to the station-specific variant. The slight differences are caused by the bilinear interpolation from the grid points to the actual station location. In contrast, GPT3 a priori gradient delays show large discrepancies in the hydrostatic and wet components in both north-south (D_{GNH}, D_{GNW}) and east-west (D_{GEH}, D_{GEW}) directions. The estimated residual gradient delays ($\Delta\hat{D}_{\mathrm{GN}}$, $\Delta\hat{D}_{\mathrm{GE}}$) then appear to largely compensate for these discrepancies. This is in accordance with Landskron (2017), where analyses revealed that empirical gradient delays cannot describe the random, short-term variations caused by weather events sufficiently.

These analyses show that it is preferable to use gridded VMF3 data over the empirical model GPT3. The main advantage is that the 6-hourly data from VMF3 better represents short-term variations in zenith and gradient delays. The estimated troposphere parameters cannot always compensate an insufficient modeling of these variations. For this reason, the gridded VMF3 variant was used as the a priori tropospheric model for the reprocessing campaign.

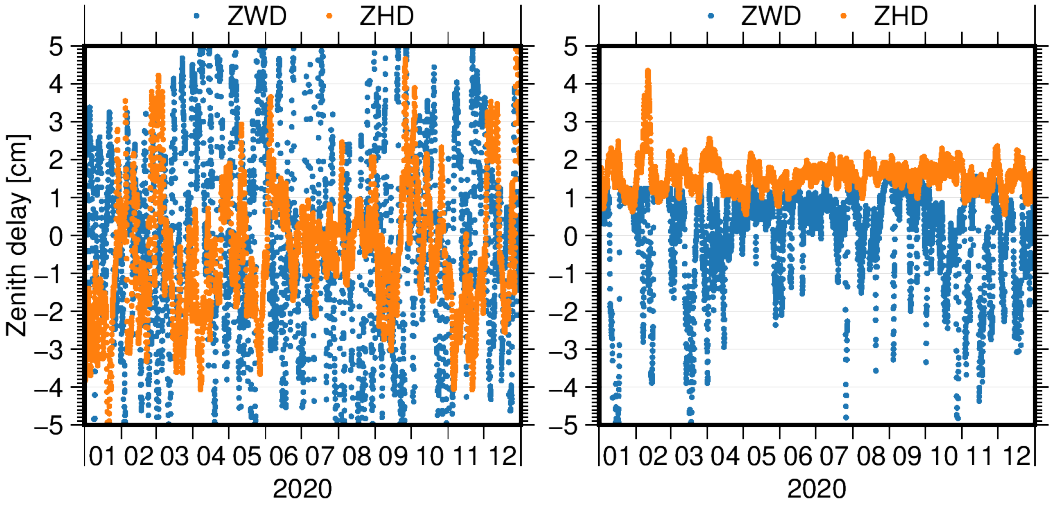

(a) Station GRAZ (Austria) **(b)** Station MKEA (Hawaii)

Figure 6.18: Difference in a priori zenith hydrostatic (orange) and wet (blue) delay between GPT3 and station-wise VMF3 data

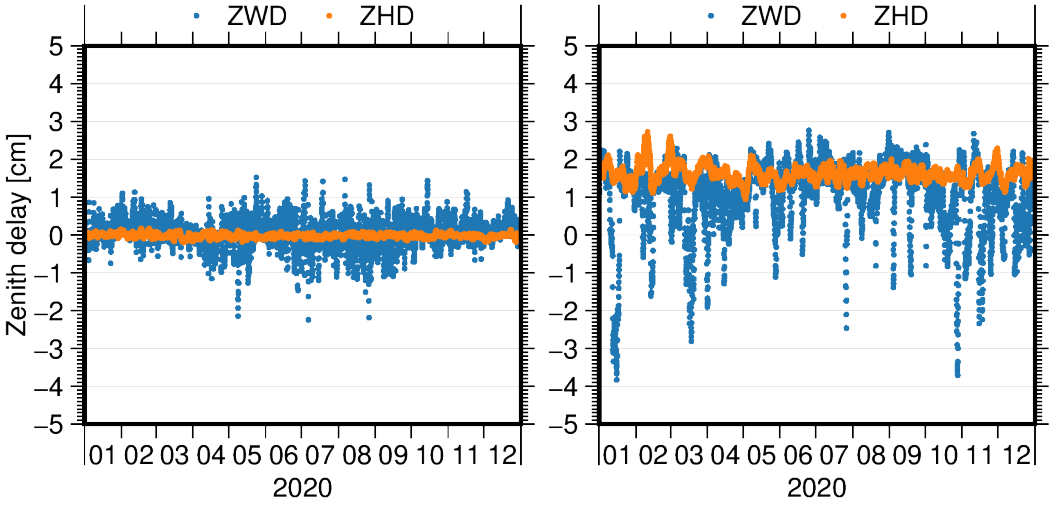

(a) Station GRAZ (Austria) **(b)** Station MKEA (Hawaii)

Figure 6.19: Difference in a priori zenith hydrostatic (orange) and wet (blue) delay between grid-interpolated and station-wise VMF3 data (including height correction)

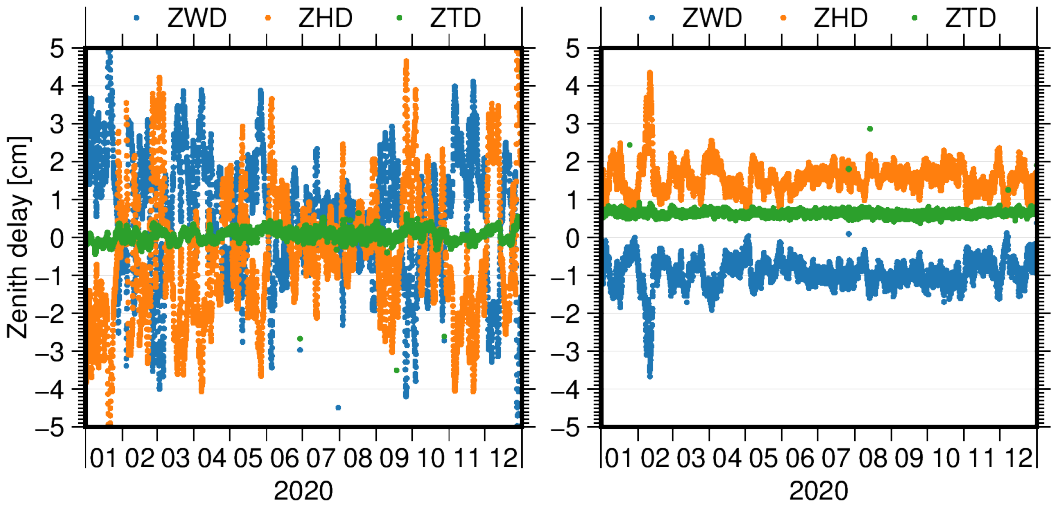

(a) Station GRAZ (Austria) **(b)** Station MKEA (Hawaii)

Figure 6.20: Difference in zenith hydrostatic (orange), wet (blue), and total (green) delay between GPT3 and station-wise VMF3 data (including residual wet delay estimation)

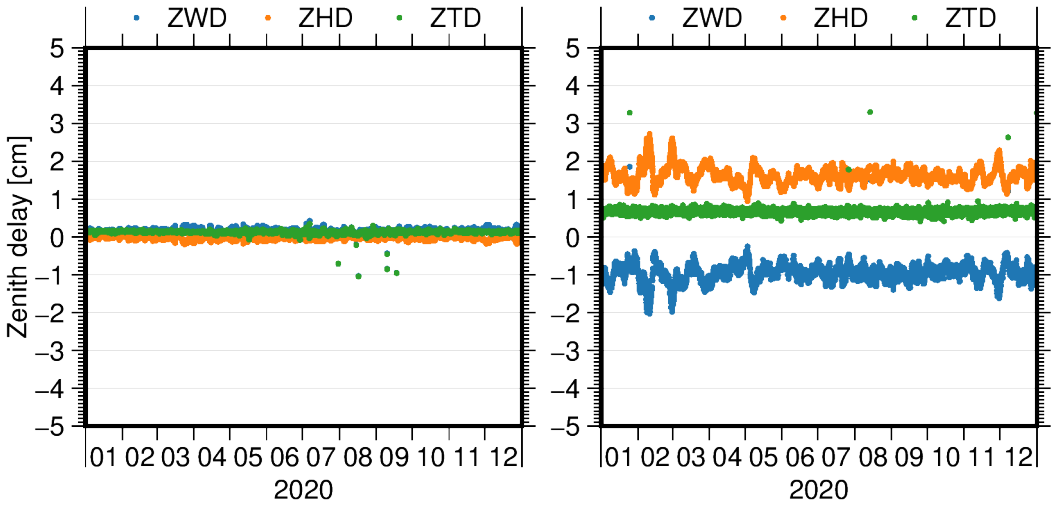

(a) Station GRAZ (Austria) **(b)** Station MKEA (Hawaii)

Figure 6.21: Difference in zenith hydrostatic (orange), wet (blue), and total (green) delay between grid-interpolated and station-wise VMF3 data (including height correction and residual wet delay estimation)

6.8 Earth orientation

In GNSS processing, satellite orbits realize a celestial reference frame (CRF) and station coordinates realize a terrestrial reference frame (TRF). Thus, the transformation between these two frames has to be taken into account when processing observations between satellites and ground-based receivers.

Following the IERS conventions (Petit and Luzum, 2010), the transformation

$$\mathbf{r}_{\text{GCRS}} = \mathbf{Q}(t)\,\mathbf{R}(t)\,\mathbf{W}(t)\,\mathbf{r}_{\text{ITRS}} \tag{6.96}$$

relates the Geocentric Celestial Reference System (GCRS) to the ITRS. Here, the matrix $\mathbf{Q}(t)$ represents the precession and nutation of the celestial pole in the GCRS, $\mathbf{R}(t)$ is the rotation of Earth around the pole axis, and $\mathbf{W}(t)$ describes polar motion.

These transformation matrices are based on conventional models and a set of Earth orientation parameters (EOPs). The conventional model for precession and nutation is provided by the International Astronomical Union (IAU) via the Standards of Fundamental Astronomy (SOFA) service (IAU SOFA Board, 2022). The IERS conventions define the conventional model for the rotation around the pole axis and polar motion. The IERS further provides daily EOPs (Bizouard et al., 2019) as a correction for these conventional models. They comprise the correction parameters ΔX and ΔY for the precession-nutation model, the difference $\Delta\mathrm{UT1} = \mathrm{UT1} - \mathrm{UTC}$ between UT1 and Coordinated Universal Time (UTC), the so-called length of day (LOD), which is the rate of $\Delta\mathrm{UT1}$, and the pole coordinates x_p and y_p.

The precession-nutation matrix $\mathbf{Q}(t)$ can be determined as

$$\mathbf{Q}(t) = \mathbf{R}_z(-E)\,\mathbf{R}_y(-d)\,\mathbf{R}_z(E)\,\mathbf{R}_z(s) \tag{6.97}$$

using the angles

$$E = \operatorname{atan2}(Y,\, X) \tag{6.98}$$

and

$$d = \operatorname{atan}\sqrt{\frac{X^2 + Y^2}{1 - X^2 + Y^2}}\,. \tag{6.99}$$

The matrices $\mathbf{R}_x$, $\mathbf{R}_y$, and $\mathbf{R}_z$ represent the basic rotations around the x, y, and z axes, respectively. The angle s in (6.97) can be computed via the SOFA routines. The

coordinates $X = X_{\text{model}} + \Delta X_{\text{EOP}}$ and $Y = Y_{\text{model}} + \Delta Y_{\text{EOP}}$ of the so-called Celestial Intermediate Pole (CIP) used in (6.98) and (6.99) are composed of those of the conventional model (X_{model}, Y_{model}) and the EOPs corrections (ΔX_{EOP}, ΔY_{EOP}).

The matrix describing the rotation of Earth around the pole axis is

$$\mathbf{R}(t) = \mathbf{R}_z(-\mathrm{ERA})\,, \tag{6.100}$$

where ERA is the Earth Rotation Angle. Following the IERS conventions,

$$\mathrm{ERA}(T_{\mathrm{UT1}}) = 2\pi\,(0.7790572732640 + 1.00273781191135448\,T_{\mathrm{UT1}}) \tag{6.101}$$

with $T_{\mathrm{UT1}} = (t_{\mathrm{UTC}} + \Delta\mathrm{UT1} - 2451545.0)$ in units of days. t_{UTC} is the Julian UTC date and $\Delta\mathrm{UT1} = \Delta\mathrm{UT1}_{\text{model}} + \Delta\mathrm{UT1}_{\text{EOP}}$, also expressed in days.

The polar motion matrix

$$\mathbf{W}(t) = \mathbf{R}_z(-s')\,\mathbf{R}_y(x_p)\,\mathbf{R}_x(y_p) \tag{6.102}$$

requires the angle s', which can be determined using SOFA routines, as well as the compound pole coordinates $x_p = x_{p,\text{model}} + x_{p,\text{EOP}}$ and $y_p = y_{p,\text{model}} + y_{p,\text{EOP}}$.

6.8.1 High-frequency tidal model

The conventional IERS model for $x_{p,\text{model}}$, $y_{p,\text{model}}$, and $\Delta\mathrm{UT1}_{\text{model}}$ describes diurnal and semidiurnal variations in these parameters caused by ocean tides and libration in the form (Petit and Luzum, 2010)

$$\square^{\text{IERS}}_{\text{model}} = \square^{\text{IERS}}_{\text{ocean tides}} + \square^{\text{IERS}}_{\text{libration}}\,. \tag{6.103}$$

The ocean tidal part includes variations at 41 diurnal and 30 semidiurnal tidal frequencies. Desai and Sibois (2016) developed a high-frequency model that comprises 86 diurnal and 73 semidiurnal tidal components. This model was adopted for IGS repro3 to replace the IERS model. The model is distributed in the form of Fourier coefficients at the 159 tidal frequencies for each of the parameters. Thus, the parameters $x_{p,\text{model}}$, $y_{p,\text{model}}$, and $\Delta\mathrm{UT1}_{\text{model}}$ can be determined as

$$\square^{\text{HF}}_{\text{model}} = \square^{\text{HF}}_{\text{ocean tides}} + \square^{\text{IERS}}_{\text{libration}}\,, \tag{6.104}$$

where $\square^{\text{HF}}_{\text{ocean tides}}$ is the sum of the evaluated Fourier series at all provided tidal frequencies, while $\square^{\text{IERS}}_{\text{libration}}$ comes from the IERS software routines.

6.8.2 Parametrization of Earth orientation

In Section 5.1, it was mentioned that Equation (5.2) implies that both the transmitter and receiver coordinates are in the same reference frame. When the observation equations are set up in the CRF, the intermediate parameters described in Section 5.3 contain the receiver position also in the CRF. Therefore, only the relation

$$\mathbf{r}_r^{\mathrm{CRF}} = \mathbf{R}_{\mathrm{TRF}}^{\mathrm{CRF}}(t)\,\mathbf{r}_r^{\mathrm{TRF}} = \mathbf{Q}(t)\,\mathbf{R}(t)\,\mathbf{W}(t)\,\mathbf{r}_r^{\mathrm{TRF}} \tag{6.105}$$

has to be considered for the design matrix $\mathbf{D}_g$. This can be interpreted as the design matrix $\mathbf{C}_g$ containing the exterior derivative of (5.2) with respect to Earth rotation parameters while $\mathbf{D}_g$ contains the interior derivative.

Earth rotation parameters can have different temporal representations. They can be described by a linear combination

$$x(t) = \sum_i x_i\,\psi_i(t)\,, \tag{6.106}$$

where $\psi_i(t)$ are basis functions in time and x_i are the coefficients of these functions. Bizouard et al. (2019) lists the Earth rotation parameters typically estimated via GNSS. They include polar motion (x_p, y_p), polar motion rate ($\dot{x}_p$, $\dot{y}_p$) and LOD (i.e., the rate of $\Delta\mathrm{UT1}$). The absolute value of $\Delta\mathrm{UT1}$ cannot be determined directly by GNSS. However, it is commonly set up as a parameter that is tightly constrained to its a priori value in order to facilitate combination of the normal equations with other space-geodetic techniques that can determine this parameter, for example VLBI. While the absolute values of the nutation parameters X and Y can also not be determined by GNSS, their rates ($\dot{X}$, $\dot{Y}$) can be estimated (Rothacher et al., 1999).

6.8.2.1 Nutation

Partially derivating (6.105) with respect to the nutation parameters X and Y leads to

$$\frac{\partial \mathbf{r}_r^{\mathrm{CRF}}}{\partial X} = \frac{\partial \mathbf{Q}(t)}{\partial X}\,\mathbf{R}(t)\,\mathbf{W}(t)\,\mathbf{r}_r^{\mathrm{TRF}} \tag{6.107}$$

and

$$\frac{\partial \mathbf{r}_r^{\mathrm{CRF}}}{\partial Y} = \frac{\partial \mathbf{Q}(t)}{\partial Y}\,\mathbf{R}(t)\,\mathbf{W}(t)\,\mathbf{r}_r^{\mathrm{TRF}}\,. \tag{6.108}$$

Alternatively to Equation (6.97), the precession-nutation matrix can also be stated as

$$\mathbf{Q}(t) = \begin{bmatrix} 1 - aX^2 & -aXY & X \\ -aXY & 1 - aY^2 & Y \\ -X & -Y & 1 - a(X^2 + Y^2) \end{bmatrix} \mathbf{R}_z(s) \tag{6.109}$$

with

$$a = \frac{1}{2} + \frac{1}{8}(X^2 + Y^2)\,. \tag{6.110}$$

This alternative form simplifies the formation of the partial derivatives

$$\frac{\partial \mathbf{Q}(t)}{\partial X} = \begin{bmatrix} -2aX - \frac{X^3}{4} & -aY - \frac{X^2 Y}{4} & 1 \\ -aY - \frac{X^2 Y}{4} & -\frac{XY^2}{4} & 0 \\ -1 & 0 & -2aX - \frac{X(X^2+Y^2)}{4} \end{bmatrix} \mathbf{R}_z(s) \tag{6.111}$$

and

$$\frac{\partial \mathbf{Q}(t)}{\partial Y} = \begin{bmatrix} -\frac{X^2 Y}{4} & -aX - \frac{XY^2}{4} & 0 \\ -aX - \frac{XY^2}{4} & -2aY - \frac{Y^3}{4} & 1 \\ 0 & -1 & -2aY - \frac{Y(X^2+Y^2)}{4} \end{bmatrix} \mathbf{R}_z(s)\,. \tag{6.112}$$

As mentioned above, the absolute values for the nutation parameters cannot be estimated via GNSS. Their rates can be parameterized by using the basis function $\psi(t) = t - t_0$ as a temporal representation. The entries in the design matrix $\mathbf{D}_g$ then are

$$\frac{\partial \mathbf{r}_r^{\text{CRF}}}{\partial \mathbf{x}_X} = \frac{\partial \mathbf{r}_r^{\text{CRF}}}{\partial X} \left[t - t_0\right] \tag{6.113}$$

and

$$\frac{\partial \mathbf{r}_r^{\text{CRF}}}{\partial \mathbf{x}_Y} = \frac{\partial \mathbf{r}_r^{\text{CRF}}}{\partial Y} \left[t - t_0\right]\,. \tag{6.114}$$

6.8.2.2 Rotation around the pole axis

The partial derivative of (6.105) with respect to ΔUT1 (in seconds) is

$$\frac{\partial \mathbf{r}_r^{\text{CRF}}}{\partial \Delta\text{UT1}} = 1.00273781191135448\, \frac{2\pi}{86400}\, \mathbf{Q}(t)\, \frac{\partial \mathbf{R}(t)}{\partial \Delta\text{UT1}}\, \mathbf{W}(t)\, \mathbf{r}_r^{\text{TRF}} \tag{6.115}$$

with

$$\frac{\partial \mathbf{R}(t)}{\partial \Delta\mathrm{UT1}} = \begin{bmatrix} \sin(-\mathrm{ERA}) & -\cos(-\mathrm{ERA}) & 0 \\ \cos(-\mathrm{ERA}) & \sin(-\mathrm{ERA}) & 0 \\ 0 & 0 & 0 \end{bmatrix} . \tag{6.116}$$

In case the absolute value of $\Delta\mathrm{UT1}$ should be part of the normal equations, its temporal basis function is just $\psi(t) = 1$. LOD is parameterized as the rate of $\Delta\mathrm{UT1}$, although with opposing sign due to convention. Therefore, its temporal basis function is $\psi(t) = -(t - t_0)$. The entries in the design matrix $\mathbf{D}_g$ then follow as

$$\frac{\partial \mathbf{r}_r^{\mathrm{CRF}}}{\partial \mathbf{x}_{\Delta\mathrm{UT1}}} = \frac{\partial \mathbf{r}_r^{\mathrm{CRF}}}{\partial \Delta\mathrm{UT1}} \begin{bmatrix} 1 & -(t - t_0) \end{bmatrix} . \tag{6.117}$$

6.8.2.3 Polar motion

The partial derivatives of (6.105) with respect to the polar coordinates x_p and y_p are

$$\frac{\partial \mathbf{r}_r^{\mathrm{CRF}}}{\partial x_p} = \mathbf{Q}(t)\,\mathbf{R}(t)\,\frac{\partial \mathbf{W}(t)}{\partial x_p}\,\mathbf{r}_r^{\mathrm{TRF}} \tag{6.118}$$

and

$$\frac{\partial \mathbf{r}_r^{\mathrm{CRF}}}{\partial y_p} = \mathbf{Q}(t)\,\mathbf{R}(t)\,\frac{\partial \mathbf{W}(t)}{\partial y_p}\,\mathbf{r}_r^{\mathrm{TRF}} . \tag{6.119}$$

Due to the infinitesimal nature of the polar motion angles, small-angle approximations can be used to obtain the partial derivatives

$$\frac{\partial \mathbf{W}(t)}{\partial \Delta x_p} \simeq \mathbf{R}_z(-s') \begin{bmatrix} 0 & 0 & -1 \\ 0 & 0 & 0 \\ 1 & 0 & 0 \end{bmatrix} \mathbf{R}_x(y_p) \tag{6.120}$$

and

$$\frac{\partial \mathbf{W}(t)}{\partial \Delta y_p} \simeq \mathbf{R}_z(-s')\,\mathbf{R}_y(x_p) \begin{bmatrix} 0 & 0 & 0 \\ 0 & 0 & 1 \\ 0 & -1 & 0 \end{bmatrix} . \tag{6.121}$$

Since both the absolute values and the rates of polar motion can be determined by GNSS, the entries in the design matrix $\mathbf{D}_g$ follow as

$$\frac{\partial \mathbf{r}_r^{\mathrm{CRF}}}{\partial \mathbf{x}_{x_p}} = \frac{\partial \mathbf{r}_r^{\mathrm{CRF}}}{\partial x_p} \begin{bmatrix} 1 & t - t_0 \end{bmatrix} \tag{6.122}$$

and

$$\frac{\partial \mathbf{r}_r^{\text{CRF}}}{\partial \mathbf{x}_{y_p}} = \frac{\partial \mathbf{r}_r^{\text{CRF}}}{\partial y_p} \begin{bmatrix} 1 & t - t_0 \end{bmatrix} . \tag{6.123}$$

6.9 Station coordinates

Equation (5.2) in Section 5.1 describes the geometric range within the observation equations (5.1). When the observation equations are set up in the CRF, the receiver position is

$$\mathbf{r}_r^{\text{CRF}}(t) = \mathbf{R}_{\text{TRF}}^{\text{CRF}}(t) \left(\mathbf{r}_r^{\text{TRF}}(t) + \Delta\mathbf{r}_{r,\text{tides}}^{\text{TRF}}(t) + \Delta\mathbf{r}_{r,\text{loading}}^{\text{TRF}}(t) \right) . \tag{6.124}$$

Here, $\mathbf{R}_{\text{TRF}}^{\text{CRF}}$ is the Earth rotation matrix (see Section 6.8) and $\mathbf{r}_r^{\text{TRF}}$ is the receiver position in the TRF corrected for displacements due to tidal ($\Delta\mathbf{r}_{r,\text{tides}}^{\text{TRF}}$) and loading ($\Delta\mathbf{r}_{r,\text{loading}}^{\text{TRF}}$) deformations acting on the station.

Time-variable tidal displacements $\Delta\mathbf{r}_{r,\text{tides}}^{\text{TRF}}(t)$ include

- Solid Earth tides,
- Ocean tides,
- Atmospheric tides,
- Pole tides, and
- Ocean pole tides.

These effects are briefly summarized in Section 6.2.2, while extensive descriptions are available in the IERS conventions (Petit and Luzum, 2010). Section 8.1.1 lists the specific models that were used in the reprocessing. In addition, variations in atmospheric pressure, wind-induced ocean currents, and changes in terrestrial water storage induce loading displacements $\Delta\mathbf{r}_{r,\text{loading}}^{\text{TRF}}(t)$ (e.g., Klos et al., 2021).

Receiver positions $\mathbf{r}_r^{\text{TRF}}$ are usually assumed to be static within one day. The design matrix $\mathbf{C}_g$ already contains the partial derivatives of the observation equations with respect to the receiver position in the CRF. Therefore, only the partial derivatives of (6.124) with respect to the receiver position in the TRF are needed for the design matrix $\mathbf{D}_g$. They are simply

$$\frac{\partial \mathbf{r}_r^{\text{CRF}}}{\partial \mathbf{r}_r^{\text{TRF}}} = \mathbf{R}_{\text{TRF}}^{\text{CRF}}(t) . \tag{6.125}$$

The linearization of the GNSS observation equations requires approximate station coordinates. They are usually provided by station operators via station log files. Alternatively, precise coordinates can be obtained for stations that are part of a TRF. Current versions of the ITRF (e.g., ITRF2014) describe station positions as

$$\mathbf{r}_r^{\text{ITRF}}(t) = \mathbf{r}_r(t_0) + \dot{\mathbf{r}}_r(t_0)\,(t - t_0) + \Delta\mathbf{r}_{r,\text{PSD}}(t)\,, \tag{6.126}$$

where $\mathbf{r}_r(t_0)$ and $\dot{\mathbf{r}}_r(t_0)$ are the station position and velocity at a reference time t_0. $\Delta\mathbf{r}_{r,\text{PSD}}(g)$ is a correction for post-seismic deformation in case the station was affected by an earthquake (Altamimi et al., 2016).

A receiver or station position usually refers to a so-called station marker. This is the physical or virtual reference point of the GNSS station. In most cases, the receiving antenna is mounted close to the station marker (usually above, on a monument). This eccentricity from the station marker to the antenna reference point is covered in Section 6.10 along with other antenna offsets.

Antennas of IGS stations are supposed to be horizontally aligned towards north (IGS Infrastructure Committee, 2015). However, for a variety of reasons, not all antennas are or have always been oriented in that way. Until repro3, this misalignment had not been considered by IGS analysis centers. Depending on the misalignment and antenna type, this can lead to offsets of several centimeters in the station coordinates. Section 6.10.3 covers this topic in more detail and provides some examples of the effect of such a misalignment on the estimated station coordinates.

6.9.1 No-net constraints and alignment

No-net constraints are a common tool to resolve certain rank deficiencies in GNSS processing and to align the solution to a reference frame. They can be separated into three constituents: rotation, translation, and scale. A no-net rotation (NNR) constraint is mandatory when station coordinates and satellite orbits are estimated together. In this case, a rank deficiency arises because the absolute orientation of the system cannot be determined by the relative GNSS observations. When geocenter coordinates are set up as additional parameters, it is also necessary to apply a no-net translation (NNT) constraint. A no-net scale (NNS) constraint is only needed in special cases, for example when antenna center z-offsets are estimated.

Section 3.7 describes the principle of the 7-parameter Helmert transformation. It also shows how the transformation parameters between two reference frames A and B can be estimated. The goal of no-net constraints is to constrain these parameters to zero.

This aligns the estimated station coordinates (i.e., frame B) to the reference coordinates (i.e., frame A). The resulting absolute alignment also resolves the rank deficiencies mentioned above. Equation (3.13) can be written in matrix notation as

$$\Delta\mathbf{x}_{\mathbf{r}_{\mathrm{NN}}} = \mathbf{B}\mathbf{y}\,. \tag{6.127}$$

Here, the coordinate differences in $\Delta\mathbf{x}_{\mathbf{r}_{\mathrm{NN}}}$ are those between the estimated coordinates (i.e., the station coordinate parameters) and the reference coordinates for all stations used in the no-net constraint. The no-net constraint can then be applied by introducing pseudoobservation equations

$$\mathbf{0} = \left(\mathbf{B}^T\mathbf{B}\right)^{-1}\mathbf{B}^T\Delta\mathbf{x}_{\mathbf{r}_{\mathrm{NN}}} \tag{6.128}$$

into the estimation process described in Chapter 5 (e.g., Zajdel et al., 2019). The strength of the constraints is controlled by the standard deviations assigned to these constraint equations. Usually, only a subset of all stations are used for no-net constraints (e.g., IGS reference frame stations). In this case, the columns of the matrix $\left(\mathbf{B}^T\mathbf{B}\right)^{-1}\mathbf{B}^T$ from (6.128) have to be mapped to those of the respective station coordinate parameters in the design matrix $\mathbf{A}$ of the full equation system.

Equation (6.128) gives equal weight to all stations. Processing issues of specific stations (e.g., gross outliers, systematic effects) can lead to erroneous station coordinate estimates. In extreme cases, using such a station for no-net constraints can result in a misalignment of the whole solution. Therefore, it is preferable to use weighted no-net constraints. A robust least-squares adjustment based on the equation system in (3.13) can be used for this purpose. The three coordinate differences of each station form a pseudoobservation group and the same weight is assigned to each group initially. The system is then solved iteratively and outlying stations are weighted down using a modified Huber estimator (Huber, 1981), similar to the procedure described in Section 5.8.1. Once the solution converges, the resulting weights for each group can be introduced into the constraint equations by homogenizing (6.128) as described in Section 4.2.1.

6.10 Antennas

Various antenna-related offsets and corrections have to be taken into account in GNSS processing (e.g., Maqsood et al., 2017). Figure 6.22 illustrates them at the transmitter and receiver end. The geometric range in the observation equation (5.1) described in Section 5.1 is defined between the antenna reference points (ARPs) of the satellite and receiver antennas. However, the satellite orbits refer to center-of-mass positions, while

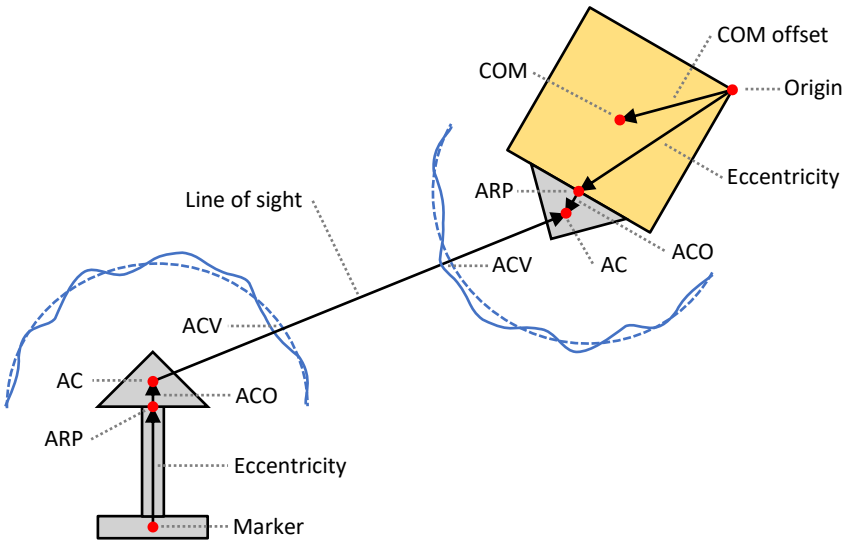

Figure 6.22: Illustration of connection between station marker, antenna reference points (ARPs), antenna centers (ACs), and satellite center of mass (COM) considering antenna eccentricities, antenna center offsets (ACOs), and antenna center variations (ACVs) (partly adapted from Maqsood et al., 2017)

the receiver coordinates refer to the position of a marker that represents the station. These antenna offsets are detailed in Section 6.10.1. In addition, the electronic center of an antenna can vary for different frequencies. Section 6.10.2 describes these antenna center offsets and also discusses direction-dependent variations.

6.10.1 Antenna offsets

At the station, the ARP is usually located at the bottom of the physical antenna. Since ground station antennas are often mounted on monuments, the connection between station marker and ARP is

$$\mathbf{r}^{\mathrm{TRF}}_{\mathrm{ARP},r} = \mathbf{r}^{\mathrm{TRF}}_{\mathrm{Marker},r} + \mathbf{T}^{\mathrm{TRF}}_{\mathrm{LRF}} \Delta\mathbf{r}^{\mathrm{LRF}}_{\mathrm{Eccentricity},r} \,. \tag{6.129}$$

Station operators usually provide $\Delta\mathbf{r}^{\mathrm{LRF}}_{\mathrm{Eccentricity},r}$ in a local topocentric reference frame (i.e., north, east, up). Therefore, this vector has to be transformed to the TRF via $\mathbf{T}^{\mathrm{TRF}}_{\mathrm{LRF}}$ (see Section 3.3).

At the satellite, the center of mass (COM) and the ARP are related via

$$\mathbf{r}^{\mathrm{CRF},s}_{\mathrm{ARP}} = \mathbf{r}^{\mathrm{CRF},s}_{\mathrm{COM}} + \mathbf{R}^{\mathrm{CRF}}_{\mathrm{SRF}} \left(\Delta\mathbf{r}^{\mathrm{SRF},s}_{\mathrm{Eccentricity}} - \Delta\mathbf{r}^{\mathrm{SRF},s}_{\mathrm{COM}} \right) \,. \tag{6.130}$$

Here, the center-of-mass offset $\Delta\mathbf{r}_{\text{COM}}^{\text{SRF},s}$ and the eccentricity of the ARP $\Delta\mathbf{r}_{\text{Eccentricity}}^{\text{SRF},s}$ are given in the SRF with respect to a physical origin. The location of this origin and the orientation of the SRF depend on the satellite type (Montenbruck et al., 2015b). For this reason, the IGS has adopted a common SRF for all GNSS satellites (see Section 3.4). The ARP and the origin are tied to the physical structure of the satellite, making $\Delta\mathbf{r}_{\text{Eccentricity}}^{\text{SRF},s}$ constant over time. In contrast, the position of the center of mass can change over time, mainly due to the usage of propellant to maneuver the satellite. An example for this are the two Galileo satellites that were launched into highly elliptical orbits (Navarro-Reyes et al., 2015). After the maneuvers to correct their orbits, which consumed a large part of their on-board propellant, the center of mass has changed by about 5 cm (European GNSS Service Centre, 2017).

The formulation in (6.130) assumes that values for $\Delta\mathbf{r}_{\text{Eccentricity}}^{\text{SRF},s}$ and $\Delta\mathbf{r}_{\text{COM}}^{\text{SRF},s}$ are known (i.e., have been published by satellite manufacturers). However, of the three GNSS constellations considered in this thesis, Galileo is the only one where this is the case (European GNSS Service Centre, 2017). For GPS and GLONASS satellites only estimated offsets between the satellite center of mass and the antenna center are available (e.g., Schmid et al., 2007; Schmid et al., 2016; Villiger et al., 2020). Lockheed Martin has recently started to publish calibrated offset values for the new GPS-IIIA satellites.

One way to work around the missing information is to assume that the origin and center of mass of the satellite are identical (i.e., $\Delta\mathbf{r}_{\text{COM}}^{\text{SRF},s} = \mathbf{0}$). The offset between a virtual antenna reference point and the origin can then be determined as the mean of the AC-COM offsets for the n_ν frequencies such that

$$\Delta\mathbf{r}_{\text{Eccentricity}}^{\text{SRF},s} = \frac{1}{n_\nu}\sum_{\nu}^{n_\nu}\Delta\mathbf{r}_{\text{AC-COM}}^{\text{SRF}}[\nu]^s\,. \tag{6.131}$$

The antenna center offset (ACO) between this virtual antenna reference point and the electronic antenna center at frequency ν then is

$$\Delta\mathbf{r}_{\text{ACO}}^{\text{ARF}}[\nu]^s = \mathbf{T}_{\text{SRF}}^{\text{ARF}}\left(\Delta\mathbf{r}_{\text{AC-COM}}^{\text{SRF}}[\nu]^s - \Delta\mathbf{r}_{\text{Eccentricity}}^{\text{SRF},s}\right)\,. \tag{6.132}$$

6.10.2 Antenna center offsets and variations

Following the sign conventions of the IGS ANTEX file format (Rothacher and Schmid, 2010), antenna center offset and variation corrections for a satellite or receiver antenna can be applied as

$$\text{ant}[\tau\nu a](\mathbf{k}^{\text{ARF}}) = -\mathbf{k}^{\text{ARF}}\cdot\Delta\mathbf{r}_{\text{ACO}}^{\text{ARF}}[\tau\nu a] + \Delta r_{\text{ACV}}[\tau\nu a](A,e)\,. \tag{6.133}$$

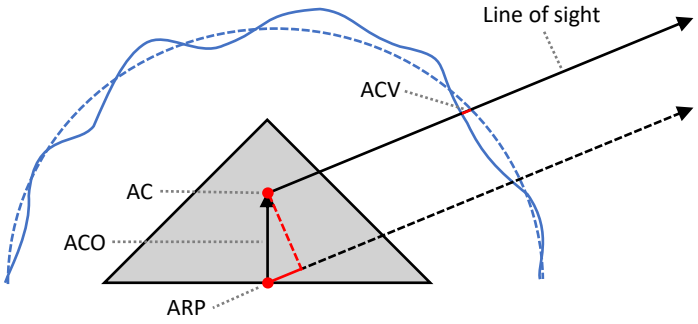

Figure 6.23: Projection of antenna center offset (ACO) into line of sight and antenna center variation (ACV) correction (adapted from Maqsood et al., 2017)

Here, $\Delta\mathbf{r}^{\text{ARF}}_{\text{ACO}}[\tau\nu a]$ is the offset from the antenna reference point to the electronic antenna center for a signal $[\tau\nu a]$. Figure 6.23 shows that it is projected into the line-of-sight vector $\mathbf{k}^{\text{ARF}}$, which is defined from the local antenna center to the remote antenna center. Due to the large distance between GNSS transmitters and receivers, this vector is equivalent to the line-of-sight vector between the antenna reference points, which was defined in Equation (5.13). Therefore, in case of the satellite antenna correction $\text{ant}[\tau\nu a]^s(\boldsymbol{p}^s_r)$ listed in the observation equation (5.1), the vector

$$\mathbf{k}^{\text{ARF},s} = \mathbf{T}^{\text{ARF}}_{\text{SRF}}\,\mathbf{R}^{\text{SRF}}_{\text{CRF}}\,\mathbf{k}^{\text{CRF}} \tag{6.134}$$

is substituted into (6.133). In case of the receiver antenna correction $\text{ant}[\tau\nu a]_r(\boldsymbol{p}^s_r)$, the substituted vector is

$$\mathbf{k}^{\text{ARF}}_r = -\mathbf{R}^{\text{ARF}}_{\text{LRF}}\,\mathbf{T}^{\text{LRF}}_{\text{TRF}}\,\mathbf{R}^{\text{TRF}}_{\text{CRF}}\,\mathbf{k}^{\text{CRF}}\,. \tag{6.135}$$

ACOs are not commonly estimated in GNSS processing because it would lead to a rank deficiency in the normal equation system. However, it is possible to set up ACO parameters and tightly constrain them to their a priori value. The resulting normal equations, for example from a daily processing, can then be stacked over long time periods to estimate a stable set of ACOs if needed. The intermediate parameters (see Section 5.3) already contain one bias parameter for each transmitted and received signal. An example for the partial derivatives of an observation group with respect to these parameters (i.e., their entries in the design matrix $\mathbf{C}_g$) is given in Equation (5.22). Consequently, the slice in the design matrix $\mathbf{D}_g$ that corresponds to the partial derivatives of one such bias parameter to its respective ACO parameters $\Delta\mathbf{r}^{\text{ARF}}_{\text{ACO}}[\tau\nu a]$ is simply

$$\frac{\partial b[\tau\nu a]}{\partial\Delta\mathbf{r}^{\text{ARF}}_{\text{ACO}}[\tau\nu a]} = \frac{\partial\,\text{ant}[\tau\nu a](\mathbf{k}^{\text{ARF}})}{\partial\Delta\mathbf{r}^{\text{ARF}}_{\text{ACO}}[\tau\nu a]} = (-\mathbf{k}^{\text{ARF}})^T\,. \tag{6.136}$$

Here, $\mathbf{k}^{\mathrm{ARF}}$ is either (6.134) in case of satellite ACOs or (6.135) in case of receiver ACOs.

The antenna center variation (ACV) correction $\Delta r_{\mathrm{ACV}}[\tau\nu a]$ in (6.133) describes direction-dependent variations for a signal $[\tau\nu a]$ (e.g. Maqsood et al., 2017). The azimuth and elevation angles A and e are those of $\mathbf{k}^{\mathrm{ARF}}$ in the respective ARF. Figure 6.24 shows examples for variations of a Galileo satellite and a receiver antenna on two different frequencies. As can be seen, the patterns clearly differ between the two frequencies both at the satellite and receiver antenna. Depending on the antenna and signal direction, ACV corrections can range from a few millimeters to several centimeters.

ACV patterns are usually determined from calibrations or, if such data is not available, they can be estimated. Fully calibrated Galileo ACV patterns have been published in European GNSS Service Centre (2017). For GPS and GLONASS satellites, only estimated circular patterns are available in the IGS ANTEX file (e.g., Schmid and Rothacher, 2003; Schmid et al., 2007; Schmid et al., 2016). Zehentner (2016) and Zehentner and Mayer-Gürr (2016) estimated full GPS satellite ACV patterns from LEO satellite observations, which indicate that there are also significant noncircular variations present at those antennas. They also showed that code observations can have distinct patterns from phase observations. Satellite ACVs are limited to a maximum opening angle of 15° to 20°, which covers the whole Earth and, in the latter case, also most LEO satellites. Receiver ACV patterns are determined using robot or anechoic chamber calibrations (e.g., Görres et al., 2006; Schmid et al., 2007; Schmid et al., 2016; Villiger et al., 2020). They typically cover the full hemisphere of the antenna.

6.10.3 Orientation of receiver antennas

Section 3.5 mentions that IGS stations are instructed to orient their receiver antennas towards geographic north (IGS Infrastructure Committee, 2015). This has the benefit that the axes of the ARF are aligned to those of the LRF. Therefore, this frame transition does not have to be considered when applying antenna center offsets and variations. However, for a variety of reasons, not all receiver antennas are or always have been oriented towards north. Information about the misalignment of receiver antennas can usually be found in the station log files provided by station operators, but was not reported together with other station metadata in commonly used file formats such as SINEX (Rothacher and Thaller, 2006). As a result, receiver antenna misorientations were typically disregarded by IGS analysis centers.

Depending on the antenna type, this disregard can lead to significant horizontal offsets in the estimated station coordinates. For example, the receiver antenna of IGS

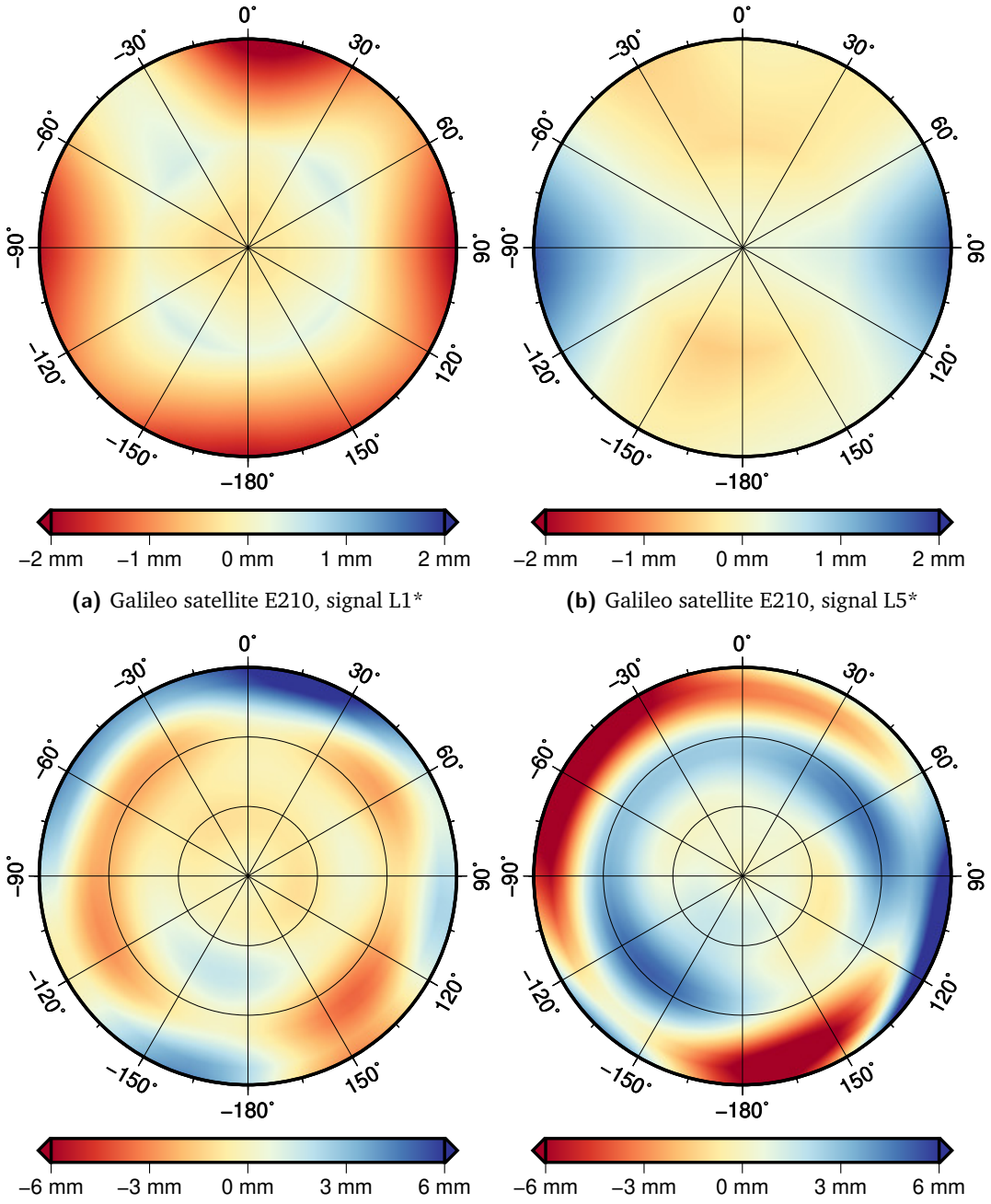

(a) Galileo satellite E210, signal L1*

(b) Galileo satellite E210, signal L5*

(c) Receiver antenna JAV_GRANT-G3T, signal L1*

(d) Receiver antenna JAV_GRANT-G3T, signal L5*

Figure 6.24: Antenna center variations (ACVs) for Galileo satellite E210 (top) and receiver antenna JAV_GRANT-G3T (bottom) for signals L1* (left) and L5* (right). Satellite figures are limited to 15° opening angle from boresight direction. Note the different colorbar limits for satellite and receiver antennas.

station ABPO (Ambohimpanompo, Madagascar) was misaligned by 180° (i.e., oriented towards geographic south) from 2007 to 2018. The antenna used during that time (ASH701945G_M with SCIT radome) only has calibrations for GPS L1 and L2 phase observations. ACVs are circular for both frequencies, which means they are irrelevant for this example.

The horizontal phase center offsets in the ARF are $x_1 = 0.8\,\mathrm{mm}$, $y_1 = -0.4\,\mathrm{mm}$ for L1 and $x_2 = -0.4\,\mathrm{mm}$, $y_2 = -0.5\,\mathrm{mm}$ for L2. In this case, the actual effect on the station coordinates is approximately that of the ionosphere-free linear combination (e.g., Hauschild, 2017b) of the ACOs. It is $x = \frac{\nu_1^2 x_1 - \nu_2^2 x_2}{\nu_1^2 - \nu_2^2} = 2.5\,\mathrm{mm}$ and $y = \frac{\nu_1^2 y_1 - \nu_2^2 y_2}{\nu_1^2 - \nu_2^2} = -0.4\,\mathrm{mm}$. An experiment where this station was processed over the period of 2014 with and without considering the antenna misalignment lead to median horizontal coordinate differences of $\Delta r_n = 5.1\,\mathrm{mm}$ in north-south direction and $\Delta r_e = -0.8\,\mathrm{mm}$ in east-west direction. This is almost exactly two times the ionosphere-free offset, which is the result of the ACOs being applied in opposite directions in the two solutions.

Another example is the IGS station ULAB (Ulaanbataar, Mongolia), whose antenna was also misaligned by 180° from 2011 to 2018. Its antenna at the time (JAV_RINGANT_G3T without radome) has multi-GNSS calibrations and features noncircular ACVs. Repeating the experiment from above for this station lead to mean horizontal coordinate differences of $\Delta r_n = -27.8\,\mathrm{mm}$ and $\Delta r_e = 18.2\,\mathrm{mm}$. Figure 6.25 displays the daily station coordinate differences, confirming that this offset is very stable over time. This station was processed using all available GPS, GLONASS, and Galileo signals. Therefore, the combined effect of the varying ACOs as well as the noncircular ACVs on the station coordinates becomes much more obfuscated. Nonetheless, the determined horizontal coordinate differences closely matched to an average of linear combinations for the different signals weighted by the number of observed satellites of that constellation. Table 6.12 shows results for further stations.

The issue of antenna misalignments first came up during preliminary station coordinate combinations of an IGS repro3 test processing. For the stations with misaligned antennas, TUG's contribution, which considered these misalignments, showed offsets close to those showcased in Table 6.12 compared to other analysis centers. After extended discussions, most analysis centers participating in repro3 started to consider antenna misalignments in their contribution. One important reason is that several GNSS stations that have or had misaligned receiver antennas are colocated with other space-geodetic techniques. Biases in the coordinates of such stations would negatively affect the determination of the ITRF, which combines these techniques based on local ties at colocation sites (e.g., Altamimi et al., 2016). Analysis centers also agreed to include metadata on antenna rotations in their solutions (e.g., SINEX files).

Table 6.12: Median coordinate differences (in LRF) between receiver antenna misalignments from geographic north being considered or not over the period of 2014 for several GNSS stations

Station	Rotation [°]	North [mm]	East [mm]	Up [mm]
ABPO	180	5.1	-0.8	0.0
BSMK	165	3.3	-2.9	0.1
CALL	121	5.2	5.1	-0.5
CHPI	-20	-0.4	-0.3	-0.4
GDMA	110	0.6	-0.1	-0.3
GLSV	160	12.3	-4.0	1.4
GSR1	1	0.1	-0.0	-0.0
HALY	3	-0.0	-0.1	0.0
HIL1	-15	0.7	-0.4	-0.6
HOLB	40	0.8	-0.7	-0.3
HYDE	3	0.2	-0.1	0.1
IQUI	-120	-2.0	7.0	0.2
JOEN	10	-0.4	-0.1	-0.2
JOZE	4	-0.7	-0.2	-0.2
KATC	4	0.0	-0.0	-0.0
KHAR	45	1.0	-4.5	0.3
KTVL	30	0.1	-3.0	-0.2
MCHN	180	0.9	0.6	0.1
NAMA	2	-0.0	-0.1	0.0
NAUR	-13	-0.5	0.2	0.2
NHIL	-18	-0.2	0.8	-0.2
NTJN	17	0.7	-0.0	0.2
POHN	180	4.2	6.8	-0.4
PPER	28	1.2	-0.1	1.6
PTAG	-1	-0.1	0.0	-0.0
RCMN	-170	1.5	8.3	0.1
SHE2	43	1.7	-0.1	2.3
STJ3	-85	-1.6	1.3	0.3
SVTL	5	-0.1	0.1	-0.1
TEHN	3	0.0	-0.2	0.1
ULAB	180	-27.8	18.2	-1.2
UZHL	180	12.9	-2.1	1.5
YCBA	83	4.9	2.3	0.3

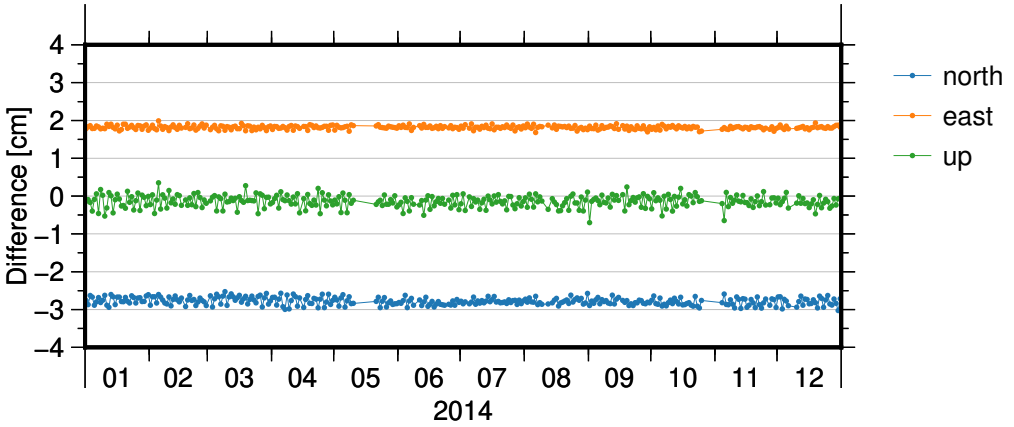

Figure 6.25: Differences between station coordinates when considering or disregarding the 180° antenna misalignment from geographic north for station ULAB

6.11 Other effects and corrections

The term $\mathrm{other}(\ldots)$ in the observation equation (5.1) described in Section 5.1 represents corrections that do not fit in any of the previous sections. They comprise several relativistic effects and phase wind-up.

6.11.1 Relativistic effects

Various relativistic effects have to be considered in GNSS processing (e.g., Ashby, 2003; Hofmann-Wellenhof et al., 2008; Formichella et al., 2021). Section 6.2.2.4 describes a relativistic correction of the equation of motion that forms the basis of dynamic satellite orbits. In addition, relativity affects satellite clocks and signal propagation. These effects can be directly applied to the observation equations in the form of range corrections.

First of all, time dilation and gravitational redshift cause a constant frequency offset in the satellite clocks (e.g., Ashby, 2003). The offset depends on the semimajor axis of the satellite orbit and thus differs per GNSS constellation. However, this offset is corrected for on a hardware level directly in the satellites so that for ground-based receivers the apparent satellite clock frequency conforms to its nominal value. Therefore, no explicit correction of this constant offset is required when processing GNSS observations.

Next to this constant offset, satellite clock frequencies are also affected by periodic variations. The main effect is caused by the slight eccentricity of the satellite orbits. Following Ashby (2003), this effect can be modeled directly as a range correction

$$\delta^{\text{eccentricity}}_{\text{relativity}}(t) = \frac{2}{c}\mathbf{r}^s(t) \cdot \dot{\mathbf{r}}^s(t)\,. \tag{6.137}$$

Here, $\mathbf{r}^s$ and $\dot{\mathbf{r}}^s$ are the satellite position and velocity in the CRF and c is the speed of light.

Kouba (2004) describes an additional periodic variation in the satellite clock frequency. This effect is caused by variations in Earth's gravitational potential due to Earth's oblateness. It can be modeled as a range correction

$$\delta^{J_{2,0}}_{\text{relativity}}(t) = \frac{3}{2} J_{2,0} \frac{R^2}{c} \sqrt{\frac{GM}{a^3}} \sin^2 i \sin 2u(t)\,, \tag{6.138}$$

where $J_{2,0} = 1.083 \cdot 10^{-3}$ is the potential coefficient describing Earth's oblateness, R is Earth's equatorial radius, c is the speed of light, GM is Earth's gravitational constant, a is the semimajor axis of the satellite's orbit, and i is its inclination angle. The argument of latitude $u(t) = \omega + \nu(t)$ describes the position of the satellite in the Keplerian orbit based on the argument of perigee ω and the true anomaly ν. It can also be obtained via Equation (6.9). According to Kouba (2009a) it is IGS convention to not apply this correction in GNSS processing.

GNSS signals are additionally delayed due to the curvature of spacetime (e.g., Ashby, 2003). The range correction due to this delay can be modeled as

$$\delta^{\text{spacetime}}_{\text{relativity}}(t) = 2 \frac{GM}{c^2} \ln \frac{\|\mathbf{r}_r(t)\| + \|\mathbf{r}^s(t)\| + \rho^s_r(t)}{\|\mathbf{r}_r(t)\| + \|\mathbf{r}^s(t)\| - \rho^s_r(t)}\,. \tag{6.139}$$

Here, GM is Earth's gravitational constant, c is the speed of light, $\mathbf{r}_r$ and $\mathbf{r}^s$ are the receiver and satellite position, and ρ^s_r is the geometric range between receiver and satellite as described in Equation (5.2).

A correction for the Sagnac effect is necessary in case the computations are conducted in an Earth-fixed reference frame (e.g., Ashby, 2003). However, in the context of this thesis, the observation equations are set up in an inertial reference frame and receiver positions and velocities are rotated into this frame when needed. Therefore, this correction can be disregarded and is not further discussed here.

6.11.2 Phase wind-up

The circularly polarized nature of GNSS signals leads to variations in the phase measurements. This effect is called phase wind-up and is caused by changes in the relative orientation of transmitter and receiver antennas (J. T. Wu et al., 1993). From the perspective of an inertial frame, a ground-based receiver antenna rotates with Earth. At the same time, a GNSS satellite orbits Earth while constantly adjusting its attitude

(see Section 6.1) and thus its antenna orientation. Therefore, the relative orientation between these two antennas continuously changes over time.

Beyerle (2009) derived an analytical formula to correct for this effect. Based on the two satellite antenna dipoles $\mathbf{e}_x^{\text{SARF}} = [\,1\;0\;0\,]^T$ and $\mathbf{e}_y^{\text{SARF}} = [\,0\;1\;0\,]^T$ in the satellite ARF, the effective dipoles of the transmitted signal in the receiver ARF are

$$\mathbf{x} = \mathbf{T}_{\text{CRF}}^{\text{RARF}} \left[\left(\mathbf{k} \times \mathbf{T}_{\text{SARF}}^{\text{CRF}}\, \mathbf{e}_x^{\text{SARF}} \right) \times \mathbf{k} \right] \tag{6.140}$$

and

$$\mathbf{y} = \mathbf{T}_{\text{CRF}}^{\text{RARF}} \left[\left(\mathbf{k} \times \mathbf{T}_{\text{SARF}}^{\text{CRF}}\, \mathbf{e}_y^{\text{SARF}} \right) \times \mathbf{k} \right] . \tag{6.141}$$

Here, $\mathbf{k}$ is the line-of-sight unit vector from the satellite to the receiver in the CRF as defined in Equation (5.13). The transformation matrix $\mathbf{T}_{\text{SARF}}^{\text{CRF}} = \mathbf{R}_{\text{SRF}}^{\text{CRF}}\, \mathbf{T}_{\text{SARF}}^{\text{SRF}}$ describes the transition from the left-handed satellite ARF to the right-handed CRF. Similarly, $\mathbf{T}_{\text{CRF}}^{\text{RARF}} = \mathbf{R}_{\text{LRF}}^{\text{RARF}}\, \mathbf{T}_{\text{TRF}}^{\text{LRF}}\, \mathbf{R}_{\text{CRF}}^{\text{TRF}}$ is the transformation matrix from the CRF to the left-handed receiver ARF. The individual transformation and rotation matrices are described in Section 3. The phase wind-up in units of length for a signal at frequency ν then follows as

$$\delta_{\text{PWU}}[\text{L}\nu] = \frac{c}{2\pi\nu} \left[2\pi N + \operatorname{atan2}\left(\mathbf{x}_y + \mathbf{y}_x,\, \mathbf{y}_y - \mathbf{x}_x \right) \right] , \tag{6.142}$$

where the subscripts refer to the x and y components of the respective vectors and c is the speed of light. Equation (6.142) considers that both ARFs are left-handed frames. The integer number of full phase cycles N must be taken into account by continuously tracking the phase wind-up angle between a satellite and receiver over time.

7 Observation preprocessing

Observation preprocessing is one of the first steps in GNSS processing. The goal is to detect observations that are faulty or of poor quality in order to remove them or weight them down. The reason for this is that they might negatively affect the least-squares solution and resulting products.

In the context of this thesis, observation preprocessing comprises the following steps. They are performed independently for each receiver.

1. **Observation initialization** All observations are checked against an inclusion/exclusion list of signal types. For example, observations with a certain attribute or frequency (e.g., GLONASS G3, Galileo E6) might want to be excluded from the processing. Observations are also checked for their reasonableness. Some RINEX observation files contain observations of a signal type that is not actually transmitted by the respective satellites. GLONASS observations are also checked to have the correct frequency number.
2. **Track definition** Continuous observations to the same satellite are linked to form tracks. They are used to define the ambiguity parameters in the processing (see Section 6.6.1). A track must contain continuous phase observations of the same phase types on at least two frequencies. A new track is formed in case a gap of more than one epoch (e.g., 30 seconds) occurs or the set of phase types changes.
3. **Initial clock estimation from code observations** A small equation system using only code observations is set up to get a rough estimation of the receiver clock errors. The parameters comprise a static receiver position, one clock error per epoch and observed GNSS constellation, and an STEC parameter per observation group. Separate clock errors are necessary because no code bias and satellite clock parameters are set up in this simplified equation system. The STEC parameters are preeliminated as described in Section 5.5. The equation system is then solved using a robust least-squares adjustment. It operates iteratively and weights down outlying observations based on a modified Huber estimator (see Section 5.8.1). The approximate clock error at each epoch then follows as the mean over all system-specific clock errors.

The whole process described above is performed iteratively until no clock error changes by more than some threshold (e.g., 100 m) from one iteration to the next or ten iterations have been reached. Any epoch where the clock error did not converge is disabled at the receiver. The whole receiver is disabled in case the static position did not converge below the above threshold.

4. **Removal of observations with gross code outliers** Observation groups that contain gross code outliers above a certain threshold (e.g., 100 m) are removed. This check uses reduced observations (i.e., "observed minus computed") based on all a priori models, approximate satellite orbits, satellite clocks, and receiver positions, as well as the estimated receiver clock errors from the previous step. If the observation groups to more than, for example, half of all satellites at one epoch contain gross code outliers, the whole epoch is disabled at the receiver.
5. **Cycle slip detection** Each track is analyzed with respect to possible cycle slips. Section 7.1 describes this process in detail. Tracks are split at each detected cycle slip. This can result in some very short tracks, especially close to the horizon, which are subsequently removed in the next step.
6. **Removal of poorly defined tracks** Tracks that do not fulfill certain criteria are removed. A track must contain a minimum number of epochs with observations (i.e., have a certain length). In addition, tracks that never exceed an elevation angle threshold (e.g., 15°) are removed as well. Such tracks containing almost exclusively observations close to the horizon, where the noise level is significantly higher, often result in inaccurate ambiguity parameters that can hamper the ambiguity resolution process (see Section 6.6.2).
7. **Outlier detection** In this final step, each track is checked for outliers. This procedure is described in Section 7.2. Observation groups with gross outliers are weighted down and these weights are carried over to the full processing.

The above steps ensure an overall high quality of the observation data used in the full processing. However, these methods are not perfect and some bad data is inadvertently going to end up in the processing. The combination of iterative least-squares adjustment and variance component estimation described in Chapter 5 mitigates this by automatically weighting down any remaining problematic observations.

7.1 Cycle slip detection

There are numerous studies on methods for cycle slip detection in GNSS phase observations (e.g., Beutler et al., 1984; Blewitt, 1990; Bisnath, 2000; de Lacy et al., 2008; Dai

et al., 2009; Banville and Langley, 2013; Cai et al., 2013). It is also still an active field of research, especially in the context of multi-GNSS and multi-frequency observations (e.g., Zhang and Li, 2016; Xiao et al., 2017; Li and Melachroinos, 2018; B. Li et al., 2019). Many of these methods use linear combinations of specific signals, such as the Hatch-Melbourne-Wübbena (HWM) linear combination (Hatch, 1983; Melbourne, 1985; Wübbena, 1985; Hauschild, 2017b). However, in a modern GNSS environment with a multitude of signals on several frequencies, it becomes more and more challenging to select a set of signal combinations in advance.

7.1.1 Estimation of epoch-wise ambiguities

The cycle slip detection method applied in this thesis is based on generalized HWM-like linear combinations. Using the simplified observation equations

$$f[\tau\nu a](t) = \rho(t) + I[\tau\nu]\,\mathrm{STEC}(t) + \lambda[\mathrm{L}\nu]\,n[\mathrm{L}\nu a](t)\,, \tag{7.1}$$

an equation system

$$\begin{bmatrix}\Delta\mathbf{l}[\mathrm{C}]\\ \Delta\mathbf{l}[\mathrm{L}]\end{bmatrix} = \begin{bmatrix}\mathbf{1} & \mathbf{I}[\mathrm{C}] & \mathbf{0}\\ \mathbf{1} & \mathbf{I}[\mathrm{L}] & \boldsymbol{\lambda}[\mathrm{L}]\end{bmatrix}\begin{bmatrix}\rho\\ \mathrm{STEC}\\ \mathbf{n}[\mathrm{L}]\end{bmatrix} \tag{7.2}$$

is set up for each epoch of a track. In Equation (7.1), ρ and STEC are the geometric and ionospheric components and $n[\mathrm{L}\nu a]$ is a biased ambiguity (see Section 6.6) for a specific phase type. The ionospheric factor I represents the first-order ionospheric correction and is $I[\mathrm{C}\nu] = \frac{q}{\nu}$ for code observations and $I[\mathrm{L}\nu] = -\frac{q}{\nu}$ for phase observations (see Section 6.4.1 for the definition of q). $\lambda[\mathrm{L}\nu]$ is the wavelength of a phase observation at frequency ν in meters, implying that the biased ambiguities are estimated in cycles. In (7.2), $\Delta\mathbf{l}[\mathrm{C}]$ and $\Delta\mathbf{l}[\mathrm{L}]$ are vectors containing reduced code and phase observations, respectively. $\mathbf{1}$ is a vector of ones, $\mathbf{I}[\mathrm{C}]$ and $\mathbf{I}[\mathrm{L}]$ are vectors consisting of the respective ionospheric factors, $\mathbf{0}$ is a matrix of zeros, and $\boldsymbol{\lambda}[\mathrm{L}]$ is a diagonal matrix containing the wavelengths of the corresponding phase observations. Finally, $\mathbf{n}[\mathrm{L}]$ is the vector of biased ambiguities linked to each phase observation. A simple example of (7.2) with two GPS code and phase observations on two frequencies is

$$\begin{bmatrix}\Delta l[\mathrm{C1W}]\\ \Delta l[\mathrm{C2W}]\\ \Delta l[\mathrm{L1W}]\\ \Delta l[\mathrm{L2W}]\end{bmatrix} = \begin{bmatrix}1 & I[\mathrm{C1}] & 0 & 0\\ 1 & I[\mathrm{C2}] & 0 & 0\\ 1 & I[\mathrm{L1}] & \lambda[\mathrm{L1}] & 0\\ 1 & I[\mathrm{L2}] & 0 & \lambda[\mathrm{L2}]\end{bmatrix}\begin{bmatrix}\rho\\ \mathrm{STEC}\\ n[\mathrm{L1W}]\\ n[\mathrm{L2W}]\end{bmatrix}. \tag{7.3}$$

The equation system is solved separately for each epoch using a weighted least-squares adjustment. The resulting time series of the biased ambiguities $n[\mathrm{L}\nu a]$ should be constant over the track, except if a cycle slip occurs. However, the noise of the time series is usually too high to confidently detect cycle slips. This is because the geometric and ionospheric components are determined solely by the code observations. For this reason, linear combinations of the individual biased ambiguities are formed. Such linear combinations result in different wavelengths and noise levels. For example, the popular wide-lane combination (e.g., Hauschild, 2017b) of phase ambiguities on the GPS L1 and L2 frequencies results in a wavelength of 86 cm. This makes it much easier to detect cycle slips.

7.1.2 Automatic determination of linear combinations

A modern GNSS environment usually involves more than two frequencies and possibly multiple phase signals per frequency. Therefore, it is favorable to automatically determine the optimal linear combinations of all available signals. The decorrelation/reduction process of the LAMBDA method (Teunissen, 1995; Al Borno et al., 2014) can be used to achieve this. Section 6.6.2.1 describes how this process is originally applied in preparation of integer ambiguity resolution. It automatically forms linear combinations that maintain the integer nature of the ambiguities while minimizing their correlations. The resulting linear combinations are sorted by their accuracy.

The determined linear combinations for the example from (7.3) are $n_{\mathrm{LC1}} = -7\,n[\mathrm{L1W}] + 8\,n[\mathrm{L2W}]$ and $n_{\mathrm{LC2}} = n[\mathrm{L1W}] - n[\mathrm{L2W}]$. The latter is the same as the aforementioned wide-lane combination, while the former is a less accurate linear combination. Another example, which involves five phase signals on three GPS frequencies, results in a transformation matrix

$$\mathbf{T} = \begin{array}{c} \\ n_{\mathrm{LC1}} \\ n_{\mathrm{LC2}} \\ n_{\mathrm{LC3}} \\ n_{\mathrm{LC4}} \\ n_{\mathrm{LC5}} \end{array} \begin{array}{c} \begin{array}{ccccc} n[\mathrm{L1C}] & n[\mathrm{L1L}] & n[\mathrm{L2W}] & n[\mathrm{L2L}] & n[\mathrm{L5Q}] \end{array} \\ \begin{bmatrix} -12 & -11 & 72 & 73 & -121 \\ & & 1 & -2 & -1 & 2 \\ & & & 1 & & -1 \\ 1 & -1 & & & & \\ & & & 1 & -1 & \end{bmatrix} \end{array} . \tag{7.4}$$

Here, it becomes obvious that the most accurate linear combinations are those between signals on the same frequency (n_{LC4} and n_{LC5}). This is because the geometric and ionospheric influence are completely removed by forming the difference of two such signals. The next most accurate linear combination is $n_{\mathrm{LC3}} = n[\mathrm{L2W}] - n[\mathrm{L5Q}]$ because

those two frequencies are close together, resulting in a long wavelength of 5.86 m. Another linear combination (n_{LC2}) combines four signals, and the least accurate linear combination (n_{LC1}) uses all original signals. The advantage of the LAMBDA algorithm is that it finds the optimal set of linear combinations for any mix of signals occurring in a track.

In the next step, the time series of biased ambiguities are transformed based on the determined linear combinations. A total variation denoising algorithm (Condat, 2013) is then performed on each linear combination time series except for the least accurate one. Then, cycle slips can be detected by forming epoch-wise differences of the denoised time series and checking them against a threshold of, for instance, 0.75 cycles. In case a cycle slip is detected, the track is split at this epoch.

7.1.3 Analysis of the ionospheric STEC

At this point, it is assumed that all cycle slips in the analyzed linear combinations have been detected successfully with the approach described above. Therefore, only the least accurate linear combination can still contain potential cycle slips. However, this linear combination is too noisy to reliably detect cycle slips. The time series of STEC estimates is analyzed instead to circumvent this issue. The assumption is that the STEC is a continuous function over time and any remaining jumps in this time series must be caused by cycle slips in the least accurate linear combination. Since the STEC values from solving (7.2) are determined solely from code observations and thus have a relatively low accuracy, a new equation system

$$\Delta\mathbf{l}[\mathrm{L}] = \begin{bmatrix} \mathbf{1} & \mathbf{I}[\mathrm{L}] \end{bmatrix} \begin{bmatrix} \rho \\ \mathrm{STEC} \end{bmatrix} \tag{7.5}$$

using only phase observation is set up for each epoch. Here, the only parameters are the geometric range ρ and the ionospheric STEC. This is similar to forming the geometry-free linear combination (e.g., Hofmann-Wellenhof et al., 2008), except that the equation system is overdetermined when more than two phase observations on two frequencies are involved. Solving this equation system using a weighted least-squares adjustment results in a time series of STEC values that are estimated purely from phase observations. This significantly reduces the noise of this time series.

The question now is how much a slip of one cycle in the least accurate linear combination amounts to in TEC units. This can be determined by setting up another equation system in the same form as Equation (7.5). However, in this case, $\Delta\mathbf{l}[\mathrm{L}]$ contains the first column of the inverse transformation matrix $\mathbf{T}^{-1}$ from (7.4) multiplied by the respective

wavelengths as pseudoobservations. In other words, the pseudoobservations represent the effect a jump of one cycle in the least accurate linear combination has on the original ambiguities. Taking the example from (7.4), the pseudoobservation vector is

$$\Delta\mathbf{l}[\mathrm{L}] = \begin{bmatrix} \lambda[\mathrm{L1}] \\ \lambda[\mathrm{L1}] \\ \lambda[\mathrm{L2}] \\ \lambda[\mathrm{L2}] \\ \lambda[\mathrm{L5}] \end{bmatrix} . \tag{7.6}$$

The equation system from (7.5) is then solved. In this example, the result is $\mathrm{STEC} = -0.501$ TEC units. A cycle slip in the least accurate linear combination then must amount to an integer multiple of the resulting STEC value. In the simpler example using only two phase signals on two GPS frequencies (i.e., n[L1W] and n[L2W]), the determined jump threshold is $\mathrm{STEC} = -0.513$ TEC units. This amounts to a jump of $\lambda[\mathrm{L2}] - \lambda[\mathrm{L1}] = 5.4\,\mathrm{cm}$ in the classic geometry-free linear combination of these two signals.

As summarized by Wei et al. (2019), there are many different methods to detect jumps of the determined size in the STEC time series. Some of those methods are polynomial fitting (e.g., Beutler et al., 1984; Lichtenegger and Hofmann-Wellenhof, 1990), Kalman filtering (e.g., Bastos and Landau, 1988), or higher-order time differencing (e.g., Hofmann-Wellenhof et al., 2008). Cai et al. (2013) proposed a method that is effective even under high ionospheric activity, where STEC values can rapidly change in time. Any jumps detected by these methods that are close to or exceed the threshold determined above then point to cycle slips in the least accurate linear combination. Same as with cycle slips in the other, more accurate linear combinations, the track is then split at the these epochs. In principle, it is also possible to repair some of the detected cycle slips instead of splitting the track. However, this was not done within the context of this thesis and the associated reprocessing and thus it is not discussed further here.

Figure 7.1 visualizes the effect of several simulated cycle slips on the linear combinations and STEC. This example uses real data of a track observed between station KOUR (Kourou, French Guiana) and GPS-IIIA satellite G04, The observed phase types and corresponding linear combinations match those of the example from Equation (7.4). The first simulated cycle slip of $\Delta n[\mathrm{L1C}] = 1$ at 12:00 is visible in the linear combination $n_{\mathrm{LC4}} = n[\mathrm{L1C}] - n[\mathrm{L1L}]$ of the two signals on L1. It cannot be detected by the other linear combinations because they do not involve this signal. The two cycle slips $\Delta n[\mathrm{L2W}] = 1$ and $\Delta n[\mathrm{L5Q}] = 1$ at 15:00 are visible in $n_{\mathrm{LC5}} = n[\mathrm{L2W}] - n[\mathrm{L2L}]$, but not in $n_{\mathrm{LC3}} = n[\mathrm{L2W}] - n[\mathrm{L5Q}]$. The latter is insensitive to this specific combination of cycle slips on the two signals, even though it involves both signals. The last cycle slip of $\Delta n[\mathrm{L5Q}] = 1$

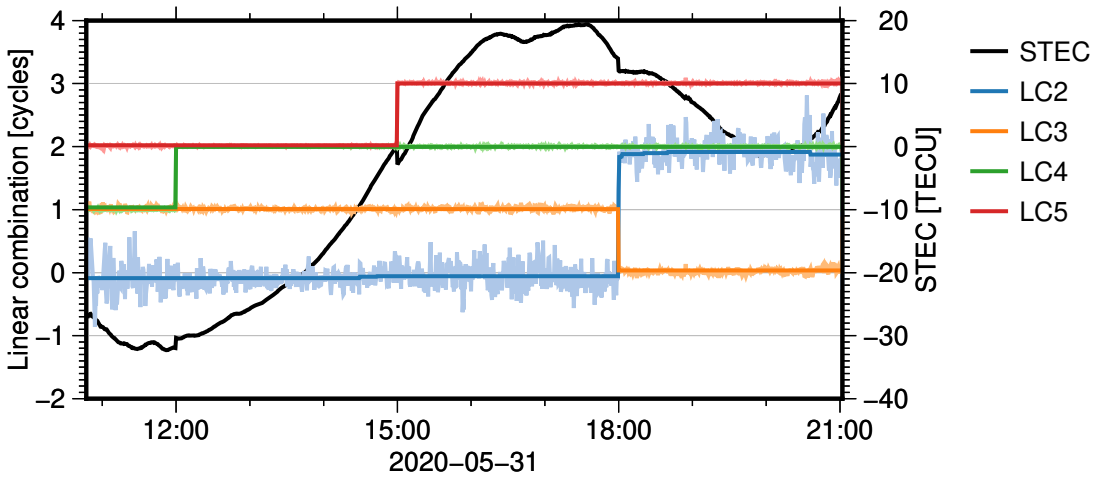

Figure 7.1: Noisy (light) and denoised (dark) linear combinations as well as STEC for track between station KOUR (Kourou, French Guiana) and GPS-IIIA satellite G04 using real data in combination with simulated cycle slips of $\Delta n[\mathrm{L1C}] = 1$ at 12:00, $\Delta n[\mathrm{L2W}] = 1$ and $\Delta n[\mathrm{L5Q}] = 1$ at 15:00, and $\Delta n[\mathrm{L5Q}] = 1$ at 18:00

at 18:00 is visible in both $n_{\mathrm{LC3}} = n[\mathrm{L2W}] - n[\mathrm{L5Q}]$ and $n_{\mathrm{LC2}} = n[\mathrm{L1L}] - 2\,n[\mathrm{L2W}] - n[\mathrm{L2L}] + 2\,n[\mathrm{L5Q}]$. The STEC time series is continuous and relatively smooth, except for the epochs where cycle slips were simulated into the observations. In this particular case, all of the simulated cycle slips are also visible as jumps in the STEC.

7.2 Outlier detection

Outlier detection is performed separately for each track. An equation system is set up based on the simplified observation equation

$$f[\tau\nu a](t) = \rho(t) + I[\tau\nu]\,\mathrm{STEC}(t) + b[\tau\nu a]\,, \tag{7.7}$$

where ρ and STEC are epoch-wise parameters for the range and ionospheric influence and $b[\tau\nu a]$ is a signal-specific bias parameter that is constant over the track. In case of phase observations, these bias parameters also contain the respective ambiguities. The ionospheric factor $I[\mathrm{C}\nu] = \frac{q}{\nu}$ for code observations and $I[\mathrm{L}\nu] = -\frac{q}{\nu}$ for phase observations considers the first-order ionospheric correction, with q being defined in Equation (6.48).

Estimating range and STEC parameters together with signal-specific bias parameters leads to a rank deficiency. Therefore, a set of estimable bias linear combinations has to

be determined. This step only has to be performed once per track using the full set of occurring signal types. A design matrix

$$\mathbf{B} = \begin{bmatrix} 1 & I_1 \\ \vdots & \vdots \\ 1 & I_n \end{bmatrix} \tag{7.8}$$

containing one row per occurring signal type and two columns for the range and STEC parameters is set up. It contains the partial derivatives of (7.7) with respect to these parameters. After QR decomposing (e.g., Golub and Van Loan, 2013) this matrix into

$$\mathbf{B} = \begin{bmatrix} \mathbf{Q}_1 & \mathbf{Q}_2 \end{bmatrix} \begin{bmatrix} \mathbf{R}_1 \\ \mathbf{0} \end{bmatrix}, \tag{7.9}$$

the matrix $\mathbf{Q}_2$ then defines the estimable bias linear combinations for this track. Next, observation equations

$$\Delta\mathbf{l} = \mathbf{A}\mathbf{x} + \mathbf{B}\mathbf{y} \tag{7.10}$$

are set up for each epoch. Here, $\mathbf{x}$ contains the estimable bias linear combinations using $\mathbf{A} = \mathbf{Q}_2$ and $\mathbf{y}$ contains the range and STEC parameters based on $\mathbf{B}$ as defined in (7.8). These observation equations are homogenized following Section 4.2.1. The range and STEC parameters are then eliminated on the observation equation level as detailed in Section 4.2.2.1. The resulting equation system now only contains parameters for the estimable bias linear combinations, which are constant over the track. A robust least-squares adjustment is then used to solve the equation system. This iterative process is similar to the one described in Section 5.8. It estimates variance factors for each observation group (i.e., epoch) and adjusts their weights based on the factor stated in Equation (5.48). As a result, observations above a certain threshold are weighted down. The lowered weights of these gross outliers are then adopted as initial weights in the actual processing.

8 Reprocessing campaign

This chapter describes the reprocessing conducted within the context of this thesis. The resulting GNSS products represent the contribution of Graz University of Technology (TUG) to the third reprocessing campaign (repro3) of the IGS. Section 8.1 provides details on the processing setup. This comprises information on the used models, settings, data, and metadata as well as the resulting products. It also briefly discusses some of the challenges a reprocessing of this scale brings with it.

The results are then evaluated and summarized in Section 8.2. This includes internal and external evaluations. The former focus on the internal consistency of the products, for example by looking at orbit midnight discontinuities or the noise level of station time series. External evaluations are mainly conducted by comparing the results to products from other analysis centers.

8.1 Processing setup

8.1.1 Models and settings

Table 8.1 lists the force models that were used to determine the dynamic satellite orbits (see Section 6.2). Earth's gravity field comprised the static field as well as trend and annual components. All components were evaluated up to a maximum spherical harmonics degree of 60. The grid-based ocean tide model FES2014b was converted to spherical harmonics and evaluated up to degree 10. Nontidal atmosphere and ocean mass variations from the model AOD1B RL06 were limited to degree 60. All other models were utilized up to their respective maximum resolution, if applicable. Following the v1.2.0 update of the IERS conventions (Petit and Luzum, 2010), the mean pole representation was replaced by the secular pole (Ries, 2017).

The surface areas and optical properties of the satellite box-wing models originated from various sources. Rodriguez-Solano et al. (2014) provided values for all GPS and GLONASS satellite types except for GPS-IIIA, which were taken from Steigenberger et al. (2020). The official box-wing models from European GNSS Service Centre (2017) were

Table 8.1: A priori force models used in satellite orbit integration

Effect	Model	Reference
Earth's gravity field	GOCO06s	Kvas et al. (2021)
Astronomical tides	JPL DE432	Folkner et al. (2009)
Solid Earth tides	IERS 2010	Petit and Luzum (2010)
Ocean tides	FES2014b	Lyard et al. (2021)
Pole tides	IERS 2010	Petit and Luzum (2010)
Ocean pole tides	IERS 2010	Petit and Luzum (2010)
Atmospheric tides	AOD1B RL06	Dobslaw et al. (2017)
Nontidal mass variations	AOD1B RL06	Dobslaw et al. (2017)
General relativity	IERS 2010	Petit and Luzum (2010)
Solar radiation pressure	Box-wing	Rodriguez-Solano et al. (2014)
Earth radiation pressure	Box-wing (CERES)	Rodriguez-Solano (2009)
Antenna thrust	Measured values	Steigenberger et al. (2018)

used for Galileo satellites. In the absence of information about the infrared properties of the materials used on satellites, the values $\alpha_I = 0.8$, $\delta_I = 0.1$, and $\rho_I = 0.1$ for absorption, diffuse reflection, and specular reflection were used for all satellite surfaces. These approximate properties were derived empirically and may significantly deviate from the actual material properties. Thus, modeling of infrared radiation pressure would benefit from officially published values.

Sixteen parameters were set up per satellite orbit on each day. They comprised six initial state parameters, seven solar radiation parameters from the ECOM2-7 model, and three pseudostochastic pulse parameters at the center of each 24-hour orbit arc (see Section 6.2). The pseudostochastic pulse parameters were constrained with $\sigma = 0.1\,\mu\mathrm{m/s}$ in the along-track, cross-track, and radial directions of a local orbit reference frame. The same parametrization was used for all satellite types of all three constellations.

Constant station coordinate parameters were set up for each day. The network was aligned to the IGSR3 reference frame by applying no-net rotation and no-net translation constraints (see Section 6.9.1) with standard deviations of $\sigma_{\mathrm{NNR/NNT}} = 0.01\,\mathrm{mm}$. The no-net translation constraint was added so that the resulting orbits refer to the center of network/figure.

Tidal deformations acting on station coordinates (see Section 6.9) were accounted for using the models listed in Table 8.2. In this case, the ocean tide model was evaluated up to degree 720 in order to capture localized effects, especially in coastal areas. The secular pole from the updated IERS conventions (Petit and Luzum, 2010) was also used in the tidal deformation models. Following the ITRF conventions, loading deformations due to nontidal mass variations were not applied as corrections and are thus present in the resulting station coordinates.

Table 8.2: Tidal deformation models applied to station positions

Effect	Model	Reference
Solid Earth tides	IERS 2010	Petit and Luzum (2010)
Ocean tides	FES2014b	Lyard et al. (2021)
Pole tides	IERS 2010	Petit and Luzum (2010)
Ocean pole tides	IERS 2010	Petit and Luzum (2010)
Atmospheric tides	AOD1B RL06	Dobslaw et al. (2017)

Tropospheric slant delays were modeled based on Vienna Mapping Functions 3 (VMF3) (Landskron and Böhm, 2018). The $1\times1^\circ$ grid-based version of VMF3 with included a priori gradients was used. As described in Section 6.7, the grid-based values were interpolated to the actual station positions. This model comes in two variants, one based on an ERA-Interim reanalyis and one based on the operational model of the ECMWF. The former provides a consistent model from 1979 to 2019, which is why it was chosen for the reprocessing conducted within the context of this thesis. Since the ERA-Interim version was only available until August 2019, the operational variant had to be used from that point until the end of 2020.

Tropospheric residual zenith wet delays were estimated at each station using first-degree splines with two-hourly knots (i.e., a piecewise linear representation). Horizontal gradient delays in north-south and east-west direction were parameterized as constant and trend components over the full day for each station. Therefore, 17 tropospheric parameters (13 for wet delays and two each for both gradient directions) were set up per station and day.

8.1.2 Station network

A list of 1212 stations for consideration in repro3 was proposed within the IGS. These stations were ordered by their priority with respect to the ITRF. IGS14 stations and sites co-located with other space-geodetic techniques had the highest priority, while regional networks and other IGS stations had lower priorities. Figure 8.1 visualizes the locations of all stations on a global map. The color coding represents how long each station has been operating within the repro3 time period.

One aim of this thesis was to process as many of these stations as possible. In total, 1182 (or 97.5%) of all 1212 suggested stations have been processed. However, as Figure 8.1 shows, not all stations have been active over the full period. Figure 8.2 displays the number of stations processed each day. The station count linearly increases from 1994 to 2015 and then plateaus around 850 stations per day before it slightly decreases towards

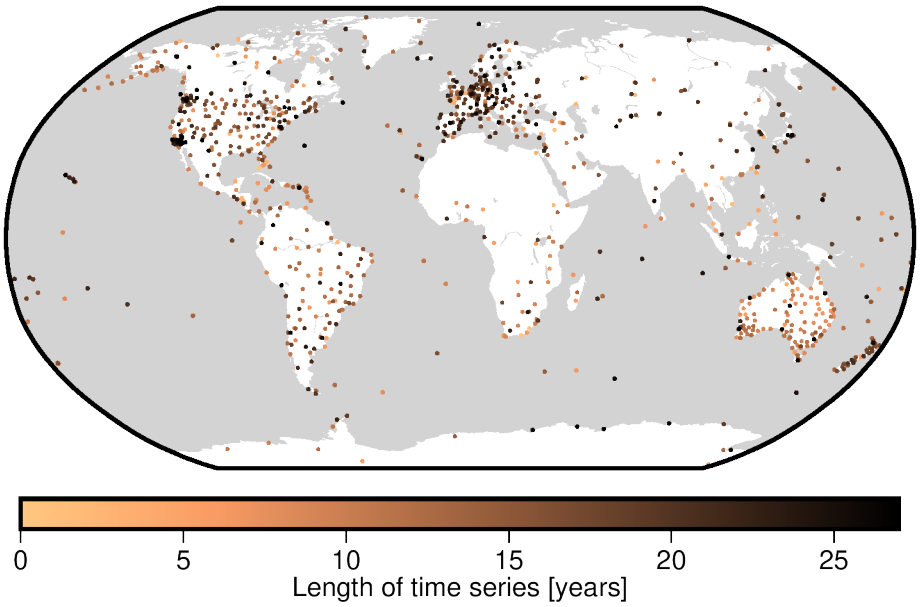

Figure 8.1: Stations used in the reprocessing and their time series lengths (adapted from Rebischung, 2021)

the end of the time series. The main reason for this drop at the end is that observation data from a number of stations could not be obtained in time for the processing, which was conducted with a short delay of some weeks throughout large parts of 2020.

The processing scheme described in Section 5.9.2 relies on the definition of a core network. There are two main requirements for this network. Firstly, it should be well and evenly distributed around the globe. This was achieved by splitting Earth's surface into 78 regions based on a Reuter grid (Reuter, 1982). Such a grid has equidistant spacing along the meridians and the number of points per circle of latitude decreases with increasing latitude (Eicker, 2008). All stations were then assigned to grid points based on a nearest neighbor algorithm. The resulting core station list consisted of 69 groups, as nine grid cells over the oceans contained no stations. Figure 8.3 shows the distribution of the Reuter grid points, the corresponding Voronoi regions, and the resulting groups of stations.

The second requirement for the core network is that it should cover all signal types observed by any receiver in the full network. This implies that it should consist mainly of multi-GNSS receivers so that all constellations are covered by the core network. The stations within each group defined above were prioritized by their multi-GNSS capability. Galileo-capable receivers gained the highest priority, followed by GLONASS-capable receivers and lastly by GPS-only receivers. This prioritization was chosen because almost all Galileo-capable receivers can also observe GLONASS satellites and all receivers can track GPS satellites. Within each category, stations were ordered by the earliest date they

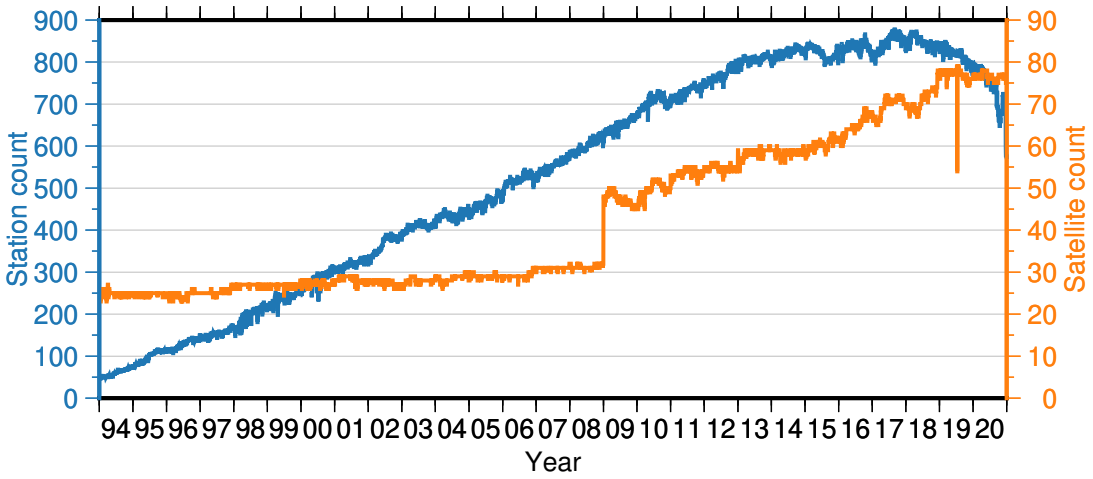

Figure 8.2: Number of processed stations and satellites per day

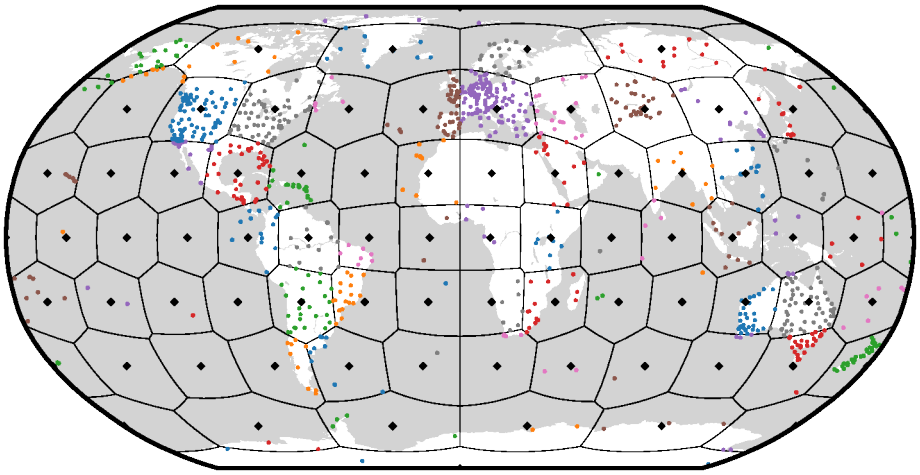

Figure 8.3: Definition of the core network groups. Black diamonds represent Reuter grid points and colored points are stations. Different colors are only used for easier differentiation between groups

operated a receiver capable of tracking the respective constellation. For the processing of a particular day, the core network was then defined by choosing the first available station per group.

8.1.3 Data and metadata

A brief summary about the data and metadata used in the reprocessing follows below.

Observations The processing used the full 30-second observation sampling period. Observation data in RINEX 3 format was prioritized over the older RINEX 2 format for stations that provided both. GLONASS observations on frequency G3 were

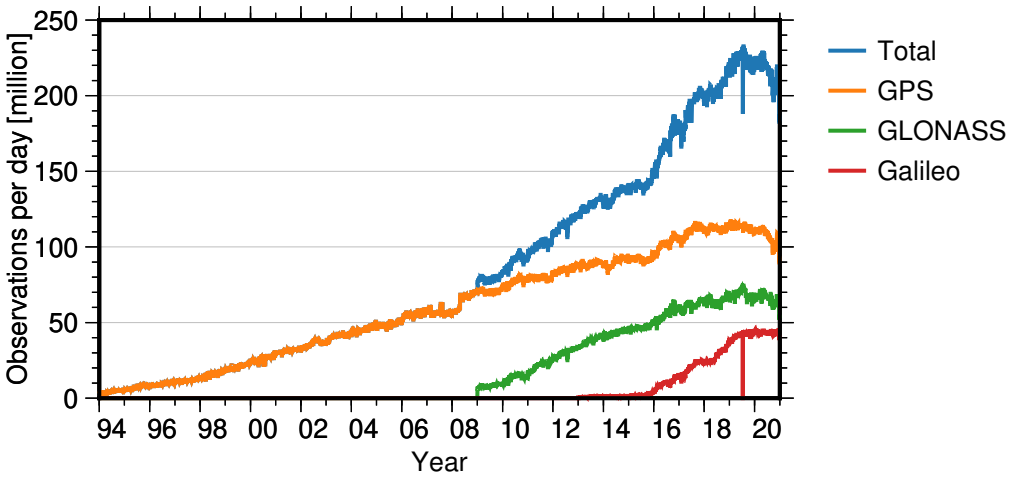

Figure 8.4: Number of processed observations per day

excluded because only a few satellites transmitted on this frequency and a mix of FDMA and CDMA signals further complicates the definition of signal biases. Galileo observations on frequency E6 were excluded as well. Tests before the start of the reprocessing revealed processing issues in the early Galileo years, where only a few stations tracked this frequency. For reasons of consistency, it was decided to exclude this frequency over the full period, even though the situation significantly improved towards the end of the time series. Figure 8.4 shows the number of processed observations per day over the full period. In total, around 1.65 trillion code and phase observations were processed over the 27 years.

Antenna calibrations Satellite and receiver antenna calibrations were taken from the igsR3_2135.atx ANTEX file. In case no satellite antenna calibrations were available for signals on a specific frequency (e.g., GPS L5), the calibrations from the nearest frequency were used. The IGS repro3 conventions for receiver antenna calibrations were stricter. All observations on frequencies without antenna calibrations at the respective receiver had to be excluded from the processing.

Station data and metadata The approximate position and the history of used antenna and receiver types for each station were extracted from the respective station log files. This included the eccentricity and orientation of the antennas (see Section 6.10.3). The solution was aligned to the IGSR3 reference frame using precise station positions from the IGSR3_2077.snx SINEX file. The instantaneous position on a particular day was determined from the linear motion in combination with possible post-seismic deformation effects. In case a station experienced a discontinuity occurring after the definition of the reference frame, it was excluded from the no-net constraints from this point onward.

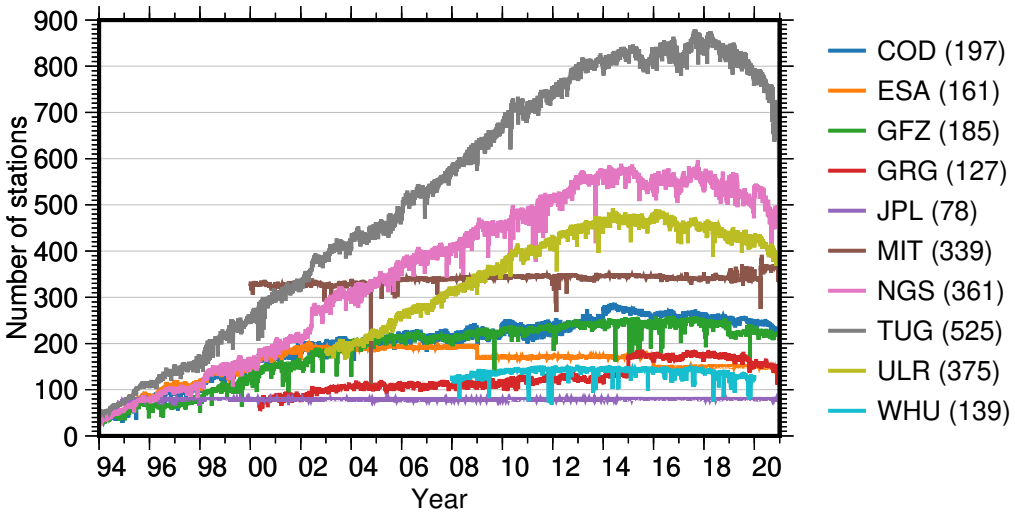

Figure 8.5: Daily number of stations contributing to the IGS combination for each analysis center. Average over full period in parenthesis (adapted from Rebischung, 2021)

8.1.4 Processing challenges

The reprocessing conducted within the context of this thesis was very computationally challenging. The main reason for this was the aim of including as many signals and stations as possible in the processing. Figure 8.5 shows that the number of stations included in the contribution by TUG is significantly higher than in any other contribution. As displayed in Figure 8.4, this led to a very high number of observation per day, especially once GLONASS and Galileo entered the processing in 2009 and 2013, respectively.

The large number of parameters was even more of a challenge. Figure 8.6 displays the number of parameters that had to be set up for each day. While the ionospheric STEC parameters were preeliminated (see Section 5.5), there still remained millions of parameters per day during the later periods of the time series. This issue was mitigated to some degree by applying the strategies for solving large systems described in Section 5.9.

The computations were performed on a cluster of servers owned by the Institute of Geodesy at Graz University of Technology. It featured a total of 248 processor cores and 2.2 terabytes of memory at the time. Several days were processed simultaneously on the cluster, with each day using 16 cores in parallel. Figure 8.7 shows the time it took to process each daily solution on one of these servers. While the GPS-only periods up until 2009 only took 1–3 hours on average per day, the processing runtime started to increase significantly once GLONASS and Galileo were included. The spread increases towards the end of the time series because the differences between the various server hardware

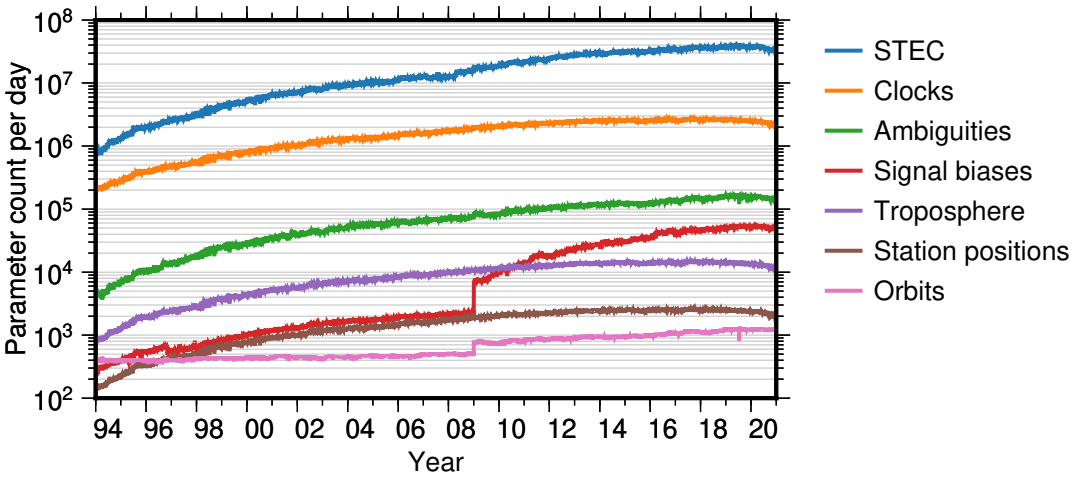

Figure 8.6: Number of estimated parameters per day

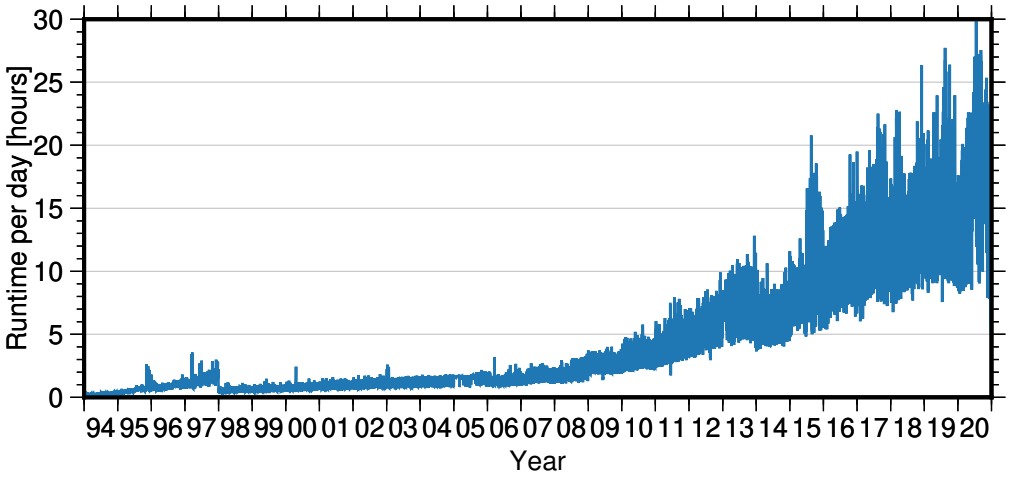

Figure 8.7: Processing runtime per day

configurations became more pronounced the longer each day took to process. It took around 685 000 core hours in total to process the full 27-year time period.

The processing scheme described in Section 5.9.2 was not applied from 1994 to the end of 1997. The reason for this was that the limited number of stations and their unfavorable global distribution during that period did not facilitate the utilization of a core network. Therefore, all stations were processed together from the start, which was more computationally demanding, but still feasible with the low number of stations operating at the time. The increased runtimes during this period are clearly visible in Figure 8.7.

Finally, Figure 8.8 shows the memory usage throughout the processing for one exemplary day in 2020. The color coding in the background represents the steps of the processing

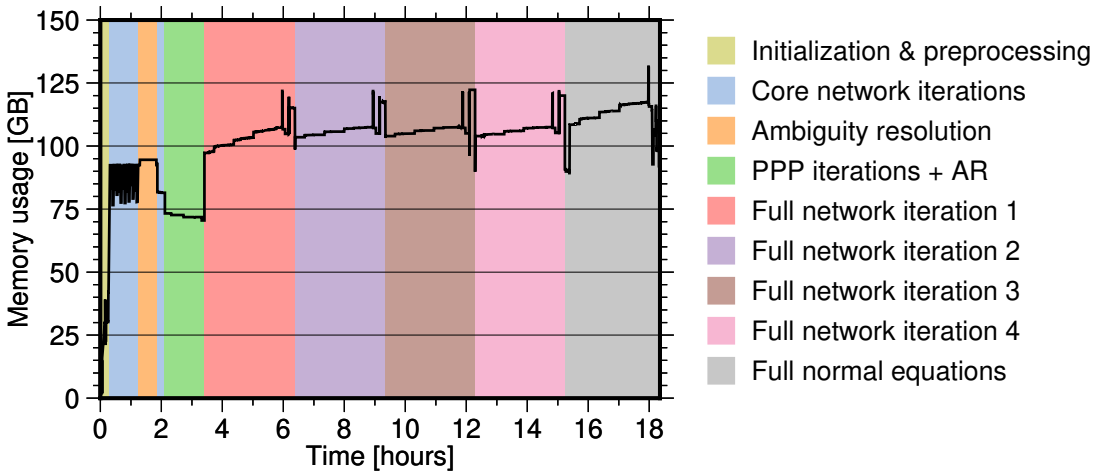

Figure 8.8: Example of memory usage and runtime for a day in 2020

scheme described in Section 5.9.2. It becomes obvious that most of the time was spent on the four full network iterations. The initial iterations using only the core network and the subsequent ambiguity resolution step finished in less than two hours. Processing the around 700 other stations individually then only took about 1.5 hours. The final step of setting up the full normal equation system including the antenna center offset parameters also took a significant amount of time. These normal equations are one of the products provided to users.

8.1.5 Products

Table 8.3 lists the GNSS products resulting from the reprocessing conducted within the context of this thesis. These files are available in the data repository of Graz University of Technology (Strasser and Mayer-Gürr, 2021) and in the IGS global data centers. Satellite orbits and troposphere parameters are provided at a 5-minute sampling period, while satellite attitude as well as satellite and receiver clock errors are provided at a 30-second sampling period. All other products have a daily sampling period. The only exception are the GPS L5 phase biases, which are provided in the form of piecewise linear functions with 15-minute intervals within the SINEX_BIAS file format (Schaer, 2018). The clock files only contain receiver clock errors for a subset of stations connected to Hydrogen masers or timing laboratories. This is because the large number of processed stations would otherwise result in very large clock files and clock errors of receivers with low-quality internal clocks are of limited interest to users.

Table 8.3: IGS repro3 products by Graz University of Technology (TUG). `yyyy` and `ddd` are placeholders for year and day of year, respectively

Product	Filename
Satellite orbits	`TUG0R03FIN_yyyyddd0000_01D_05M_ORB.SP3.gz`
Satellite attitude	`TUG0R03FIN_yyyyddd0000_01D_30S_ATT.OBX.gz`
Satellite/receiver clock errors	`TUG0R03FIN_yyyyddd0000_01D_30S_CLK.CLK.gz`
Satellite/receiver signal biases	`TUG0R03FIN_yyyyddd0000_01D_01D_OSB.BIA.gz`
Station coordinates	`TUG0R03FIN_yyyyddd0000_01D_01D_CRD.SNX.gz`
Solution and normal equations	`TUG0R03FIN_yyyyddd0000_01D_01D_SOL.SNX.gz`
Earth rotation parameters	`TUG0R03FIN_yyyyddd0000_01D_01D_ERP.ERP.gz`
Troposphere parameters	`TUG0R03FIN_yyyyddd0000_01D_05M_TRO.TRO.gz`

Some postprocessing steps were performed on clock errors and code biases during the conversion to the IGS file formats. Firstly, satellite clocks were absolutely aligned to the daily mean of the broadcast clocks for each constellation. The mean clock offset

$$\bar{\delta} = \frac{1}{S} \sum_{s}^{S} \frac{1}{N^s} \sum_{i}^{N^s} \left(\hat{\delta}_i^s - \delta_{i,0}^s \right) \tag{8.1}$$

between the estimated clocks $\hat{\delta}_i^s$ and the broadcast clocks $\delta_{i,0}^s$ over all epochs N^s and satellites S of one constellation was determined. This constant offset was then shifted from the respective satellite clock errors to the receiver code biases of the corresponding system. For GLONASS, the offset was determined per frequency number and shifted to the receiver code biases linked to the respective frequency number. The offset for GPS was always zero since the time system was aligned to the GPS broadcast clocks in the processing (see Section 6.3.2).

Secondly, GLONASS satellite signal biases were aligned so the differences between the frequency numbers are minimal at the receivers. This is beneficial for PPP users that do not set up individual signal biases per frequency number at the receiver. For this alignment, the mean signal bias

$$\bar{b}[\tau\nu a]_r = \frac{1}{K} \sum_{k}^{K} \hat{b}[\tau\nu_k a]_r \tag{8.2}$$

over all frequency numbers K was determined per signal type $[\tau\nu a]$ at each receiver r. It was used to obtain bias residuals $\tilde{b}[\tau\nu_k a]_r = \hat{b}[\tau\nu_k a]_r - \bar{b}[\tau\nu a]_r$ for the individual signal biases. Then, the mean of the bias residuals

$$\bar{b}[\tau\nu_k a] = \frac{1}{R} \sum_{r}^{R} \tilde{b}[\tau\nu_k a]_r \tag{8.3}$$

over all receivers R for a signal type and frequency number was shifted from the respective receiver biases to the satellite biases. Both of these alignments do not affect the internal consistency of the products.

8.2 Evaluation of results

8.2.1 Station positions

Station positions are the most important product of the reprocessing. The solutions of all IGS analysis centers are combined to form the contribution of GNSS to the next ITRF. Rebischung (2021) states that the combination process for the IGS contribution to ITRF2020 was similar to that of ITRF2014 (Rebischung et al., 2016) with only some minor changes. Section 8.2.1.1 evaluates the station positions by comparing the contributions of the analysis centers with respect to the combination. Section 8.2.1.2 then analyzes the internal quality of the station positions by determining upper bounds of their noise. This includes an investigation about remaining geophysical signals that artificially increase the determined noise floor.

8.2.1.1 External evaluation via combination results

The external evaluation is based on the residuals and formal errors from the IGS combination process. Rebischung (2021) features an in-depth analysis of these and other combination results. One of the conclusions is that TUG is the clear front runner among all analysis center contributions. Another conclusion is that the combined IGS time series is only marginally cleaner than the TUG time series, which further confirms the high quality of the contribution by TUG.

Figure 8.9 compares the RMS values of station position residuals from the different analysis center contributions. The time series have been smoothed with a 91-day median filter to facilitate an easier interpretation of the otherwise noisy original time series. It is clearly visible that the TUG solution has a significantly smaller RMS in all three coordinate components than other solutions over most of the repro3 period. This is confirmed by the median values of the daily station position residuals RMS, which are listed in Table 8.4 for all analysis centers. Here, TUG is the only solution with submillimeter RMS values in the horizontal components and an up component RMS below 3 mm.

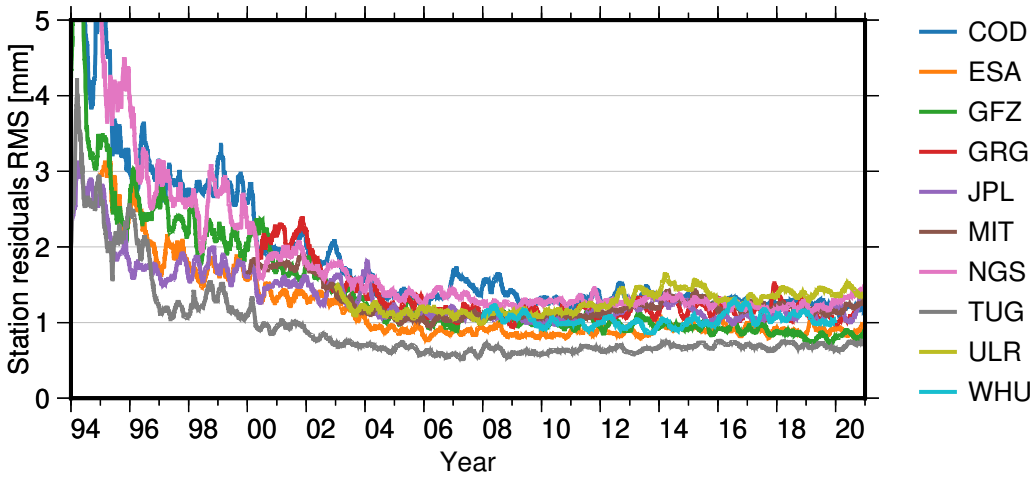

(a) North component

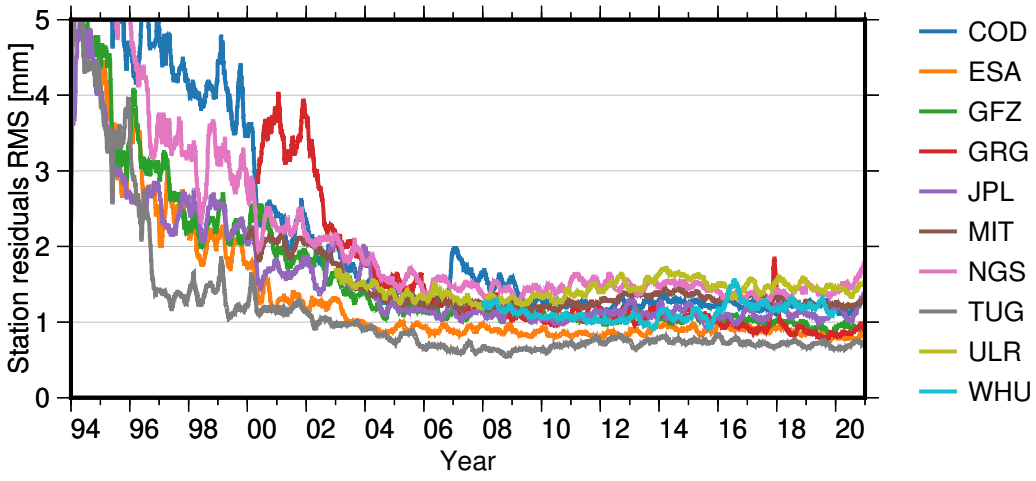

(b) East component

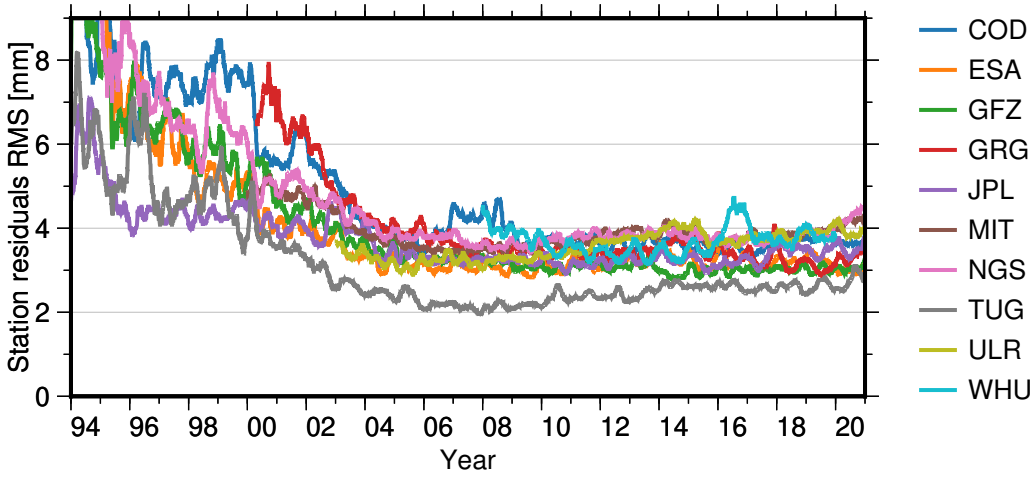

(c) Up component

Figure 8.9: Smoothed (i.e., 91-day median filtered) station position residuals RMS of individual analysis center solutions with respect to the IGS combination. Note the different y-axis scale for the up component

Table 8.4: Median values of daily station position residuals RMS for individual analysis center solutions with respect to the IGS combination and their median formal errors after optimal weighting

Analysis	Median residuals RMS [mm]			Median formal errors [mm]		
center	North	East	Up	North	East	Up
COD	1.5	1.5	4.1	1.3	1.2	4.2
ESA	1.0	1.0	3.3	1.0	0.9	3.3
GFZ	1.1	1.2	3.4	1.0	1.0	3.5
GRG	1.2	1.2	3.6	1.1	0.9	3.3
JPL	1.2	1.3	3.5	1.2	1.1	3.6
MIT	1.2	1.3	3.8	1.2	1.2	3.7
NGS	1.4	1.6	4.1	1.3	1.1	3.9
TUG	0.7	0.8	2.7	0.7	0.7	2.5
ULR	1.3	1.4	3.6	1.2	1.2	3.6
WHU	1.0	1.1	3.6	1.0	1.0	3.3

Table 8.4 also lists the median formal errors of the analysis center contributions. According to Rebischung (2021), the daily formal errors can be seen as a proxy for the analysis center weights in the combined solution. The median formal errors of the TUG solution are significantly smaller than those of other analysis centers, which implies that it got the highest weight on average over the full time series. Figure 8.10 shows the time series of formal errors for the TUG contribution. The daily variation of the formal errors is very small from the mid 2000s onward. This means the solution has a consistently high quality during that period. Earlier in the repro3 period, especially in the 1990s, the daily variations are much higher. This increased variation can be mainly attributed to processing difficulties caused by the limited quality of the station network and GPS constellation at the time.

8.2.1.2 Internal evaluation and geophysical signal analysis

The individual station position time series can provide an insight into their noise levels without relying on external products. However, it is difficult to separate the actual noise from remaining geophysical signals. Such signals can remain in the position time series because the applied correction models are neither perfect nor complete. For example, loading effects caused by high-frequency nontidal variations in the atmosphere, oceans, and continental hydrology were not considered in repro3 by convention. These geophysical processes mainly affect the up component, where they can amount to several millimeters to centimeters depending on the location of the station.

However, several more prominent signals had to be considered in the following noise analysis. First, the time series had to be split at known discontinuities. For instance,

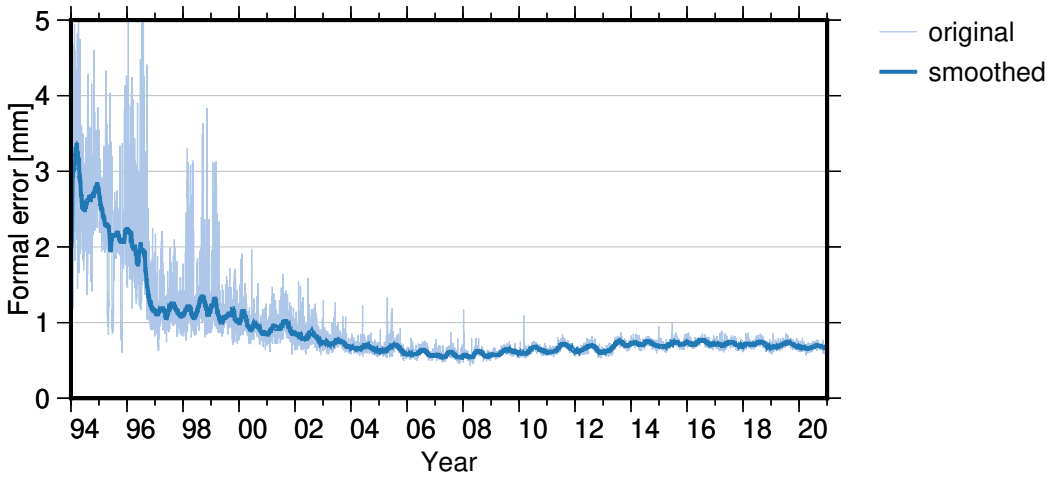

(a) North component

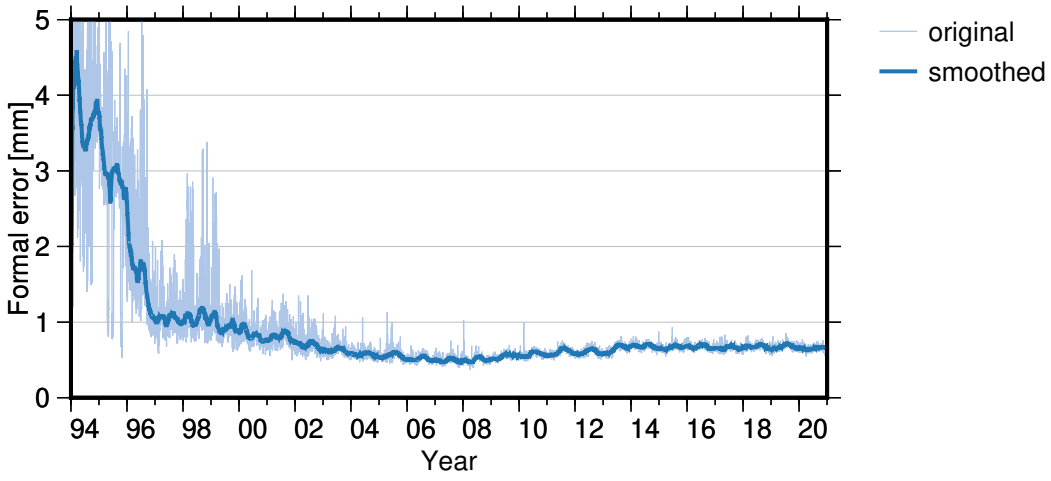

(b) East component

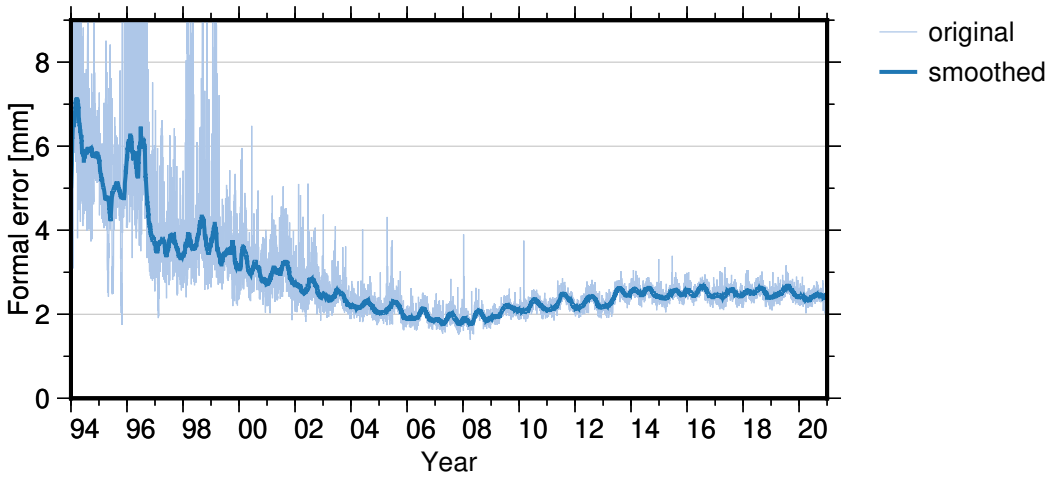

(c) Up component

Figure 8.10: Original and smoothed (i.e., 91-day median filtered) station position formal errors of TUG solution from the IGS combination. Note the different y-axis scale for the up component

equipment changes or earthquakes can lead to jumps in one or more coordinate components. For this reason, the analysis was limited to 257 stations from the IGb14 reference frame for which these discontinuities are known. Four other IGb14 stations (METS, RIOG, TAH1, VACS) had to be excluded since their position time series contained remaining jumps or other large systematic effects. Intervals shorter than two years were removed as they might misrepresent the long-term noise behavior. Finally, constant, trend, and annual components were estimated for and removed from each interval. This was done to remove large geophysical signals such as those from plate tectonics and the seasonal water cycle.

Figure 8.11 shows the standard deviations over the resulting time series for each station. The stations are ordered by the standard deviation for each coordinate component. The median standard deviations for the north, east, and up components are 1.76 mm, 1.88 mm, and 5.34 mm, respectively. A few stations have significantly higher standard deviations than the rest, pointing to remaining systematic effects in their time series.

As mentioned at the beginning of this section, the up component potentially includes remaining signals that might be explained by geophysical models. The following analysis focused on loading effects caused by high-frequency nontidal variations in the atmosphere, oceans, and continental hydrology. The former two were determined using the model AOD1B RL06 (Dobslaw et al., 2017) and the latter using the Land Surface Discharge Model (LSDM; Dill, 2008). Both models were evaluated up to a spherical harmonics degree of 180. Their time series were processed in the same way as the station position time series. This included splitting at IGb14 discontinuities and removing constant, trend, and annual components. They were then removed from the station position time series before computing updated standard deviations.

Figure 8.12 visualizes the changes in standard deviations of the up component due to the removal of these geophysical signals. The order of the stations corresponds to that of Figure 8.11c. It can be seen that removing atmospheric and oceanic loading had the most significant effect. The standard deviations decreased by a median of 6.6% (to 4.99 mm) over all stations and up to around 30% for individual stations. Some stations showed an increase in their standard deviations, which might be caused by model insufficiencies or its limited spatial resolution.

The influence of removing a hydrological model was much lower. The median standard deviation over all stations only decreased by 0.5% (to 5.31 mm), with the highest reduction being around 10%. On the other hand, some stations showed a large degradation of their standard deviations of up to 30%. A possible explanation is that continental hydrology is difficult to model and its effects are often very localized (Döll et al., 2016), resulting in unrealistic corrections at some locations. Finally, removing both models

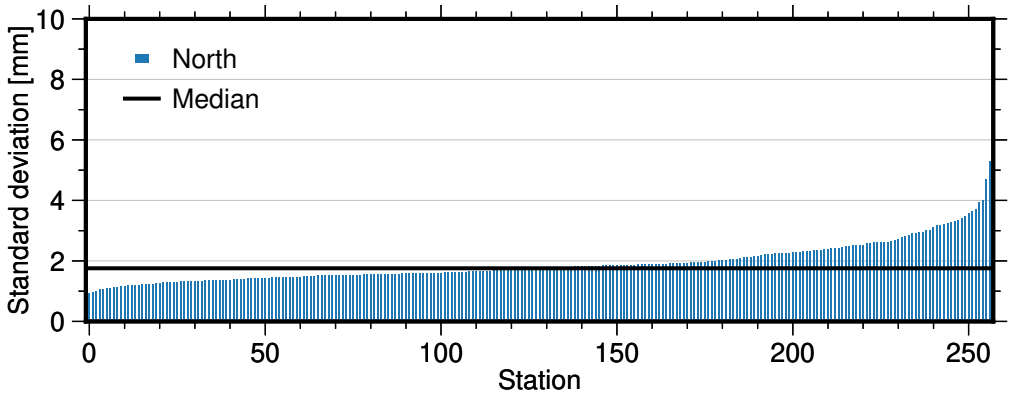

(a) North component

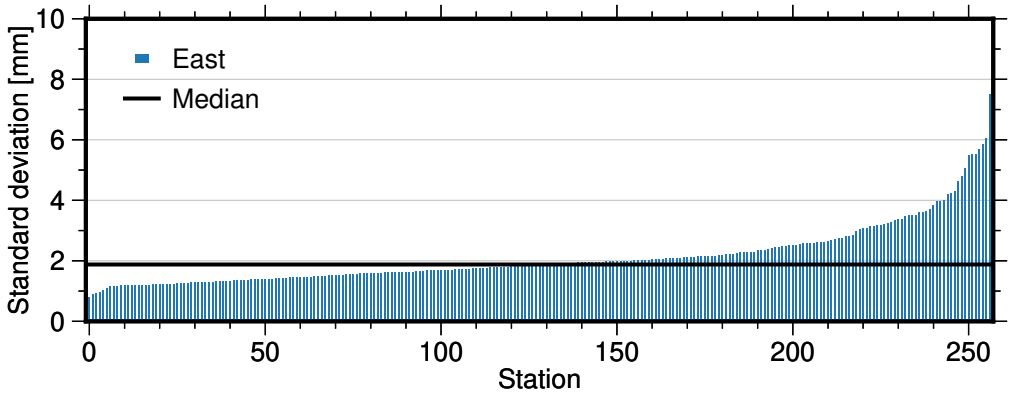

(b) East component

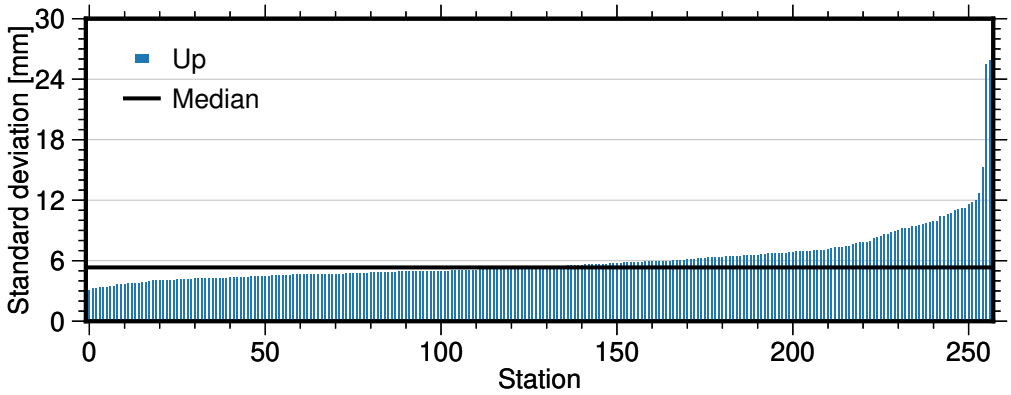

(c) Up component

Figure 8.11: Coordinate standard deviations of IGb14 stations after considering discontinuities and removing constant, trend, and annual signals. Stations are ordered by standard deviation per component. Note the different y-axis scale for the up component

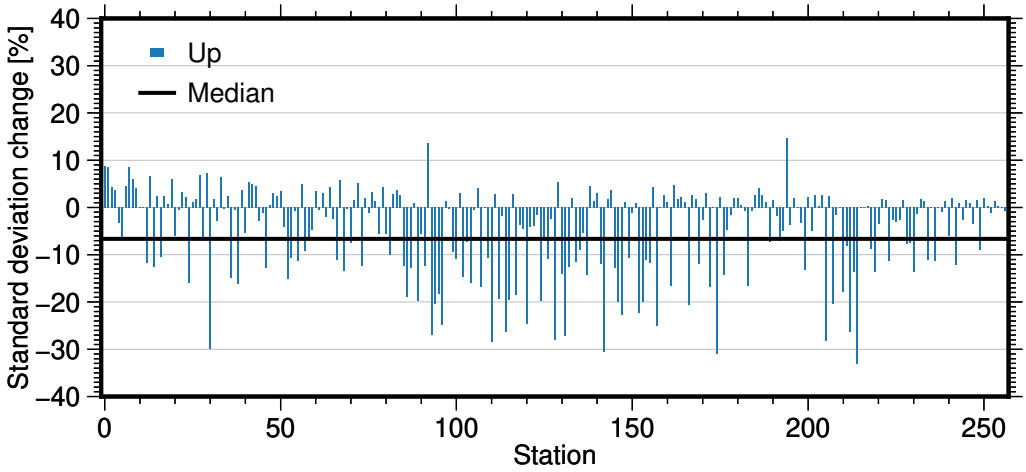

(a) Up component change due to removal of atmospheric and oceanic (AOD1B) loading

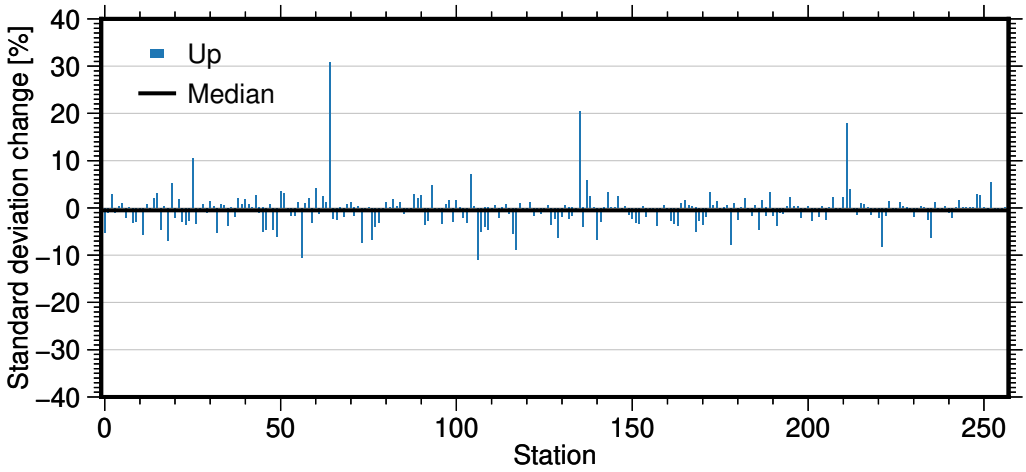

(b) Up component change due to removal of hydrological (LSDM) loading

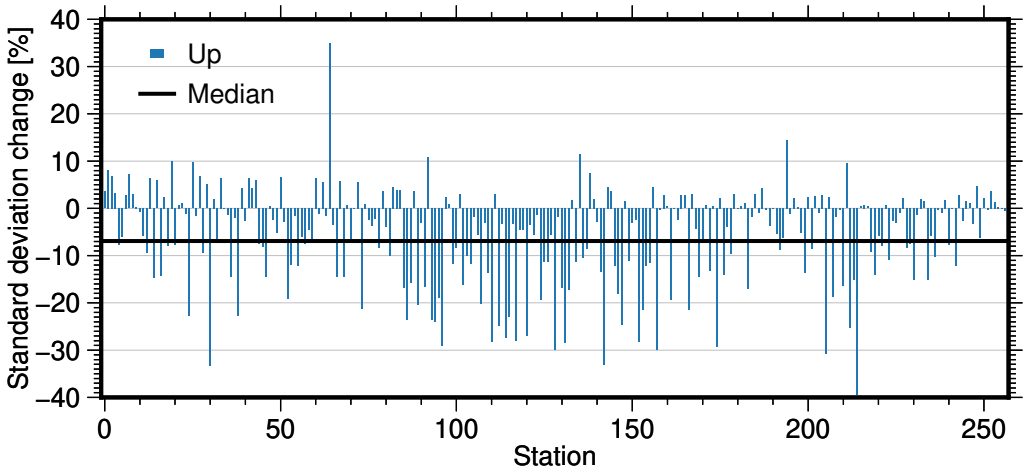

(c) Up component change due to removal of atmospheric and ocean (AOD1B) loading and hydrological (LSDM) loading

Figure 8.12: Change in standard deviations of up coordinate components for IGb14 stations due to the removal of atmospheric, oceanic, and hydrological loading. Stations are ordered by original standard deviation (see Figure 8.11c)

resulted in a decrease of 6.9% (to 4.97 mm) in the median over all station standard deviations. Interestingly, for some stations the compound effect is higher than the sum of the individual effects while for others the effects partially cancel.

Overall, the obtained standard deviations in the three coordinate components can be seen as upper bounds for the noise levels at the various stations. Some of the signals remaining in the time series could be explained by loading effects caused by high-frequency nontidal variations in the atmosphere, oceans, and continental hydrology. However, other systematic effects possibly remain in the time series, for example variations introduced by snow accumulating on the antenna. Nonetheless, median standard deviations of 1.76 mm and 1.88 mm in the north and east components as well as 4.97 mm in the up component (after removing nontidal loading) over the 257 IGb14 stations used in this analysis confirm the high quality of the determined station positions.

8.2.2 Earth rotation and reference frame parameters

The combination of station positions also considered Earth rotation and reference frame parameters. This section provides a brief summary of the results that confirms the high quality of the TUG products also with respect to these parameters. A more detailed analysis can be found in Rebischung (2021).

Table 8.5 lists median residuals and formal errors for the daily Earth rotation parameters from the combination of the analysis center solutions. They comprise polar motion (x_p, y_p), polar motion rate ($\dot{x}_p$, $\dot{y}_p$), and length of day (LOD). The median residuals for polar motion of the TUG solution are among the smallest of all analysis centers. The corresponding median formal errors are at least 40% smaller than those of other solutions. The polar motion rate residuals are also among the smallest of all contributions, with $\dot{x}_p$ being about two times larger than $\dot{y}_p$. Again, the median formal errors are more than 40% smaller than those of the closest other analysis center. Finally, LOD median residuals are similar among most solutions, which is also the case for its formal errors.

The reference frame parameters that were determined during the combination process include geocenter motion (X_{GC}, Y_{GC}, Z_{GC}) and scale (s). The median geocenter residuals are similar among most analysis centers, with TUG having the smallest overall. The same is the case for their formal errors, where those of TUG are 30-50% smaller than those of the closest other solution depending on the axis. The median residuals of the scale parameter are comparable between most contributions. Again, the median formal errors from the TUG solution are around a third smaller than those of other analysis centers.

Table 8.5: Median values of daily Earth rotation parameter residuals for individual analysis center solutions with respect to the IGS combination and their median formal errors after optimal weighting. Units: x_p and y_p in microarcseconds, $\dot{x}_p$ and $\dot{y}_p$ in microarcseconds/day, and LOD in microseconds

	Median residuals					Median formal errors				
AC	x_p	y_p	$\dot{x}_p$	$\dot{y}_p$	LOD	x_p	y_p	$\dot{x}_p$	$\dot{y}_p$	LOD
COD	1.4	14.1	-58.5	-0.6	-0.7	15.1	16.2	42.8	44.1	2.4
ESA	0.1	7.3	-61.6	-2.3	-0.1	7.5	8.1	36.9	33.8	3.2
GFZ	3.7	7.0	-7.5	35.7	0.0	11.2	11.0	44.9	46.3	2.9
GRG	-1.4	-0.1	14.1	6.5	-0.0	10.9	9.4	40.2	61.2	2.1
JPL	2.8	10.1	-76.5	-17.2	0.4	13.4	15.0	54.0	50.7	8.0
MIT	-6.0	-7.4	83.6	22.6	-0.2	8.2	7.9	27.5	30.2	1.2
NGS	0.0	-5.4	24.7	-1.8	-0.1	14.8	13.1	61.7	78.5	3.1
TUG	0.7	0.9	-9.2	4.0	0.0	4.6	4.5	14.8	17.7	1.0
ULR	-11.6	-7.3	116.2	15.6	-0.1	11.6	11.4	45.3	53.0	1.9
WHU	-4.4	2.7	7.9	-1.5	-0.1	9.9	11.1	39.7	46.3	2.1

Table 8.6: Median values of daily geocenter and scale residuals for individual analysis center solutions with respect to the IGS combination and their median formal errors after optimal weighting. Units: X_{GC}, Y_{GC}, and Z_{GC} in millimeters and s in parts per billion

	Median residuals				Median formal errors			
AC	X_{GC}	Y_{GC}	Z_{GC}	s	X_{GC}	Y_{GC}	Z_{GC}	s
COD	1.5	1.6	-2.1	0.12	2.3	2.2	3.1	0.12
ESA	-0.4	0.4	1.2	0.13	2.0	2.0	2.5	0.09
GFZ	0.5	0.0	-2.6	-0.07	1.9	1.9	2.7	0.09
GRG	2.9	-1.0	-1.7	0.06	2.2	2.3	4.8	0.08
JPL	-0.4	0.6	1.5	0.01	3.3	3.2	3.3	0.10
MIT	-1.1	0.3	1.6	-0.04	1.4	1.4	1.9	0.09
NGS	-0.5	-1.0	2.0	-0.05	2.3	2.4	5.3	0.10
TUG	-0.3	-0.3	-0.7	-0.04	0.8	0.7	1.4	0.06
ULR	2.3	0.3	1.0	0.01	1.7	1.7	2.7	0.09
WHU	-0.1	-0.8	2.1	0.04	2.0	2.1	3.7	0.09

8.2.3 Satellite orbits

Satellite orbits are another important product of the reprocessing. Together with satellite clock errors, signal biases, and attitude, they enable PPP and other applications that depend on precise satellite products. The benefit of the reprocessing products over operational products is that they offer a consistent modeling from 1994 to 2020. Section 8.2.3.1 analyzes the quality of the obtained orbits via an internal evaluation on the basis of orbit discontinuities. Results from preliminary external evaluations are then summarized in Section 8.2.3.2, together with an independent comparison to the orbit products from ESA's repro3 contribution.

8.2.3.1 Internal evaluation of orbit quality

Orbit midnight discontinuities are an effective way to determine the quality and internal consistency of orbit products. Each daily solution is processed independently and results in a 24-hour orbit arc per satellite. This means two subsequent daily solutions overlap at the day boundary epoch (i.e., midnight). The difference between these two independent orbit positions should be zero in theory. In practice, however, imperfections in orbit modeling and the GNSS observation model lead to discontinuities in the orbits at this epoch. The magnitude of these orbit discontinuities, therefore, indicates the quality and consistency of subsequent daily solutions.

Figure 8.13 shows the median orbit discontinuity RMS over all satellites of the three processed constellations. These values were obtained by computing orbit midnight discontinuities between all satellites for each subsequent pair of daily solutions. Any systematic differences between the reference frames realized by the two sets of orbit positions at an overlapping epoch were removed via a 7-parameter Helmert transformation (see Section 3.7). Next, RMS values were computed for each obtained coordinate difference. The light-colored lines in Figure 8.13 represent the medians over the RMS values of all satellites from one GNSS constellation at each day boundary. In addition, a smoothed version of these values is shown in dark colors to improve the readability of the figure.

Several conclusions can be drawn from Figure 8.13. First, the initial periods of each constellation display significantly larger discontinuities than later periods. This is expected and is mainly caused by the status of the station network and/or satellite constellations at the respective periods. In the 1990s, the station network featured a limited number of stations with poor global distribution and less sophisticated receiver hardware. The GPS constellation at that time consisted mainly of GPS-I, GPS-II, and

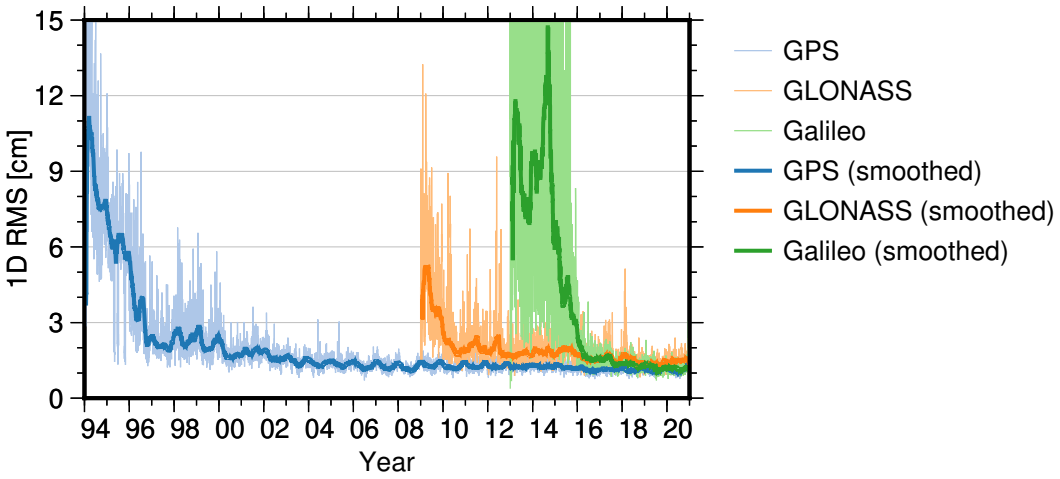

Figure 8.13: Original and smoothed (i.e., 91-day median filtered) median orbit discontinuity RMS over all satellites per constellation

GPS-IIA satellites that also used less advanced technologies. In addition, GPS applied selective availability (e.g., Hegarty, 2017), which artificially degraded the signal quality for public users, until May 2000. From 2000 onward, the GPS orbit discontinuities stabilized at a level of 1–2 cm.

The situation was similar for GLONASS and Galileo. Initially, only few stations were able to track the respective systems, leading to poor observation geometry. The GLONASS discontinuities significantly decreased in 2010 and stabilized in 2013, although on a higher level than the other two systems. Until 2015, the Galileo constellation only comprised the four GAL-1 in-orbit validation satellites and the first two GAL-2 satellites that were launched into incorrect orbits. As a result, the orbit discontinuities only improved once more GAL-2 satellites became operational, but then quickly stabilized at a level similar to that of GPS.

The median discontinuities over the full time series are 1.44 cm for GPS, 1.79 cm for GLONASS, and 1.41 cm for Galileo. These values were computed over all satellites and day boundary epochs for each constellation. They confirm that the quality of GPS and Galileo orbits is very similar, while GLONASS performs slightly worse. However, the higher level of GLONASS discontinuities can be mostly attributed to a set of satellites that perform worse than the rest.

This can be seen in Figure 8.14, which shows orbit discontinuities of all satellites for the year 2020. Here, it becomes obvious that the discontinuities for the majority of GLONASS satellites are on a similar level to those of GPS and Galileo satellites. On the other hand, the satellites R01 (R730), R12 (R858), R13 (R721), R16 (R736), R19 (R720), R20 (R719), and R22 (R735) show a clear degradation throughout most of the

year. This degradation can also be observed in other years. It is unclear what exactly causes these issues that manifest in a degraded orbit quality. A similar degradation for these satellites can also be observed in the midnight discontinuities of ESA's contribution to repro3 (not shown here). Dach et al. (2019) detected antenna offset changes for most of the above-mentioned satellites, which point to issues with their antennas or other hardware components. While some of these changes have been considered in the ANTEX file used in repro3, others have not. In summary, more investigations are necessary to determine the origin of these issues and to see if they can be remedied in the future.

Figure 8.15 visualizes the median orbit discontinuity RMS per satellite over their full operational period. It further shows the median values over all satellites of a specific type. A clear evolution can be observed in the GPS satellites, with each new type performing similar to or better than the previous one. Some specific satellites stand out from others of their type. For example, the navigation payload of G028 failed after only 4.5 years (Inside GNSS, 2016). The GPS-IIR-M satellite G049 additionally transmitted a demonstration signal on the L5 frequency, which was later introduced with the subsequent GPS-IIF satellites. It was found that this had an inadvertent negative effect on the signals transmitted on L1 and L2 (Goldstein, 2010), which explains the decreased orbit quality. G077 is a GPS-IIIA satellite that was launched in November 2020 and thus was only processed for slightly more than one month (see G14 in Figure 8.14). It is not unusual that the orbit quality is worse in the first few weeks to months after a satellite becomes operational.

Some of the misbehaving GLONASS satellites mentioned above can be clearly identified in Figure 8.15. Several other GLONASS satellites that were not operational in 2020 anymore also show significantly higher discontinuities than most other satellites of their type. Many of these satellites can also be found in the list of detected antenna changes provided in Dach et al. (2019). The quality of Galileo orbits is very consistent within their two types, with one outlying satellite each. Satellite E104 experienced a power loss and permanent failure of signal transmission at frequencies E5 and E6 in 2014 (Steigenberger and Montenbruck, 2017). Satellite E204 was removed from operational services in 2017 due to issues with its on-board clocks (Bury et al., 2020). The two satellites E201 and E202, which were incorrectly launched into a nonnominal orbit, do not show degraded orbit discontinuities.

8.2.3.2 External evaluation of orbits

An external evaluation of the obtained satellite orbits is more difficult. The main reason is that the combined IGS repro3 orbits have not been published at the time of this writing.

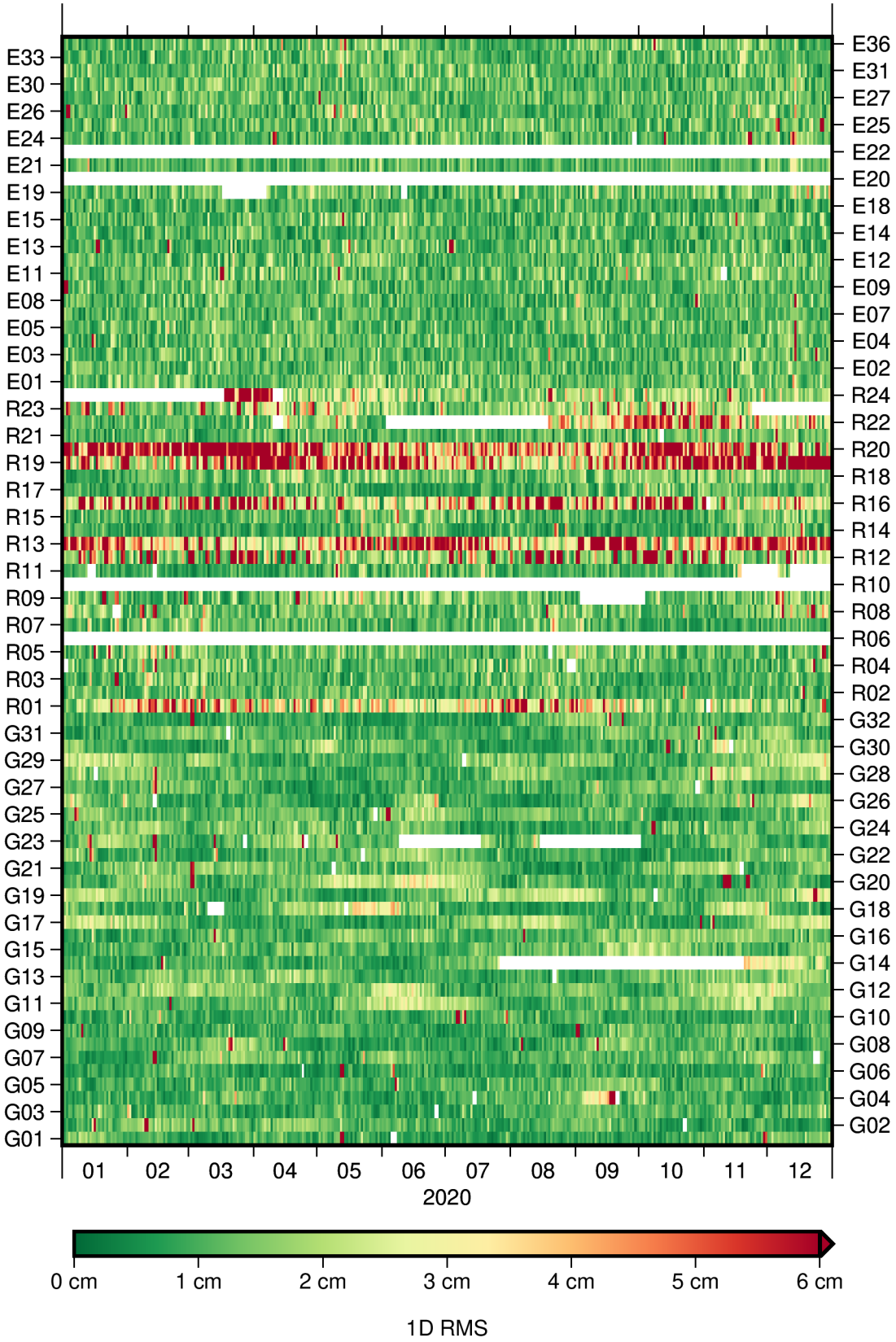

Figure 8.14: Orbit discontinuity RMS per satellite and day boundary for the year 2020

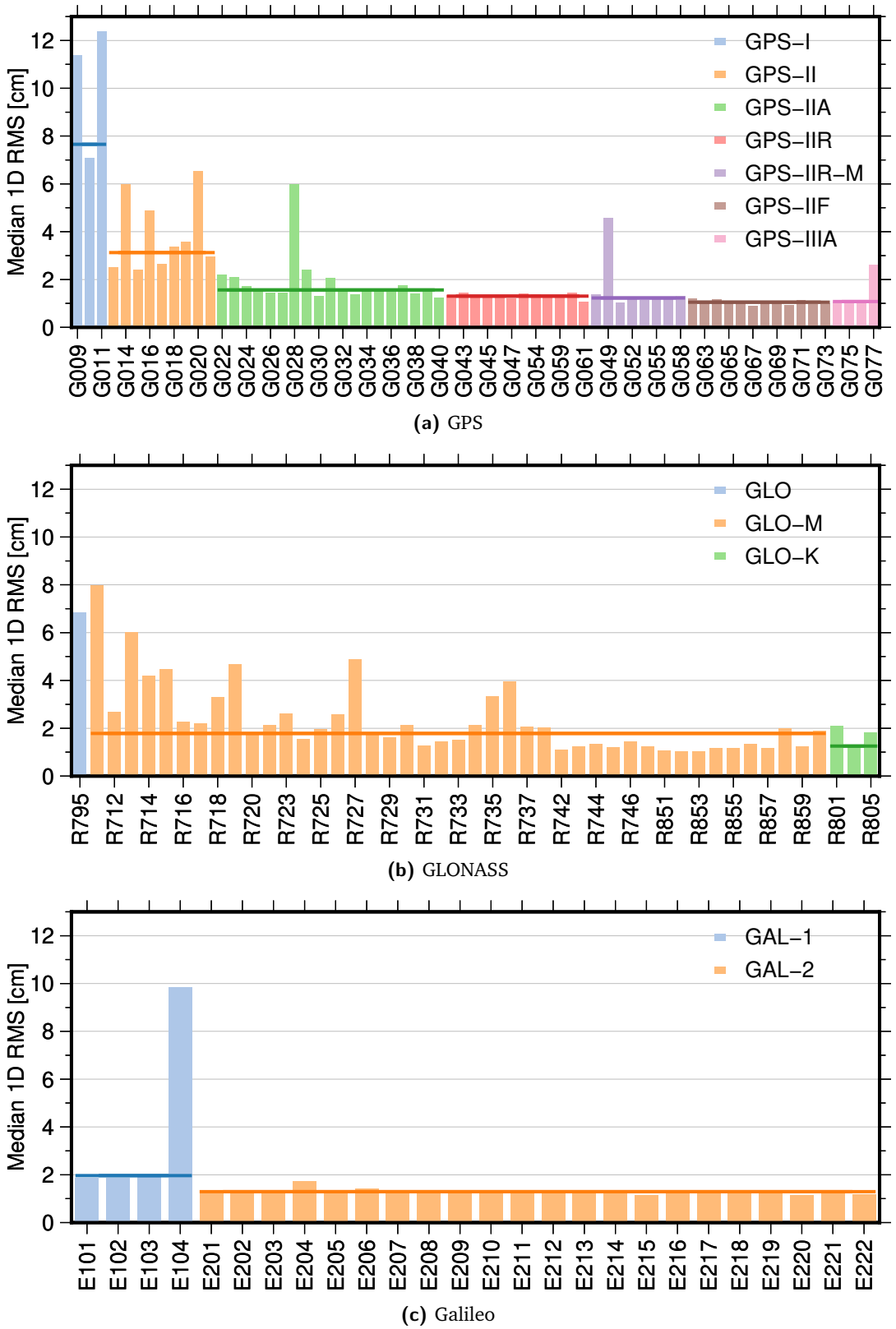

Figure 8.15: Median of discontinuity RMS per satellite for each constellation. Solid lines represent median over all satellites of one type

However, Masoumi and Moore (2021) provides an overview of preliminary combination results. The results of this combination show that the TUG orbits obtained the highest overall weight for GPS over most of the test period. The residuals RMS for most Galileo satellites is also among the smallest of all analysis centers. The results for GLONASS confirm that several of the misbehaving satellites mentioned in the previous section also show high residuals in other solutions. For most other GLONASS satellites, the TUG orbits are, again, among those with the smallest residuals.

Sakic et al. (2022) presents results of an independent experimental orbit combination. This combination uses a newly developed approach based on variance component estimation. In this study, the TUG solution also obtained the lowest residuals RMS and highest weight in case of GPS. The TUG GLONASS orbits did not perform as well in this combination, most likely due the poor quality of the specific satellites identified above. For Galileo satellites, on the other hand, the orbits from TUG again are those with the highest weight for large parts of the time series.

Zajdel et al. (2022) used the TUG repro3 products to analyze orbital artifacts in station time series obtained via multi-GNSS PPP. The study found that each system introduces significant artifacts reaching the centimeter level. Galileo offered the best results in terms of single-system solutions. However, a combined GPS and Galileo solution was found to be beneficial for the quality of the obtained station coordinate time series compared to a single-system solution. A three-system solution including GLONASS did not result in significant further benefits.

Another way to evaluate orbit products is to compare the orbit midnight discontinuities of different analysis center contributions. As noted in the previous section, these discontinuities give an indication about the quality and internal consistency of a solution. Unfortunately, only COD and ESA provide full 24-hour arcs that enable such a comparison for all three constellations. The other analysis centers contributing to repro3 do not provide the last (i.e., midnight) epoch of a daily solution in their SP3 files. Furthermore, the orbits from COD are based on 3-day arcs (Dach et al., 2021), which significantly reduces the orbit discontinuities, making a direct comparison not meaningful.

Figure 8.16 displays the smoothed median orbit discontinuity RMS per constellation for TUG and ESA. These values were obtained as described at the beginning of Section 8.2.3.1. However, to enable a proper comparison, only orbits processed by both analysis centers were used in this case. TUG shows smaller discontinuities for all three systems. The largest difference is visible for GLONASS. This is because ESA did not resolve the ambiguities to integer values for GLONASS (Tim Springer, personal communication). Overall, these external evaluations confirm the high quality of the orbits

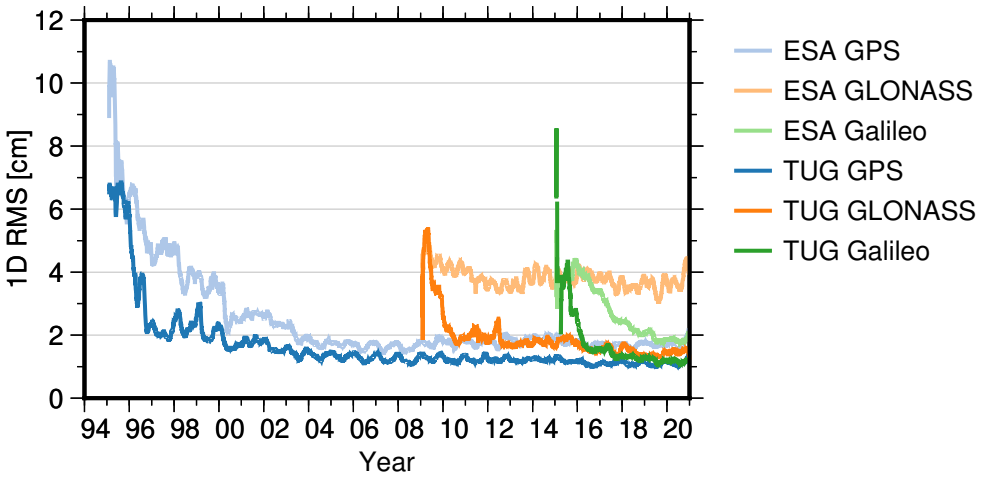

Figure 8.16: Smoothed (i.e., 91-day median filtered) median orbit discontinuity RMS over all satellites per constellation for ESA and TUG

produced in the context of this thesis, with the exception of issues with specific GLONASS satellites.

8.2.4 Signal biases

Evaluating signal biases is very complex. The approaches of resolving the rank deficiencies during their estimation usually differ in the various analysis center solutions. This results in different types of bias products with possibly differing datum definitions (e.g, Banville et al., 2020). In addition, only some analysis centers actually provide bias products and their signal type coverage can vary significantly. COD and TUG are the only analysis centers that provided observable-specific pseudo-absolute satellite code biases for their repro3 solutions. However, the repro3 code biases from COD stem from a clock analysis and not from a combined analysis of clocks and the ionosphere (Selmke et al., 2020).

For this reason, the satellite code bias products provided as a supplement to Villiger et al. (2019) were used in this evaluation. These biases were determined in a combined clock and ionosphere analysis in the frame of COD's Multi-GNSS Experiment and Pilot Project (MGEX) contribution. They cover the year 2016 and comprise an extensive set of signal types on multiple frequencies for GPS, GLONASS, and Galileo. According to Villiger et al. (2019), the biases were aligned to a common datum over the whole time series. This was done by realigning the daily solutions to their means values over the full year.

The satellite code biases estimated in the reprocessing presented in this thesis were aligned to those from Villiger et al. (2019). This alignment was performed on a daily

basis. For each signal type, the mean difference between the COD and TUG code biases over all satellites of one GNSS was determined. This system-wide shift was then removed from the TUG biases of that signal type to align them to those of COD. Such an alignment preserves the relative bias differences between the satellites within one signal type. System-wide differences between signal types depend on the respective datum definition, as they can be freely shifted between satellites and receivers. The described alignment uses the datum definition of the COD solution (see Villiger et al., 2019).

Figure 8.17 compares the aligned code biases of the two solutions. The biases are grouped by satellite and the satellites are grouped by their type. Each signal type is visualized in a different color using dark colors for TUG's biases and light colors in the background for COD's biases. The vertical spread represents the temporal variations of the daily values over the full year.

The comparisons reveal that the code biases from the two solutions agree very well for GPS and Galileo. This includes both the relative offsets between satellites as well as the spread over the time series. In case of GPS, the differences between the various satellite types are very clear. The offset between the GPS-IIF satellites and the other types is most prominent. GPS-IIR-B satellites also show significantly different biases to the GPS-IIR-A satellites, both of which are very similar in many other respects. The most homogeneous satellite type is GPS-IIR-M, where only G052 and G058 deviate somewhat from the other satellites.

The relative offsets between satellites are much larger for Galileo. GAL-2 satellites E201, E202, and E205 show offsets of 10–25 m compared to the mean over the other satellites of that type. The periods from 26 February to 3 March and from 2 to 6 October 2016 had to be excluded from the Galileo bias comparison. These were the first days after the inclusion of newly launched satellites (E208 and E209 in the former and E210 and E211 in the latter case). During these days, untypically large variations could be observed in the TUG biases, pointing to processing issues during the initial days of these satellites.

The GLONASS code biases largely differ between the two solutions. The main reason is that the COD solution was based on a simplified parametrization that only considered a common receiver bias for all GLONASS satellites per signal type (Villiger et al., 2019). In contrast, the reprocessing described in this thesis comprised separate receiver code biases per frequency number (see Section 6.5.2). As a result, the relative offsets between GLONASS satellites differ significantly. The TUG solution also shows a higher spread for several satellites, including some outliers. Furthermore, day 2016-12-24 had to be excluded due to an exceptionally large outlier.

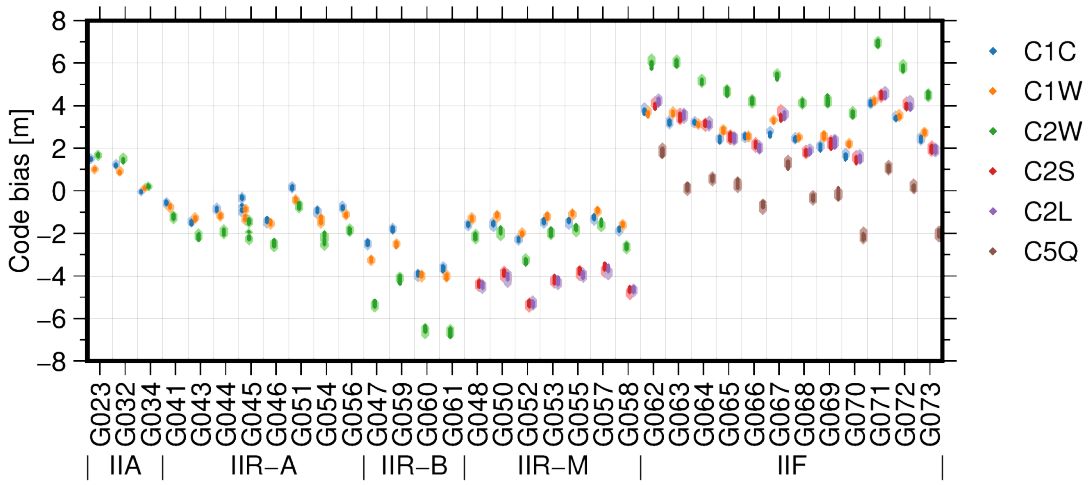

(a) GPS

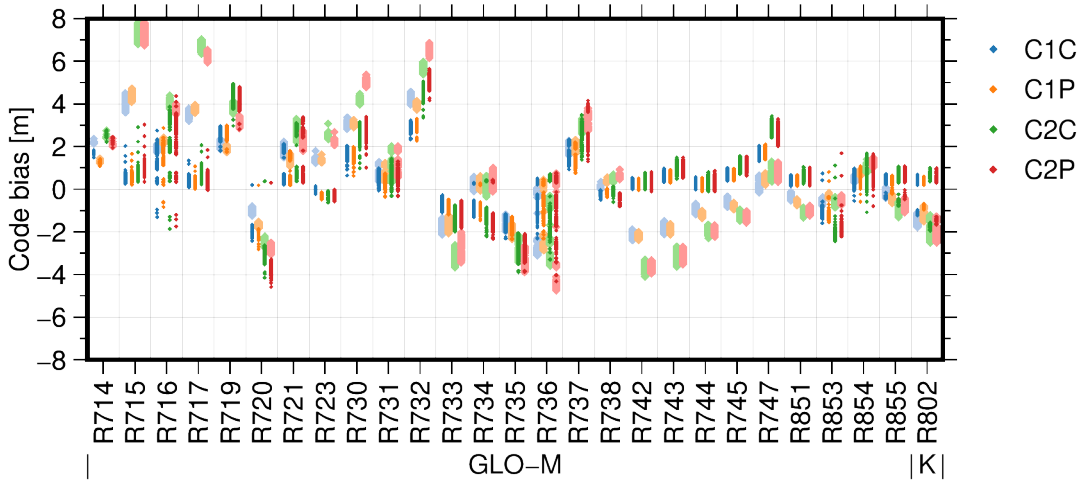

(b) GLONASS

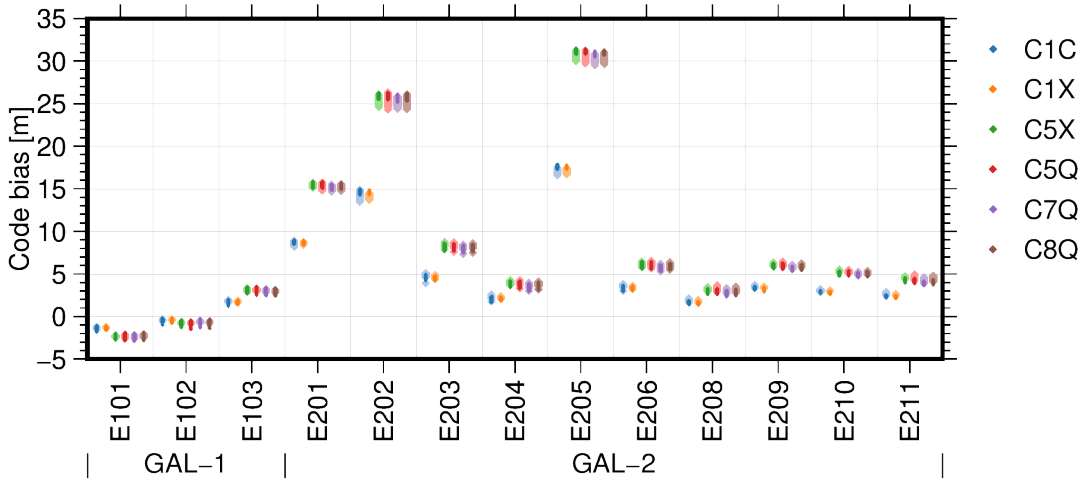

(c) Galileo

Figure 8.17: Comparison of aligned TUG repro3 (dark) and COD MGEX (light; taken from Villiger et al., 2019) code biases for the year 2016. Note the different y-axis scale for Galileo

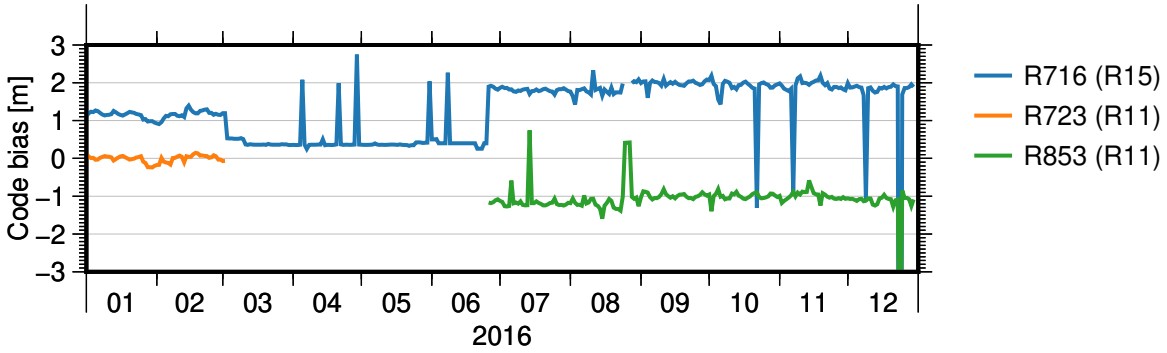

(a) R716

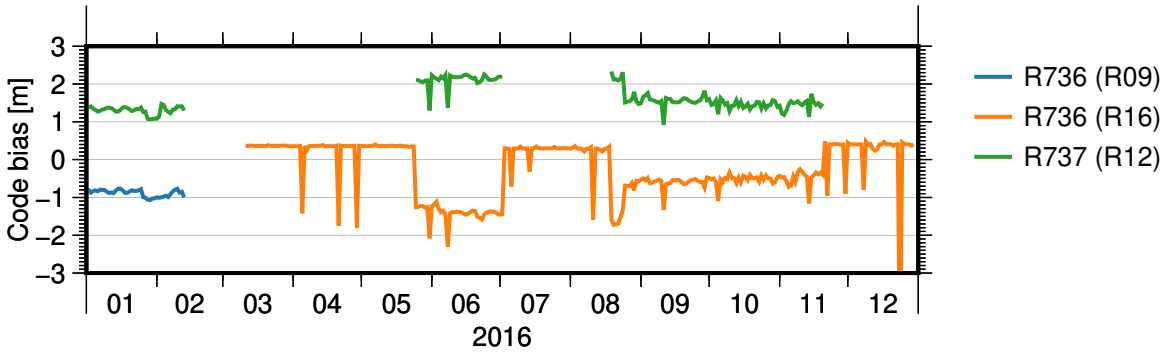

(b) R736

Figure 8.18: Aligned C1C code bias time series for satellites R716 and R736 in 2016

Satellites R716 and R736 show the largest spread over the time series. This can be explained by jumps in the time series of TUG's code biases for these satellites, as shown in Figure 8.18. Setting up receiver code bias parameters per frequency number means that each bias is defined by two antipodal satellites transmitting on the same frequency. When something changes in this setup, for example because one satellite is decommissioned or replaced by another, the code biases of the other satellite might be affected as well. Figure 8.18a shows a jump in the time series of satellite R716 in slot number R15 when its antipodal counterpart (R723 in slot R11) stopped transmission in March 2016. In June 2016, satellite R853 started operating in slot R11, which, again, resulted in a jump in the time series of R716.

A similar behavior can be observed for satellite R736 (see Figure 8.18b). This satellite operated in slot R09 until February 2016, after which it changed to slot R16. This transition included a change from frequency number -2 to -1. From March 2016 onward it is clearly visible that whenever its antipodal counterpart (R737 in slot R12) was active, the bias time series shifted to a different level. In the periods when its counterpart was not part of the processed constellation, the biases shifted back to the original level. These changes are induced by the fact that code biases cannot be determined absolutely because of the rank deficiencies described in Section 6.5.3.

The estimated code and phase biases have also been evaluated in independent studies. Banville et al. (2020) and Glaner and Weber (2021) both used preliminary versions of the TUG repro3 products to perform PPP with ambiguity resolution. In both studies, the results obtained with the TUG products were competitive with those of other analysis centers. This confirms that the signal biases are of good quality and enable users to perform PPP with ambiguity resolution using an extensive set of signal types.

9 Conclusion

This thesis detailed the methodologies behind the IGS repro3 contribution by Graz University of Technology. This included a thorough description of the applied raw observation approach as well as all parametrizations, models, and corrections. All of these methods and models are implemented in the open-source software GROOPS, which was used to conduct the reprocessing. As a result, the combination of this thesis and the open-source nature of GROOPS provides a complete and transparent documentation of TUG's repro3 contribution.

One of the main points of this thesis was to present the intricacies of the raw observation approach as implemented at Graz University of Technology. This included an effective method of preeliminating the ionospheric influence on the observation equation level. It was also shown how ordering the parameters in a specific way results in a normal equation matrix structure that contains both highly dense as well as fully unpopulated parts. Dividing this matrix into subblocks and only storing the populated ones in memory significantly reduces the memory requirements and thus enables the processing of large systems with millions of parameters. In addition, strategies that further decrease the computational complexity were delineated, such as the elimination and reconstruction of epoch parameters, a processing scheme that initially uses only a core network, and the separation of the ionosphere and signal biases in an intermediate step. The description of the processing approach included the application of variance component estimation to determine new weights for the observations based on their residuals and redundancies. This has the benefit that outliers are automatically weighted down with each iteration of the least-squares adjustment, resulting in a more robust solution.

Another focus was the extensive elaboration of the parametrizations, models, and corrections used in the GNSS observation equations. For example, a generalization of satellite attitude models focusing on simple implementations that maintain the ability to handle special cases was presented. The sections about satellite orbits, clock errors, station positions, Earth orientation, ionosphere, troposphere, and antennas featured descriptions of state-of-the-art models and well-established parametrizations. Another important aspect was the sophisticated handling of GNSS signal biases required when applying the raw observation approach. A method for determining estimable linear combinations of observable-specific code biases that considers the various rank

deficiencies was detailed. In terms of phase biases and ambiguities, this thesis presented an algorithm that automatically determines an estimable set of corresponding parameters. Additional details on the blocked ambiguity resolution procedure developed at Graz University of Technology were given as well.

The evaluation of the resulting GNSS products showed that they are of very high quality. In fact, TUG's repro3 contribution gained the highest weight on average in the IGS reference frame combination. The consistency of the obtained satellite orbits is also very high, which was confirmed by preliminary orbit combination results. This means that the methods delineated in this thesis lead to GNSS products that are very competitive with those of other IGS analysis centers. Therefore, the targets of reaching this quality level and providing a valuable contribution to ITRF2020 were successfully achieved.

There are a wide variety of research topics that could further improve the applied methods and obtained results in the future. It is well known that the modeling of solar radiation pressure is the main limiting factor in terms of orbit quality. Furthermore, orbit modeling issues can propagate into station position and Earth rotation parameters, resulting in undesired effects in their time series. A better understanding of the signal biases occurring in satellite and receiver hardware could lead to improved parametrizations. This is especially important considering the diverse set of signals that is available in a modern multi-GNSS environment. Finally, a more realistic consideration of the correlations between observations and among certain parameters would certainly also benefit the quality of the resulting products.

Bibliography

Al Borno, M., Chang, X.-W., and Xie, X. H. (2014). "On 'Decorrelation' in Solving Integer Least-Squares Problems for Ambiguity Determination". In: *Survey Review* 46.334, pp. 37–49. DOI: 10.1179/1752270612Y.0000000029.

Al-Shaery, A., Zhang, S., and Rizos, C. (2013). "An Enhanced Calibration Method of GLONASS Inter-Channel Bias for GNSS RTK". In: *GPS Solutions* 17.2, pp. 165–173. DOI: 10.1007/s10291-012-0269-5.

Alken, P., Thébault, E., Beggan, C. D., et al. (2021). "International Geomagnetic Reference Field: The Thirteenth Generation". In: *Earth, Planets and Space* 73.1, p. 49. DOI: 10.1186/s40623-020-01288-x.

Altamimi, Z., Rebischung, P., Métivier, L., and Collilieux, X. (2016). "ITRF2014: A New Release of the International Terrestrial Reference Frame Modeling Nonlinear Station Motions". In: *Journal of Geophysical Research: Solid Earth* 121.8, pp. 6109–6131. DOI: 10.1002/2016JB013098.

Amiri-Simkooei, A. R., Jazaeri, S., Zangeneh-Nejad, F., and Asgari, J. (2016). "Role of Stochastic Model on GPS Integer Ambiguity Resolution Success Rate". In: *GPS Solutions* 20.1, pp. 51–61. DOI: 10.1007/s10291-015-0445-5.

Arnold, D., Meindl, M., Beutler, G., Dach, R., Schaer, S., Lutz, S., Prange, L., Sośnica, K., Mervart, L., and Jäggi, A. (2015). "CODE's New Solar Radiation Pressure Model for GNSS Orbit Determination". In: *Journal of Geodesy* 89.8, pp. 775–791. DOI: 10.1007/s00190-015-0814-4.

Ashby, N. (2003). "Relativity in the Global Positioning System". In: *Living Reviews in Relativity* 6.1, p. 1. DOI: 10.12942/lrr-2003-1.

Ashby, N. and Bertotti, B. (1986). "Relativistic Effects in Local Inertial Frames". In: *Physical Review D* 34.8, pp. 2246–2259. DOI: 10.1103/PhysRevD.34.2246.

Ashkenazi, V., Hill, C., Moore, T., and Whalley, S. (1990). "Orbit Determination for GPS Satellites". In: *Global Positioning System: An Overview*. Ed. by Y. Bock and N. Leppard. International Association of Geodesy Symposia. New York, NY: Springer, pp. 187–194. DOI: 10.1007/978-1-4615-7111-7_18.

Askne, J. and Nordius, H. (1987). "Estimation of Tropospheric Delay for Microwaves from Surface Weather Data". In: *Radio Science* 22.3, pp. 379–386. DOI: 10.1029/RS022i003p00379.

Banville, S., Collins, P., and Lahaye, F. (2013). "Concepts for Undifferenced GLONASS Ambiguity Resolution". In: *Proceedings of the 26th International Technical Meeting of the Satellite Division of The Institute of Navigation (ION GNSS+ 2013), Nashville, TN, September 2013*, pp. 1186–1197.

Banville, S. (2016). "GLONASS Ionosphere-Free Ambiguity Resolution for Precise Point Positioning". In: *Journal of Geodesy* 90.5, pp. 487–496. DOI: 10.1007/s00190-016-0888-7.

Banville, S., Geng, J., Loyer, S., Schaer, S., Springer, T., and Strasser, S. (2020). "On the Interoperability of IGS Products for Precise Point Positioning with Ambiguity Resolution". In: *Journal of Geodesy* 94.1. DOI: 10.1007/s00190-019-01335-w.

Banville, S. and Langley, R. B. (2013). "Mitigating the Impact of Ionospheric Cycle Slips in GNSS Observations". In: *Journal of Geodesy* 87.2, pp. 179–193. DOI: 10.1007/s00190-012-0604-1.

Bar-Sever, Y. E. (1996). "A New Model for GPS Yaw Attitude". In: *Journal of Geodesy* 70.11, pp. 714–723. DOI: 10.1007/BF00867149.

Bar-Sever, Y. E., Kroger, P. M., and Borjesson, J. A. (1998). "Estimating Horizontal Gradients of Tropospheric Path Delay with a Single GPS Receiver". In: *Journal of Geophysical Research: Solid Earth* 103.B3, pp. 5019–5035. DOI: 10.1029/97JB03534.

Bar-Sever, Y. E. and Kuang, D. (2004). "New Empirically Derived Solar Radiation Pressure Model for Global Positioning System Satellites". In: *Interplanetary Network Progress Report* 42.159.

Bassiri, S. and Hajj, G. (1993). "Higher-Order Ionospheric Effects on the GPS Observables and Means of Modeling Them". In: *Proceedings of the AAS/AIAA Space Flight Mechanics Meeting*. Pasadena, CA. URL: https://trs.jpl.nasa.gov/handle/2014/34918 (visited on 2022-03-01).

Bastos, M. and Landau, H. (1988). "Fixing Cycle Slips in Dual-Frequency Kinematic GPS Applications Using Kalman Filtering". In: *Manuscripta Geodaetica* 13, pp. 249–256.

Beard, R. and Senior, K. (2017). "Clocks". In: *Springer Handbook of Global Navigation Satellite Systems*. Ed. by P. J. G. Teunissen and O. Montenbruck. Springer Handbooks. Cham: Springer International Publishing, pp. 121–164. DOI: 10.1007/978-3-319-42928-1_5.

Beutler, G., Brockmann, E., Gurtner, W., Hugentobler, U., Mervart, L., Rothacher, M., and Verdun, A. (1994). "Extended Orbit Modeling Techniques at the CODE Processing Center of the International GPS Service for Geodynamics (IGS)". In: *Manuscripta Geodaetica* 19.6, pp. 367–386.

Beutler, G., Davidson, D. A., Langley, R. B., Santerre, R., Vanĩcek, P., and Wells, D. E. (1984). *Some Theoretical and Practical Aspects of Geodetic Positioning Using Carrier Phase Difference Observations of GPS Satellites*. Technical Report 109. Fredericton, NB, Canada: University of New Brunswick. URL: https://unbscholar.lib.unb.ca/islandora/object/unbscholar%3A8567/ (visited on 2022-03-01).

Beutler, G. (2005). *Methods of Celestial Mechanics – Volume I: Physical, Mathematical, and Numerical Principles*. Astronomy and Astrophysics Library. Berlin, Heidelberg: Springer. DOI: 10.1007/b138225.

Beyerle, G. (2009). "Carrier Phase Wind-up in GPS Reflectometry". In: *GPS Solutions* 13.3, pp. 191–198. DOI: 10.1007/s10291-008-0112-1.

Bhattarai, S., Ziebart, M., Allgeier, S., Grey, S., Springer, T., Harrison, D., and Li, Z. (2019). "Demonstrating Developments in High-Fidelity Analytical Radiation Force Modelling Methods for Spacecraft with a New Model for GPS IIR/IIR-M". In: *Journal of Geodesy* 93.9, pp. 1515–1528. DOI: 10.1007/s00190-019-01265-7.

Bisnath, S. B. (2000). “Efficient, Automated Cycle-Slip Correction Of Dual-Frequency Kinematic GPS Data”. In: *Proceedings of the 13th International Technical Meeting of the Satellite Division of The Institute of Navigation (ION GPS 2000)*. Salt Lake City, UT, USA, pp. 145–154.

Bizouard, C., Lambert, S., Gattano, C., Becker, O., and Richard, J.-Y. (2019). “The IERS EOP 14C04 Solution for Earth Orientation Parameters Consistent with ITRF 2014”. In: *Journal of Geodesy* 93.5, pp. 621–633. DOI: 10.1007/s00190-018-1186-3.

Blackford, L., Choi, J., Cleary, A., Demmel, J., Dhillon, I. S., Dongarra, J., Hammarling, S., Henry, G., Petitet, A., Stanley, K., Walker, D., and Whaley, R. C. (1997). *ScaLAPACK Users’ Guide*. SIAM. ISBN: 0-89871-397-8. URL: http://www.netlib.org/scalapack/slug/ (visited on 2022-03-01).

Blewitt, G. (1990). “An Automatic Editing Algorithm for GPS Data”. In: *Geophysical Research Letters* 17.3, pp. 199–202. DOI: 10.1029/GL017i003p00199.

Blewitt, G. (2008). “Fixed Point Theorems of GPS Carrier Phase Ambiguity Resolution and Their Application to Massive Network Processing: Ambizap”. In: *Journal of Geophysical Research: Solid Earth* 113.B12. DOI: 10.1029/2008JB005736.

Böhm, J., Werl, B., and Schuh, H. (2006). “Troposphere Mapping Functions for GPS and Very Long Baseline Interferometry from European Centre for Medium-Range Weather Forecasts Operational Analysis Data”. In: *Journal of Geophysical Research: Solid Earth* 111.B2. DOI: 10.1029/2005JB003629.

Borden, B. and Luscombe, J. (2017). “Spherical Harmonics and Friends”. In: *Essential Mathematics for the Physical Sciences*. 2053-2571. Morgan & Claypool Publishers. DOI: 10.1088/978-1-6817-4485-8ch6.

Borio, D. and Lo Presti, L. (2008). “Data and Pilot Combining for Composite GNSS Signal Acquisition”. In: *International Journal of Navigation and Observation* 2008, e738183. DOI: 10.1155/2008/738183.

Boxhammer, C. and Schuh, W.-D. (2006). “GOCE Gravity Field Modeling: Computational Aspects — Free Kite Numbering Scheme”. In: *Observation of the Earth System from Space*. Ed. by J. Flury, R. Rummel, C. Reigber, M. Rothacher, G. Boedecker, and U. Schreiber. Berlin, Heidelberg: Springer, pp. 209–224. DOI: 10.1007/3-540-29522-4_15.

Brunner, F. K. and Gu, M. (1991). “An Improved Model for the Dual Frequency Ionospheric Correction of GPS Observations”. In: *Manuscripta Geodaetica* 16, pp. 205–214.

Budden, K. G. (1985). *The Propagation of Radio Waves: The Theory of Radio Waves of Low Power in the Ionosphere and Magnetosphere*. Cambridge: Cambridge University Press. DOI: 10.1017/CBO9780511564321.

Bury, G., Sośnica, K., Zajdel, R., and Strugarek, D. (2020). “Toward the 1-Cm Galileo Orbits: Challenges in Modeling of Perturbing Forces”. In: *Journal of Geodesy* 94.2, p. 16. DOI: 10.1007/s00190-020-01342-2.

Cabinet Office, Government of Japan (2021). *QZSS Satellite Information*. URL: https://qzss.go.jp/en/technical/qzssinfo/index.html (visited on 2022-03-01).

Cai, C., Liu, Z., Xia, P., and Dai, W. (2013). “Cycle Slip Detection and Repair for Undifferenced GPS Observations under High Ionospheric Activity”. In: *GPS Solutions* 17.2, pp. 247–260. DOI: 10.1007/s10291-012-0275-7.

Cao, X., Li, J., Zhang, S., Kuang, K., Gao, K., Zhao, Q., and Hong, H. (2019). “Uncombined Precise Point Positioning with Triple-Frequency GNSS Signals”. In: *Advances in Space Research* 63.9, pp. 2745–2756. DOI: 10.1016/j.asr.2018.03.030.

Chang, X.-W., Yang, X., and Zhou, T. (2005). “MLAMBDA: A Modified LAMBDA Method for Integer Least-Squares Estimation”. In: *Journal of Geodesy* 79.9, pp. 552–565. DOI: 10.1007/s00190-005-0004-x.

Chapman, S. (1931). “The Absorption and Dissociative or Ionizing Effect of Monochromatic Radiation in an Atmosphere on a Rotating Earth Part II. Grazing Incidence”. In: 43.5, pp. 483–501. DOI: 10.1088/0959-5309/43/5/302.

Chen, G. and Herring, T. A. (1997). “Effects of Atmospheric Azimuthal Asymmetry on the Analysis of Space Geodetic Data”. In: *Journal of Geophysical Research: Solid Earth* 102.B9, pp. 20489–20502. DOI: 10.1029/97JB01739.

Choi, J., Dongarra, J. J., Ostrouchov, L. S., Petitet, A. P., Walker, D. W., and Whaley, R. C. (1996). “Design and Implementation of the ScaLAPACK LU, QR, and Cholesky Factorization Routines”. In: *Scientific Programming* 5, p. 483083. DOI: 10.1155/1996/483083.

Collins, P., Bisnath, S., Lahaye, F., and Héroux, P. (2010). “Undifferenced GPS Ambiguity Resolution Using the Decoupled Clock Model and Ambiguity Datum Fixing”. In: *Navigation* 57.2, pp. 123–135. DOI: 10.1002/j.2161-4296.2010.tb01772.x.

Condat, L. (2013). “A Direct Algorithm for 1-D Total Variation Denoising”. In: *IEEE Signal Processing Letters* 20.11, pp. 1054–1057. DOI: 10.1109/LSP.2013.2278339.

Dach, R., Selmke, I., Villiger, A., Arnold, D., Prange, L., Schaer, S., Sidorov, D., Stebler, P., Jäggi, A., and Hugentobler, U. (2021). “Review of Recent GNSS Modelling Improvements Based on CODEs Repro3 Contribution”. In: *Advances in Space Research* 68.3, pp. 1263–1280. DOI: 10.1016/j.asr.2021.04.046.

Dach, R., Sušnik, A., Grahsl, A., Villiger, A., Schaer, S., Arnold, D., Prange, L., and Jäggi, A. (2019). “Improving GLONASS Orbit Quality by Re-Estimating Satellite Antenna Offsets”. In: *Advances in Space Research* 63.12, pp. 3835–3847. DOI: 10.1016/J.ASR.2019.02.031.

Dai, Z., Knedlik, S., and Loffeld, O. (2009). “Instantaneous Triple-Frequency GPS Cycle-Slip Detection and Repair”. In: *International Journal of Navigation and Observation* 2009, e407231. DOI: 10.1155/2009/407231.

De Lacy, M. C., Reguzzoni, M., Sansò, F., and Venuti, G. (2008). “The Bayesian Detection of Discontinuities in a Polynomial Regression and Its Application to the Cycle-Slip Problem”. In: *Journal of Geodesy* 82.9, pp. 527–542. DOI: 10.1007/s00190-007-0203-8.

Desai, S. D. and Sibois, A. E. (2016). “Evaluating Predicted Diurnal and Semidiurnal Tidal Variations in Polar Motion with GPS-based Observations”. In: *Journal of Geophysical Research: Solid Earth* 121.7, pp. 5237–5256. DOI: 10.1002/2016JB013125.

Dill, R. (2008). *Hydrological Model LSDM for Operational Earth Rotation and Gravity Field Variations*. Scientific Technical Report STR 08/09. Potsdam: Deutsches GeoForschungsZentrum GFZ, p. 35. DOI: 10.2312/GFZ.b103-08095.

Dilssner, F. (2010). "GPS IIF-1 Satellite-Antenna Phase Center and Attitude Modeling". In: *Inside GNSS* 5.6, pp. 59–64. URL: https://www.insidegnss.com/auto/sep10-Dilssner.pdf (visited on 2022-03-01).

Dilssner, F., Läufer, G., Springer, T., Schönemann, E., and Enderle, W. (2018). "The BeiDou Attitude Model for Continuous Yawing MEO and IGSO Spacecraft". EGU General Assembly 2018, Vienna, 4–13 Apr 2018. URL: http://navigation-office.esa.int/attachments_29393052_1_EGU2018_Dilssner_Final.pdf (visited on 2022-03-01).

Dilssner, F., Springer, T., and Enderle, W. (2011a). "GPS IIF Yaw Attitude Control during Eclipse Season". AGU Fall Meeting 2011, San Francisco, 5–9 Dec 2011. URL: http://acc.igs.org/orbits/yaw-IIF_ESOC_agu11.pdf (visited on 2022-03-01).

Dilssner, F., Springer, T., Gienger, G., and Dow, J. (2011b). "The GLONASS-M Satellite Yaw-Attitude Model". In: *Advances in Space Research* 47.1, pp. 160–171. DOI: 10.1016/J.ASR.2010.09.007.

Dobslaw, H., Bergmann-Wolf, I., Dill, R., Poropat, L., Thomas, M., Dahle, C., Esselborn, S., König, R., and Flechtner, F. (2017). "A New High-Resolution Model of Non-Tidal Atmosphere and Ocean Mass Variability for de-Aliasing of Satellite Gravity Observations: AOD1B RL06". In: *Geophysical Journal International* 211.1, pp. 263–269. DOI: 10.1093/gji/ggx302.

Döll, P., Douville, H., Güntner, A., Müller Schmied, H., and Wada, Y. (2016). "Modelling Freshwater Resources at the Global Scale: Challenges and Prospects". In: *Surveys in Geophysics* 37.2, pp. 195–221. DOI: 10.1007/s10712-015-9343-1.

Duan, B. and Hugentobler, U. (2021). "Enhanced Solar Radiation Pressure Model for GPS Satellites Considering Various Physical Effects". In: *GPS Solutions* 25.2, p. 42. DOI: 10.1007/s10291-020-01073-z.

Duan, B., Hugentobler, U., Hofacker, M., and Selmke, I. (2020). "Improving Solar Radiation Pressure Modeling for GLONASS Satellites". In: *Journal of Geodesy* 94.8, p. 72. DOI: 10.1007/s00190-020-01400-9.

Duan, B., Hugentobler, U., and Selmke, I. (2019). "The Adjusted Optical Properties for Galileo/BeiDou-2/QZS-1 Satellites and Initial Results on BeiDou-3e and QZS-2 Satellites". In: *Advances in Space Research* 63.5, pp. 1803–1812. DOI: 10.1016/J.ASR.2018.11.007.

Eicker, A. (2008). "Gravity Field Refinement by Radial Basis Functions from In-situ Satellite Data". PhD thesis. University of Bonn. URL: https://hdl.handle.net/20.500.11811/3245 (visited on 2022-03-01).

Eissfeller, B. and Won, J.-H. (2017). "Receiver Architecture". In: *Springer Handbook of Global Navigation Satellite Systems*. Ed. by P. J. G. Teunissen and O. Montenbruck. Springer Handbooks. Cham: Springer International Publishing, pp. 365–400. DOI: 10.1007/978-3-319-42928-1_13.

El-Rabbany, A. (1994). “The Effect of Physical Correlations on the Ambiguity Resolution and Accuracy Estimation in GPS Differential Positioning”. University of New Brunswick, Canada. 161 pp. URL: https://www2.unb.ca/gge/Pubs/TR170.pdf (visited on 2022-03-01).

Ellmer, M. (2018). “Contributions to GRACE Gravity Field Recovery: Improvements in Dynamic Orbit Integration, Stochastic Modelling of the Antenna Offset Correction, and Co-Estimation of Satellite Orientations”. PhD thesis. Graz University of Technology. 185 pp. DOI: 10.3217/978-3-85125-646-8.

European GNSS Service Centre (2017). *Galileo Satellite Metadata*. URL: https://www.gsc-europa.eu/support-to-developers/galileo-satellite-metadata (visited on 2022-03-01).

Falcone, M., Hahn, J., and Burger, T. (2017). “Galileo”. In: *Springer Handbook of Global Navigation Satellite Systems*. Ed. by P. J. G. Teunissen and O. Montenbruck. Springer Handbooks. Cham: Springer International Publishing, pp. 247–272. DOI: 10.1007/978-3-319-42928-1_9.

Feltens, J., Bellei, G., Springer, T., Kints, M. V., Zandbergen, R., Budnik, F., and Schönemann, E. (2018). “Tropospheric and Ionospheric Media Calibrations Based on Global Navigation Satellite System Observation Data”. In: *Journal of Space Weather and Space Climate* 8, A30. DOI: 10.1051/swsc/2018016.

Fliegel, H. F., Gallini, T. E., and Swift, E. R. (1992). “Global Positioning System Radiation Force Model for Geodetic Applications”. In: *Journal of Geophysical Research* 97.B1, p. 559. DOI: 10.1029/91JB02564.

Fliegel, H. F. and Gallini, T. E. (1996). “Solar Force Modeling of Block IIR Global Positioning System Satellites”. In: *Journal of Spacecraft and Rockets* 33.6, pp. 863–866. DOI: 10.2514/3.26851.

Folkner, W. M., Williams, J. G., and Boggs, D. H. (2009). “The Planetary and Lunar Ephemeris DE 421”. In: *The Interplanetary Network Progress Report* 42.178, pp. 1–34.

Formichella, V., Galleani, L., Signorile, G., and Sesia, I. (2021). “Time–Frequency Analysis of the Galileo Satellite Clocks: Looking for the J2 Relativistic Effect and Other Periodic Variations”. In: *GPS Solutions* 25.2, p. 56. DOI: 10.1007/s10291-021-01094-2.

Fritsche, M., Dietrich, R., Knöfel, C., Rülke, A., Vey, S., Rothacher, M., and Steigenberger, P. (2005). “Impact of Higher-Order Ionospheric Terms on GPS Estimates”. In: *Geophysical Research Letters* 32.23, p. L23311. DOI: 10.1029/2005GL024342.

Ge, M., Gendt, G., Rothacher, M., Shi, C., and Liu, J. (2008). “Resolution of GPS Carrier-Phase Ambiguities in Precise Point Positioning (PPP) with Daily Observations”. In: *Journal of Geodesy* 82.7, pp. 389–399. DOI: 10.1007/s00190-007-0187-4.

Geng, J., Meng, X., Dodson, A. H., and Teferle, F. N. (2010). “Integer Ambiguity Resolution in Precise Point Positioning: Method Comparison”. In: *Journal of Geodesy* 84.9, pp. 569–581. DOI: 10.1007/s00190-010-0399-x.

Glaner, M. and Weber, R. (2021). “PPP with Integer Ambiguity Resolution for GPS and Galileo Using Satellite Products from Different Analysis Centers”. In: *GPS Solutions* 25.3, p. 102. DOI: 10.1007/s10291-021-01140-z.

Goldstein, D. (2010). “Request for Feedback on GPS IIR-20 (SVN-49) Mitigation Options”. Global Positioning Systems Wing, US Air Force. URL: https://www.navcen.uscg.gov/pdf/gps/news/Mar2010_svn49/GPSW_SVN_49_inf_Brief_Mar_2010_Final.pdf (visited on 2022-03-01).

Golub, G. H. and Van Loan, C. F. (2013). *Matrix Computations*. 4th ed. Baltimore: John Hopkins University Press. ISBN: 978-1-4214-0794-4.

Görres, B., Campbell, J., Becker, M., and Siemes, M. (2006). “Absolute Calibration of GPS Antennas: Laboratory Results and Comparison with Field and Robot Techniques”. In: *GPS Solutions* 10.2, pp. 136–145. DOI: 10.1007/s10291-005-0015-3.

Goto, K. and Van De Geijn, R. (2008). “High-Performance Implementation of the Level-3 BLAS”. In: *ACM Transactions on Mathematical Software* 35.1. DOI: 10.1145/1377603.1377607.

Hackel, S., Steigenberger, P., Hugentobler, U., Uhlemann, M., and Montenbruck, O. (2015). “Galileo Orbit Determination Using Combined GNSS and SLR Observations”. In: *GPS Solutions* 19.1, pp. 15–25. DOI: 10.1007/s10291-013-0361-5.

Håkansson, M., Jensen, A. B. O., Horemuz, M., and Hedling, G. (2017). “Review of Code and Phase Biases in Multi-GNSS Positioning”. In: *GPS Solutions* 21.3, pp. 849–860. DOI: 10.1007/s10291-016-0572-7.

Hatch, R. (1983). “The Synergism of GPS Code and Carrier Measurements”. In: *Proceedings of the International Geodetic Symposium on Satellite Doppler Positioning*. Vol. 2. Las Cruces, NM, USA: New Mexico State University, pp. 1213–1231.

Hauschild, A. (2017a). “Basic Observation Equations”. In: *Springer Handbook of Global Navigation Satellite Systems*. Ed. by P. J. G. Teunissen and O. Montenbruck. Springer Handbooks. Cham: Springer International Publishing, pp. 561–582. DOI: 10.1007/978-3-319-42928-1_19.

Hauschild, A. (2017b). “Combinations of Observations”. In: *Springer Handbook of Global Navigation Satellite Systems*. Ed. by P. J. G. Teunissen and O. Montenbruck. Springer Handbooks. Cham: Springer International Publishing, pp. 583–604. DOI: 10.1007/978-3-319-42928-1_20.

Hauschild, A. and Montenbruck, O. (2016). “A Study on the Dependency of GNSS Pseudorange Biases on Correlator Spacing”. In: *GPS Solutions* 20.2, pp. 159–171. DOI: 10.1007/s10291-014-0426-0.

Hauschild, A., Steigenberger, P., and Rodriguez-Solano, C. (2012). “Signal, Orbit and Attitude Analysis of Japan’s First QZSS Satellite Michibiki”. In: *GPS Solutions* 16.1, pp. 127–133. DOI: 10.1007/s10291-011-0245-5.

Hegarty, C. J. (2017). “The Global Positioning System (GPS)”. In: *Springer Handbook of Global Navigation Satellite Systems*. Ed. by P. J. G. Teunissen and O. Montenbruck. Springer Handbooks. Cham: Springer International Publishing, pp. 197–218. DOI: 10.1007/978-3-319-42928-1_7.

Hernández-Pajares, M., Juan, J. M., Sanz, J., and Orús, R. (2007). “Second-Order Ionospheric Term in GPS: Implementation and Impact on Geodetic Estimates”. In: *Journal of Geophysical Research: Solid Earth* 112.B8. DOI: 10.1029/2006JB004707.

Hernández-Pajares, M., Juan, J. M., Sanz, J., Orus, R., Garcia-Rigo, A., Feltens, J., Komjathy, A., Schaer, S. C., and Krankowski, A. (2009). "The IGS VTEC Maps: A Reliable Source of Ionospheric Information since 1998". In: *Journal of Geodesy* 83.3, pp. 263–275. DOI: 10.1007/s00190-008-0266-1.

Hernández-Pajares, M., Juan, J. M., Sanz, J., Aragón-Àngel, À., García-Rigo, A., Salazar, D., and Escudero, M. (2011). "The Ionosphere: Effects, GPS Modeling and the Benefits for Space Geodetic Techniques". In: *Journal of Geodesy* 85.12, pp. 887–907. DOI: 10.1007/s00190-011-0508-5.

Herring, T. A. (1992). "Modeling Atmospheric Delays in the Analysis of Space Geodetic Data". In: *Proceedings of Refraction of Transatmospheric Signals in Geodesy*. Ed. by J. C. DeMunck and T. A. T. Spoelstra. Vol. 36. Netherlands Geodetic Commission Series. The Hague, Netherlands, pp. 57–164.

Hobiger, T. and Jakowski, N. (2017). "Atmospheric Signal Propagation". In: *Springer Handbook of Global Navigation Satellite Systems*. Ed. by P. J. G. Teunissen and O. Montenbruck. Springer Handbooks. Cham: Springer International Publishing, pp. 165–193. DOI: 10.1007/978-3-319-42928-1_6.

Hofmann-Wellenhof, B., Lichtenegger, H., and Wasle, E. (2008). *GNSS — Global Navigation Satellite Systems*. Vienna: Springer. DOI: 10.1007/978-3-211-73017-1.

Hoque, M. M. and Jakowski, N. (2008). "Estimate of Higher Order Ionospheric Errors in GNSS Positioning". In: *Radio Science* 43.5. DOI: 10.1029/2007RS003817.

Huber, P. J. (1981). *Robust Statistics*. Wiley Series in Probability and Statistics. Hoboken, NJ, USA: John Wiley & Sons, Inc. DOI: 10.1002/0471725250.

Hugentobler, U. and Montenbruck, O. (2017). "Satellite Orbits and Attitude". In: *Springer Handbook of Global Navigation Satellite Systems*. Ed. by P. J. G. Teunissen and O. Montenbruck. Springer Handbooks. Cham: Springer International Publishing, pp. 59–90. DOI: 10.1007/978-3-319-42928-1_3.

IAU SOFA Board (2022). *IAU SOFA Software Collection*. URL: http://iausofa.org (visited on 2022-03-01).

IGS Infrastructure Committee (2015). "IGS Site Guidelines". URL: https://igs.org/wp-content/uploads/2019/08/IGS-Site-Guidelines-July-2015.pdf (visited on 2022-03-01).

Inside GNSS (2016). *Air Force Disposes of Long-Serving GPS IIA Satellite*. Inside GNSS - Global Navigation Satellite Systems Engineering, Policy, and Design. URL: https://insidegnss.com/air-force-disposes-of-last-gps-iia-satellite/ (visited on 2022-03-01).

Jäggi, A., Hugentobler, U., and Beutler, G. (2006). "Pseudo-Stochastic Orbit Modeling Techniques for Low-Earth Orbiters". In: *Journal of Geodesy* 80.1, pp. 47–60. DOI: 10.1007/s00190-006-0029-9.

Jäggi, A. (2007). *Pseudo-Stochastic Orbit Modeling of Low Earth Satellites Using the Global Positioning System*. Geodätisch-Geophysikalische Arbeiten in Der Schweiz 73. Schweizerische Geodätische Kommission. ISBN: 978-3-908440-17-8. URL: https://www.sgc.ethz.ch/sgc-volumes/sgk-73.pdf (visited on 2022-03-01).

Jazaeri, S., Amiri-Simkooei, A. R., and Sharifi, M. A. (2012). “Fast Integer Least-Squares Estimation for GNSS High-Dimensional Ambiguity Resolution Using Lattice Theory”. In: *Journal of Geodesy* 86.2, pp. 123–136. DOI: 10.1007/s00190-011-0501-z.

Jekeli, C. and Montenbruck, O. (2017). “Time and Reference Systems”. In: *Springer Handbook of Global Navigation Satellite Systems*. Ed. by P. J. G. Teunissen and O. Montenbruck. Springer Handbooks. Cham: Springer International Publishing, pp. 25–58. DOI: 10.1007/978-3-319-42928-1_2.

Johnston, G., Riddell, A., and Hausler, G. (2017). “The International GNSS Service”. In: *Springer Handbook of Global Navigation Satellite Systems*. Ed. by P. J. G. Teunissen and O. Montenbruck. Springer Handbooks. Cham: Springer International Publishing, pp. 967–982. DOI: 10.1007/978-3-319-42928-1_33.

Kermarrec, G. (2018). “Stochastic Modelling of GNSS Phase Observations with Focus on Correlations”. PhD thesis. Karlsruhe Institute of Technology. DOI: 10.5445/IR/1000079152.

Klos, A., Dobslaw, H., Dill, R., and Bogusz, J. (2021). “Identifying the Sensitivity of GPS to Non-Tidal Loadings at Various Time Resolutions: Examining Vertical Displacements from Continental Eurasia”. In: *GPS Solutions* 25.3, p. 89. DOI: 10.1007/s10291-021-01135-w.

Knocke, P., Ries, J., and Tapley, B. (1988). “Earth Radiation Pressure Effects on Satellites”. In: *Proceedings of the Astrodynamics Conference*. Minneapolis, MN, USA: American Institute of Aeronautics and Astronautics, pp. 577–587. DOI: 10.2514/6.1988-4292.

Koch, D., Rothacher, M., Meindl, M., Wang, K., Schoenemann, E., and Enderle, W. (2017). “Kinematic Determination Of GNSS Orbits Including Clock Modeling”. In: *6th International Colloquium on Scientific and Fundamental Aspects of GNSS / Galileo, Valencia, Spain, October 25-27, 2017*. ESA. DOI: 20.500.11850/257810.

Koch, K.-R. and Kusche, J. (2002). “Regularization of Geopotential Determination from Satellite Data by Variance Components”. In: *Journal of Geodesy* 76.5, pp. 259–268. DOI: 10.1007/s00190-002-0245-x.

Koch, K.-R. (1999). *Parameter Estimation and Hypothesis Testing in Linear Models*. 2nd ed. Berlin, Heidelberg: Springer. DOI: 10.1007/978-3-662-03976-2.

Kouba, J. (2004). “Improved Relativistic Transformations in GPS”. In: *GPS Solutions* 8.3, pp. 170–180. DOI: 10.1007/s10291-004-0102-x.

Kouba, J. (2008). “Implementation and Testing of the Gridded Vienna Mapping Function 1 (VMF1)”. In: *Journal of Geodesy* 82.4-5, pp. 193–205. DOI: 10.1007/s00190-007-0170-0.

Kouba, J. (2009a). *A Guide to Using International GNSS Service (IGS) Products*. URL: https://www.igs.org/wp-content/uploads/2019/08/UsingIGSProductsVer21_cor.pdf (visited on 2022-03-01).

Kouba, J. (2009b). “A Simplified Yaw-Attitude Model for Eclipsing GPS Satellites”. In: *GPS Solutions* 13.1, pp. 1–12. DOI: 10.1007/s10291-008-0092-1.

Kouba, J. (2013). *A Note on the December 2013 Version of the Eclips.f Subroutine*. URL: http://acc.igs.org/orbits/eclipsDec2013note.pdf (visited on 2022-03-01).

Kouba, J. and Héroux, P. (2001). “Precise Point Positioning Using IGS Orbit and Clock Products”. In: *GPS Solutions* 5.2, pp. 12–28. DOI: 10.1007/PL00012883.

Kouba, J., Lahaye, F., and Tétreault, P. (2017). “Precise Point Positioning”. In: *Springer Handbook of Global Navigation Satellite Systems*. Ed. by P. J. G. Teunissen and O. Montenbruck. Springer Handbooks. Cham: Springer International Publishing, pp. 723–751. DOI: 10.1007/978-3-319-42928-1_25.

Krakiwsky, E. J. and Wells, D. E. (1971). *Coordinate Systems in Geodesy*. Department of Geodesy and Geomatics Engineering, University of New Brunswick. URL: http://www2.unb.ca/gge/Pubs/LN16.pdf (visited on 2022-03-01).

Kuang, D., Desai, S., and Sibois, A. (2017). “Observed Features of GPS Block IIF Satellite Yaw Maneuvers and Corresponding Modeling”. In: *GPS Solutions* 21.2, pp. 739–745. DOI: 10.1007/s10291-016-0562-9.

Kvas, A., Brockmann, J. M., Krauss, S., Schubert, T., Gruber, T., Meyer, U., Mayer-Gürr, T., Schuh, W. D., Jäggi, A., and Pail, R. (2021). “GOCO06s - A Satellite-Only Global Gravity Field Model”. In: *Earth System Science Data* 13.1, pp. 99–118. DOI: 10.5194/essd-13-99-2021.

Landskron, D. (2017). “Modeling Tropospheric Delays for Space Geodetic Techniques”. PhD thesis. Technische Universität Wien. URL: https://hdl.handle.net/20.500.12708/6797 (visited on 2022-03-01).

Landskron, D. and Böhm, J. (2018). “VMF3/GPT3: Refined Discrete and Empirical Troposphere Mapping Functions”. In: *Journal of Geodesy* 92.4, pp. 349–360. DOI: 10.1007/s00190-017-1066-2.

Laurichesse, D., Mercier, F., Berthias, J.-P., Broca, P., and Cerri, L. (2009). “Integer Ambiguity Resolution on Undifferenced GPS Phase Measurements and Its Application to PPP and Satellite Precise Orbit Determination”. In: *Navigation* 56.2, pp. 135–149. DOI: 10.1002/j.2161-4296.2009.tb01750.x.

Li, B., Qin, Y., and Liu, T. (2019). “Geometry-Based Cycle Slip and Data Gap Repair for Multi-GNSS and Multi-Frequency Observations”. In: *Journal of Geodesy* 93.3, pp. 399–417. DOI: 10.1007/s00190-018-1168-5.

Li, B. and Teunissen, P. J. G. (2011). “High Dimensional Integer Ambiguity Resolution: A First Comparison between LAMBDA and Bernese”. In: *The Journal of Navigation* 64.S1, pp. 192–210. DOI: 10.1017/S037346331100035X.

Li, P., Zhang, X., Ge, M., and Schuh, H. (2018). “Three-Frequency BDS Precise Point Positioning Ambiguity Resolution Based on Raw Observables”. In: *Journal of Geodesy* 92.12, pp. 1357–1369. DOI: 10.1007/s00190-018-1125-3.

Li, T. and Melachroinos, S. (2018). “An Enhanced Cycle Slip Repair Algorithm for Real-Time Multi-GNSS, Multi-Frequency Data Processing”. In: *GPS Solutions* 23.1, p. 1. DOI: 10.1007/s10291-018-0792-0.

Li, Z., Ziebart, M., Bhattarai, S., Harrison, D., and Grey, S. (2018). “Fast Solar Radiation Pressure Modelling with Ray Tracing and Multiple Reflections”. In: *Advances in Space Research* 61.9, pp. 2352–2365. DOI: 10.1016/J.ASR.2018.02.019.

Lichtenegger, H. and Hofmann-Wellenhof, B. (1990). “GPS-Data Preprocessing for Cycle-Slip Detection”. In: *Global Positioning System: An Overview*. Ed. by Y. Bock and N. Leppard. International Association of Geodesy Symposia. New York, NY: Springer, pp. 57–68. DOI: 10.1007/978-1-4615-7111-7_4.

Lou, Y., Liu, Y., Shi, C., Yao, X., and Zheng, F. (2014). “Precise Orbit Determination of BeiDou Constellation Based on BETS and MGEX Network”. In: *Scientific Reports* 4.1, p. 4692. DOI: 10.1038/srep04692.

Loyer, S., Banville, S., Geng, J., and Strasser, S. (2021). “Exchanging Satellite Attitude Quaternions for Improved GNSS Data Processing Consistency”. In: *Advances in Space Research* 68.6, pp. 2441–2452. DOI: 10.1016/j.asr.2021.04.049.

Loyer, S., Perosanz, F., Mercier, F., Capdeville, H., and Marty, J.-C. (2012). “Zero-Difference GPS Ambiguity Resolution at CNES–CLS IGS Analysis Center”. In: *Journal of Geodesy* 86.11, pp. 991–1003. DOI: 10.1007/s00190-012-0559-2.

Lyard, F. H., Allain, D. J., Cancet, M., Carrère, L., and Picot, N. (2021). “FES2014 Global Ocean Tide Atlas: Design and Performance”. In: *Ocean Science* 17.3, pp. 615–649. DOI: 10.5194/os-17-615-2021.

Maqsood, M., Gao, S., and Montenbruck, O. (2017). “Antennas”. In: *Springer Handbook of Global Navigation Satellite Systems*. Ed. by P. J. G. Teunissen and O. Montenbruck. Springer Handbooks. Cham: Springer International Publishing, pp. 505–534. DOI: 10.1007/978-3-319-42928-1_17.

Masoumi, S. and Moore, M. (2021). “Multi-GNSS Orbit Solutions from the Third IGS Reprocessing”. Presentation. Tour de l’IGS (online). URL: https://files.igs.org/pub/resource/pubs/workshop/2021/04-Masoumi.pdf (visited on 2022-03-01).

Massarweh, L., Strasser, S., and Mayer-Gürr, T. (2021). “On Vectorial Integer Bootstrapping Implementations in the Estimation of Satellite Orbits and Clocks Based on Small Global Networks”. In: *Advances in Space Research* 68.11, pp. 4303–4320. DOI: 10.1016/j.asr.2021.09.023.

Mayer-Gürr, T. (2006). “Gravitationsfeldbestimmung Aus Der Analyse Kurzer Bahnbögen Am Beispiel Der Satellitenmissionen CHAMP Und GRACE”. Rheinische Friedrich-Wilhelms-Universität Bonn. URL: https://hdl.handle.net/20.500.11811/2388 (visited on 2022-03-01).

Mayer-Gürr, T., Behzadpour, S., Eicker, A., Ellmer, M., Koch, B., Krauss, S., Pock, C., Rieser, D., Strasser, S., Süsser-Rechberger, B., Zehentner, N., and Kvas, A. (2021). “GROOPS: A Software Toolkit for Gravity Field Recovery and GNSS Processing”. In: *Computers & Geosciences* 155, p. 104864. DOI: 10.1016/j.cageo.2021.104864.

Meindl, M., Schaer, S., Hugentobler, U., and Beutler, G. (2004). “Tropospheric Gradient Estimation at CODE: Results from Global Solutions”. In: *Journal of the Meteorological Society of Japan. Ser. II* 82 (1B), pp. 331–338. DOI: 10.2151/jmsj.2004.331.

Melbourne, W. G. (1985). “The Case for Ranging in GPS-based Geodetic Systems”. In: *Proceedings of the First International Symposium on Precise Positioning with the Global Positioning System*. Rockville, MD: National Geodetic Survey (NGS), pp. 373–386.

Meurer, M. and Antreich, F. (2017). “Signals and Modulation”. In: *Springer Handbook of Global Navigation Satellite Systems*. Ed. by P. J. G. Teunissen and O. Montenbruck. Springer Handbooks. Cham: Springer International Publishing, pp. 91–119. DOI: 10.1007/978-3-319-42928-1_4.

Meyer, U., Sosnica, K., Arnold, D., Dahle, C., Thaller, D., Dach, R., and Jäggi, A. (2019). “SLR, GRACE and Swarm Gravity Field Determination and Combination”. In: *Remote Sensing* 11.8 (8), p. 956. DOI: 10.3390/rs11080956.

Milani, A., Nobili, A. M., and Farinella, P. (1987). *Non-Gravitational Perturbations and Satellite Geodesy*. Adam Hilger, Bristol, England. 129 pp. ISBN: 0-85274-538-9.

Misra, P. and Enge, P. (2011). *Global Positioning System: Signals, Measurements, and Performance*. 2nd ed. Lincoln: Ganga-Jamuna Press. ISBN: 0-9709544-1-7.

Montenbruck, O., Hauschild, A., and Steigenberger, P. (2014). “Differential Code Bias Estimation Using Multi-GNSS Observations and Global Ionosphere Maps”. In: *Navigation* 61.3, pp. 191–201. DOI: 10.1002/navi.64.

Montenbruck, O., Schmid, R., Mercier, F., Steigenberger, P., Noll, C., Fatkulin, R., Kogure, S., and Ganeshan, A. (2015a). “GNSS Satellite Geometry and Attitude Models”. In: *Advances in Space Research* 56.6, pp. 1015–1029. DOI: 10.1016/j.asr.2015.06.019.

Montenbruck, O., Steigenberger, P., and Hugentobler, U. (2015b). “Enhanced Solar Radiation Pressure Modeling for Galileo Satellites”. In: *Journal of Geodesy* 89.3, pp. 283–297. DOI: 10.1007/s00190-014-0774-0.

Montenbruck, O. and Gill, E. (2000). *Satellite Orbits – Models, Methods and Applications*. Berlin, Heidelberg: Springer. DOI: 10.1007/978-3-642-58351-3.

Montenbruck, O., Hugentobler, U., Dach, R., Steigenberger, P., and Hauschild, A. (2012). “Apparent Clock Variations of the Block IIF-1 (SVN62) GPS Satellite”. In: *GPS Solutions* 16.3, pp. 303–313. DOI: 10.1007/s10291-011-0232-x.

Montenbruck, O., Steigenberger, P., Prange, L., Deng, Z., Zhao, Q., Perosanz, F., Romero, I., Noll, C., Stürze, A., Weber, G., Schmid, R., MacLeod, K., and Schaer, S. (2017). “The Multi-GNSS Experiment (MGEX) of the International GNSS Service (IGS) – Achievements, Prospects and Challenges”. In: *Advances in Space Research* 59.7, pp. 1671–1697. DOI: 10.1016/j.asr.2017.01.011.

Montenbruck, O., van Helleputte, T., Kroes, R., and Gill, E. (2005). “Reduced Dynamic Orbit Determination Using GPS Code and Carrier Measurements”. In: *Aerospace Science and Technology* 9.3, pp. 261–271. DOI: 10.1016/j.ast.2005.01.003.

Navarro-Reyes, D., Castro, R., and Ramos Bosch, P. (2015). “Galileo First FOC Launch: Recovery Mission Design”. In: *Proceedings of the 25th International Symposium on Space Flight Dynamics*. ISSFD. Munich, Germany. URL: https://issfd.org/2015/files/downloads/papers/057_Navarro-Reyes.pdf (visited on 2022-03-01).

Niell, A. E. (1996). “Global Mapping Functions for the Atmosphere Delay at Radio Wavelengths”. In: *Journal of Geophysical Research: Solid Earth* 101.B2, pp. 3227–3246. DOI: 10.1029/95JB03048.

Niell, A. E. (2000). “Improved Atmospheric Mapping Functions for VLBI and GPS”. In: *Earth, Planets and Space* 52.10, pp. 699–702. DOI: 10.1186/BF03352267.

Niell, A. E. (2001). “Preliminary Evaluation of Atmospheric Mapping Functions Based on Numerical Weather Models”. In: *Physics and Chemistry of the Earth, Part A: Solid Earth and Geodesy*. Proceedings of the First COST Action 716 Workshop Towards Operational GPS Meteorology and the Second Network Workshop of the International GPS Service (IGS) 26.6, pp. 475–480. DOI: 10.1016/S1464-1895(01)00087-4.

Orliac, E., Dach, R., Wang, K., Rothacher, M., Voithenleitner, D., Hugentobler, U., Heinze, M., and Svehla, D. (2012). “Deterministic and Stochastic Receiver Clock Modeling in Precise Point Positioning”. EGU General Assembly 2012, Abstract EGU2012-7199. Vienna, Austria, p. 7199.

Petit, G. and Luzum, B., eds. (2010). *IERS Conventions (2010), IERS Technical Note 36*. Frankfurt am Main: Verlag des Bundesamts für Kartographie und Geodäsie. 179 pp. ISBN: 3-89888-989-6. URL: https://www.iers.org/IERS/EN/Publications/TechnicalNotes/tn36.html (visited on 2022-03-01).

Petrie, E. J., King, M. A., Moore, P., and Lavallée, D. A. (2010). “Higher-Order Ionospheric Effects on the GPS Reference Frame and Velocities”. In: *Journal of Geophysical Research* 115.B3, B03417. DOI: 10.1029/2009JB006677.

Prange, L., Orliac, E., Dach, R., Arnold, D., Beutler, G., Schaer, S., and Jäggi, A. (2017). “CODE’s Five-System Orbit and Clock Solution—the Challenges of Multi-GNSS Data Analysis”. In: *Journal of Geodesy* 91.4, pp. 345–360. DOI: 10.1007/s00190-016-0968-8.

Qing, Y., Lou, Y., Dai, X., and Liu, Y. (2017). “Benefits of Satellite Clock Modeling in BDS and Galileo Orbit Determination”. In: *Advances in Space Research* 60.12, pp. 2550–2560. DOI: 10.1016/J.ASR.2017.03.040.

re3data.org (2016). “VMF Data Server”. Editing Status 2020-12-14. re3data.org - Registry of Research Data Repositories. DOI: 10.17616/R3RD2H.

Rebischung, P. (2021). “Terrestrial Frame Solutions from the IGS Third Reprocessing”. EGU General Assembly 2021, Online, 19–30 Apr 2021. DOI: 10.5194/egusphere-egu21-2144.

Rebischung, P., Altamimi, Z., Ray, J., and Garayt, B. (2016). “The IGS Contribution to ITRF2014”. In: *Journal of Geodesy* 90.7, pp. 611–630. DOI: 10.1007/s00190-016-0897-6.

Reckeweg, F. (2020). “Integer Ambiguity Resolution for Multi-GNSS and Multi-Signal Raw Phase Observations”. PhD thesis. Technische Universität Darmstadt. URL: https://tuprints.ulb.tu-darmstadt.de/11483/1/Dissertation_TUDa_FReckeweg_2020.pdf (visited on 2022-03-01).

Reuter, R. (1982). “Über Integralformeln der Einheitssphäre und harmonische Splinefunktionen”. PhD thesis. Aachen: Geodät. Inst. d. Rhein.-Westfäl. Techn. Hochsch. 197 pp.

Revnivykh, S., Bolkunov, A., Serdyukov, A., and Montenbruck, O. (2017). “GLONASS”. In: *Springer Handbook of Global Navigation Satellite Systems*. Ed. by P. J. G. Teunissen and O. Montenbruck. Springer Handbooks. Cham: Springer International Publishing, pp. 219–245. DOI: 10.1007/978-3-319-42928-1_8.

Ries, J. (2017). “Conventional Model Update for Rotational Deformation”. AGU Fall Meeting 2017. New Orleans, LA, USA. DOI: 10.26153/tsw/2659.

Rodriguez-Solano, C. J., Hugentobler, U., and Steigenberger, P. (2012a). "Adjustable Box-Wing Model for Solar Radiation Pressure Impacting GPS Satellites". In: *Advances in Space Research* 49.7, pp. 1113–1128. DOI: 10.1016/j.asr.2012.01.016.

Rodriguez-Solano, C. J., Hugentobler, U., and Steigenberger, P. (2012b). "Impact of Albedo Radiation on GPS Satellites". In: *Geodesy for Planet Earth*. Ed. by S. Kenyon, M. C. Pacino, and U. Marti. Vol. 136. International Association of Geodesy Symposia. Springer, Berlin, Heidelberg, pp. 113–119. DOI: 10.1007/978-3-642-20338-1_14.

Rodriguez-Solano, C. J., Hugentobler, U., Steigenberger, P., Bloßfeld, M., and Fritsche, M. (2014). "Reducing the Draconitic Errors in GNSS Geodetic Products". In: *Journal of Geodesy* 88.6, pp. 559–574. DOI: 10.1007/s00190-014-0704-1.

Rodriguez-Solano, C. J., Hugentobler, U., Steigenberger, P., and Lutz, S. (2012c). "Impact of Earth Radiation Pressure on GPS Position Estimates". In: *Journal of Geodesy* 86.5, pp. 309–317. DOI: 10.1007/s00190-011-0517-4.

Rodriguez-Solano, C. J. (2009). "Impact of Albedo Modelling on GPS Orbits". MA thesis. München: Technische Universität München. URL: https://mediatum.ub.tum.de/doc/1368717/file.pdf (visited on 2022-03-01).

Rodriguez-Solano, C. J. (2014). "Impact of Non-Conservative Force Modeling on GNSS Satellite Orbits and Global Solutions". PhD thesis. München: Technische Universität München. URL: https://mediatum.ub.tum.de/doc/1188612/file.pdf (visited on 2022-03-01).

Romero, I., ed. (2020). *RINEX: The Receiver Independent Exchange Format Version 3.05*. IGS/RTCM RINEX Working Group. URL: https://files.igs.org/pub/data/format/rinex305.pdf (visited on 2022-03-01).

Rothacher, M., Beutler, G., Herring, T. A., and Weber, R. (1999). "Estimation of Nutation Using the Global Positioning System". In: *Journal of Geophysical Research: Solid Earth* 104.B3, pp. 4835–4859. DOI: 10.1029/1998JB900078.

Rothacher, M., Springer, T. A., Schaer, S., and Beutler, G. (1998). "Processing Strategies for Regional GPS Networks". In: *Advances in Positioning and Reference Frames*. Ed. by F. K. Brunner. Vol. 118. International Association of Geodesy Symposia. Springer, Berlin, Heidelberg, pp. 93–100. DOI: 10.1007/978-3-662-03714-0_14.

Rothacher, M. and Schmid, R. (2010). *ANTEX: The Antenna Exchange Format, Version 1.4*. International GNSS Service. URL: https://files.igs.org/pub/data/format/antex14.txt (visited on 2022-03-01).

Rothacher, M. and Thaller, D., eds. (2006). *SINEX - Solution (Software/Technique) INdependent EXchange Format Version 2.02*. IERS Analysis Coordination. URL: https://www.iers.org/SharedDocs/Publikationen/EN/IERS/Documents/ac/sinex/sinex_v202_pdf.pdf?__blob=publicationFile&v=2 (visited on 2022-03-01).

Saastamoinen, J. (1972). "Atmospheric Correction for the Troposphere and Stratosphere in Radio Ranging Satellites". In: *The Use of Artificial Satellites for Geodesy*. Ed. by S. W. Henriksen, M. Armando, and B. H. Chovitz. Washington, D. C.: American Geophysical Union, pp. 247–251. DOI: 10.1029/GM015p0247.

Sakic, P., Mansur, G. B., Männel, B., Brack, A., and Schuh, H. (2022). "An Experimental Combination of IGS Repro3 Campaign's Orbit Products Using a Variance Component Estimation Strategy". Preprint submitted to International Association of Geodesy Symposia proceedings. DOI: 10.31223/X5K614.

Sanz, J., Miguel Juan, J., Rovira-Garcia, A., and González-Casado, G. (2017). "GPS Differential Code Biases Determination: Methodology and Analysis". In: *GPS Solutions* 21.4, pp. 1549–1561. DOI: 10.1007/s10291-017-0634-5.

Schaer, S. (1999). *Mapping and Predicting the Earth's Ionosphere Using the Global Positioning System*. Geodätisch-Geophysikalische Arbeiten in Der Schweiz 59. Schweizerische Geodätische Kommission. ISBN: 3-908440-01-7. URL: https://www.sgc.ethz.ch/sgc-volumes/sgk-59.pdf (visited on 2022-03-01).

Schaer, S. (2018). *SINEX_BIAS—Solution (Software/Technique) INdependent EXchange Format for GNSS Biases Version 1.00*. IGS Bias and Calibration Working Group. URL: https://files.igs.org/pub/data/format/sinex_bias_100.pdf (visited on 2022-03-01).

Schmid, R., Dach, R., Collilieux, X., Jäggi, A., Schmitz, M., and Dilssner, F. (2016). "Absolute IGS Antenna Phase Center Model igs08.atx: Status and Potential Improvements". In: *Journal of Geodesy* 90.4, pp. 343–364. DOI: 10.1007/s00190-015-0876-3.

Schmid, R. and Rothacher, M. (2003). "Estimation of Elevation-Dependent Satellite Antenna Phase Center Variations of GPS Satellites". In: *Journal of Geodesy* 77.7, pp. 440–446. DOI: 10.1007/s00190-003-0339-0.

Schmid, R., Steigenberger, P., Gendt, G., Ge, M., and Rothacher, M. (2007). "Generation of a Consistent Absolute Phase-Center Correction Model for GPS Receiver and Satellite Antennas". In: *Journal of Geodesy* 81.12, pp. 781–798. DOI: 10.1007/s00190-007-0148-y.

Schön, S. and Brunner, F. K. (2008). "Atmospheric Turbulence Theory Applied to GPS Carrier-Phase Data". In: *Journal of Geodesy* 82.1, pp. 47–57. DOI: 10.1007/s00190-007-0156-y.

Schönemann, E. (2014). "Analysis of GNSS Raw Observations in PPP Solutions". In: *Schriftenreihe der Fachrichtung Geodäsie* 42. URL: https://tuprints.ulb.tu-darmstadt.de/3843/ (visited on 2022-03-01).

Schönemann, E., Becker, M., and Springer, T. (2011). "A New Approach for GNSS Analysis in a Multi-GNSS and Multi-Signal Environment". In: *Journal of Geodetic Science* 1.3, pp. 204–214. DOI: 10.2478/v10156-010-0023-2.

Selmke, I., Dach, R., Arnold, D., Prange, L., Schaer, S., Sidorov, D., Stebler, P., Villiger, A., Jäggi, A., and Hugentobler, U. (2020). *CODE Repro3 Product Series for the IGS*. Bern. DOI: 10.7892/boris.135946.

Shi, J. and Gao, Y. (2014). "A Comparison of Three PPP Integer Ambiguity Resolution Methods". In: *GPS Solutions* 18.4, pp. 519–528. DOI: 10.1007/s10291-013-0348-2.

Sleewaegen, J.-M. and Clemente, F. (2018). "Quantifying the Pilot-Data Bias on All Current GNSS Signals and Satellites". IGS Workshop 2018. Wuhan, China. URL: https://files.igs.org/pub/resource/pubs/workshop/2018/IGSWS-2018-PY05-05.pdf (visited on 2022-03-01).

Sleewaegen, J.-M., Simsky, A., Wilde, W., Boon, F., and Willems, T. (2012). "Demystifying GLONASS Inter-Frequency Carrier Phase Biases". In: *Inside GNSS* 7.3, pp. 57–61. URL: https://www.insidegnss.com/auto/mayjune12-Sleewaegen.pdf (visited on 2022-03-01).

Springer, T. A., Beutler, G., and Rothacher, M. (1999a). "A New Solar Radiation Pressure Model for GPS Satellites". In: *GPS Solutions* 2.3, pp. 50–62. DOI: 10.1007/PL00012757.

Springer, T. A., Beutler, G., and Rothacher, M. (1999b). "Improving the Orbit Estimates of GPS Satellites". In: *Journal of Geodesy* 73.3, pp. 147–157. DOI: 10.1007/s001900050230.

Steigenberger, P. and Montenbruck, O. (2017). "Galileo Status: Orbits, Clocks, and Positioning". In: *GPS Solutions* 21.2, pp. 319–331. DOI: 10.1007/s10291-016-0566-5.

Steigenberger, P., Thoelert, S., and Montenbruck, O. (2018). "GNSS Satellite Transmit Power and Its Impact on Orbit Determination". In: *Journal of Geodesy* 92.6, pp. 609–624. DOI: 10.1007/s00190-017-1082-2.

Steigenberger, P., Thoelert, S., and Montenbruck, O. (2020). "GPS III Vespucci: Results of Half a Year in Orbit". In: *Advances in Space Research* 66.12, pp. 2773–2785. DOI: 10.1016/j.asr.2020.03.026.

Strasser, S., Banville, S., Kvas, A., Loyer, S., and Mayer-Gürr, T. (2021). "Comparison and Generalization of GNSS Satellite Attitude Models". EGU General Assembly 2021, Online, 19–30 Apr 2021. DOI: 10.5194/egusphere-egu21-7825.

Strasser, S. and Mayer-Gürr, T. (2020). "Efficient Multi-GNSS Processing Based on Raw Observations from Large Global Station Networks". EGU General Assembly 2020, Online, 3–8 May 2020. DOI: 10.5194/egusphere-egu2020-3014.

Strasser, S. and Mayer-Gürr, T. (2021). *IGS Repro3 Products by Graz University of Technology (TUG)*. Version 1. DOI: 10.3217/dataset-4528-0723-0867.

Strasser, S., Mayer-Gürr, T., and Zehentner, N. (2019). "Processing of GNSS Constellations and Ground Station Networks Using the Raw Observation Approach". In: *Journal of Geodesy* 93.7, pp. 1045–1057. DOI: 10.1007/s00190-018-1223-2.

Švehla, D. and Rothacher, M. (2005). "Kinematic Precise Orbit Determination for Gravity Field Determination". In: *A Window on the Future of Geodesy*. Ed. by P. D. F. Sansò. International Association of Geodesy Symposia. Berlin/Heidelberg: Springer-Verlag, pp. 181–188. DOI: 10.1007/3-540-27432-4_32.

Teunissen, P. J. G. (1995). "The Least-Squares Ambiguity Decorrelation Adjustment: A Method for Fast GPS Integer Ambiguity Estimation". In: *Journal of Geodesy* 70.1-2, pp. 65–82. DOI: 10.1007/BF00863419.

Teunissen, P. J. G., Massarweh, L., and Verhagen, S. (2021). "Vectorial Integer Bootstrapping: Flexible Integer Estimation with Application to GNSS". In: *Journal of Geodesy* 95.9, p. 99. DOI: 10.1007/s00190-021-01552-2.

Teunissen, P. J. G. (2017). "Carrier Phase Integer Ambiguity Resolution". In: *Springer Handbook of Global Navigation Satellite Systems*. Ed. by P. J. G. Teunissen and O. Montenbruck. Springer Handbooks. Cham: Springer International Publishing, pp. 661–685. DOI: 10.1007/978-3-319-42928-1_23.

Tewarson, R. P. and Cheng, K. Y. (1973). “A Desirable Form for Sparse Matrices When Computing Their Inverse in Factored Forms”. In: *Computing* 11.1, pp. 31–38. DOI: 10.1007/BF02239469.

United Nations General Assembly (2015). *A Global Geodetic Reference Frame for Sustainable Development*. Resolution 69/266 adopted by the General Assembly on 26 February 2015. New York, NY, USA. URL: http://www.un.org/en/ga/search/view_doc.asp?symbol=A/RES/69/266 (visited on 2022-03-01).

Verhagen, S., Tiberius, C., Li, B., and Teunissen, P. J. G. (2012). “Challenges in Ambiguity Resolution: Biases, Weak Models, and Dimensional Curse”. In: *2012 6th ESA Workshop on Satellite Navigation Technologies (Navitec 2012) & European Workshop on GNSS Signals and Signal Processing*, pp. 1–8. DOI: 10.1109/NAVITEC.2012.6423075.

Vermeer, M. (1997). “The Precision of Geodetic GPS and One Way of Improving It”. In: *Journal of Geodesy* 71.4, pp. 240–245. DOI: 10.1007/s001900050091.

Villiger, A., Dach, R., Schaer, S., Prange, L., Zimmermann, F., Kuhlmann, H., Wübbena, G., Schmitz, M., Beutler, G., and Jäggi, A. (2020). “GNSS Scale Determination Using Calibrated Receiver and Galileo Satellite Antenna Patterns”. In: *Journal of Geodesy* 94.9, p. 93. DOI: 10.1007/s00190-020-01417-0.

Villiger, A., Schaer, S., Dach, R., Prange, L., Sušnik, A., and Jäggi, A. (2019). “Determination of GNSS Pseudo-Absolute Code Biases and Their Long-Term Combination”. In: *Journal of Geodesy*, pp. 1–14. DOI: 10.1007/s00190-019-01262-w.

Wang, C., Guo, J., Zhao, Q., and Liu, J. (2018). “Yaw Attitude Modeling for BeiDou I06 and BeiDou-3 Satellites”. In: *GPS Solutions* 22.4, p. 117. DOI: 10.1007/s10291-018-0783-1.

Wang, N., Li, Z., Duan, B., Hugentobler, U., and Wang, L. (2020). “GPS and GLONASS Observable-Specific Code Bias Estimation: Comparison of Solutions from the IGS and MGEX Networks”. In: *Journal of Geodesy* 94.8, p. 74. DOI: 10.1007/s00190-020-01404-5.

Wang, N., Yuan, Y., Li, Z., Montenbruck, O., and Tan, B. (2016). “Determination of Differential Code Biases with Multi-GNSS Observations”. In: *Journal of Geodesy* 90.3, pp. 209–228. DOI: 10.1007/s00190-015-0867-4.

Wanninger, L. (2012). “Carrier-Phase Inter-Frequency Biases of GLONASS Receivers”. In: *Journal of Geodesy* 86.2, pp. 139–148. DOI: 10.1007/s00190-011-0502-y.

Wei, H., Li, J., Zhang, S., and Xu, X. (2019). “Cycle Slip Detection and Repair for Dual-Frequency LEO Satellite GPS Carrier Phase Observations with Orbit Dynamic Model Information”. In: *Remote Sensing* 11.11 (11), p. 1273. DOI: 10.3390/rs11111273.

Weinbach, U. and Schön, S. (2011). “GNSS Receiver Clock Modeling When Using High-Precision Oscillators and Its Impact on PPP”. In: *Advances in Space Research* 47.2, pp. 229–238. DOI: 10.1016/J.ASR.2010.06.031.

Weiss, J. P., Steigenberger, P., and Springer, T. (2017). “Orbit and Clock Product Generation”. In: *Springer Handbook of Global Navigation Satellite Systems*. Ed. by P. J. G. Teunissen and O. Montenbruck. Springer Handbooks. Cham: Springer International Publishing, pp. 983–1010. DOI: 10.1007/978-3-319-42928-1_34.

Wielgosz, P., Milanowska, B., Krypiak-Gregorczyk, A., and Jarmołowski, W. (2021). "Validation of GNSS-derived Global Ionosphere Maps for Different Solar Activity Levels: Case Studies for Years 2014 and 2018". In: *GPS Solutions* 25.3, p. 103. DOI: 10.1007/s10291-021-01142-x.

Wielicki, B. A., Barkstrom, B. R., Harrison, E. F., Lee, R. B., Louis Smith, G., and Cooper, J. E. (1996). "Clouds and the Earth's Radiant Energy System (CERES): An Earth Observing System Experiment". In: *Bulletin of the American Meteorological Society* 77.5, pp. 853–868. DOI: 10.1175/1520-0477(1996)077<0853:CATERE>2.0.CO;2.

Won, J.-H. and Pany, T. (2017). "Signal Processing". In: *Springer Handbook of Global Navigation Satellite Systems*. Ed. by P. J. G. Teunissen and O. Montenbruck. Springer Handbooks. Cham: Springer International Publishing, pp. 401–442. DOI: 10.1007/978-3-319-42928-1_14.

Woo, K. T. (2000). "Optimum Semicodeless Carrier-Phase Tracking of L2". In: *Navigation* 47.2, pp. 82–99. DOI: 10.1002/j.2161-4296.2000.tb00204.x.

Wu, J. T., Wu, S. C., Hajj, G. A., Bertiger, W. I., and M., L. S. (1993). "Effects of Antenna Orientation on GPS Carrier Phase". In: *Manuscripta Geodaetica* 18.2, pp. 91–98.

Wu, S. C., Yunck, T. P., and Thornton, C. L. (1991). "Reduced-Dynamic Technique for Precise Orbit Determination of Low Earth Satellites". In: *Journal of Guidance, Control, and Dynamics* 14.1, pp. 24–30. DOI: 10.2514/3.20600.

Wübbena, G. (1985). "Software Developments of Geodetic Positioning with GPS Using TI 4100 Code and Carrier Measurements". In: *Proceedings of the First International Symposium on Precise Positioning with the Global Positioning System*. Rockville, MD: National Geodetic Survey (NGS), pp. 403–412.

Xiao, G., Mayer, M., Heck, B., Sui, L., Zeng, T., and Zhao, D. (2017). "Improved Time-Differenced Cycle Slip Detect and Repair for GNSS Undifferenced Observations". In: *GPS Solutions* 22.1, p. 6. DOI: 10.1007/s10291-017-0677-7.

Xue, J., Song, S., and Zhu, W. (2016). "Estimation of Differential Code Biases for Beidou Navigation System Using Multi-GNSS Observations: How Stable Are the Differential Satellite and Receiver Code Biases?" In: *Journal of Geodesy* 90.4, pp. 309–321. DOI: 10.1007/s00190-015-0874-5.

Zajdel, R., Sośnica, K., Dach, R., Bury, G., Prange, L., and Jäggi, A. (2019). "Network Effects and Handling of the Geocenter Motion in Multi-GNSS Processing". In: *Journal of Geophysical Research: Solid Earth* 124.6, pp. 5970–5989. DOI: 10.1029/2019JB017443.

Zajdel, R., Kazmierski, K., and Sośnica, K. (2022). "Orbital Artifacts in Multi-GNSS Precise Point Positioning Time Series". In: *Journal of Geophysical Research: Solid Earth* 127.2, e2021JB022994. DOI: 10.1029/2021JB022994.

Zehentner, N. (2016). "Kinematic Orbit Positioning Applying the Raw Observation Approach to Observe Time Variable Gravity". PhD thesis. Graz University of Technology. DOI: 10.13140/RG.2.2.33916.33927.

Zehentner, N. and Mayer-Gürr, T. (2014). "New Approach to Estimate Time Variable Gravity Fields from High-Low Satellite Tracking Data". In: *Gravity, Geoid and Height Systems*. Ed. by U. Marti. Vol. 141. International Association of Geodesy Symposia. Cham: Springer International Publishing, pp. 111–116. DOI: 10.1007/978-3-319-10837-7_14.

Zehentner, N. and Mayer-Gürr, T. (2016). “Precise Orbit Determination Based on Raw GPS Measurements”. In: *Journal of Geodesy* 90.3, pp. 275–286. DOI: 10.1007/s00190-015-0872-7.

Zeng, T., Sui, L., Ruan, R., Jia, X., Feng, L., and Xiao, G. (2021). “GPS Triple-Frequency Undifferenced and Uncombined Precise Orbit Determination with the Consideration of Receiver Time-Variant Bias”. In: *Measurement* 169, p. 108281. DOI: 10.1016/j.measurement.2020.108281.

Zhang, X. and Li, P. (2016). “Benefits of the Third Frequency Signal on Cycle Slip Correction”. In: *GPS Solutions* 20.3, pp. 451–460. DOI: 10.1007/s10291-015-0456-2.

Ziebart, M. and Dare, P. (2001). “Analytical Solar Radiation Pressure Modelling for GLONASS Using a Pixel Array”. In: *Journal of Geodesy* 75.11, pp. 587–599. DOI: 10.1007/s001900000136.

Ziebart, M., Edwards, S., Adhya, S., Sibthorpe, A., Arrowsmith, P., and Cross, P. (2004). “High Precision GPS IIR Orbit Prediction Using Analytical Non-conservative Force Models”. Proceedings of the 17th International Technical Meeting of the Satellite Division of The Institute of Navigation (ION GNSS 2004), pp. 1764–1770.

Zumberge, J. F., Heflin, M. B., Jefferson, D. C., Watkins, M. M., and Webb, F. H. (1997). “Precise Point Positioning for the Efficient and Robust Analysis of GPS Data from Large Networks”. In: *Journal of Geophysical Research: Solid Earth* 102.B3, pp. 5005–5017. DOI: 10.1029/96jb03860.

Acronyms

AC	Antenna center
ACO	Antenna center offset
ACV	Antenna center variation
ANTEX	Antenna Exchange
AOD1B	Atmosphere and Ocean De-aliasing Level 1B
ARF	Antenna reference frame
ARP	Antenna reference point
AU	Astronomical unit
BDS	BeiDou Navigation Satellite System
CDMA	Code division multiple access
CERES	Clouds and the Earth's Radiant Energy System
CIP	Celestial Intermediate Pole
COD	Center for Orbit Determination in Europe
COM	Center of mass
CRF	Celestial reference frame
DORIS	Doppler orbitography and radiopositioning integrated by satellite
ECMWF	European Centre for Medium-Range Weather Forecasts
ECOM	Empirical CODE Orbit Model
EOP	Earth orientation parameter
ERA	Earth Rotation Angle
ERP	Earth radiation pressure
ESA	European Space Agency
FDMA	Frequency division multiple access
FOC	Full operational capability

GCRS	Geocentric Celestial Reference System
GLONASS	Globalnaya Navigatsionnaya Sputnikovaya Sistema
GNSS	Global navigation satellite system
GPS	Global Positioning System
GPT3	Global Pressure and Temperature 3
GRACE	Gravity Recovery And Climate Experiment
GROOPS	Gravity Recovery Object Oriented Programming System
GSPM	GPS Solar Pressure Model
HWM	Hatch-Melbourne-Wübbena
IAG	International Association of Geodesy
IAU	International Astronomical Union
ICRF	International Celestial Reference Frame
ICRS	International Celestial Reference System
IERS	International Earth Rotation and Reference Systems Service
IGRF	International Geomagnetic Reference Field
IGS	International GNSS Service
ILS	Integer least-squares
IMF	Isobaric Mapping Function
IOV	In-orbit validation
ITRF	International Terrestrial Reference Frame
ITRS	International Terrestrial Reference System
JPL	Jet Propulsion Laboratory
LAMBDA	Least-squares ambiguity decorrelation adjustment
LEO	Low Earth orbit
LOD	Length of day
LRF	Local topocentric reference frame
LSDM	Land Surface Discharge Model
MEO	Medium Earth orbit
MGEX	Multi-GNSS Experiment and Pilot Project
MPI	Message Passing Interface

NMF Niell Mapping Function
NNR No-net rotation
NNS No-net scale
NNT No-net translation

ORF Local orbit reference frame

PPP Precise point positioning
PRN Pseudorandom noise

QZSS Quasi-Zenith Satellite System

repro3 Third reprocessing campaign
RINEX Receiver Independent Exchange
RMS Root mean square

SINEX Solution Independent Exchange
SLR Satellite laser ranging
SOFA Standards of Fundamental Astronomy
SRF Satellite body reference frame
SRP Solar radiation pressure
STEC Slant total electron content
SVN Space vehicle number

TEC Total electron content
TECU Total electron content unit
TRF Terrestrial reference frame
TRR Thermal reradiation
TUG Graz University of Technology

UT1 Universal Time 1
UTC Coordinated Universal Time

VCE Variance component estimation

VLBI Very long baseline interferometry
VMF1 Vienna Mapping Functions 1
VMF3 Vienna Mapping Functions 3
VTEC Vertical total electron content

ZHD Zenith hydrostatic delay
ZTD Zenith total delay
ZWD Zenith wet delay

List of figures

List of tables

List of listings